CARBON ENRICHED THERMAL SPRAYED HARD METAL COATINGS USED IN PCD SINTERING

Amanda Lynne McKie

A PhD thesis submitted to the Faculty of Engineering and the Built Environment, University of the Witwatersrand, in fulfillment of the requirements for the degree of Doctor of Philosophy.

Johannesburg 2012

Declaration

I declare that this thesis is my own unaided work. It is being submitted to the degree of Doctor of Philosophy to the University of the Witwatersrand, Johannesburg. It has not been submitted before for any degree or examination to any other University.

Amanda Lynne McKie

_____ day of _____ 2012

Abstract

During the sintering of fine grain (0.5µm) polycrystalline diamond (PCD) composite materials under high pressure-high temperature (HPHT) conditions, abnormal grain growth (AGG) of the diamond is observed at the diamond/substrate interface. These abnormally grown diamond particles can be several hundreds of microns in diameter and are major flaws in the material that can cause premature fail during application. Understanding of the mechanisms of grain growth in fine grained PCD can bring about ways to eliminate this defect.

This project aimed to investigate the reduction of AGG diamond in 0.5µm diamond by changing the solubility of the infiltrating molten Co liquid used in PCD sintering. By increasing the carbon saturation level of the infiltrating Co melt, the chance for Ostwald ripening conditions of the diamond during sintering is reduced and AGG is eliminated.

Modification of the carbon saturation within the Co melt can be achieved by carbon enriching the WC-Co substrate. Carbon enrichment can be achieved by carbon enriching a WC-Co powder and then HVOF thermal spraying it onto a WC-Co substrate. Results showed that carbon enrichment of coatings (2-6wt%C) was possible using a phenolic resin precursor followed by pyrolysis. Higher carbon contents added presented HVOF spraying problems; high free carbon burn off and lowered melting points which can lead to poor spraying and lower deposition rates.

Carbon enrichment of WC-Co powders was also thought to potentially reduce undesirable eta phase generation during thermal spraying and thus result in an improvement in the wear resistance of the coatings on metal substrates (mild steel). These tests were performed and showed that eta phase generation can to be suppressed during thermal spraying of the carbon enriched powders. Wear resistance and hardness effects on the carbon enriched coatings before and after

annealing heat treatment were also analysed and good results were obtained but contradictory is some cases when compared to other authors. Overall, 2wt%C samples showed the most improved properties in terms of WC and eta phase suppression and improved wear resistance, although at the expense of hardness.

Another method of carbon enrichment was by using a graphite/diamond enhanced carbide (GDEC) interlayer. Both methods were analysed in this project. Carbon coatings were determined not to be very effective in eliminating AGG of fine grain diamond due to limited retained carbon in the coatings to sufficiently saturate the infiltrating melt. GDEC substrates on the other hand show a better possibility, a full 10vol.% GDEC was proved to suppress AGG formation at the diamond/substrate interface of 0.5µm diamond PCD.

Alternatively, the reduction of AGG in fine grain diamond can also be eliminated by changing the interfacial energy of the diamond during sintering; this could be achieved by addition of a grain growth inhibitor. This project investigated the potential of a strong carbide former such as VC as a grain growth inhibitor in fine grain diamond. Addition of 2wt%VC proved to be sufficient to modify the interfacial energy to suppress AGG grain growth of fine (0.5µm) diamond.

A model was developed comparing the grain growth mechanisms within a conventional carbide substrate and a carbon enriched substrate (coating or GDEC). Both grain growth of the diamond and formation of Co pool formation were discussed.

Dedication

I dedicate this work to the most important people in my life; my mom, dad and brother.

Thanks so all your love and support. I love you all.

Acknowledgements

I would like to acknowledge and thank the following people and organizations for their valuable contribution to this project and which facilitated the completion of this work.

a) Prof. I. Sigalas for suggestions and supervising this work.

b) Dr. Mathias Herrmann for his advice, useful comments, time, suggestions and constructive criticism which without his help this project would have failed.

c) Dr Roger Nilen for help, suggestions and facilitation of this project at Element Six.

d) Element Six (Pty) Ltd – Diamond Research Laboratory for their financial support and use of their facilities.

e) University of the Witwatersrand, Johannesburg for the use of their facilities.

f) NRF/DST Centre of Excellence in Strong Materials (CoE-SM), NRF/DST for their financial support.

g) Hugo Howse and ThermaSpray SA (Pty) Ltd for help and advice and the use of their facilities.

h) My fellow colleagues at Wits, especially Peter and TK, for the advice and friendship.

i) The staff at Element Six (DRL), especially Geoff Davies, Kabelo Kekane, Johan Myburgh for their help and advice.

j) O. Johnson for his time and assistance with achieving good SEM images.

k) Lastly my family, the support and sacrifices they have throughout this time period. I love you all.

Table of Content

List of Figures

List of Tables

List of Symbols

t – Time (s)

K – Constant

r – Average particle size

γ_{sl} – Solid-liquid interfacial energy

Ω – Atomic volume

T – Temperature

k – Boltzmann constant

C - Concentration

C_o – Equilibrium concentration

v – Growth rate

v_D – Growth rate of diffusion

v_R – Growth rate of interface reaction

R – Distance from center of equilibrium shape facet

R* - Critical nucleus size (i.e. particle size of zero growth)

R_{ave} – Average particle size

R_{max} – Maximum particle size

h – Height of the 2D nucleus

A – Grain facet area

υ – Vibration frequency of atom in liquid

n_o – Atom density

n*- Number of atoms in a position close to critical nucleus

σ – Step/edge free energy of the 2D nucleus

θ – Contact angle between the original surface and the titled surface of a double twin

Δg_m – Activation energy of migration across the interface

Δg_v – Volumetric Gibbs free energy (Volumetric driving force)

Δg_c – Critical driving force for growth

Δg_{max} – Maximum driving force for growth

V_m – Volumetric …

NGG - Normal grain growth

AGG – Abnormal grain growth

H_v – Vickers Hardness

η – eta phases (Co_6W_6C, Co_3W_3C etc…)

Chapter 1: Introduction and Motivation

Polycrystalline diamond (PCD) materials are used extensively for their excellent properties such as high hardness, good thermal conductivity and good wear resistance. Diamond compacts are used for various applications such as cutting tools, drawing dies and drill bits for gas and oil drilling. Fine grained PCD materials often exhibit large abnormally grown diamond particles at the PCD/substrate interface after sintering. These abnormally grown particles are in the region of 50 - 200 μm in diameter and are major flaws in the material that can cause the material to fail prematurely during application.

There have been various studies (Akaishi, 1991; Hong et al., 1991; Yu et al., 1994; Yazu, 1997) already undertaken to suppress AGG in fine grain PCD; these methods usually consist of introducing a grain growth inhibitor. All studies report the introduction of small amounts of additives such as cBN (Akaishi, 1991), SiC (Hong et al., 1991) , Ni-Zr alloy (Yu et al., 1994) and WC (Yazu, 1997) to suppress AGG formation.

This project aimed to investigate the reduction of abnormal grain growth of diamond and WC in fine grained PCD material by changing the infiltrating molten Co liquid of the WC-Co substrate used in PCD sintering. The manipulation of the infiltrating Co metal was tackled by changing the carbon gradient of the infiltrating Co metal. The method for altering the infiltrating Co liquid is achieved by carbon enrichment of a WC-Co substrate. Saturating the infiltrating Co metal before it reaches the fine grained diamond should have resulted in a reduction of the number and size the abnormally grown diamond particles by removing the driving force for Ostwald ripening. The methods of carbon enrichment of the WC-Co substrate are by:

a) Producing a carbon enriched coating on the WC-Co substrate by carbon enriching a WC-Co powder which is then HVOF thermally sprayed onto a WC-Co substrate,
b) Producing graphite/diamond enhanced carbide (GDEC) substrate interlayer.

Alternatively, a grain growth inhibitor such as VC was investigated to reduce AGG formation in fine grain diamond by lowering the overall interfacial energy.

The carbon enriched thermally sprayed powder used for coating a substrate can potentially result in a reduction of hard and brittle eta phases resulting from decomposition of WC-Co during thermal spraying; these results in an increased wear resistance. The effects of carbon enrichment on the wear resistance of coatings were also investigated.

In this thesis the ideas behind reducing abnormal grain growth of fine grained PCD were discussed and the undesirable eta phase achieved through thermal spraying. The effect on the wear resistance was reported and analysed. This project provided a better understanding on the mechanisms of abnormal grain growth especially relating to fine grain PCD. The effect the driving force has on the grain growth of fine grain diamonds in the context of solution modification was explained. The effect of carbon enrichment on the wear resistance was also studied.

Chapter 2 gives a detailed overview of literature on PCD materials, grain growth mechanisms, thermal spraying techniques and wear resistance mechanisms.

Chapter 3 describes all the experimental procedures that were carried out in this work and the equipment used.

Chapter 4 summarizes the results of powder processing and thermal spraying characterization.

Chapter 5 summarizes the results and discussion of the wear resistance tests and hardness measurements.

Chapter 6 summarizes the results of PCD sintering characterization and the effect the carbon enrichment has on the abnormal grain growth and grain growth mechanisms.

A detailed discussion of the results of PCD sintering and grain growth mechanisms is given in Chapter 7.

The conclusion and recommendations for further work are given in Chapter 8.

Chapter 2: Literature Review

2.1. Polycrystalline Diamond (PCD) Materials

2.1.1. Background of PCD materials

Polycrystalline diamond compacts or PCD materials are widely used in industry as cutting tools, drawing dies and drill bits for oil and gas drilling. PCD materials are very advantageous because of their unique properties; high hardness, excellent thermal conductivity, good wear resistance and long service life (Zhang et al., 2009; Yu et al., 1994; Akaishi, M., 1991). They are generally prepared under high pressure and high temperature (HPHT) conditions similar to those used in the commercial manufacture of synthetic diamond (Shin 2004). There are two ways to prepare PCD materials; the first method involves solid-state sintering of diamond powder without additives under very high pressure and temperature conditions (~8.5GPa, ~2170°C) (Hall, 1969; Stromberg & Stephans, 1970). The second method which is typically used in industry involves liquid-phase sintering of diamond compacts with a metal sintering aid (Co, Ni or Fe). Diamond powder is laminated onto a WC-Co substrate; Co infiltrates from the WC-Co substrate into the diamond powder layer and serves as a sintering aid for forming diamond-diamond (D-D) direct bonding. With the aid of liquid phase sintering, PCD materials can usually be produced at lower HPHT conditions (5-6.5GPa, 1400-1600°C).

Researchers have done numerous studies on PCD production, Hall (Hall, 1969) first published data for sintering of diamond powder without additives under high pressure (8.5GPa and 2170°C for 3 min). Stromberg and Stephens (Stromberg, 1970) also published a paper in the same year about sintering of diamond at 1800-1900°C and 60-

65kbar. They found that small amounts of boron, silica or beryllium aid in the sintering process and that the sintered material had a hardness of 7000-8800 $kgmm^{-2}$. Katzman and Libby (Katzman & Libby, 1971) were the first to describe the formation of sintered diamond compacts containing 20 vol.% cobalt binder which was sintered at 1590°C for 20 min at 6.2 GPa. They also discovered that sintering with diamond powders of 0 - 2µm and 1 - 5µm resulted in a harder material than using 10 - 20µm. It was only in 1973 that Wentorf and Rocco (Wentorf, 1973) described the sintering of diamond on a layer of cemented tungsten carbide (WC). The metal binder in the cemented carbide acted as a source for liquid phase sintering. Sintering experiments were done using high pressures (>5GPa) and temperatures (1400-1600°C) ranging from 10min to 1 hour. Under these conditions the cobalt melts and liquid phase sintering of the cobalt and diamond occurs. From then on researchers have been looking at ways to improve the properties of PCD materials to produce better materials, improve behaviour in application for commercial sale.

A wide variety of diamond grain sizes (0.5 – 40µm) are used to produce PCD compacts for different applications. Fine-grained PCD compacts (0.5-2µm) are used for woodworking and mirror finishing of aluminium alloys (Shin, 2004), while coarse-grained PCD compacts (4-40µm) are used for wear resistant applications. Fine grained PCD provides better edge quality on cutting tools and surface finish of product.

2.1.2. Sintering of PCD Materials

Manufacturing of PCD materials can be divided into 3 stages: cold compaction, hot compaction and liquid phase sintering (LPS) (Riedel, 2000). These stages will be discussed in more detail below.

2.1.2.1. Cold and Hot Compaction

The initial stage of PCD sintering occurs when pressure is applied to the PCD material during sintering; this is the cold compaction stage. Three processes occur within this stage; particle rearrangement, crushing of diamond and filling of voids by crushed particles. Once heat is applied with the pressure the stage changes to the hot compaction stage. During the hot compaction stage the temperatures are not high enough for infiltration to occur and therefore liquid phase sintering to occur. The processes which take place during this stage are graphitization of the diamond particles facing the voids, plastic deformation of the diamond grains and densification of the compact. Figure 0-1 shows the processes occurring during cold and hot compaction stages.

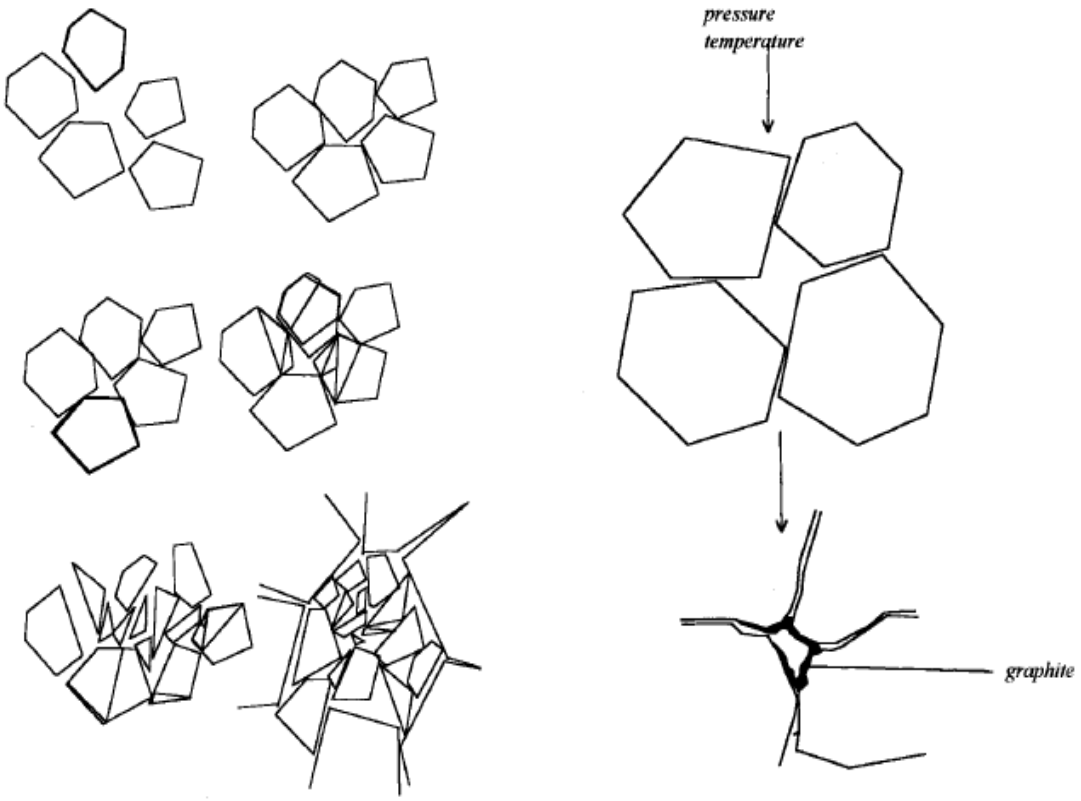

Figure 0-1: Schematic of the processes which occur during Cold and Hot Compaction; (a) particle crushing, rearrangement and void filling occurring during Cold compaction and (b) graphitization of the diamond facing the voids during Hot compaction (Riedel, 2000).

2.1.2.2. Liquid Phase Sintering of PCD Materials

The general sintering mechanism involves the partial dissolution and recrystallization of the diamond to bond the diamond particles via "intergrowth" (Shin et al., 2004). The liquid phase sintering of the PCD material requires a molten metal infiltration source

(Co, Ni, Fe, Mn) (Riedel, 2000; Akaishi, M., 1991). This metal infiltration source can be introduced to the hot pressed diamond bed by admixing and/or infiltration. Admixing involves combining the metal directly with the diamond powder before hot pressing. This can occur through various methods, such as milling metal and diamond powders together, milling precursor and diamond powders together to form a metal base or coating the diamond with a metal precursor.

Infiltration can occur in conjunction with admixing; the metal infiltration source is usually the substrate thus being separate from the diamond bed. The substrate is a tungsten carbide/cobalt (WC-Co) hardmetal, where the cobalt is the source of molten metal.

Utilization of a binder for sintering of diamond compacts has three major benefits: decreasing sintering temperatures and pressures, cleaning diamond particle surfaces of graphite, and electron discharge cutting (EDM) for tool making (Riedel, 2000). The binder (Co) in PCD compacts makes the PCD material electrically conductive which allows the material to be cut into intricate shapes which is virtually impossible with traditional machining techniques due to its high hardness.

There are four main stages in the infiltration of a diamond compact (Ozbayraktar, 1995):

(1) In the first stage, the temperature is high enough to cause melting of the cobalt with dissolved W and C at the interface; excessive amounts of carbon cause a lowering of the eutectic temperature. The melted metal immediately infiltrates into the diamond due to the high pressure gradients between the porous diamond body and the solid interface.

(2) In the second stage, the binder in the bulk substrate starts to melt. As the temperature increases and the metal in the bulk substrate melts it starts infiltrating into the diamond compact similarly due to pressure gradients.

(3) In the third stage, mass transfer of the metal decreases as the pressure gradient decreases. Once there is no pressure gradient the pores are filled completely.

(4) In the fourth stage, a change in the direction of the flow of the liquid phase occurs. The quantity of liquid phase in the diamond layer decreases and increases in the substrate. This is caused by a change in the pressure gradient between diamond and substrate.

The process of liquid phase sintering using conventional carbide substrate (WC-Co) materials occurs by the molten infiltration metal becoming a cobalt alloy with dissolved tungsten and carbon. Initially the cobalt alloy is saturated with C corresponding to the carbon activity of the WC. This activity is much lower than that of fine carbon. This results in dissolving most of the first layer of diamond in contact with the interface. Once the infiltrant is saturated with carbon it can then operate as a liquid sintering aid. The tungsten in the molten cobalt react with some of the extra carbon and precipitate as tungsten carbide (WC) crystals at the interface of the substrate and PCD layer. This results in a large depletion of diamond at the substrate interface and a thick Co layer. This causes the formation of plumes (Co and WC rich regions, several mm in dimension). If fine grained diamond powder is used, the fine diamond particles at the interface dissolve, the larger ones remain, albeit somewhat reduced in size as residual crystal seeds. These particles now have a lower solubility than the bulk of the fine diamond bed. Therefore, the chemical potential of carbon is much higher in the vicinity of the diamond bed than in the vicinity of the large diamond particles. The result is that carbon will migrate to these large diamond particles and preferentially precipitate on them, causing them to grow abnormally. The formation of plumes and AGG of diamond is disastrous for the properties of the PCD material. Figure 0-2 shows a schematic diagram of what occurs during sintering of the PCD material.

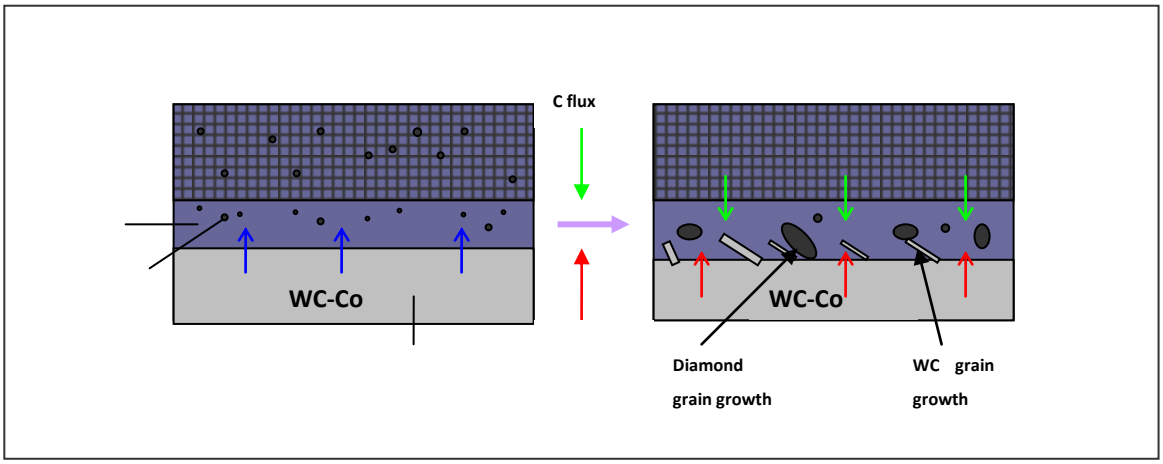

Figure 0-2: Schematic diagram of the sintering of PCD materials.

A well-known problem in sintered PCD materials is the residual amount of Co (between the PCD table and substrate). This has a negative effect on the performance of the material at high temperatures. The thermal degradation is a result of two different reasons; the first is thermal expansion differences between the Co catalyst and the diamond particles. At temperatures above 400°C the expansion of Co is much greater than that of the intergrown diamond particles, but due to the constraints of the diamond skeleton micro-fractures are generated in the diamond material. The strength of the bonded diamond is reduced. The second problem is caused by the facilitation of the Co to catalyse the transition of diamond to graphite at temperatures above 700°C. This therefore suggested that for optimum performance the PCD materials should be kept at temperatures below 700°C, thus limiting industrial application and fabrication routes (Naidoo, 2010; Belnap, J.D, 2009).

The understanding and controlling of the microstructural evolution is an important topic for the reproducible production and improvement of PCD. Therefore in the next section the theory of grain growth will be explained in more detail.

2.2. Grain Growth Theory

Grain growth or coarsening during sintering is a well-known phenomenon referred to as Ostwald ripening (Nic et al., 2006-), which results when larger particles grow at the expense of smaller ones. This occurs by a spontaneous thermodynamic process driven by the minimization of the total free energy of the system. The system of particles reduces its overall energy by reducing the amount of smaller particles which have a higher interfacial energy and growing the larger particles which have a lower interfacial energy (i.e. reducing the overall surface volume ratio between the larger particles). Material from the smaller particles (higher chemical potential) dissolves and is transported via diffusion to the surface of the larger particle (lower chemical potential). The smaller particles shrink and eventually disappear while the larger particles grow. The total energy of the system is lowered and the average particle size increases.

The classical Ostwald ripening theory was developed by Lifshitz and Slyosov (Lifshitz & Slyozov, 1961) and Wagner (Wagner, 1961) and is referred to as the LSW theory. This forms the basis of the first quantitative analytical solution to grain growth. The LSW model of grain growth is based on a zero volume fraction of the solid phase approximation system which comprises a dilute dispersion of isotropic particles in a matrix (liquid phase). The analytical solution takes into account approximations for steady state conditions. The mechanism of grain growth occurs by the simultaneous and complex behaviour of various processes of diffusion and interfacial reactions. The slowest process governs the overall kinetics. If the growth kinetics is governed by diffusion then the average particle size increases as a linear function of the cube root of time, t.

$$\boldsymbol{r(t)^3 - r(t=0)^3 = Kt} \ldots\ldots\ldots\ldots\ldots (\mathbf{2.1})$$

When the growth rate is controlled by the interfacial reaction, the average particle size increases as a linear function of the square root of the time.

$$\boldsymbol{r(t)^2 - r(t=0)^2 = Kt} \ldots\ldots\ldots\ldots\ldots (\mathbf{2.2})$$

The LSW theory is the basis of all grain growth theories; it does have limitations for real systems. The most critical limitation is the assumption of constant interfacial mobility between the atom and the matrix interface under all conditions, including driving force and crystallographic plane (equilibrium shape) of the solid (Kang, S-J L., 2005). This approach assumes that the rates of atom attachment and detachment are the same under all conditions of driving force and equilibrium shape.

There are many other limitations to the LSW theory for real systems with some being modified by other authors and described as extended LSW theories. Ardell (Ardell, A.J, 1972) modified the LSW to MLSW to include volume fraction of solid phase to get a more realistic case.

2.2.1. Mechanisms of Grain Growth

The mechanism of grain growth of solid grains during liquid-phase sintering can be described by the Gibbs/Thomson effect (Ostwald ripening) (Shin et al., 2004). The Gibbs/Thompson equation, shown in Equation 2.3 (German, R., 1996) gives the thermodynamic driving force for coarsening:

$$C = C_O exp\left[\frac{4\gamma_{sl}\Omega}{kT}\frac{1}{r}\right] \ldots\ldots\ldots\ldots\ldots\ldots\ldots (2.3)$$

where the grain size of the particles (radius), r, is related (inversely proportional) to the solubility of particle (C) in the melt and the solid-liquid interfacial energy, γ_{SL}, atomic volume, Ω, temperature, T and Boltzmann constant, k. C_o is the equilibrium concentration above an infinitively large particle. The equation shows that the solubility increases strongly with decreasing grain size. This effect is pronounced at grain sizes below 1 µm. This strong dependence of the solubility of the grain size below 0.1 µm is the reason of the often observed accelerated grain growth of nano particles during sintering.

A Taylor approximation can be used for particles with a size greater or equal to 1µm (i.e. r ≥ 1µm) given in Equation 2.4 (Salagaram, 2007).

$$C = C_O exp\left[1 + \frac{4\gamma_{sl}\Omega}{k}\frac{1}{r}\right] \ldots\ldots\ldots\ldots\ldots\ldots\ldots (2.4)$$

Comparing the Equations 2.1 and 2.4, it can be seen that as the particle size decreases below 1µm, the equilibrium concentration of the Taylor approximation series deviates from the exact Gibbs/Thompson equation (Equation 2.3). This is shown in Figure 0-3.

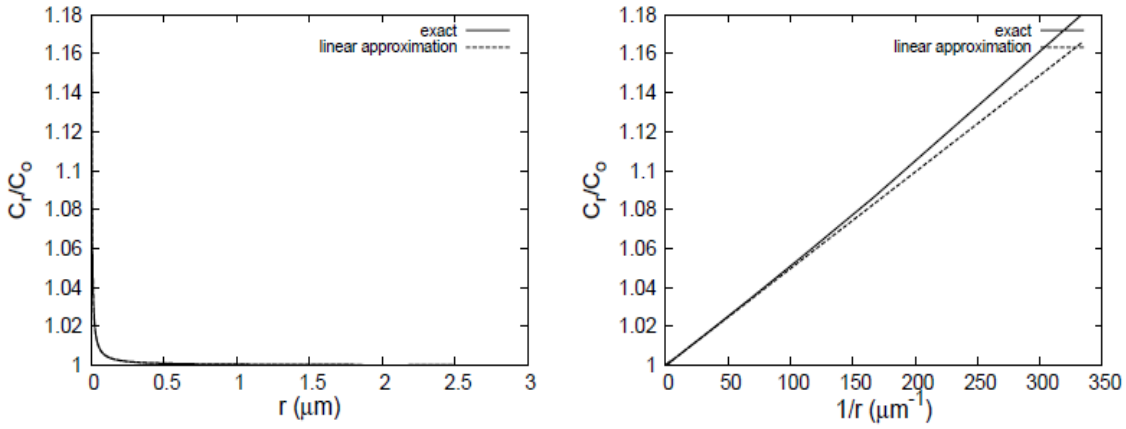

Figure 0-3: Comparisons of the exact and Taylor approximation of the Gibbs/Thompson equation (Salagaram, 2007).

As described earlier the main mechanisms for grain growth are governed by diffusion and/or interface reaction and occur simultaneously and in a complex behaviour with the slowest process governing the overall kinetics of the system. The growth rate v, can then be expressed as (Kang et al., 2009):

$$v = \frac{v_D v_R}{v_D + v_R} \ldots\ldots\ldots\ldots\ldots\ldots (2.5)$$

where v_R & v_D is the growth rate of diffusion and interface reaction respectively.

Figure 0-4 shows the growth rates as a function of the driving force for the different mechanisms; diffusion, interface reaction and mixed control.

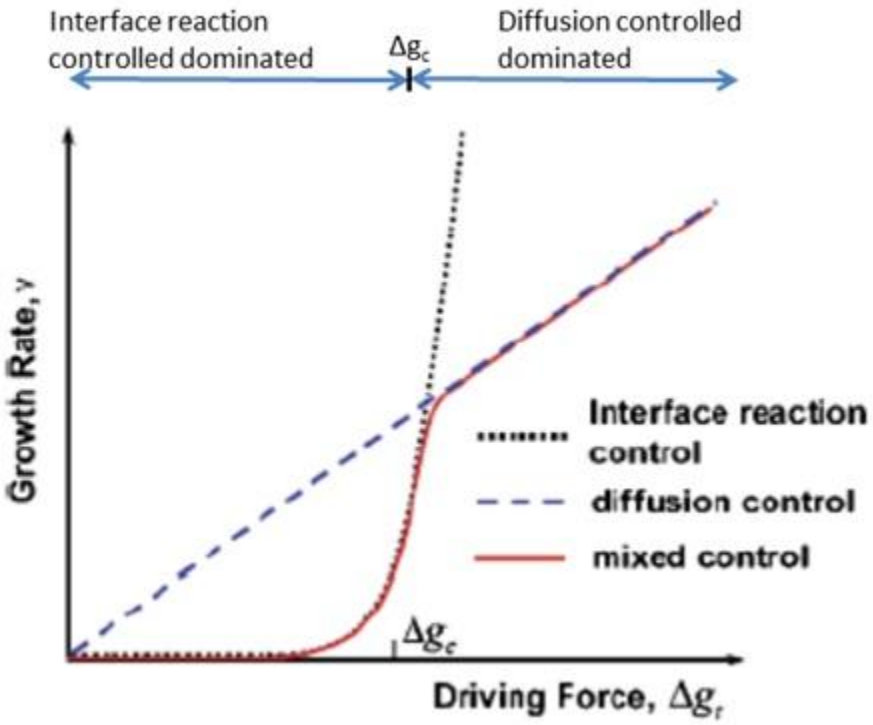

Figure 0-4: Schematic diagram of the growth rate and driving force for the various mechanisms of grain growth (diffusion, interface reaction and mixed control) (Kang et al., 2009).

The growth rate of diffusion, v_D is expressed as (Kang et al., 2002):

$$v_D = \frac{dR}{dt} = \frac{D_f C_O \gamma_{sl} V_m^2}{kT} \frac{1}{R}\left(\frac{1}{R^*} - \frac{1}{R}\right) \ldots\ldots\ldots\ldots\ldots\ldots (2.6)$$

where D_f is the diffusion coefficient of the solute, C_O is the solubility of the solute, γ_{sl} is the solid/liquid interfacial energy and V_m is the molar volume. R and R* is the distance from the centre of the equilibrium shape of the facet and critical nucleus size respectively. R*, the critical nucleus is the particle size which has a zero rate of growth i.e. doesn't grow or dissolve (Kang et al., 2002).

The diffusion controlled grain growth rate as shown in Figure 0-4 is linearly proportional to the driving force, which is also known as normal grain growth (NGG). Both the growth rate and dissolution rate is linearly proportional to the driving force. This follows the LSW theory of grain growth.

The grain growth for spherical particles follows that of diffusion grain growth, as shown in Figure 0-5. Spherical rough surface particles have a large number of sites available for solute atom deposition; the deposition kinetics is always faster than the diffusion kinetics and the growth is governed by diffusion. This means that the growth rate of spherical particles is linearly proportional to the driving force; i.e. interface mobility is constant.

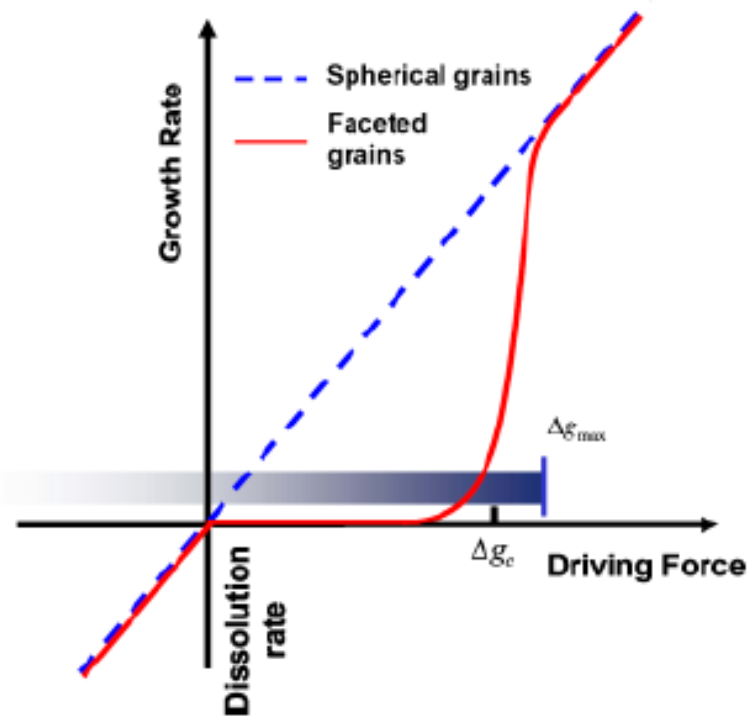

Figure 0-5: Schematic diagram of the growth rate and driving force for spherical and faceted grains (Kang et al., 2009).

Interface reaction controlled growth is not linearly proportional to the driving force, shown in Figure 0-4. It thus shows non-normal behaviour. The grain growth is zero until a critical driving force is reached, then growth increases exponentially. The growth rate for interfacial reaction control, v_R can be described by a mechanism of nucleation of the crystals on an interface. The nucleation and growth of 2D nuclei can be described by the Equation 2. 7 (Kang et al., 2009):

$$v_R = hA\psi n_0 exp\left(-\frac{\pi\sigma^2}{kTh\Delta g_v}\right) \dots\dots\dots\dots\dots (2.7)$$

$$\psi = n^* v exp\left(-\frac{\Delta g_m}{kT}\right)$$

where υ is the vibration frequency of atom in liquid, n is the number of atoms in a position close to critical nucleus, n_0 is the atom density, h is the height of the 2D nucleus, σ is the step free energy of the 2D nucleus and A is the grain facet area. Δg_m and Δg_v are the activation energy for migration across the interface and Gibbs free energy (volumetric driving force) respectively.

The volumetric driving force, Δg_v, for coarsening (Ostwald ripening) of a grain with distance from the centre of equilibrium shape to the given facet is expressed as (Kang et al., 2002):

$$\Delta g_v = 2\gamma_{sl}\left(\frac{1}{R^*} - \frac{1}{R}\right) \ldots\ldots\ldots\ldots\ldots (2.8)$$

Figure 0-5 shows the grain growth behaviour of faceted particles. Faceted atomically flat interface particles have very few deposition sites and occur with atom deposition on surface defects on the facets such as the edge of a 2D nucleus formed on the facet or with the assistance of screw dislocations and/or twins (Kang et.al. 2009). The growth rate is not linearly proportional to the driving force. This means that the interface mobility which is a function of the driving force is not constant. This therefore suggests that faceted grain growth is governed by interface reaction, thus differing from Wagner's assumption for interfacial reaction controlled processes (Kang et al., 2009). However, the dissolution rate for faceted grains is proportional to the driving force, as the corners act as a dissolution source; this suggests that dissolution is governed by diffusion. The assumption made by the LSW theory therefore only holds for the spherical grains with atomically rough interfaces while it fails for faceted grains with atomically flat surfaces.

Defects such as screw dislocations and twin boundaries assist in nucleation by lowering the activation energy barrier for nucleation to occur. Therefore for 2D nucleation growth assisted by screw dislocation the rate is expressed by (Kang et al., 2009):

$$v_R = \propto \frac{h^2}{\sigma\gamma} \Delta g_v^2 \ldots\ldots\ldots\ldots\ldots (2.9)$$

For twin-assisted growth (90° reentrant edge) (Kang et al., 2009):

$$v_R = n^* n_0 v exp\left(-\frac{\sigma^2}{kTh\Delta g_v}(\theta - sin\theta cos\theta)\right) \ldots\ldots\ldots\ldots\ldots (2.10)$$

where θ is the contact angle between the original surface and the tilted surface of a double twin.

In order for coarsening to take place by 2D nucleation, the 2D nucleation barrier should be overcome by the driving force for coarsening. By substituting Equation 2.8 into Equations 2.7, 2.9 and 2.10, the rate of growth can be related to the size of the critical nucleus (R*) and distance from the centre of the equilibrium shape facet (R) as can be seen in Equations 2.11 – 2.13.

$$v_R = hA\psi n_0 exp\left(-\frac{\pi\sigma^2}{2kTh\gamma_{sl}\left(\frac{1}{R^*} - \frac{1}{R}\right)}\right) \ldots\ldots\ldots\ldots\ldots (2.11)$$

$$v_R = \propto \frac{h^2}{\sigma}(4\gamma_{sl}\left(\frac{1}{R^*} - \frac{1}{R}\right)) \ldots\ldots\ldots\ldots\ldots (2.12)$$

$$v_R = n^* n_0 v exp\left(-\frac{\sigma^2}{2kTh\gamma_{sl}\left(\frac{1}{R^*} - \frac{1}{R}\right)}(\theta - sin\theta cos\theta)\right) \ldots\ldots\ldots\ldots\ldots (2.13)$$

Kang (Kang, S-J L., 2005) showed the variations of the growth rates for the various growth modes in Figure 0-6. The growth rate for 2D nucleation and growth is an exponential function while the defect assisted growth was parabolic.

There is a critical driving force for significant growth of a crystal, especially for growth without surface defects such as 2D nucleation and growth. The critical driving force, Δg_C (identified in Figures 2-4, 2-5 and 2-6) varies with the step free energy of a 2D nucleus and is affected by temperature and dopants. The critical driving force for 2D nucleation and growth can be expressed as (Kang et al., 2009),

$$\Delta g_C = \frac{\pi\sigma^2}{kTh}(lnK)^{-1} \ldots\ldots\ldots\ldots\ldots\ldots\ldots\ldots\ldots (2.14)$$

where *K* is a constant relating the diffusion coefficient and the number of nuclei per unit area.

Below the critical value Δg_C, the interfacial reaction grain growth is much smaller than that of diffusion (especially for 2D nucleation and growth). For normal growth (NGG) $\Delta g_C = 0$. For significant grain growth (AGG) to occur in faceted materials, the driving force must be larger than the critical driving force Δg_C, value; i.e. $\Delta g_C \leq \Delta g_{max}$. Equation 2.15 shows the inequality for grain growth for significant growth of a particle. The difference in size between the grain concerned, R, and the grain with the zero rate growth, R* (Kang, S-J L., 2005) is given in Equation 2.15 below:

$$\Delta g_C \leq 2\gamma_{sl} V_m \left(\frac{1}{R^*} - \frac{1}{R}\right) \ldots\ldots\ldots\ldots\ldots\ldots (2.15)$$

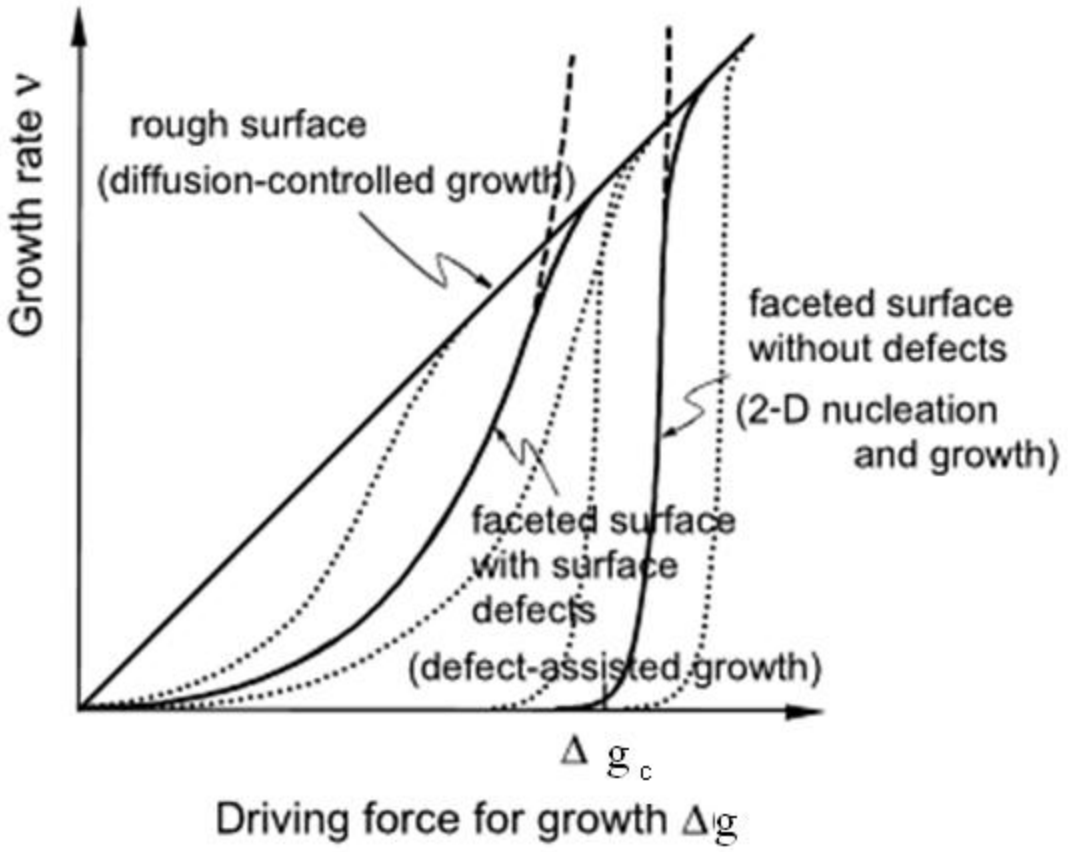

Figure 0-6: Schematic diagram showing the variations of growth rate with driving force for the various growth modes, where the dotted line depicts the growth rates for different crystallographic planes of a faceted crystal (Kang, S-J L., 2005).

For materials with a small particle size, the amount of grain growth that can occur is significant. This is because the driving force for growth of smaller particles is much higher than for large particles. Smaller grains have a higher solubility than larger grains, and thus set up the conditions for grain growth by solution-re-precipitation. Referring to Equation 2.4, the solubility of a solute particle is dependent on the solute crystal size. There is a critical particle size at which the solubility of the solute in a liquid increases exponentially, thus increasing the driving force for growth. Figure 0-7 is a schematic diagram of the solubility plot of diamond supersaturation in molten Co at HPHT (Davies et al., 2002; Davies, 2009). The critical particle size for growth of diamond is at about

1µm. Particles below 1µm tend to experience abnormal grain growth as the supersaturation of the solute (diamond) in the liquid is extremely high.

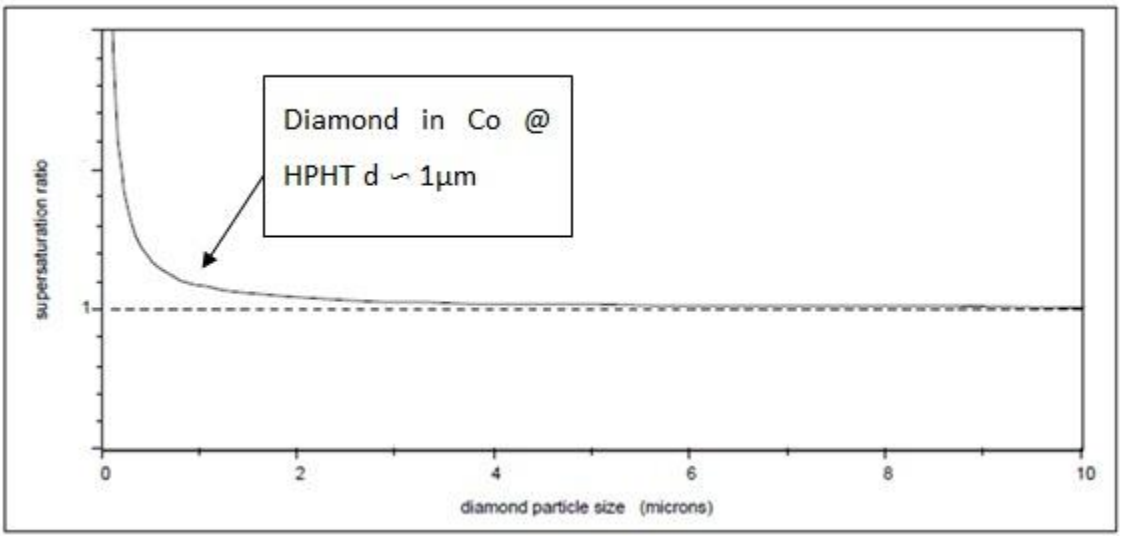

Figure 0-7: Trend plot of the solubility of diamond supersaturation ratio (C/C_o) in molten Co at high pressures and temperatures (Davies et al., 2002; Davies, 2009).

2.2.2. Abnormal Grain growth

Abnormal grain growth in a liquid matrix is a common occurrence, although most involve faceted grains such WC-Co, $BaTiO_3$ and SiC (Kang et al., 2002; Kang, S-J L., 2005). This therefore suggests that faceted grain interfaces are a necessary condition for abnormal grain growth in a liquid matrix. From crystal growth theory from a melt, it was said earlier (section 2.2) that a faceted crystal grows either by 2D nucleation or with the assistance of surface defects such as screw dislocations and twin boundaries. The faceted crystal grows by interface-reaction control if the diffusion of atoms in the matrix is sufficiently fast.

Interface roughening can be induced by: increasing sintering temperature, changing sintering atmosphere (i.e. oxygen partial pressure) or adding dopants. This will cause the grain shape to become rounded and thus result in normal grain growth behaviour.

For AGG, the following inequality criterion is often used (Kang et al., 2002):

$$\frac{d(R_{max}/R_{ave})}{dt} > 0 \ldots\ldots\ldots\ldots\ldots\ldots\ldots\ldots (2.16)$$

Where R_{max} and R_{ave} are the maximum and average particle size respectively.

2.2.3. Grain growth in PCD Materials

Grain growth in PCD materials follows the conventional mechanism of Ostwald ripening of liquid phase sintered materials described by the Gibbs/Thompson effect (Shin et al., 2004).The particle size of diamond and solubility of carbon in solution are very important aspects of PCD sintering. Abnormal grain growth usually occurs in fine grade PCD materials when the particle size is less than 1 – 2 μm (Akaishi, M., 1991; Shin et al., 2004). Diamond particles smaller than the critical particle size (1 μm) will dissolve readily into the solution and then precipitate on the undissolved (seed) diamond particles left, causing them to grow exponentially. The critical radius depends on various conditions; starting grain size, amount of liquid present and temperature.

In the PCD system grain growth is essentially caused by two regions of particles with distinctly different sizes (the fine tail and the coarse tail of the particle size distribution). Both the diffusivity and the solubility of the solid in the liquid are exponentially dependent on temperature. This then suggests that the kinetics constant is extremely

sensitive to temperature depending on the superaturation. Since the growth rate is dependent on the solubility of the solid in the liquid, it is important to understand the degree of solubility during liquid phase sintering. In the case of PCD materials it is important to be able to control the carbon solubility, and dependence of carbon concentration in the molten infiltrant. Carbon concentration in the molten infiltrant can affect the grain growth of the diamond particles, the more carbon saturated the melt is before reaching the diamond layer, the lower the dissolution of diamond particles which will reduce the driving force for grain growth of fine grain diamond particles

One important phenomenon observed in the sintering of fine-grained PCD materials is abnormal grain growth (AGG). Preferential growth of grains of up to several hundred micrometres has been reported (Yu et al., 1994; Shin et al., 2004). AGG only occurs in PCD material with a particle size distribution less than 2μm, where the driving force for coarsening is high. AGG in fine-grained PCD is detrimental for wear resistance and performance of the PCD materials.

Figure 0-8 shows the AGG of fine-grained PCD produced by Shin *et al (Shin et al., 2004)*. The PCD compacts were produced at 6GPa and 1600°C. AGG can be seen on the corners and along the tantalum shell. Shin attributed the inhomogeneous distribution of the AGG to inhomogeneous pressure distribution during sintering. The grains were faceted and faceted grain growth during liquid phase sintering is evidence of AGG by 2D nucleation. Figure 0-9 shows an SEM micrograph of the abnormally grown diamond crystals. Shin *et al.* (Shin et al., 2004) suggested that the diamond grains grew along the {111} pyramidal planes.

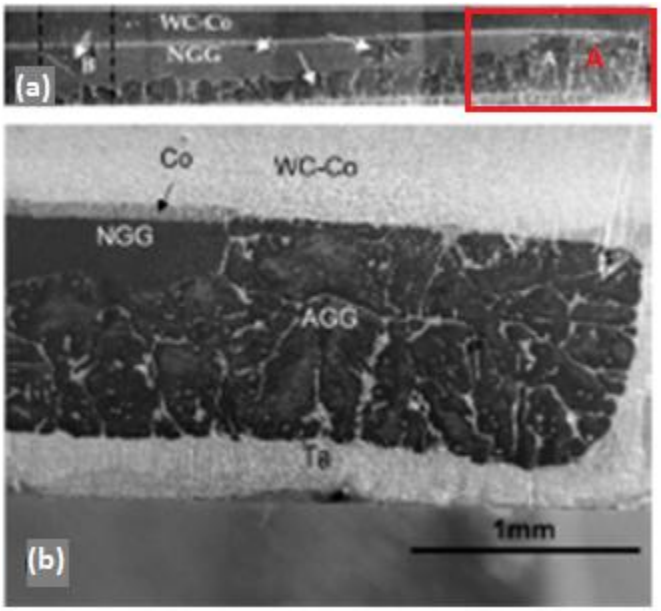

Figure 0-8: (a) Structure of cross-section of specimen. Arrows point out abnormally grown grains. (b) SEM micrograph of area A in (a) where AGG and NGG stand for AGG and NGG regions, respectively (Shin et al., 2004).

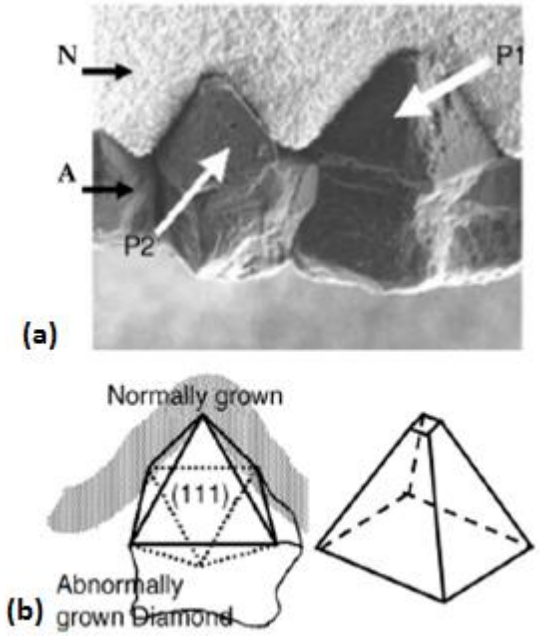

Figure 0-9: (a) SEM micrograph showing faceting of abnormally grown diamond crystals. (b) Schematic diagram showing P1 and P2 crystals with the pyramidal {111} planes. N and A are the normal and abnormal grain growth regions respectively (Shin et al., 2004).

2.2.4. Elimination of Abnormal Grain Growth in PCD Materials

Since both micron diamond and WC particles are faceted materials they will grow by 2D nucleation and growth and are governed by interface reaction controlled growth. These abnormally large grains that appear are weak points in the material and need to be eliminated to produce a homogeneous material (Shin et al., 2004).

There have been a few suggestions on ways to control the AGG in fine grained PCD; Hong et al. (Hong et al., 1991) used small amounts of SiC to suppress AGG in fine grained

PCD, while Akaishi *et al.* (Akaishi, M., 1991) found that small additions of cubic boron nitride powder suppressed AGG. Yu *et al. (Yu et al., 1994)* discussed methods to suppress AGG of diamond by involving the use of an Ni-Zr alloy as a sintering aid under HPHT. Yazu (Yazu, 1997) suggested adding quantities of fine-grained WC powder to the starting diamond powder. A patent by Smith International (Smith International, 1995) describes a method which uses a thin refractory layer of WC-Co substrate together with an admixed refractory material (TiC or TiCN) within the diamond powder layer. This is said to regulate the flow of the molten metal from the substrate into the diamond layer and therefore minimize AGG and bond metal depletion at the diamond interface.

These methods use the addition of a secondary phase to eliminate the AGG. The problems with these processes are the formation of complex intermetallics with the Co binder in the PCD layer which will rely on accurate control of the HPHT sintering conditions. The additions of these species will interfere with the kinetics of the sintering process, therefore influencing the diamond-diamond bonding especially for finer grained PCD (<2µm) (patent WO 2008/135949). It would be more useful to be able to modify the existing WC-Co substrate to reduce AGG of diamond and plume formation in fine grained PCD materials.

Other suggested methods of reducing AGG of diamond in fine grained PCD materials include altering the particle size distribution of the diamond particles at the interface. Since the diamond particle size is a very important component for the driving force of AGG, this needs to be carefully selected and controlled. Davies and Myburg (Davies & Myburgh, 2008) described a method of eliminating grain growth in fine grained PCD by using a layer of coarse grained diamonds (4 - 10µm) at the interface; a schematic diagram of this is shown in Figure 0-10. The coarse grained diamond layer (4 - 10µm) provides various advantages such as restricting the conditions required for Ostwald

ripening. The coarse diamond layer acts as a sacrificial layer by saturating the infiltrating molten metal (Co) with carbon. This occurs before the molten metal reaches the fine diamond layer. The fine diamond particles are therefore considered to be more stable in the molten metal and therefore will not grow exponentially large. The larger pores associated with the coarse diamond layer also seems to create channels for easier infiltration of the molten metal in to the fine grained diamond layer, thereby reducing poor infiltration areas near the top of the PCD compact. Zhang *et al.* (Zhang et al., 2009) also produced bi-layered PCD compacts similar to that showed in Figure 0-10, with 1 µm and 10µm for the fine and coarse diamond layers respectively. They observed no AGG at 1450°C, which produced the best wear resistance results.

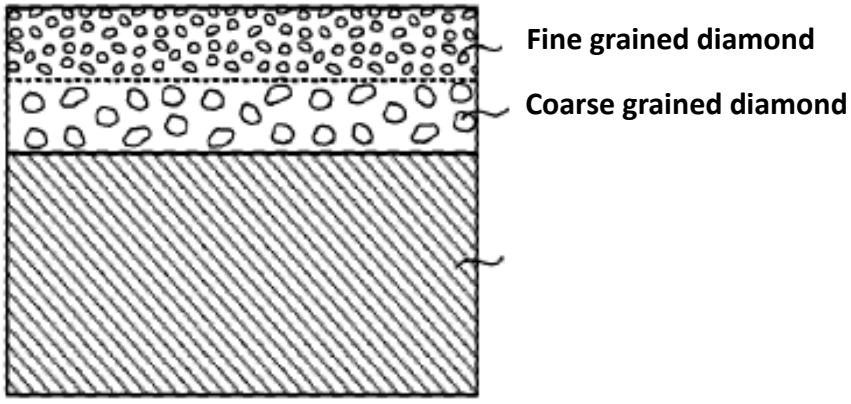

Figure 0-10: Schematic diagram of a diamond compact with layered structure.

Since AGG of the diamond particles is not the only problem in PCD sintering, it is also important to look at the WC particles that also experience exaggerated grain growth. Mukhopadhyay and Bertagnolli (Mukhopadhyay & Bertagnolli, 2011) suggested a method of controlling WC grain growth at the diamond-substrate interface in PCD cutters. They recommended that changing the C/W ratio will result in a reduction in exaggerated WC grain growth. The C/W ratio can be changed by additions of 5 wt% pure

WC powder into the diamond; this will cause a decrease in the C/W ratio which will result in no grain growth. They also suggested a carbon deficient substrate (eta (η)-phase) will also decrease WC grain growth. This did not produce any effect on the diamond particles as the diamond grain size was above 20µm. The driving force for diamond grain growth was insufficient for AGG of diamond to occur.

Grain growth inhibitors used in WC-Co alloys to reduce or eliminate AGG are VC, Cr_3C_2, NbC and TaC (Choi et al., 2000; Sun et al., 2011). Small concentrations (1 wt%) of these metal carbides can reduce AGG in fine grained WC-Co materials. VC and Cr_3C_2 are the most effective grain growth inhibitors for WC-Co based materials due to their high solubility and mobility in cobalt at low temperatures (Sun et al., 2011). Choi et. al (Choi et al., 2000) showed a fine grained (0.8 µm WC) WC-30Co materials with the addition of 1 wt% VC after heat treated for 1 – 16 hours at 1500°C, shown in Figure 0-11. The particle size of the WC particles remained small for the VC doped materials (0.6 µm and 0.7 µm for 1 hour and 16 hours heat treatment time respectively). Even after 16 hours the WC particles of the non-doped WC-30Co material grew to about 3 µm, while for 1 hour the particle size was 1.1 µm. The small addition of the VC grain growth inhibitor increases the edge energy of a WC crystal, thus retarding the 2D nucleation growth. However, Choi et. al (Choi et al., 2000) found that after prolonged heat treatment the VC doped materials exhibited an enhanced AGG behaviour. A patent (WO 2011/042566 A1) by Israelsson et al (Israelsson et al., 2011) suggested that a small (0.5 – 2 wt%) addition of refractory metals or metal carbides from the group (Ti, V, Cr, Zr, Nb, Mo, Hf and Ta) could result in a decrease in the abnormally large diamond grains in fine grain PCD. This suggests that the addition of VC and Cr_3C_2 would work as a grain growth inhibitor in fine grain PCD.

It is important to be able to accurately determine and control the carbon activity of the molten infiltrant. The carbon content will depend on the type of infiltration source, the

amount of tungsten and the active transition metals used. Conventionally available WC-Co hard metals are limited in regards to the carbon content and therefore the melting temperature of the binder and the resultant carbon and tungsten activities of the molten infiltrant. It is therefore important to develop adequate technologies to manipulate the infiltration sources.

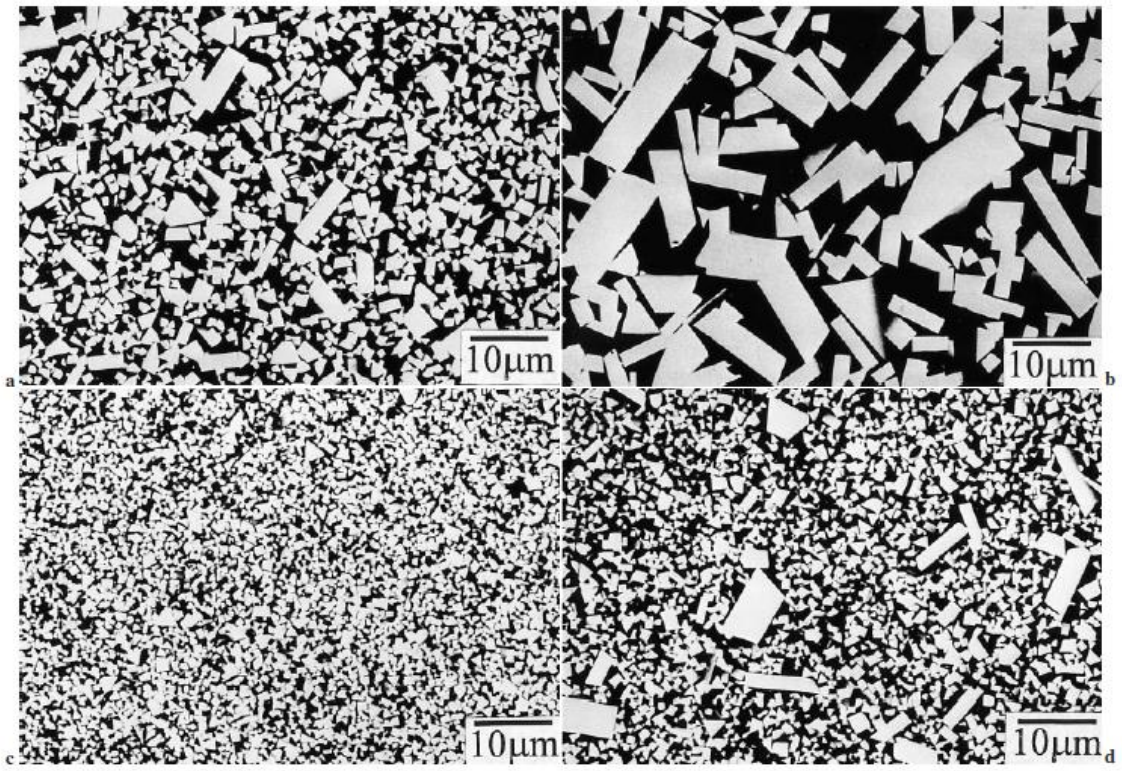

Figure 0-11: SEM-BSI micrographs of WC-30Co and WC-1VC-30Co specimens heat treated at 1500°C for given times, WC (light phase), Co (dark phase); (a) WC-30Co, 1 hr.; b) WC-30VC, 16 hrs.; c) WC-1VC-30Co, 1hr and d) WC-1VC-30Co, 16 hrs (Choi et al., 2000).

To avoid the formation of plumes and AGG of the diamond, a cobalt infiltrating metal containing high amount of carbon and a low amount of tungsten is necessary. This will produce an infiltrating metal almost saturated with carbon therefore dissolving very

little diamond. Infiltration by this metal will result in an intergrown diamond interfacial structure at the substrate boundary with very little probability of the formation of plumes and AGG of the fine diamond.

There are different methods used to provide an extra source of carbon to the PCD layer. These consist of adding extra carbon or graphite powders directly to the diamond powders, coating of the diamond powders with a carbon rich precursor, obtaining a WC-Co substrate rich in carbon, adding a sacrificial large diamond layer (as described above) or coating the substrate (Davies et al., 2002). Gas carburization of the WC-Co substrates using propane or methane have been done to produce a carbon enriched substrate (Davies, 2009). This process although producing a homogeneous distribution of graphite flakes in the substrate, is expensive to produce. Another method to produce a carbon enriched substrate is by placing graphite paper on the substrate and heat treating to allow the carbon to diffuse into the substrate (Davies, 2009). This produces very little to no free-carbon which is inhomogeneously distributed in the substrate.

Thermal sprayed coatings offer an alternative process to tailoring an interfacial layer between the substrate and the PCD layer. By manipulating the spraying powder ways can be made to produce the required infiltrating metal.

2.3. Thermal Spraying of WC-Co Coated Layers

Thermal spraying technologies have had increasing prominence in industrial applications and can be easily used to manipulate the raw material powder used to form the infiltration sources. WC-Co thermally sprayed coatings were initially produced for the

aerospace industry (Nerz et al., 1992), but have found uses in many other areas including rolling mills for paper and pulp , steel and textile industry (Perry et al., 2000; Dorfman et al., 2000) and in the protection of slurry pumps in the mining industry (Howse & van Wyk, 1998). Thermally sprayed hard metal coatings are used extensively for the protection of components as they can produce a dense wear resistant layer which can be used for abrasive, erosive and corrosive wear applications (Santana et al., 2008). They have good tribological properties due to their excellent adhesion to the substrate, good cohesion and low porosity and can also be used to provide a barrier between the substrate and the PCD bed, thus decoupling the properties of the substrate from those of the PCD layer. Thermally sprayed WC-Co coatings are an important spray powder and are widely used to produce hard coatings used for wear resistance application such as for shafts.

There are various types of thermal spraying techniques; these include wire arc, detonation, flame, plasma and high-velocity-oxygen-fuel (HVOF) spraying. An overview of the different thermal spray processes is given in

Table 0-1. HVOF spraying has become the preferred technique to produce a dense coating for WC-Co materials on a variety of substrates due to high particle velocity, high density and low decarburization.

Table 0-1: Thermal Spraying process comparison (Davies, R.J, 2004).

Attribute	Flame spray	High-velocity oxyfuel	Detonation gun	Wire arc	Air plasma	Vacuum plasma	Radiofrequency plasma
Jet							
Jet temperature, K	3500	5500	5500	>25,000	15,000	12,000	10,000
Jet velocities, m/s (ft/s)	50–100 (160–300)	500–1200 (1600–4000)	>1000 (>3300)	50–100 (160–300)	300–1000 (1000–3300)	200–600 (700–2000)	20–80 (70–300)
Gas flow, sLm	100–200	400–1100	N/A	500–3000	100–200	150–250	75–150
Gas types	O_2, acetylene	CH_4, C_3H_6, H_2, O_2	O_2, acetylene	Air, N_2, Ar	Ar, He, H_2, N_2	Ar, He, H_2	Ar, He, H_2
Power input, kW equiv.	20	150–300	N/A	2–5	40–200	40–120	40–200 (plate)
Particle feed							
Particle temperature (max), °C (°F)	2500 (4500)	3300 (6000)	N/A	>3800 (>6900)	>3800 (>6900)	>3800 (>6900)	>3800 (>6900)
Particle velocities, m/s (ft/s)	50–100 (160–300)	200–1000 (700–3300)	N/A	50–100 (160–300)	200–800 (700–2600)	200–600 (700–2000)	20–50 (70–160)
Material feed rate, g/min	30–50	15–50	N/A	150–2000	50–150	25–150	20–50
Deposit/coating							
Density range (%)	85–90	>95	>95	80–95	90–95	90–99	95–99
Bond strength, MPa (ksi:)	7–18 (1–3)	68 (10)	82 (12)	10–40 (1.5–6)	<68 (<10)	>68 (>10)	>68 (>10)
Oxides	High	Moderate to dispersed	Small	Moderate to high	Moderate to coarse	None	None

2.3.1. High-Velocity Oxyfuel (HVOF) Spraying

High velocity oxyfuel (HVOF) spraying is considered to be the best method for depositing WC-Co powders because of its high particle velocities and lower temperatures than other methods, thereby resulting in less decarburization of WC during spraying [(Santana et al., 2008) (Li et al., 1996)]. It is used to produce dense WC-Co coatings of up to 500µm thickness with good wear resistance. The gas temperature is in the range of 2600 - 3000°C and the particle velocity can reach 700 m/s (Metco, 2011). Figure 0-12 is a schematic illustration of the gun for HVOF spraying. Various fuel gases such as propane, propylene, acetylene, hydrogen and other natural gases can be used. The powders are melted by the heat source and are propelled by the carrier gases to spray onto a prepared substrate, where they solidifies and form a solid layer of alternating particles. Figure 0-13 shows how the particles form on a substrate. The molten liquid particles impact the substrate at high speeds and deform and spread out like pancakes on the substrate. Once cooled and solidified the particles bond together by mechanically locking.

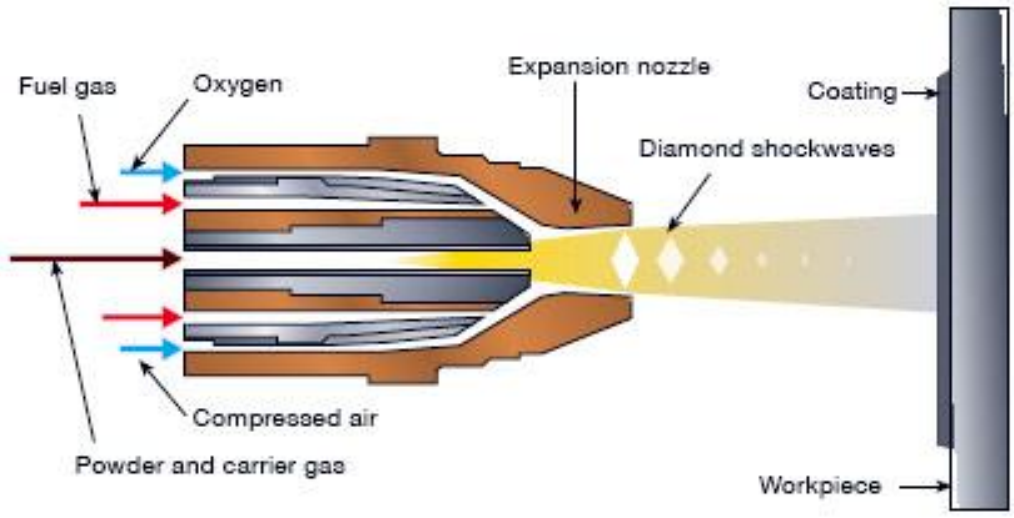

Figure 0-12: Schematic diagram of a HVOF Gun (Metco, 2011).

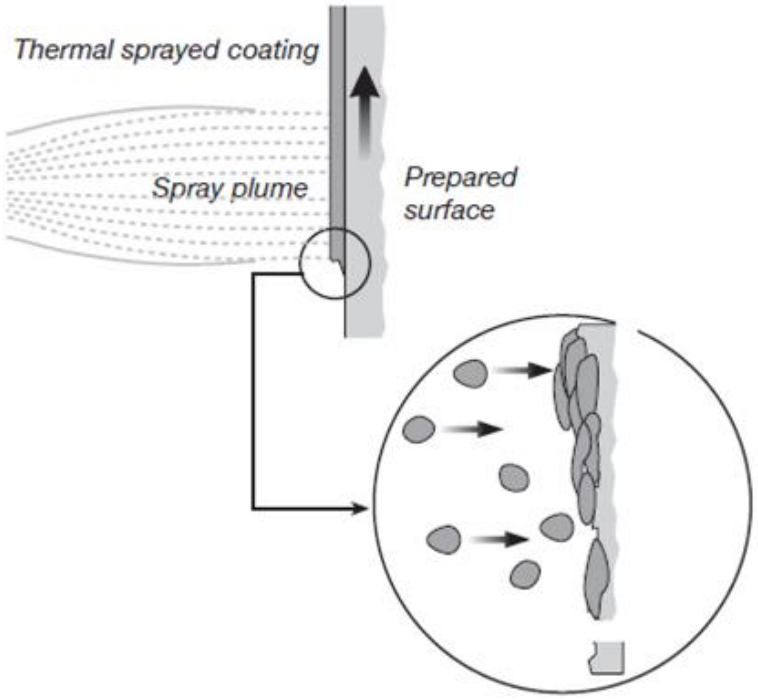

Figure 0-13: Schematic of the particle formation on substrate (Metco, 2011).

2.3.2. Decarburization during spraying

In thermal spraying, decarburization of the metal-carbide powders occurs. The Co binder in the WC-Co powders melts rapidly, and at high temperatures WC dissolves. The oxygen in the flame can then rapidly react with the C in solution, forming CO or CO_2 gas which is removed from the system. WC decomposes as the depletion of carbon occurs. The decomposition and oxidation of the WC-Co during spraying usually yields W_2C, metallic W and undesirable phases such as the eta phases ($Co_xW_yC_z$) and other complex amorphous phases (Santana et al., 2008; Li et al., 1996; Asl et al., 2006 and de Villiers Lovelock, H.L., 1998). The composition of the (eta) η-phases (Co_6W_6C, Co_3W_3C and Co_2W_4C) is not fixed and can vary with temperature. They are carbon deficient phases which result in a hard brittle material which decreases the wear resistance of the

material. The formation of these phases during spraying needs to be suppressed; this can be achieved by reducing the degree of decarburization during thermal spraying.

Decarburization steps during thermal spraying (Nerz et al., 1992):

Step 1: $$2WC \rightarrow W_2C + C \quad \text{(2.17)}$$

Step 2: $$W_2C \rightarrow 2W + C \quad \text{(2.18)}$$

$$2C + O_2 \rightarrow 2CO\ (gas) \quad \text{(2.19)}$$

Decarburization is kinetically driven; i.e. is dependent on temperature and time. The amount of decomposition can be minimized by decreasing the flame temperature and increasing the flame velocity.

A method of reducing decarburization during thermal spraying is to introduce a sufficient amount of carbon in the powder before spraying. The method for carbon enriching of the powders involves the use of a phenol formaldehyde carbon precursor and its pyrolysis procedure developed by Dr Geoff Davies at Element Six (Pty) Ltd (Davies, 2009). Enough carbon is added to the WC-Co powders before spraying to account for the decarburization during thermal spraying.

2.3.3. Thermal Sprayed Coatings used in PCD sintering

As described earlier, AGG of diamond in PCD sintering can be reduced or eliminated by changing the chemistry of the infiltrating metal. Dr Geoff Davies at Element Six (Pty) Ltd (Davies, 2009) developed a way to change the chemistry of the infiltrating Co metal in

PCD sintering by using a carbon enriched WC-Co powder (described above) and thermally spraying a coating onto a WC-Co substrate. By supplying enough carbon into the infiltrating metal a reduction in the carbon gradient between the PCD layer and the substrate can be achieved. This modification has the potential of reducing the formation of AGG of diamond and WC plumes at the interface by discouraging dissolution of the small diamond grains. Figure 0-14 shows a schematic diagram of the setup of the PCD material with the thermally sprayed WC-Co barrier between the diamond and WC-Co substrate. The coating also provides a barrier between the PCD layer and the substrate which can help improve the PCD wear properties. During wear testing of the PCD material, the worn surface gradually becomes wider and moves into the WC-Co substrate, if coupled with a more wear resistant barrier between the PCD and WC-Co substrate this would provide improved wear properties for the PCD cutter.

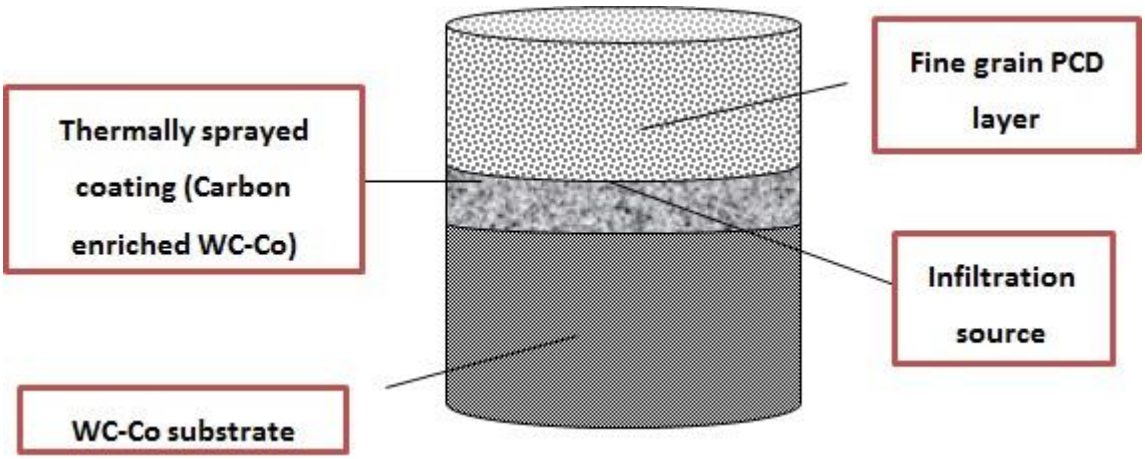

Figure 0-14: Schematic diagram showing the setup of the PCD material with the Thermally Sprayed layer (TSL).

2.4. Abrasive Wear Resistance and Mechanisms

2.4.1. Abrasive Wear

Wear is considered the loss of material from a surface by means of some mechanical action. There are various types of wear in materials; these include abrasion, adhesion, erosion and corrosion wear. Abrasive wear is considered a major failure in system components and is the loss of material due to hard particles or hard protuberances/asperities forced against and moving along a solid surface (ASTM, 1987).

Abrasive wear is commonly classified according to the type of contact and the contact environment. The type of contact determines the modes of abrasive wear; two-body or three-body abrasive wear. Abrasive wear occurs when either a rough, hard surface (protuberances) or a soft surface with hard particles embedded in its surface slides over a softer material causing a ploughing action to take place; this is known as two-body abrasion. When loose hard particles or contaminants are present and are free to roll and slide between surfaces this is known as three-body abrasion. Figures 2-15 and 2-16 show a schematic diagram of two-body and three-body abrasive wear respectively. The mechanism by which material is lost is by plastic flow which is caused by material displacement by a moving surface or foreign particle, while cutting is the removal of material usually producing material chips. Three-body abrasive wear is more important for industrial applications as it is close to what occurs in industrial processes.

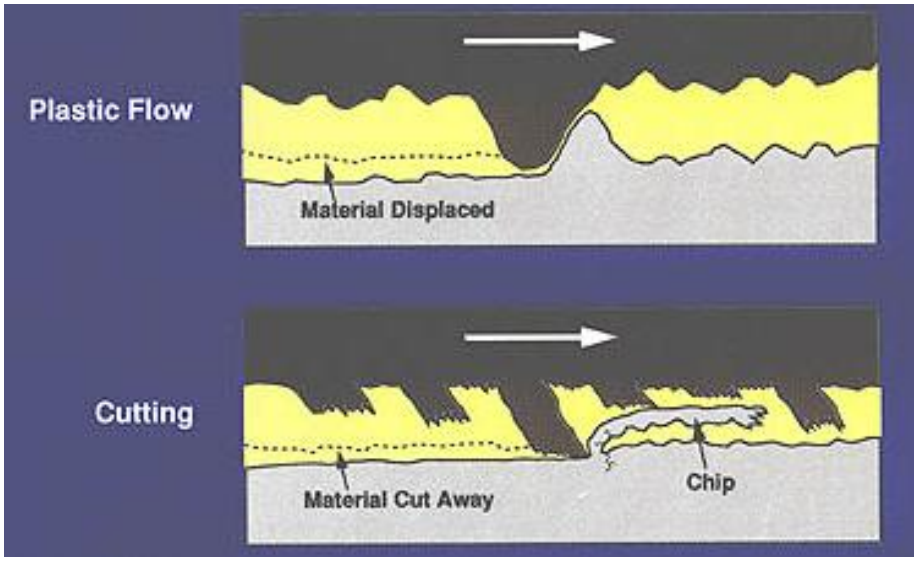

Figure 0-15: Schematic diagram of two-body abrasive wear (STLE, 2011).

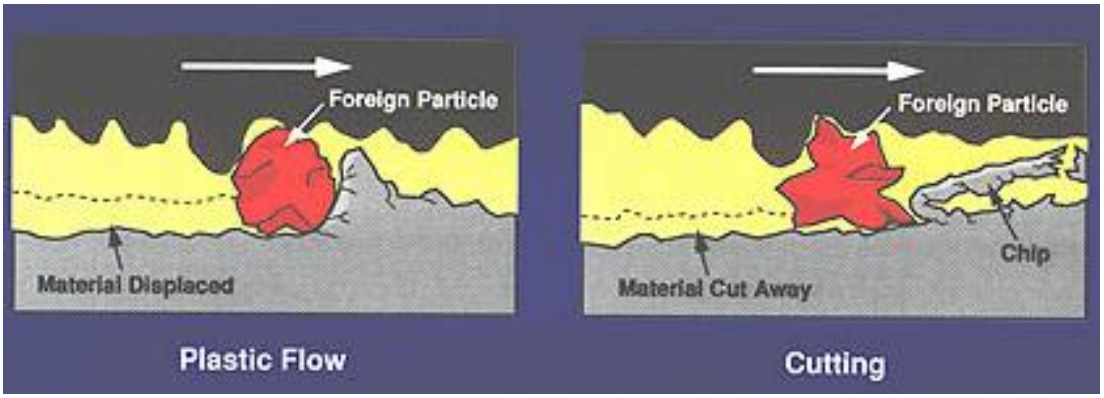

Figure 0-16: Schematic diagram of three-body abrasive wear (STLE, 2011).

Erosive wear is another important type of wear; here a solid or liquid impacts the surface of the material removing parts of it through a repeated deformation and cutting motion. This mechanism is found widely in applications of slurries moving through pipes or pumping equipment. There are a number of factors which affect the erosion wear rate; these include the shape, hardness and impact velocity of the particle as well as the impingement angle. The impingement angle is the angle at which the particle hits the material surface from the horizontal; it depends on the type of tribo-system; and when

the angle is small the wear produced is similar to that of abrasive wear while if the angle is large (between 75 - 90°) material can be removed by plastic flow or brittle failure (Poeton, 2011; GordonEngland, 2011). Figure 0-17 shows a schematic diagram of erosion wear.

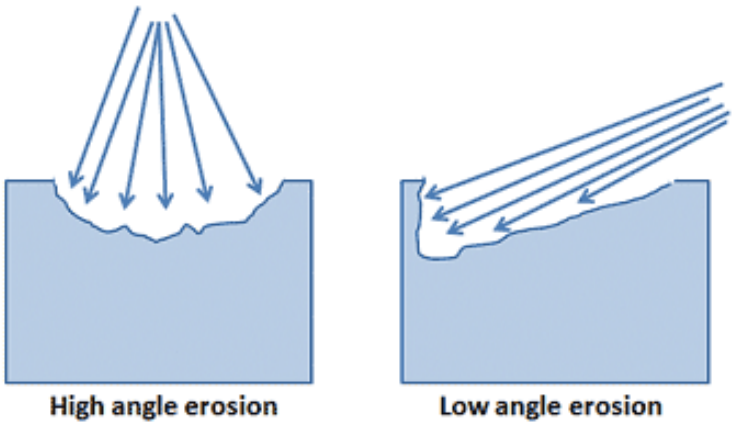

Figure 0-17: Schematic of erosion wear (Poeton, 2011).

2.4.2. Abrasive Wear Resistance of Thermally Sprayed Coating

Abrasion wear is a major mode of failure of many materials. Thermal sprayed WC-Co cermets coatings have been used due to their excellent abrasive wear resistance (Wang et al., 2009) to address this problem. The abrasive wear resistance of these coatings is controlled by a number of factors such as the coating process as well as the properties of the spraying powder, i.e. the morphology and initial particle size and distribution of the spray powder and the difference in the hardness of the carbide powder and the abrasive media.

Thermal spraying process causes residual stresses, usually tensile, to exist in the coatings. These stresses arise from impact, cooling, solidification and solid-state cooling

of the splats on the substrate and on subsequent splats where the splats cannot deform enough (Stewart et al., 1998). Thermal mismatch due to thermal expansion coefficient differences between the coating and substrates also affect the residual stress. These residual stresses have an effect on the wear resistance of the coating. Residual stresses can cause cracking and delamination of the coating thus decreasing the wear resistance. Post spray heat treatment of the coating can reduce the residual stresses in the coating and thus increase wear resistance. Heat treatment in inert atmosphere such as argon or hydrogen at temperatures above 600°C can decrease the residual stresses by recrystallization of the amorphous phases by promoting the formation of eta phases (Co_6W_6C) (Stewart et al., 1998).

Asl (Asl et al., 2006) did tests on the variation of heat treatment temperature (650 – 1100°C) in vacuum ($2.5x10^{-5}$ mbar) for 1 hour on WC-17Co coatings. These authors determined the effect heat treatment has on the mechanical properties and wear loss of the coated layers. The wear loss was determined by a pin-on-disc arrangement with a constant load of 5 N, sliding speed of 0.1 m/s and sliding distance of 100m. They found that the best mechanical properties and lowest wear resistance was achieved at about 800°C, as shown in to Figure 0-18. At 1100°C, the hardness and wear loss increased, while the fracture toughness decreased. This was due to complete transformation to crystalline eta phase, which is brittle and hard. The 800°C sample showed no significant transformation.

There are two methods used to determine the abrasive wear resistance of a material, pin on disk for two-body wear, while the rubber wheel test is used for three-body wear in either a wet or dry environment (Stevenson & Hutchings, 1996).

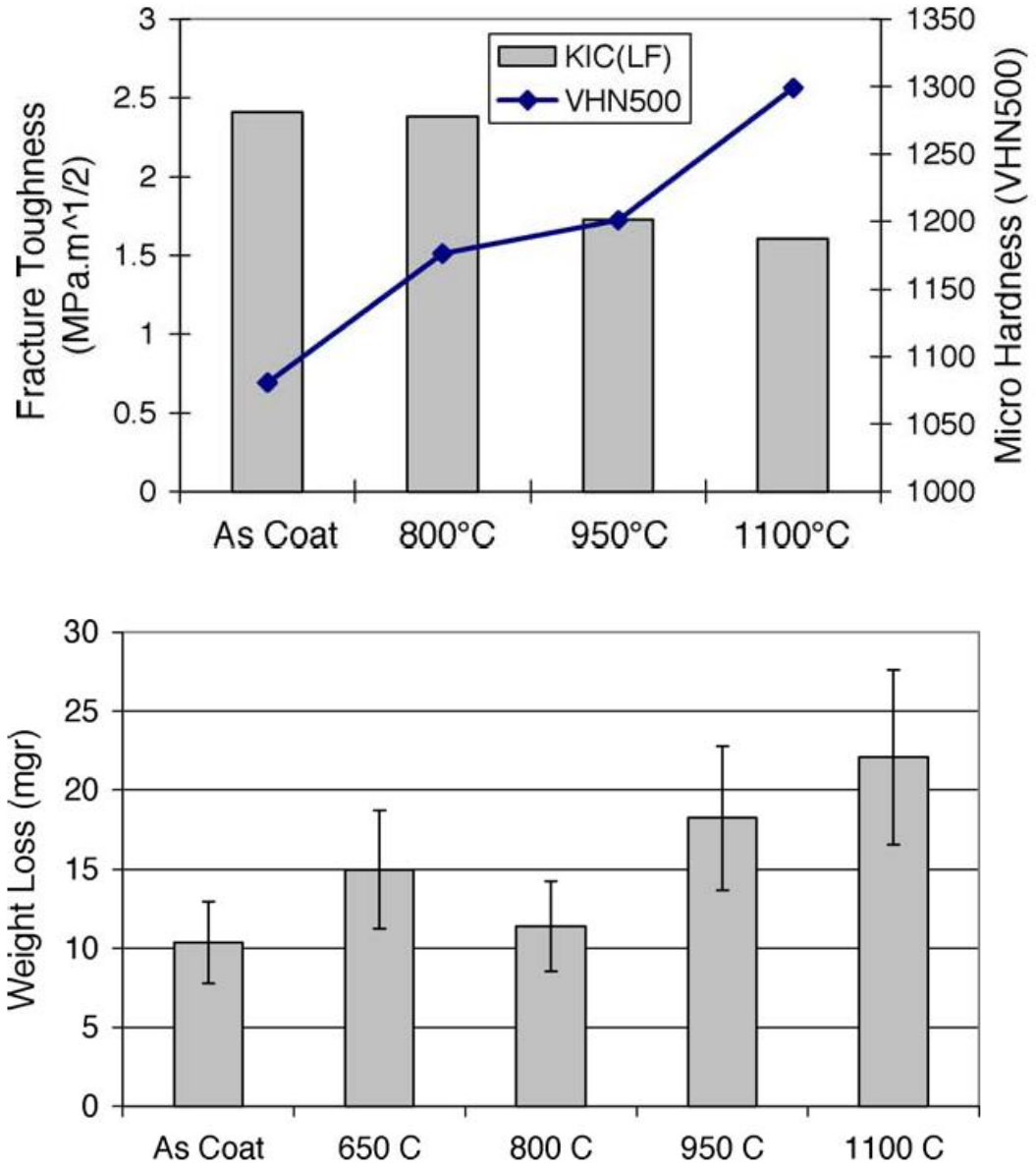

Figure 0-18: Effect of heat treatment temperature on (a) Micro-hardness and fracture toughness and (b) Wear loss on WC-17Co coatings (Pin-on-disc arrangement, 5N load, 0.1m/s sliding speed and distance of 100m) (Asl et al., 2006).

2.4.3. Dry Sand-Rubber Wheel Abrasion

The dry sand rubber wheel abrasion test (DSRW) as described by ASTM Standard G65 (ASTM G65-04, 2010) is commonly used to evaluate the abrasive wear resistance of materials under three-body conditions. The test was developed to simulate wear situations in which low-stress scratching abrasion is the primary mode of wear, i.e. loose abrasive grains being dragged across a surface under loading conditions which do not induce fracture of abrasive particles. Figure 0-19 is a schematic diagram of the dry sand-rubber wheel test apparatus.

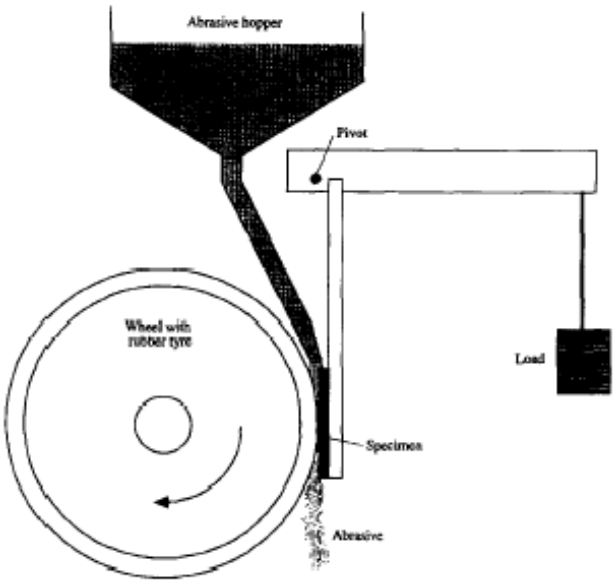

Figure 0-19: Schematic diagram of the dry sand-rubber wheel test apparatus (Stevenson & Hutchings, 1996).

Chapter 3: Experimental Procedure

This chapter details the experimental procedures used in making and characterisation of the carbon enriched WC-Co powders, sprayed coatings, sintered PCD materials and wear tests. A detailed description of all equipment used in making, characterisation and testing is also provided in this chapter.

3. Experimental Procedure

3.1. Powder Processing

3.1.1. Raw Powders

All powders used in this study are given in Tables 3-1 and 3-2. The particle size distribution and supplier are also provided. The particle size distribution of the as-received starting WC-Co powders and diamond powders are given in the results sections containing Figure 4-1 and Figure 6-2 respectively.

Table 3-1: Powders used in processing of coatings.

Material	Particle Size (µm)	Supplier
WC-12Co WOKA 3103	-45 + 11	Sultzer Metco, Fe Powder Suppliers (Pty) Ltd
WC-17Co WOKA 3203	-45 + 11	Sultzer Metco, Fe Powder Suppliers (Pty) Ltd
WC-Ni	-45 + 11	Sultzer Metco, ThermaSpray SA (Pty) Ltd
Phenolic resin	-	Element Six (Pty) Ltd

Table 3-2: Diamond powders used for sintering.

Diamond Powder	Modality	Average Particle Size (µm)	Supplier
Medium Grade (MG) + 1%SP Co	Multimodal	8 – 10	Element Six (Pty) Ltd
Fine Grade (FG-6) +1%SP Co	Multimodal	4 – 6	Element Six (Pty) Ltd
Ultra-Fine Grade (FG 0.5)	monomodal	0.5	Element Six (Pty) Ltd

3.1.2. Carbon Enrichment

Carbon enrichment of WC-Co powders was done to add up to 6wt% extra carbon. Carbon enrichment of the WC-Co powders was achieved by a two stage process. A schematic diagram of the carbon enrichment process is shown in Figure 3-1 **.** In the first stage the appropriate amount of phenolic resin (Phenol formaldehyde resin ($C_7H_6O_2$)) (grade SSA3034, from Element Six (Pty) Ltd), to achieve carbon enrichment according to Equation 3.1 (Davies & Myburgh, 2008), was placed in a beaker, 400ml of ethanol was added to dissolve the phenolic resin. The phenolic resin is an unmodified phenolic novolak resin powder of less than 75µm; it contains approximately 14% hexamethylene tetramine as a cross-linking agent. A magnetic stirrer bar and plate were used to help encourage dissolution. Once all the phenolic resin was dissolved into the ethanol, the liquid was added to a rotary evaporation flask containing the required amount of WC-Co powder. The two were mixed together then placed in a rotary evaporator to dry at 80°C and rotating 65rpm. The powder was removed while slightly damp and placed onto a watch glass and dried in an oven at 60°C overnight.

$$\%\ Carbon = \frac{\frac{100 \times weight_{resin}}{weight_{WC} + weight_{resin}}}{2.32} \quad \text{..... (3.1)}$$

The dried powder was then crushed using a mortar and pestle. The crushed powder was placed into a zirconium boat which was placed in a tube furnace for pyrolysis under H_2/Ar gas. The heat treatment cycle used consisted of heating to 450°C at a rate of 3°/min, then to 1020°C at a rate of 5°/min, holding at 1020°C for 45 minutes and then cooling slowly down to room temperature as shown in Figure 3-2. The powder was heated to 450°C as this is the temperature of the pyrolysis reaction of the phenolic resin; above 600°C the resin can be converted to carbon with a high yield. A temperature of 1020°C was used to bond the decomposed resin to the WC-Co powder. The pyrolysed WC-Co powder was partially sintered together and was crushed in a Retsch KM100 Pulveriser and sieved to a mesh size of 53 µm to restore the starting powder distribution.

After several attempts to produce a 4 and 6wt% carbon enriched powder using a single step carbon enrichment- pyrolysis method failed due to the thermosetting ability of the phenolic resin at high contents, a multi-step process was then used. The multi-step process consisted of consecutive carbon enrichment-pyrolysis steps until the required carbon content was achieved. The carbon content of the powders was set according to the description above. After the required carbon content was achieved the powders were HVOF thermally sprayed on onto a substrate.

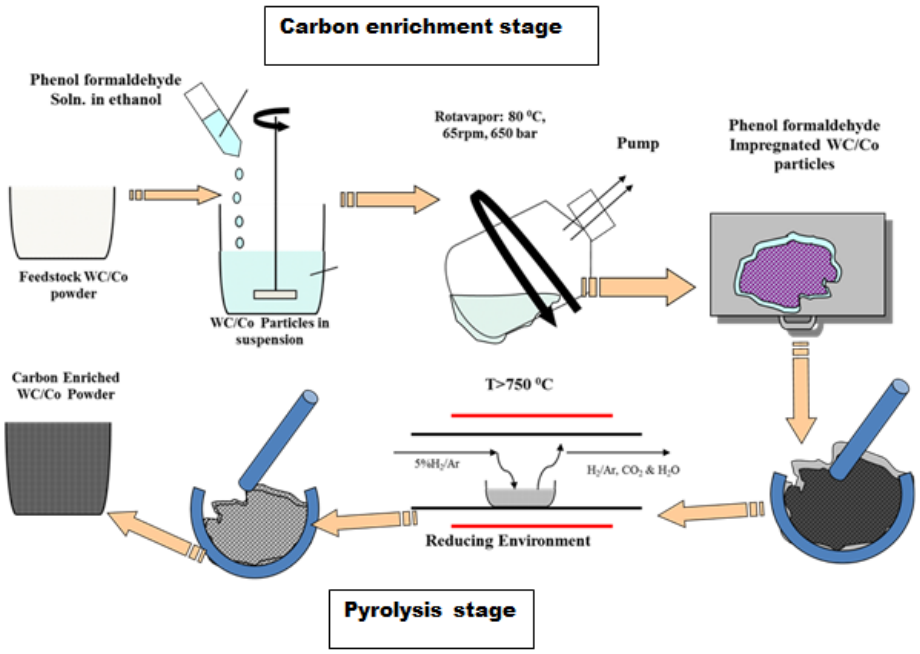

Figure 3-1: Schematic diagram of the Carbon enrichment (Davies & Myburgh, 2008).

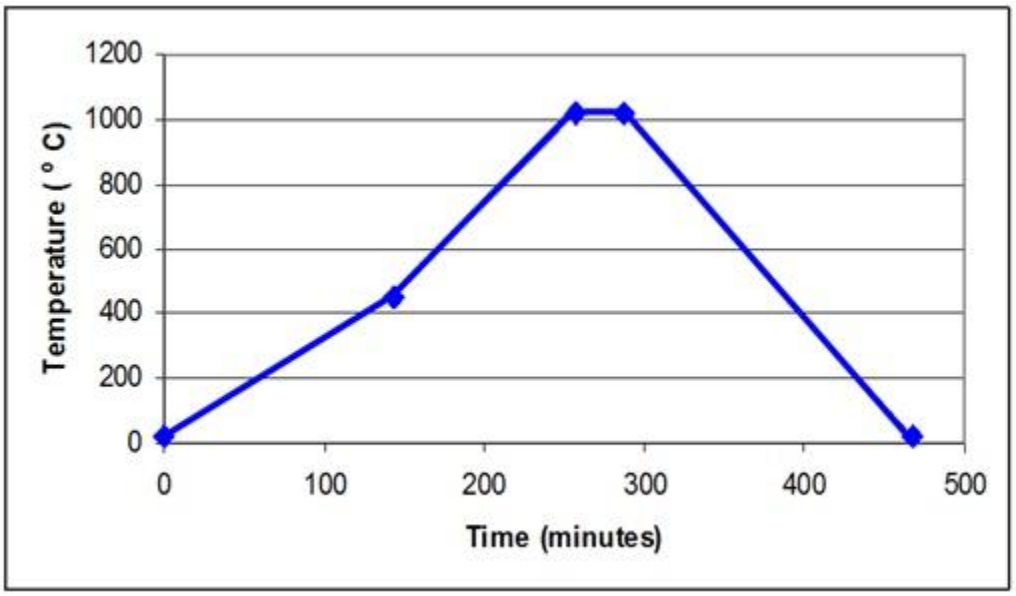

Figure 3-2: Carbon enrichment pyrolysis heat cycle.

3.2. Thermal Spraying

Thermal spraying of the WC-Co powders onto the substrates was carried out at the facilities at ThermaSpray (Pty) Ltd. There are two substrates used in thermal spraying; mild steel for wear resistance and WC-Co for PCD sintering.

3.2.1. Pre-Spraying Treatment

Pre-treatment of the substrates was done to roughen the surface for good adhesion of the coating during spraying. This was done using Al_2O_3 grit blasting.

3.2.2. HVOF Spraying Conditions

Thermal spraying was done using the High Velocity Oxy-Fuel (HVOF) method. A Metco Perkin Elmer DJC diamond gun was used. A powder feed rate of 45 g/min and a spray stand-off distance of 220 mm were used. The composition of the oxyfuel gas was set to the following ratio of Air/O_2/fuel of 32/38/38 l/min. A schematic diagram of the HVOF gun is shown in Figure 0-12. Six WC-Co powders were used for spraying; the standard WC-12Co and WC-17Co powders and the 2, 4 and 6%C coated WC-12Co and WC-17Co powders. A coated layer thickness of over 100 - 300 µm was targeted. Coated substrates were mild steel (sample dimensions 75x25x6mm^3) for wear tests and WC-Co substrates (18mm diameter, height 12.5mm) for PCD sintering. After thermal spraying, the samples were taken for further analysis and testing (i.e. microstructural analysis (XRD and SEM), PCD sintering, wear testing and hardness).

3.2.3. Post Spray Treatment

After thermal spraying some of the samples were taken for post spray treatment. Some of the coated mild steel substrates were taken for an annealing heat treatment before wear tests to determine the effect of heat treatment on the wear resistance (i.e. potential reduction of the residual stresses in the coating and improved homogenization of the microstructure). The annealing heat treatment consisted of heating the substrates in a tube furnace to 700°C with a dwell time of 1 hour in an argon atmosphere and cooled at a slow rate of 5°C/min to room temperature (Figure 3-3).

The coated WC-Co substrates for PCD sintering were also sent for post spray treatment to recrystallize the Co phase. This was done in a tube furnace to 1100°C for 1 hour in a hydrogen atmosphere and cooled at a slow rate of 5°C/min to room temperature (Figure 3-3).

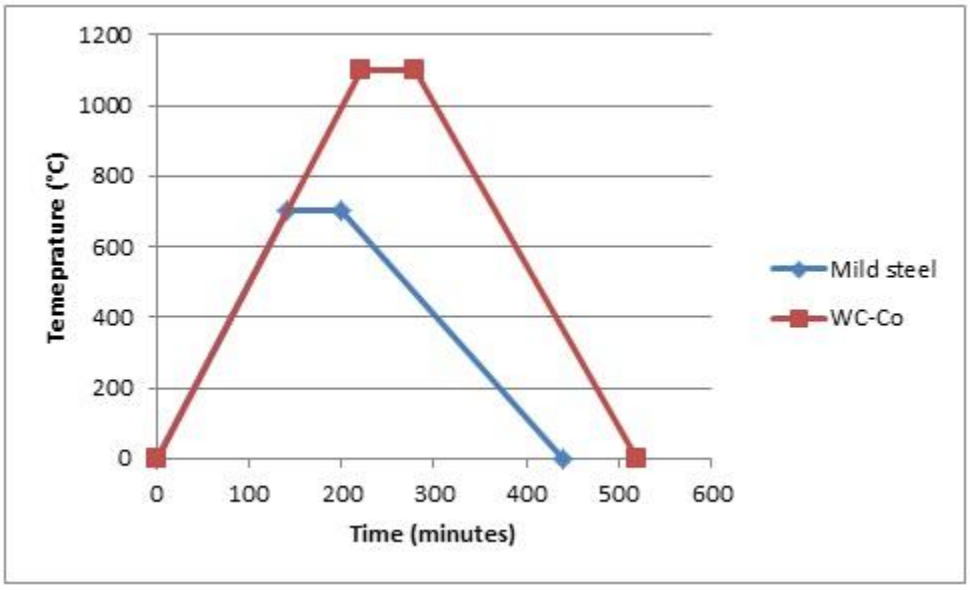

Figure 3-3: Heat treatment cycle of coated substrates; mild steel and WC-Co.

3.3. Carbon Enhanced Carbides

Carbon enhanced carbide substrates were made by mixing diamond particles with WC and Co powders. The powder was then pressed into a green body and sintered under HPHT conditions (⌣1400°C and 6.8GPa). Two types of carbon enhanced carbide substrates were produced at Element Six (Pty) Ltd; a graphite-diamond enhanced carbide (GDEC) and a diamond enhanced carbide (DEC).

The DEC substrate was produced by the standard method described in Section 3.3. The GDEC substrate was produced similarly to the DEC substrate but an extra step was added between the pressed green body step and the HPHT sintering step. This was a vacuum sintering step in which the diamond grains graphitize due to the Co while the carbide sinters around them. After the vacuum sintering the samples were HPHT sintered at ⌣1400°C and 6.8GPa, the graphitized diamond particles reconverted to diamond during this stage, but this allowed more carbon to dissolve into the WC-Co material (i.e. Co metal dissolved the graphite particles and became saturated with carbon). The diamond particles were in the range of 10-30 µm. Various volume fractions of the diamond were used ranging from 5 – 15 vol.%.

A diamond enhanced carbide sample was made with 0.5µm diamond powder, sintered by spark plasma sintering (FCT Systeme GmbH – HPD5). 10vol.% of the 0.5µm diamond powder was mixed together with WC-12Co powder in a tubular mixer for 1 hour with a tungsten ball ratio of 5:1 then SPS sintered. Powder was placed in a graphite die coated in hBN. Samples were densified for 5 min at temperature of 1200°C under a pressure of 40 MPa in a vacuum. The heating rate was maintained at 100°C/min. The samples produced were 3 mm thick and 20mm diameter.

A VC doped carbide substrate was made by adding VC powder to the WC-Co substrate as a grain growth inhibitor. This was produced by mixing 2 wt% VC powder with WC-12Co powder in a turbula mixer for 1 hour with a tungsten ball to powder ratio of 5:1 then SPS sintered. Powder was placed in a graphite die coated in hBN. Samples were densified for 5 min at temperature of 1200°C under a pressure of 40 MPa in vacuum. The heating rate was maintained at 100°C/min. The samples produced were 3 mm thick and 20mm diameter.

The SPS samples were taken for OD and surface grinding to remove any residual graphite and hBN remaining from the die and to reduce to 18 mm diameter for HPHT PCD sintering.

3.4. High Pressure High Temperature Sintering

3.4.1. Pre-HPHT Sintering

Coated substrates and PCD grit (i.e. fine grain diamond powder) used for PCD sintering were placed in the appropriate containers for sealing before sintering (i.e. Ta and Nb). The containers were placed in a Balzer vacuum furnace for outgassing; the vacuum treatment was used to remove all absorbed gases and surface impurities to prevent oxidation before sintering. This treatment takes about 14 hours and consists of heating in two steps; first to 500°C, dwell for 2 hours and then to 1050°C, dwell for 3.5 hours before cooling rapidly to room temperature under a vacuum of 10^{-3} bar. After outgassing the containers were sealed using electron beam (EB) welding.

3.4.2. HPHT Sintering

The sealed compacts were then placed in the required components (metal cups, salt nest and capsule) used for sintering of PCD samples; 5 samples were produced in each capsule per sintering run. Sintering of the PCD materials was done at high pressure and high temperature to facilitate full densification. This operation was done at the sintering facilities at Element Six (Pty) Ltd, South Africa using a HPHT belt apparatus. The sintering process used is proprietary to Element Six (Pty) Ltd and thus most aspects of the process cannot be divulged. The general sintering process involves applying a pressure and then heating to sinter and form a fully densified compact. The sintering pressure and temperatures used in this experiment were in the range of 5.6 – 6.8 GPa and between 1400-1500°C respectively.

The EDM (electric discharge machine) cutting was used to cut the sintered compacts in half for grinding and polishing for microstructural analysis.

3.5. Wear Tests

Wear tests were done on coated substrates to determine the wear resistance of the coating. The abrasive wear test used was the dry sand-rubber wheel test. A Paarl Granite Turning (PGT) test was also done on a selected PCD sintered material.

3.5.1. Dry Sand-Rubber Wheel Test

The abrasion test used for this experiment to determine the wear resistance of the WC-Co coating is the dry sand-rubber wheel test described in the ASTM standard G65 (ASTM

G65-04, 2010). In the dry sand-rubber wheel abrasion test shown in Figure 0-19, the specimen was loaded horizontally against the rim of the rotating rubber wheel. The abrasive silica sand (supplied by Rolf's Silica) with the particle size distribution given in Figure 3-4, was gravity-fed between the rubber wheel and the sample specimen. The specimen weight loss was measured and related to the wear. The rubber wheel abrasion test produces a soft abrasion, where the abrasive particles generally remain intact after the abrasion process. The wear specimen used in this experiment was mild steel substrates with a WC-Co thermal sprayed coating. The specimen dimensions were 70 x 25 x 6 mm^3. The load and rotation of the rubber wheel used in the experiments was 25 N and 200rpm respectively. The sand had a flow rate of 4.0 – 7.0 g/s (control of the rate was difficult as the speed controller was faulty). The samples were polished to eliminate surface roughness effects. The samples were initially weighed. Two wear resistance experiments were set-up:

(1) 5 min interval tests for 30 mins and

(2) full 30 min tests (no intervals).

In the first experiment the samples were weighed after 5min intervals to determine the total weight loss. The total time for each experiment was between 0 – 30 mins. The second experiment the weight loss was determined after the full 30 mins test was performed. The dry sand-rubber wheel apparatus used is shown in Figure 3-5.

The wear micro-mechanisms were characterized by using SEM. The particle size distribution of the silica sand after wear is also shown in Figure 3-4, showing only a small decrease in the mean particle size after wear.

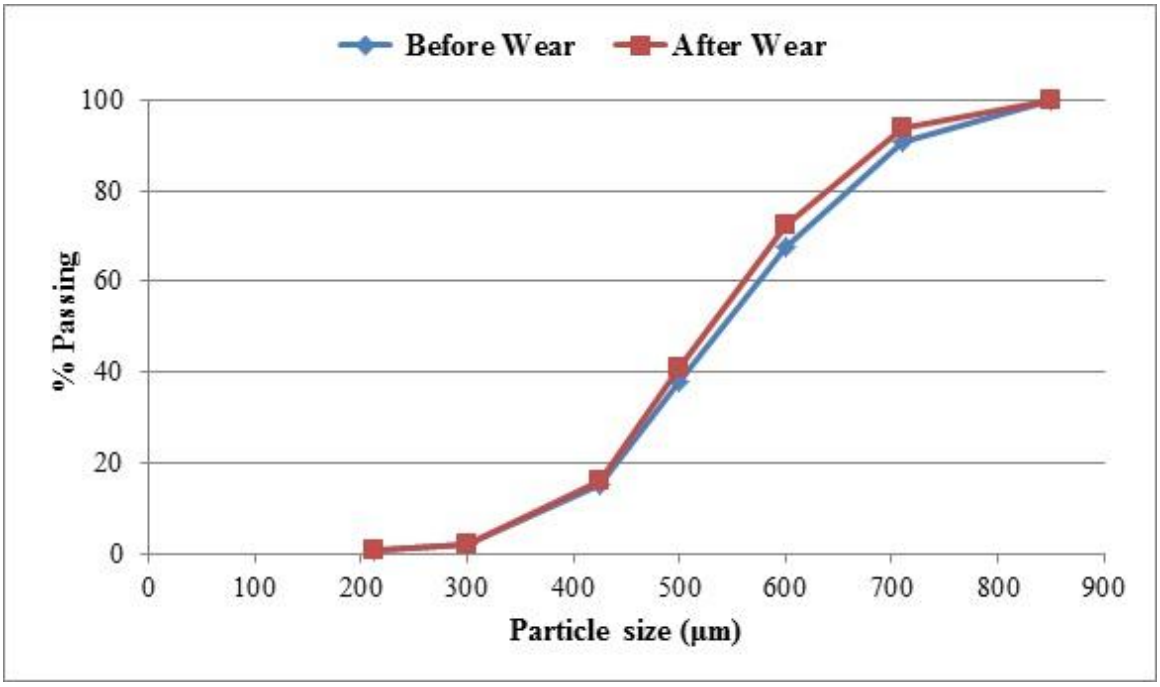

Figure 3-4: Particle size distribution of the silica sand before and after wear.

Figure 3-5: Dry sand-rubber wheel test apparatus: (a) entire apparatus and (b) rubber wheel.

3.5.2. Paarl Granite Turning (PGT) Wear Test

A Paarl Granite Turning (PGT) test was carried out to determine the wear behaviour of the PCD sintered materials. A PGT test is a turning or milling test on Paarl granite. A core (cylinder) of rock is loaded onto a lathe. The rock is rotated and the PCD sample is engaged into the rock for a set depth of cut and time. The wear scar is measured linearly from the top of the PCD sample to the bottom of the wear scar using a stereo microscope attached to a camera and analysis software. The PGT test can test both two and three body abrasion. The time for turning was 10 minutes.

3.6. Hardness

Vickers hardness measurements (H_v) were done on the coated samples used for wear tests. An indentation load (L) of 2kgf for 15s was used and the diagonals (d) of the indentation were measured. The hardness was calculated using the Vickers hardness Equation 3.2. At least 10 indentations were measured per sample and the average hardness and standard deviation were calculated.

$$H_v = 1.854 \times \frac{L}{d^2} \quad \text{.....(3.2)}$$

3.7. Characterisation

Characterisation of WC-Co powders, coated layers, sintered PCD samples and wear samples were done using the following methods:

- Particle size analysis
- XRD phase analysis

- Microstructural SEM and EDX analysis
- Image Analysis
- Carbon analysis
- Raman Analysis

3.7.1. Particle Size Analysis

The Malvern Mastersizer 2000 Particle Size Analyser (PSA) was used to determine the particle size distribution of all powders, raw and mixed, before use. The powders were suspended in a small amount of distilled water to produce a slurry, a standard dispersant (sodium hexametaphosphate) was also added (<0.05g) and ultrasonically probed. A small amount of the suspended solution was poured into the PSA analysis tank where an ultrasonic probe was used to disperse the particles into the water. The PSA measures the light intensity as a function of the scattering angle of the suspended solution and determined the particle size and particle size distribution of the suspended powder particles. The particle size analysis of each powder was performed at least three times to obtain an average of the results.

3.7.2. XRD Phase Analysis

X-Ray diffraction (XRD) was used to qualitatively determine the phases present in the composite material. The samples were examined using a Bruker AXS D2 phaser desktop powder diffractometer, using monochromatic Cu (K_α) radiation produced at 40 KV and 20 mA. Diffractograms were collected over a range of 2θ between 10 and 90^o, with a step size of 0.02^o 2θ, together with a scan step time of 0.15 s.

A Pananalytical X'pert diffractometer with Co radiation and accelerator detector with a nickel filter to remove Co (K_β) was also used. Co radiation was produced at 40kV and 20mA. Diffraction patterns were collected over a range of 2θ between 10 and 90^o, with a step size of 0.02^o 2θ, together with a scan step time of 4 s. The Co detector was used to get a clearer indication of the Co content within the samples used for PCD sintering.

3.7.3. Microstructural SEM and EDX analysis

A Scanning Electron Microscope (SEM) Philips XL 30 ESEM-FEG series was used to study the microstructure of the materials. An EDX (energy dispersive X-ray) spectrometer (EDS) was used to identify the elemental composition of the various phases in the microstructure. This was used to support the evidence of the XRD analysis and to find evidence of free carbon that could not be detected with the XRD analysis.

Double-sided carbon tape was used to mount the samples onto aluminium sample holders and also to provide the electrical conductivity. The samples were not coated. An acceleration voltage of 2 – 20 keV was used. An assortment of magnifications of micrographs were taken ranging between 30 – 10 000X.

Microstructural analysis of the sintered materials was done using SEM and EDX analysis as described above. Approximate binder pool thickness was determined. Optical microscopy was also done on the samples to measure the thickness of the AGG region. The abnormal grain growth (AGG) was measured by taking images of the entire AGG region on an optical microscope at 5X magnification. The Axiovison area measurement tool was used to measure the total area of the AGG and the distance measuring tool was used to determine the length of the AGG area along the interface. By dividing the area

by the length, the average thickness of the AGG region was determined. The standard deviation was also derived.

A SEM investigation was also carried out on the AGG region of the PCD materials using NVISION, with an attached EDX (INCAx-sight, Oxford Instruments) and NVISION 40 (Zeiss) with an EBSD (HKL, Nordlys). This was done to determine the orientation of the diamond grains.

3.7.3.1. Image Analysis

Image analysis (IA) was used to quantify and characterise the microstructure of the PCD and WC-Co substrate. IA was done by taking 10-20 SEM images of the microstructure (as described in Section 3.7.3). The magnification of the SEM images depends on the grain size of the material. A high magnification was used for fine grain size materials, while a low magnification was used for coarser grain size materials.

The IA software programme AnalySIS Pro was used to determine the phase percentage of each phase by ascribing the different light intensities to various phases. Data was then produced to determine the different binder and grain size percentage. The data generated from the AnalySIS Pro programme was used in conjunction with a programme module designed in Excel to determine the grain size and distribution, phase content, mean free path (MFP), contiguity of the PCD material and WC-Co substrate.

3.7.4. Carbon Analysis

Carbon analysis was done on the WC-Co powders to determine the percentage carbon in the powders. Carbon analysis was done using an Eltra CS 800 analyser shown in Figure 3-6. The Eltra CS800 is an induction furnace attached to a computer and an interfaced electronic balance. Sample powder of 0.5g was weighed out and ± 0.2g of flux powder (copper (Cu) filings and tungsten (W) accelerator) was added in a ceramic crucible. The lid was placed on and the crucible was placed on the furnace pedestal. The furnace was heated up by induction coils to 1250°C with medical O_2 flowing through the system. Volatile gases (CO_2 and SO_2) were burned off; they passed over an infra-red detector cell which separated the carbon from the sulphur. The carbon and sulphur content is given in either percentage (%) or ppm.

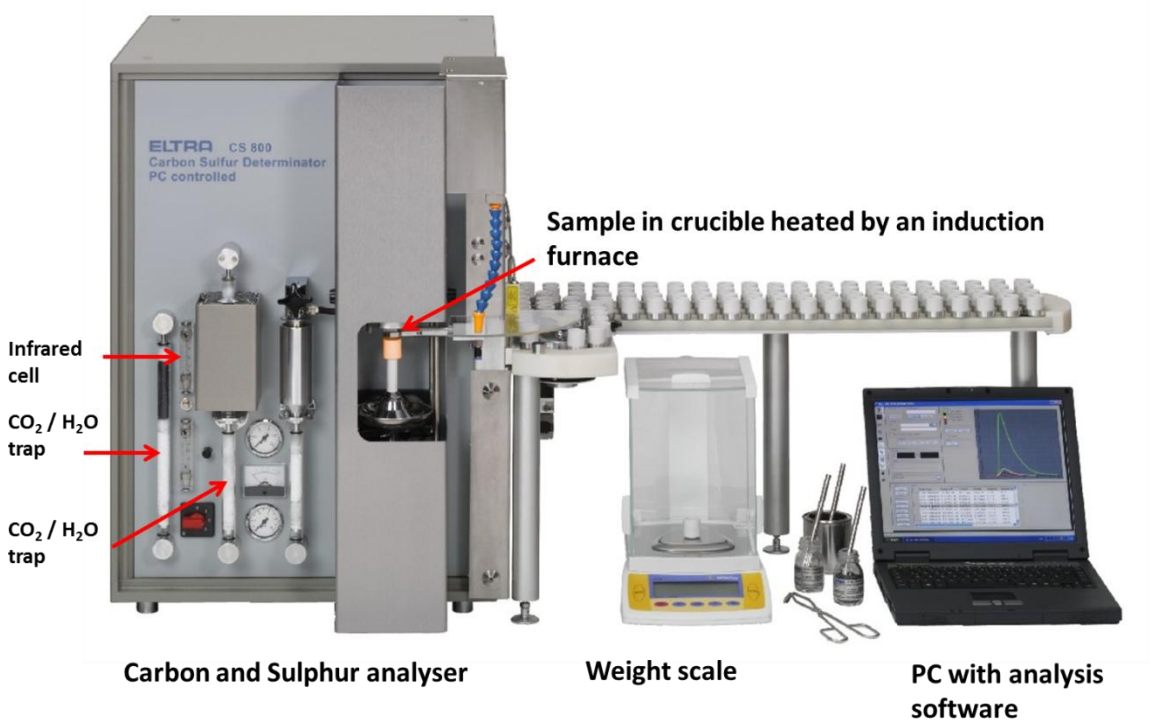

Figure 3-6: Eltra CS800 carbon and sulphur determinator.

3.7.4.1. Cutting and Polishing

For characterisation of the coated layers the samples needed to be cut in half, ground and polished. The WC-Co substrates and the steel samples were cut in half using a diamond bonded cutting blade on a Struers Secotom 10 Precision cutter. Polishing was achieved by several stages of grinding and polishing steps down to 1μm.

PCD samples were also cut using EDM and polished by first lapping and then polishing using diamond bonded wheels. Once the samples were polished they were taken for SEM analysis.

3.7.4.2. Raman Analysis

Raman analysis was done on the coated samples to determine if excess carbon exists in the coated layers. Raman analysis was done using two different Raman machines. The first was done using a Jobin-Yvon T64000. The wavelength used for the Raman tests was the 514.5 nm green laser line of an Ar ion laser. Analyses on various spots were done to determine the carbon content in the sample. The second Raman analysis was done on a Horiba Jobin Yvon HR800 with a 785 nm laser wavelength. As the Raman spot size is less than 1μm, it is only possible to analyse a very small area of each sample. An 8x8 array covering an area of 100 x 100 μm of 64 positions were examined for each sample to determine the overall carbon content in the various materials.

Chapter 4: Results of Powder Processing & Thermal Spraying

4. Results

This chapter describes the results of characterisation achieved by powder processing and thermal spraying of the WC-Co powders. The characterisation includes SEM microstructural analysis, XRD phase analysis, particle size distribution and carbon analysis of the powders and coated substrates.

4.1. Characterisation of WC-Co Powders

The WC-Co powders were characterized according to procedures described in Chapter 3.7.

4.1.1. WC-Co Powders

The particle size distributions of the as-received WC-Co powders are shown in Figure 4-1, the d(0.5) for both powders (WC-12Co and WC-17Co) is 33.7 and 32.5 µm respectively. The microstructure of the WC-12Co and WC-17Co powders are shown in Figure 4-2; the particles shown are spherical, with small WC-Co particles agglomerated together to form a spherical particle and then sintered. The spherical shape of the particles provides better spraying and densification.

XRD phase analysis of these powders is shown in Figures 4-3 and 4-4; WC and Co phases can be seen.

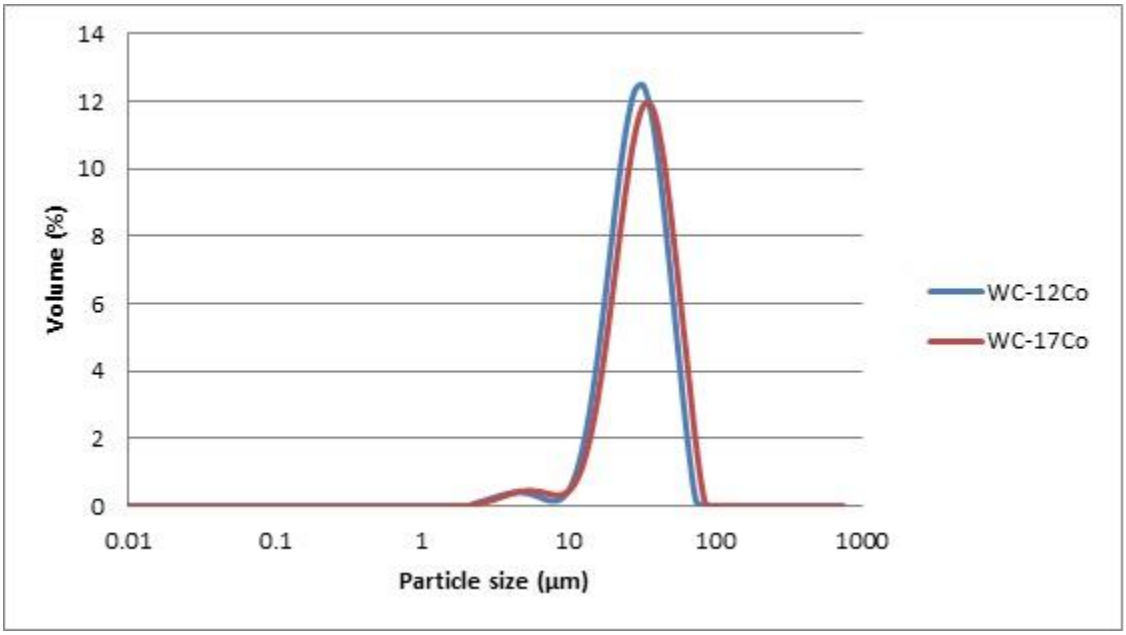

Material:	D(0.1)	D(0.5)	D(0.9)
WC-12Co	18.5 µm	33.7 µm	56.2 µm
WC-17Co	16.9 µm	32.5 µm	55.4 µm

Figure 4-1: Particle size distribution of as-received WC-Co powders.

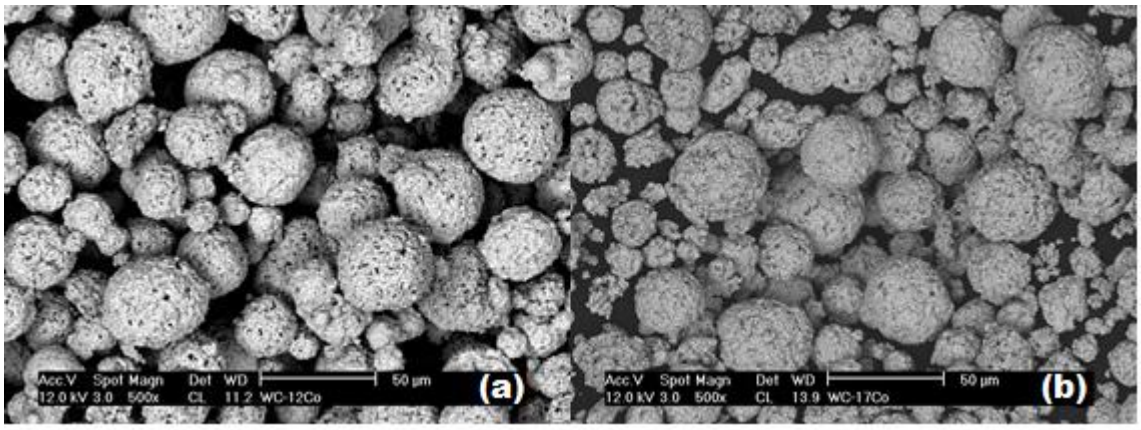

Figure 4-2: SEM-BSI micrographs of a) WC-12Co powders, b) WC-17Co powders.

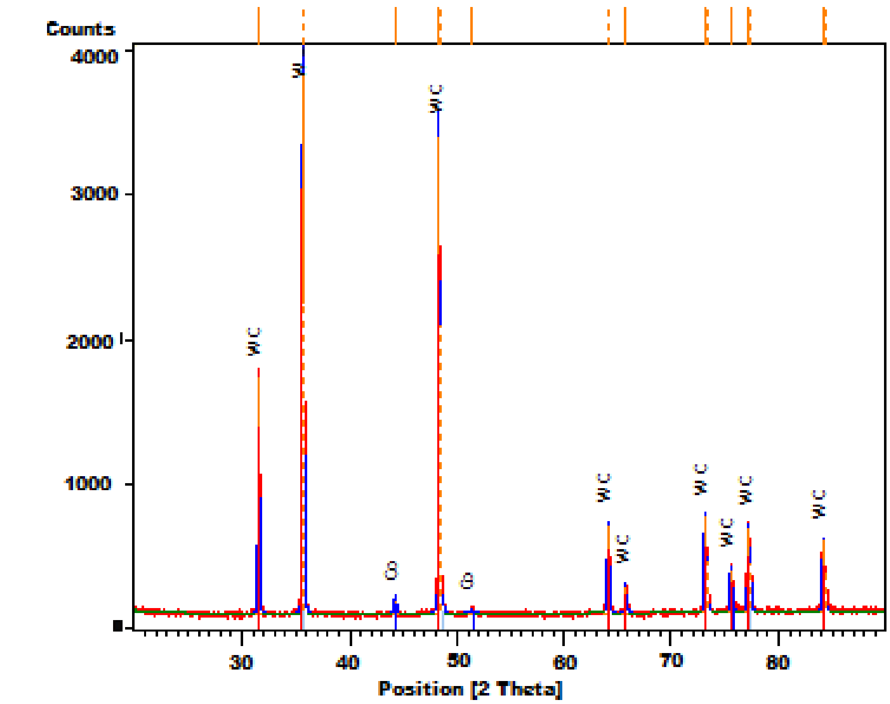

Figure 4-3: XRD scan of WC-12Co powder (Co radiation).

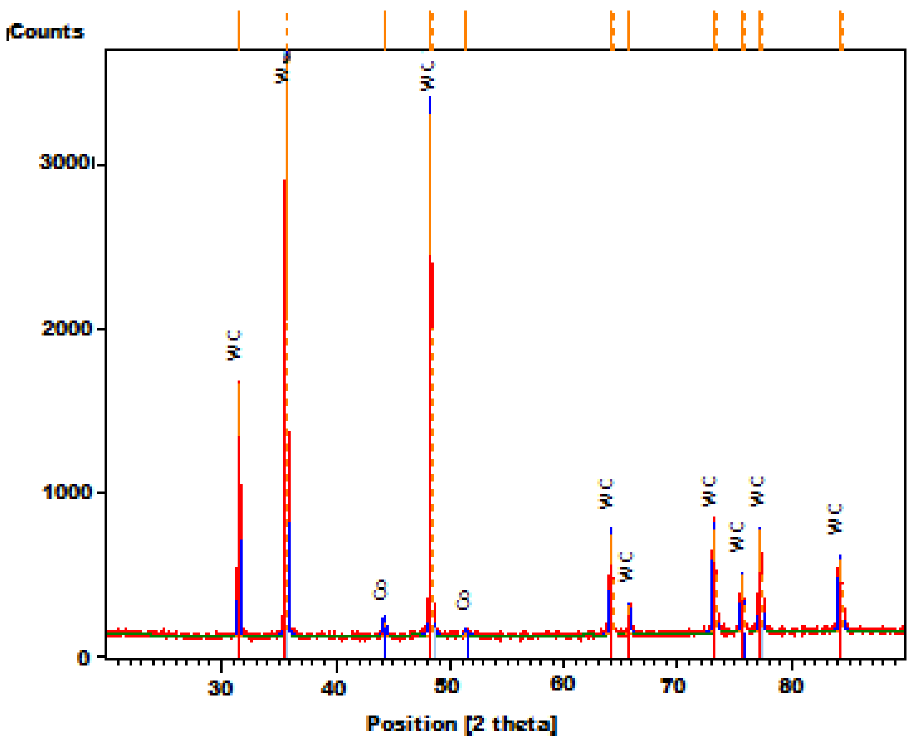

Figure 4-4: XRD scan of WC-17Co powder (Co radiation).

4.1.2. Carbon Enriched WC-Co Powders

Six carbon enriched WC-Co powders have been produced according to the method described in Chapter 3.1.2; the carbon enrichment is given in Table 4-1.

Table 4-1: Carbon Enriched Powders.

Powder	Extra Carbon (vol. %)
WC – 12Co + 2%C	2
WC – 17Co + 2%C	2
WC – 12Co + 4%C	4
WC – 17Co + 4%C	4
WC – 12Co + 6%C	6
WC – 17Co + 6%C	6

The microstructures of the carbon enriched WC-Co powders are shown in Figures 4-5 - 4-7. Figure 4-5 shows the micrographs of the WC-Co powders carbon enriched with 2%C at three different magnifications. The dark phase attached to the round WC particles is carbon. Carbon can be clearly seen bonded to the WC-Co particles creating a coating, (Figure 4-5 c and d). This indicates that the carbon enrichment of the WC-Co particles is possible. Similarly with Figure 4-6 and Figure 4-7, the micrographs show carbon enrichment of the WC-Co powders with 4%C and 6%C respectively. A larger amount of carbon can be clearly seen bonded to these WC-Co particles.

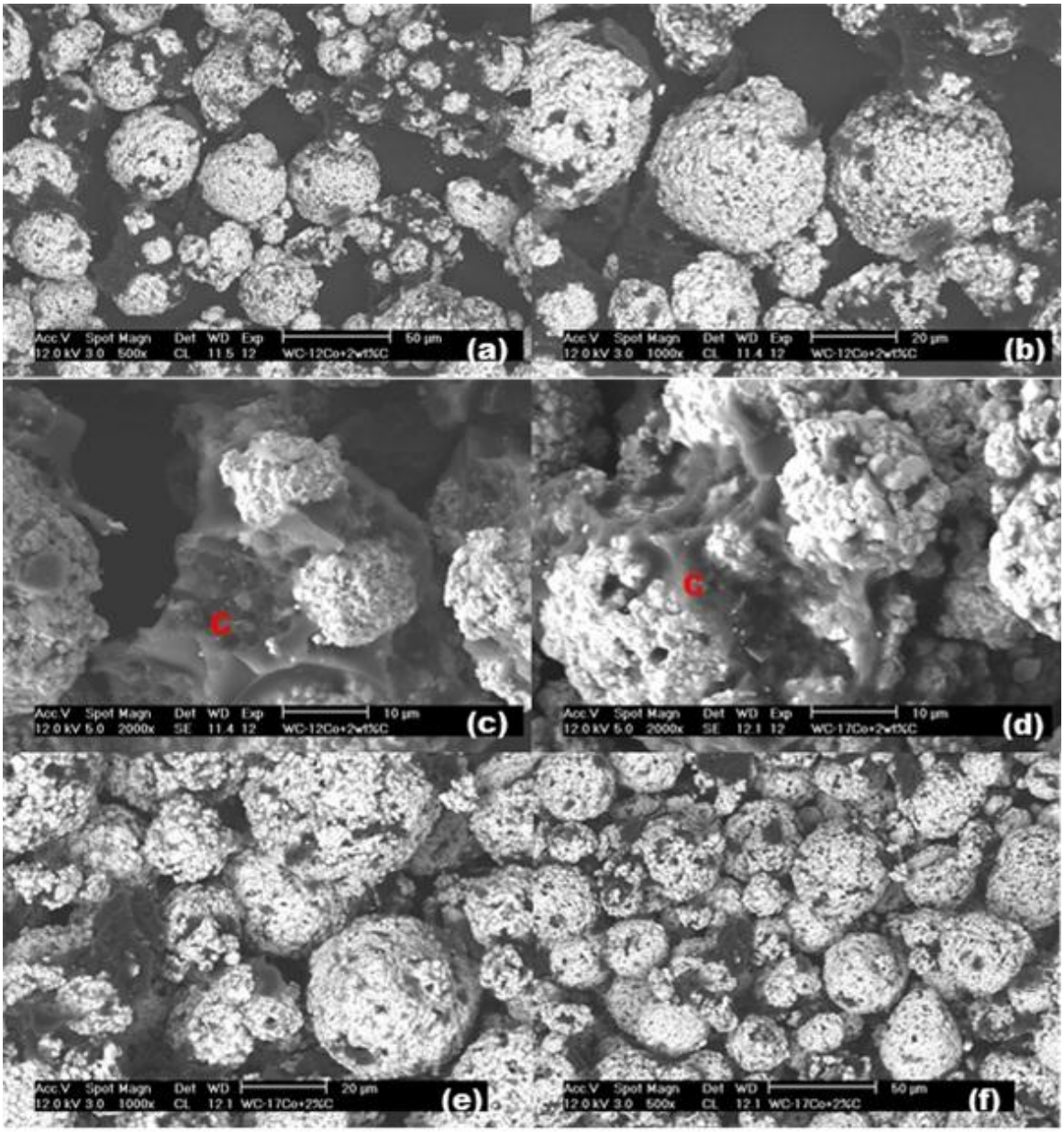

Figure 4-5: SEM-BSI micrographs of WC-Co powders carbon enriched with 2%C; a, b & c) WC-12Co powder and d, e & f) WC-17Co powder, showing Carbon (C; dark phase) coating WC-Co particles (light phase).

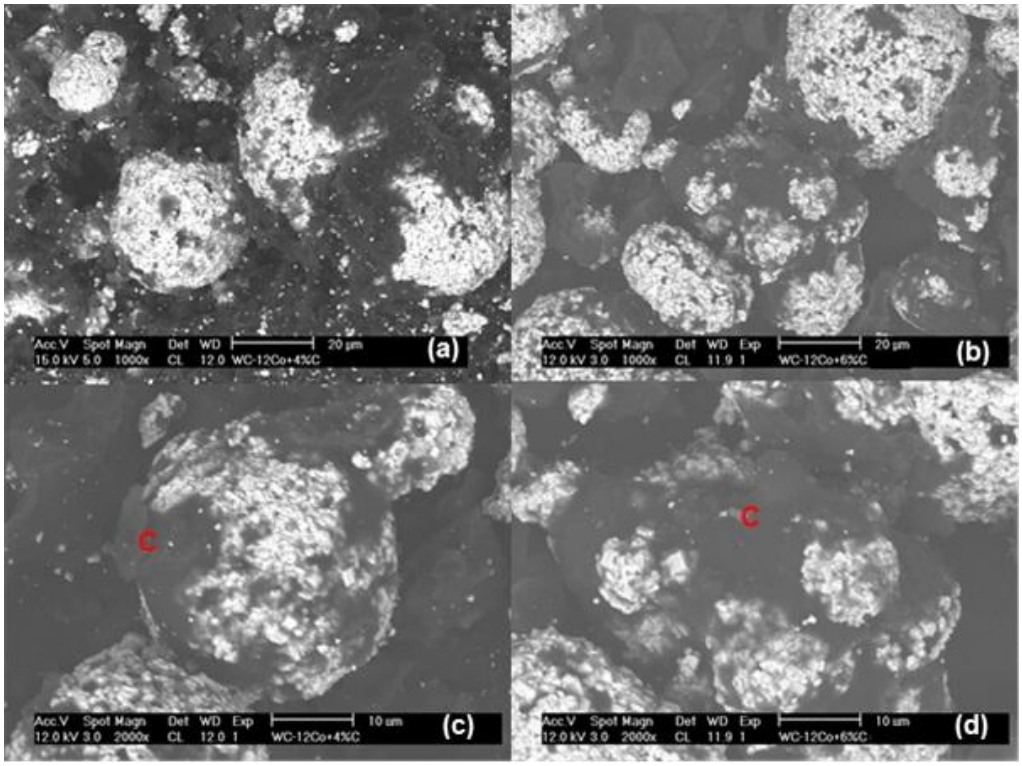

Figure 4-6: SEM-BSI micrographs of WC-Co powders carbon enriched with 4%C (a & c) and 6%C (b & d) of the WC-12Co, showing Carbon (C; dark phase) coating WC-Co particles (light phase).

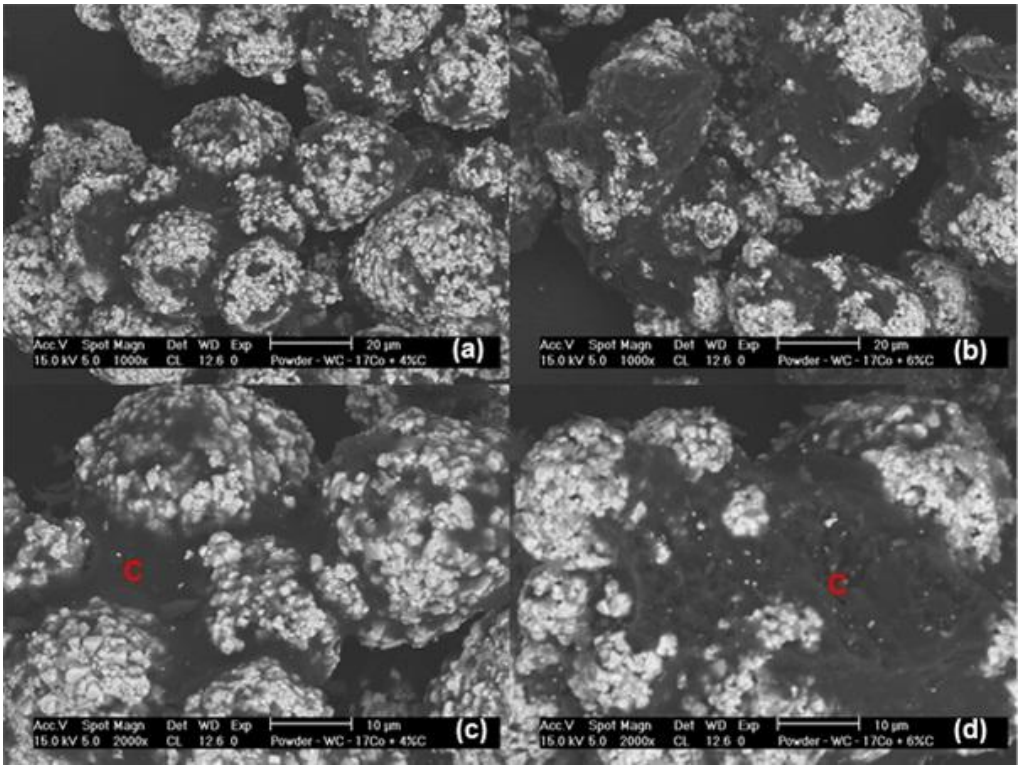

Figure 4-7: SEM-BSI micrographs of WC-Co powders carbon enriched with 4%C (a & c) and 6%C (b & d) of the WC-17Co, showing Carbon (C; dark phase) coating WC-Co particles (light phase).

Figure 4-8 and Table 4-2 shows the particle size distributions of all the carbon enriched WC-Co powders. The particles size distribution was kept in a range between a d(0.1) of 15µm – d(0.9) of 70µm; this is to ensure a good flowability. The d(0.5) for the particles is in the range of 32 – 44µm. Particles smaller than 15µm could result in clogging of the spray gun or disintegration during spraying.

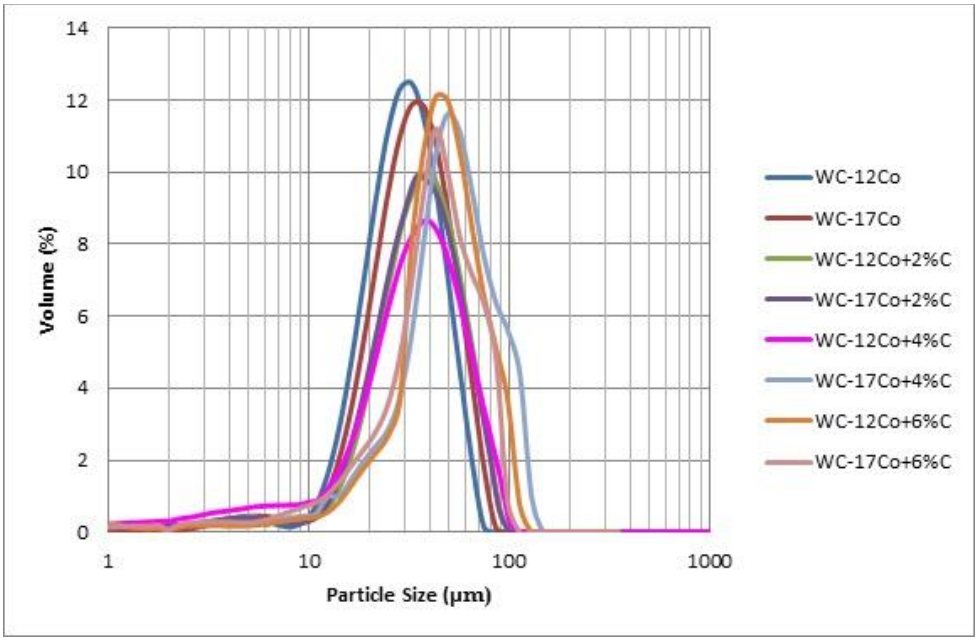

Figure 4-8: Particle size distribution of all the WC-Co powders.

Table 4-2: Particle size distribution of WC-Co powders.

Material	D(0.1)	D(0.5)	D(0.9)
WC-12Co	18.5 µm	33.7 µm	56.2 µm
WC-17Co	16.9 µm	32.5 µm	55.4 µm
WC – 12Co + 2%C	15.9 µm	34.5 µm	60.9 µm
WC – 17Co + 2%C	16.1 µm	35.2 µm	61.7 µm
WC – 12Co + 4%C	17.9 µm	39.9 µm	60.0 µm
WC – 17Co + 4%C	17.7 µm	43.4 µm	81.2 µm
WC – 12Co + 6%C	19.5 µm	44.3 µm	78.6 µm
WC – 17Co + 6%C	15.1 µm	39.3 µm	72.2 µm

4.1.3. Carbon Analysis of WC-Co Powders

Carbon analysis and coating layer thickness of the WC-Co and carbon enriched WC-Co powders were determined as described by Chapter 3.7.4 and 3.7.3 respectively and

given in Table 4-3. This shows that the powders contain the required excess carbon content before spraying.

Table 4-3: Carbon content of WC-Co powders.

Sample Material	Carbon wt%	Excess wt% Carbon	PCD sample Coating thickness (µm)	Wear sample Coating thickness (µm)
WC – 12Co	5.12	-	256.1 ± 6.9	256.5 ± 7.1
WC – 17Co	5.41	-	134.1 ± 7.1	164.7 ± 11.6
WC – 17Co + 2%C	7.40	2.00	517.8 ± 10.7	206.2 ± 10.7
WC – 12Co + 2%C	7.67	2.55	303.9 ± 2.7	190.2 ± 6.6
WC – 12Co + 4%C	9.25	4.13	221.0 ± 8.7	192.3 ± 9.4
WC – 17Co + 4%C	9.60	4.19	279.6 ± 3.2	-
WC – 12Co + 6%C	11.28	6.16	56.8 ± 9.9	-
WC – 17Co + 6%C	11.60	6.19	114.8 ± 8.5	-
WC-10Ni	-	-	-	176.7 ± 14.5

4.2. Characterisation of Thermal Sprayed Coatings

Coatings microstructures were generally analysied on the mild steel substrates. The microstructures of the as-sprayed coatings are given in Figures 4-9 – 4-11. The lighter phase is WC and the grey phase between the WC particles is the Co metal. The images show that the coatings are very porous. The particle size and phase analyses of the coatings are given in Table 4-4. The coating thickness is in the range of 50 - 520µm (Table 4-3). There was difficulty in producing the 6%C enriched coatings as the amount of carbon in the powders was too high for HVOF spraying resulting in a low or no deposition of the coating for HVOF. The carbon from the powders burnt off during

thermal spraying. It was decided to try spraying using a plasma spraying process. The microstructures of the plasma sprayed WC-12Co+6%C, WC-17Co+4 and 6%C are shown in Figure 4-11; the WC-17Co+4 and 6%C show splat formation and semi-melted material evident in the shape of the particle splats. These samples also show high porosity levels and carbon can be seen embedded in the sample. Due to this the WC-17Co+4 and 6%C samples for wear tests were not sprayed, the WC-12Co+6%C samples were sprayed but the results resulted in such low deposition on the substrate that the sample was not used.

The XRD analyses of the thermal sprayed coatings are shown in Figures 4-12 and 4-13. The XRD results of the as-sprayed (WC-12Co and WC-17Co) coatings (Figure 4-12) shows the main WC phase and the undesirable eta phases caused due to decomposition during spraying (W_2C, amorphous Co region which can consist of Co and η phase (Co_6W_6C) as broad "humps" in the region of 48-55° Co radiation and 42-50° Cu-kα radiation. The 2%C enriched coatings show no W_2C and a reduction in the eta phase (Co_6W_6C). This is evidence that carbon enrichment of the powders resulted in a reduction in the undesirable W_2C and other eta phases.

The XRD of the 4 and 6%C enriched coatings is shown in Figure 4-13. The results show that W_2C and eta phases (η) (Co_6W_6C and Co_3W_3C) are present in all the samples. This is due to decarburization of WC during plasma thermal spraying. The WC-12Co+6%C shows lots of decarburization compared to the other sprayed layers and the peak intensity is very low; this could result from the thin coating produced (50μm).

A WC-10Ni coating was also produced by HVOF spraying; this was done as a comparison for wear tests. Figures 4-14 and 4-15 show the microstructure, EDS analysis and XRD results of the WC-10Ni coating. The microstructure and EDX results confirm the WC and Ni phases present. The XRD results show WC, W_2C and Ni phases.

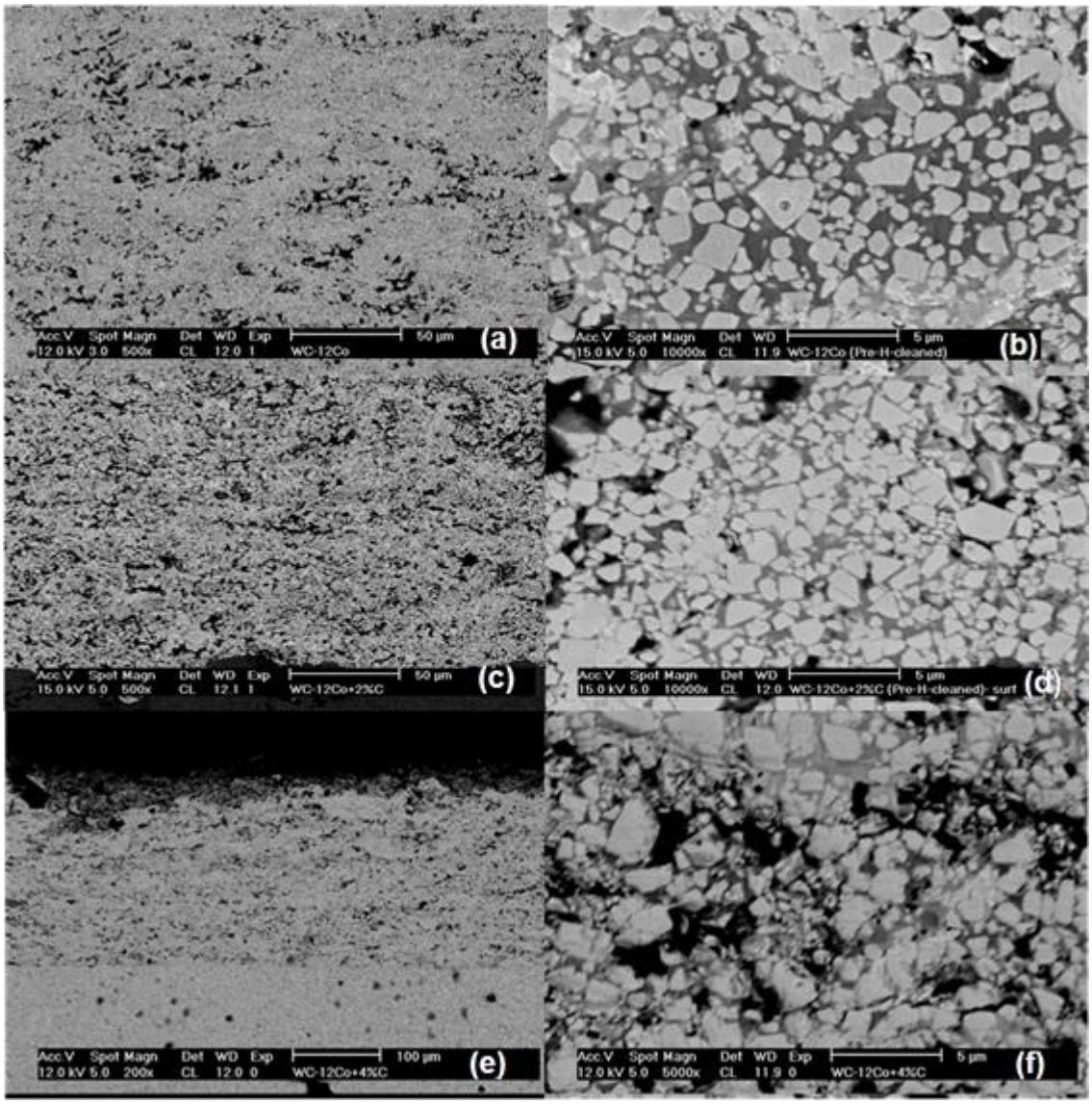

Figure 4-9: SEM-BSI micrographs of cross-section of the HVOF sprayed coatings (a & b) WC-12Co powder and (c & d) WC-12Co+2%C enriched powder, the light phase is WC, grey is cobalt and black phase is porosity.

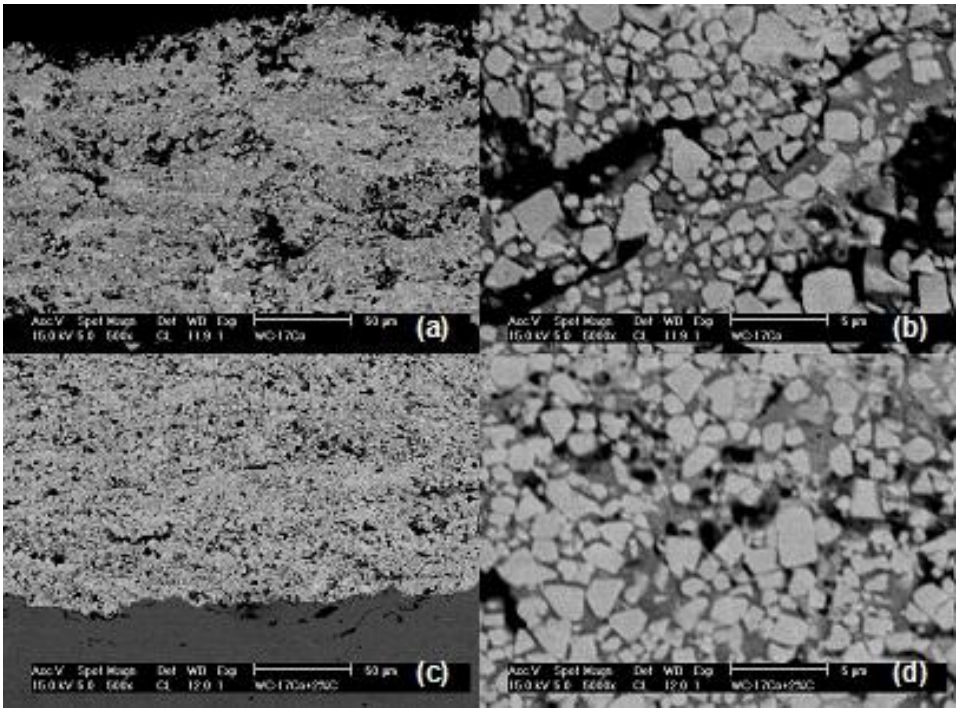

Figure 4-10: SEM-BSI micrographs of the cross-section of the HVOF sprayed coatings (a & b) WC-17Co powder and (c & d) WC-17Co+2%C enriched powder, the light phase is WC, grey is cobalt and black phase is porosity .

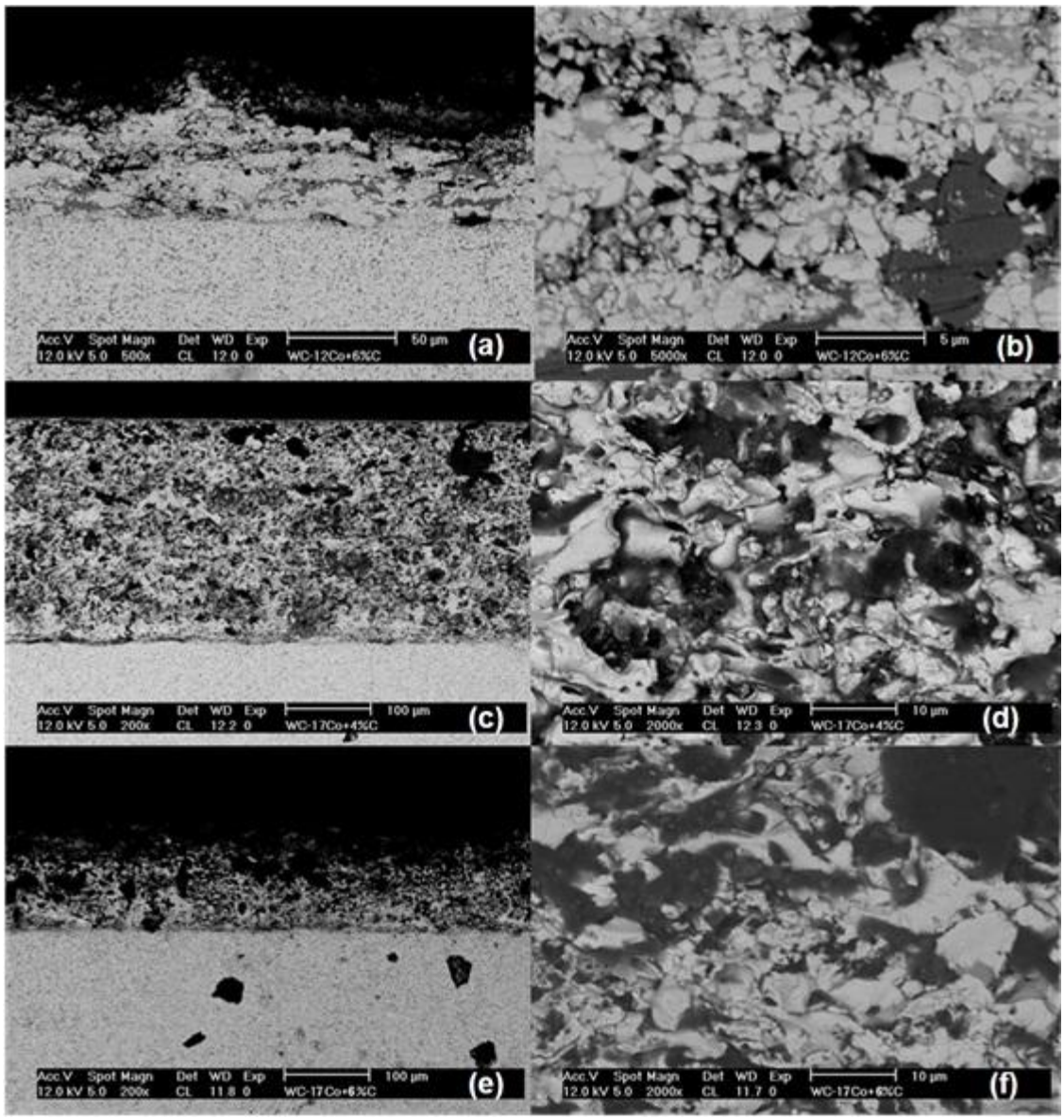

Figure 4-11: SEM-BSI micrographs of the cross-section of the plasma sprayed coatings for (a & b) WC-12Co+6%C, (c & d) WC-17Co+4%C and (e & f) WC-17Co+6%C enriched powders, the light phase is WC, grey phase is cobalt and black phase is oxides.

Table 4-4: Particle size and phase analysis of coated layers.

Sample	Particle Size (µm)	Phase Analysis		% Porosity
		Area % WC	Area % Binder	
WC-12Co	0.8 ± 0.4	61.9 ± 2.3	34.8 ± 3.2	3.0 ± 0.8
WC-12Co+2%C	0.8 ± 0.5	55.7 ± 4.0	40.7 ± 4.6	3.7 ± 0.9
WC-12Co+4%C	0.7 ± 0.5	49.5 ± 2.3	42.2 ± 2.3	8.2 ± 0.1
WC-12Co+6%C	0.7 ± 0.5	62.04 ± 2.8	31.8 ± 2.4	6.2 ± 0.4
WC-17Co	0.8 ± 0.5	56.0 ± 6.0	33.2 ± 4.9	10.0 ± 2.1
WC-17Co+2%C	0.8 ± 0.5	48.5 ± 3.4	44.68 ± 0.3	6.9 ± 3.1
WC-10Ni	0.8 ± 0.4	68.9 ± 1.4	28.3 ± 1.6	2.8 ± 0.2

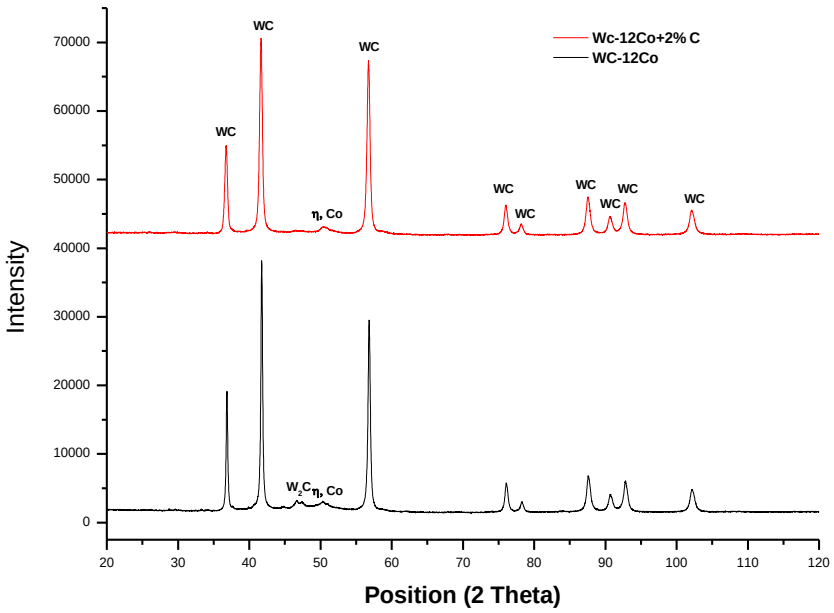

Figure 4-12: XRD scans of the HVOF sprayed coatings for 0-2%C enrichment as-sprayed: (a) WC-12Co & WC-12Co+2%C (Co radiation).

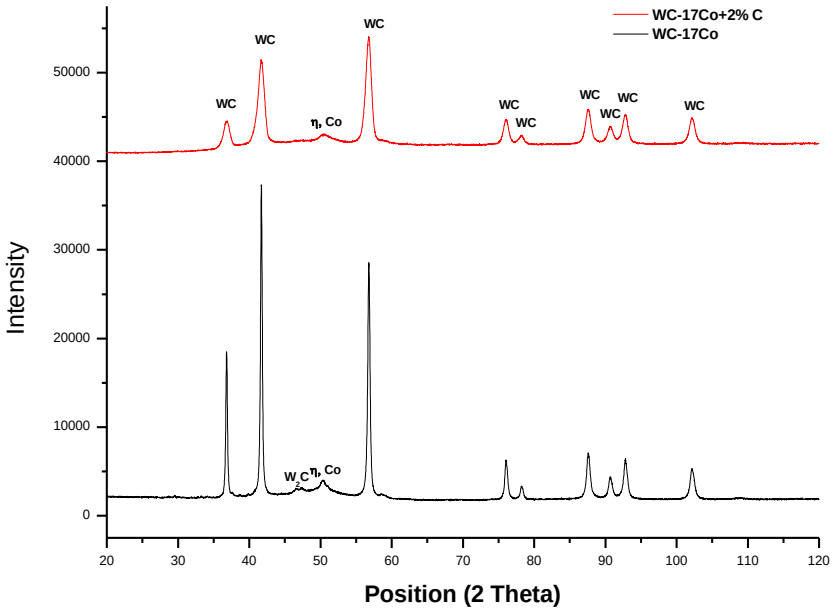

Figure 4 – 12 continued: XRD scans of the HVOF sprayed coatings for 0-2%C enrichment as-sprayed: (b) WC-17Co & WC-17Co+2%C (Co radiation).

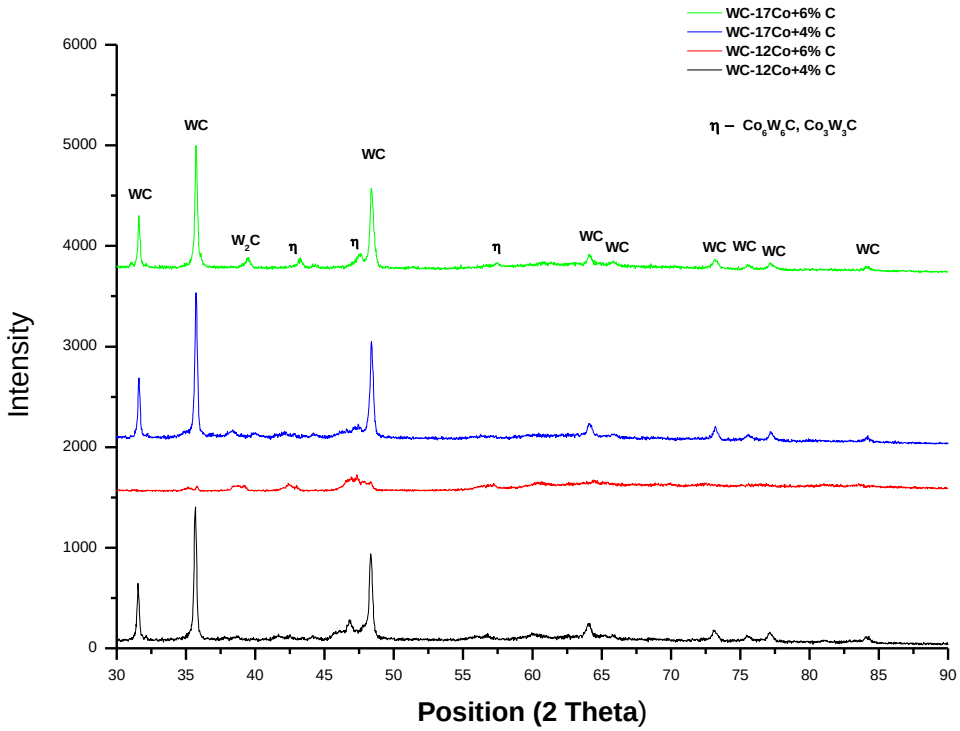

Figure 4-13: XRD scans of the HVOF sprayed coatings for 4-6%C enrichment (Cu-K_α radiation).

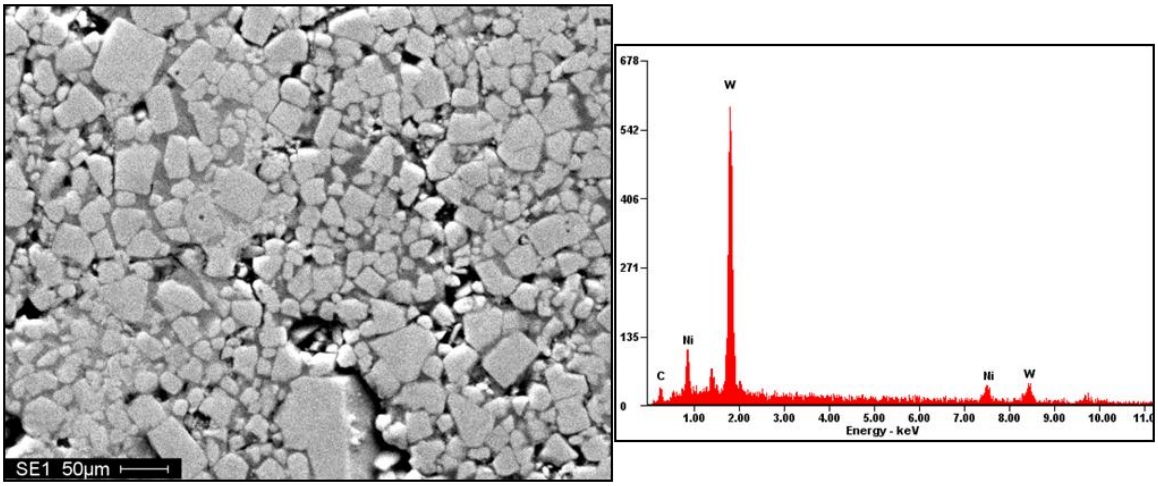

Figure 4-14: SEM-BSI image showing microstructure and EDX analysis of the HVOF sprayed WC-10Ni coating, WC (light phase) and Ni (darker phase).

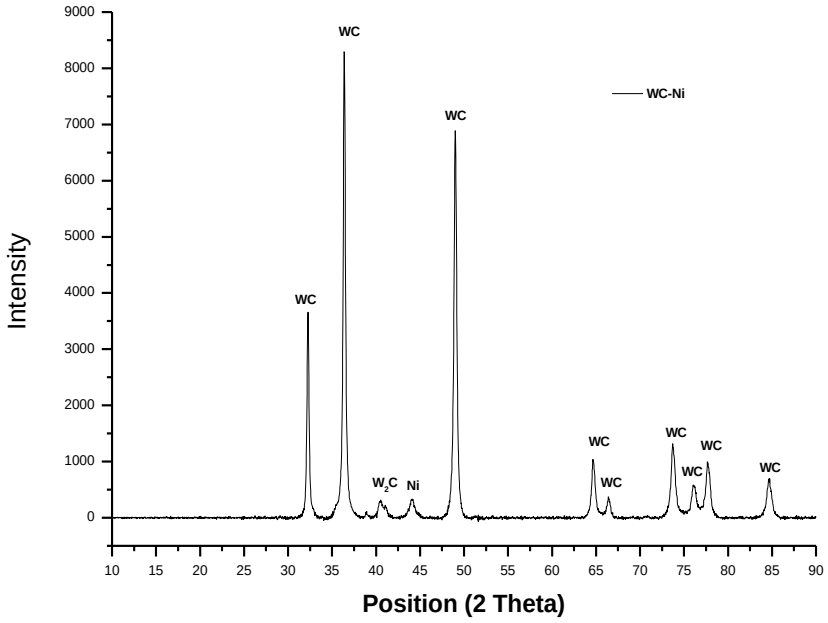

Figure 4-15: XRD scan of the HVOF sprayed WC-10Ni coating, (Cu-K_α radiation).

4.2.1. Carbon Analysis of Coatings

Carbon analysis of the coatings proved to be very difficult; this was due to the absence of any evidence of extra carbon in the XRD traces. Other means of determining if free carbon was present in the coatings were tried. Carbon analysis using the Eltra 800 Carbon and Sulphur analyser (Section to 3.7.4) was ruled out due to an insufficient amount of the coated sample required for analysis (i.e. could not scratch off enough sample for analysis). Raman was therefore used to determine if there was a change in the carbon content with increasing carbon enrichment. Figures 4-16 and 4-17 show the Raman analysis from the carbon enriched coated layers using the spot size method (section 3.7.4.2). The results show evidence of the sp^3 and sp^2 hybridization of carbon bonding indicating carbon enrichment of coated layers. The double Raman peaks

indicated by shift at ∽1320 and 1580 cm^{-1} show the carbon bonding. The 6%C enriched samples seem to have the most intense Raman peaks.

As the Raman spot size was less than 1μm, it is only possible to analyse a very small area of each sample. Therefore Raman analysis was done on 64 positions in an 8x8 array covering an area of 100 x 100 μm examined for each sample. The spectra are shown in Appendices A, the carbon enriched samples show a higher degree of phases evident. Results show that the as-received and sprayed WC-12Co and WC-17Co coatings showed very little or no evidence of any excess carbon. The Carbon enriched coatings showed evidence of graphite indicated by the double peaks shifts at ∽ 1320cm^{-1} and 1580cm^{-1}. This therefore shows that at least some carbon was retained in the coated layers. Differences in spectra can be accounted for by various surface contamination and other phases on the surface of the sample.

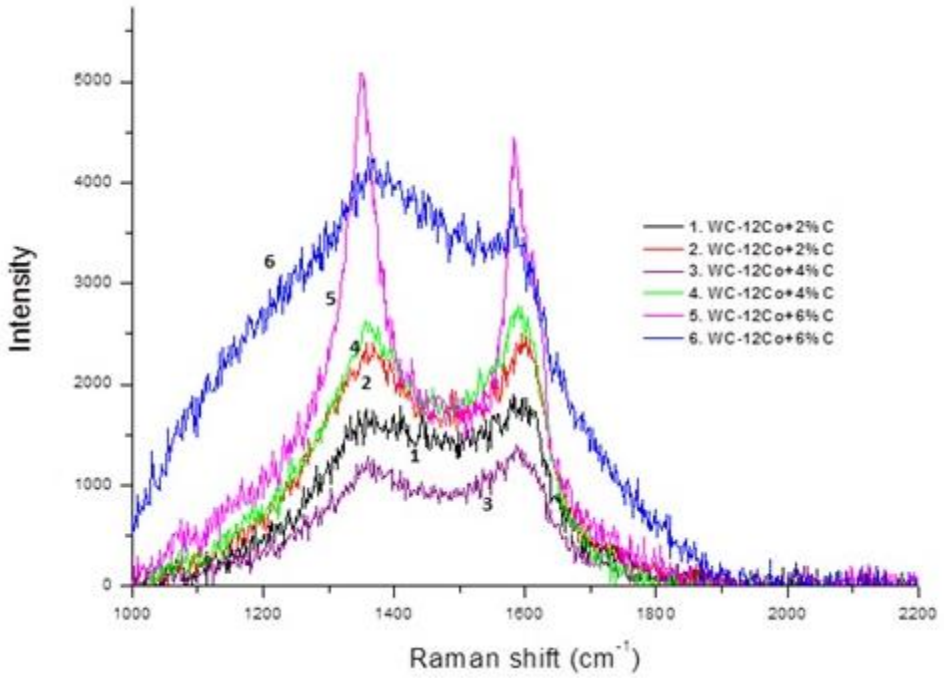

Figure 4-16: Raman analysis of the WC-12Co coated layers (spot size 1μm).

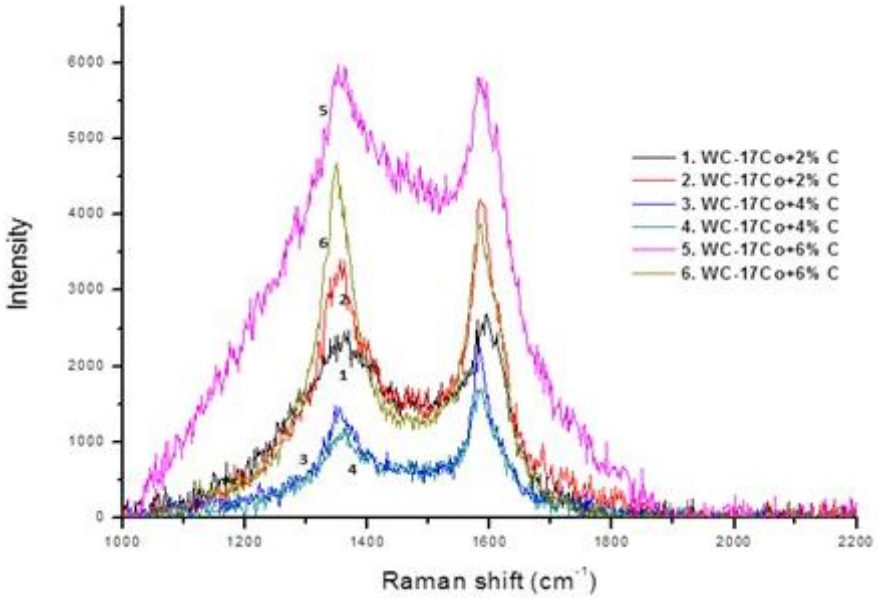

Figure 4-17: Raman analysis of WC-17Co coated layers (spot size 1µm).

4.2.2. Pre-PCD Sintering Heat treatment

Before PCD sintering of the coated substrate samples, the samples were hydrogen cleaned (as described in Section 3.2.3) to re-crystallize the Co. The XRD traces in Figure 4-18 show the change in the phases in the coating after hydrogen cleaning. As can be seen all the phases caused by decarburized of WC-Co during spraying (W_2C and eta phases) have been eliminated. Re-crystallization of the amorphous Co phase region (intense Co peak at 52°) has been achieved. Only the 0-2%C enriched samples were characterised. The microstructure of the hydrogen heat treated samples is shown in Figure 4-19. An increase in the faceting of the WC grains can be seen (grains become more angular) and the binder phase appears to have been reduced. Acicular grain growth of the WC particles is evident in Figure 4-19 d.

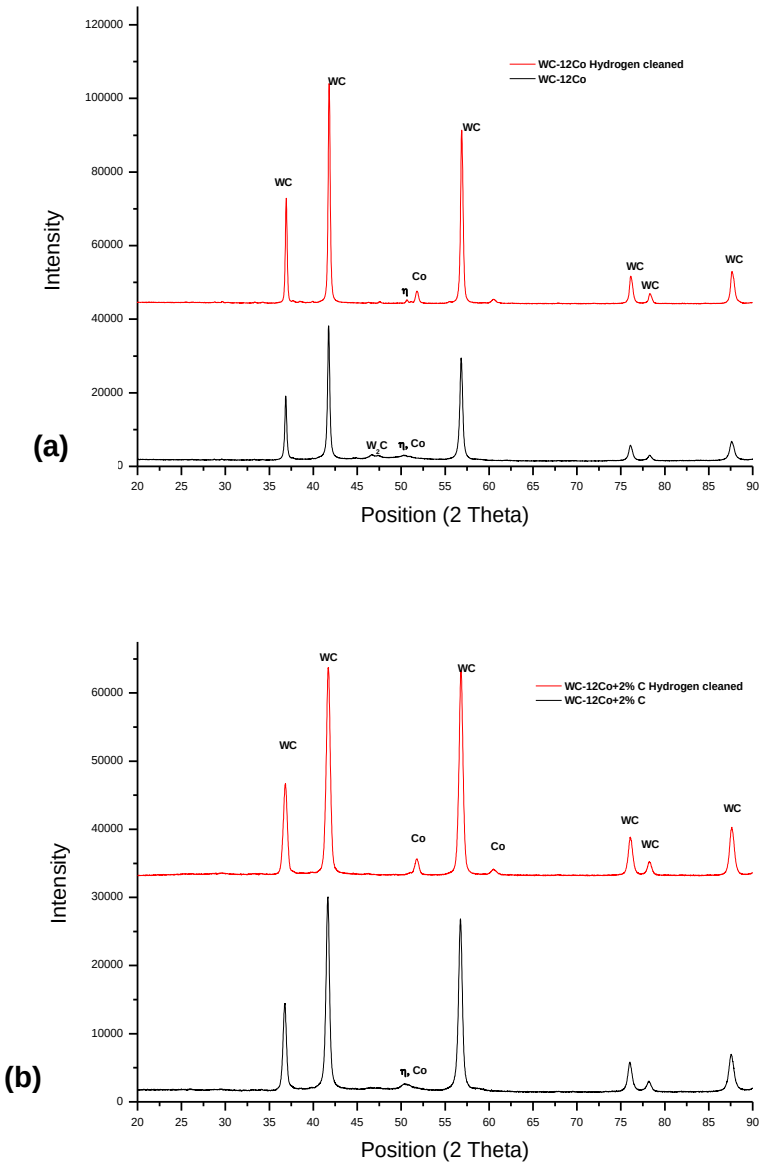

Figure 4-18: XRD scans of the WC-Co coated samples before and after hydrogen cleaning: (a) WC-12Co (b) WC-12Co+2%C, (Co radiation).

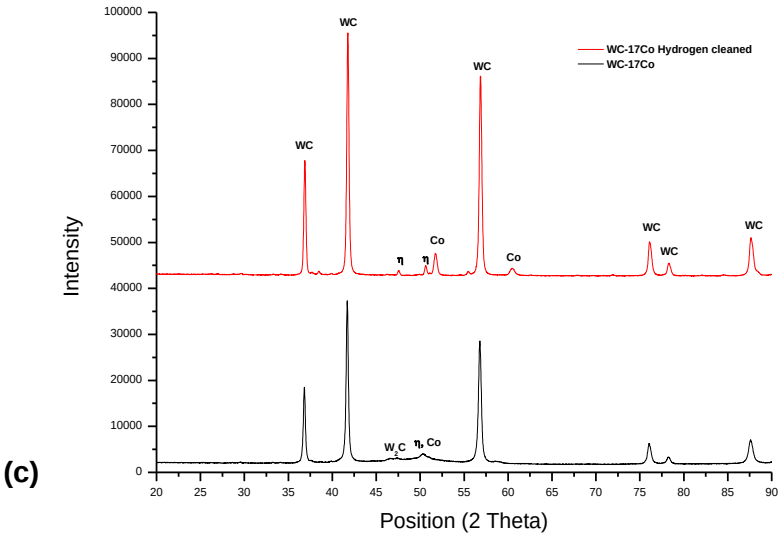

(c)

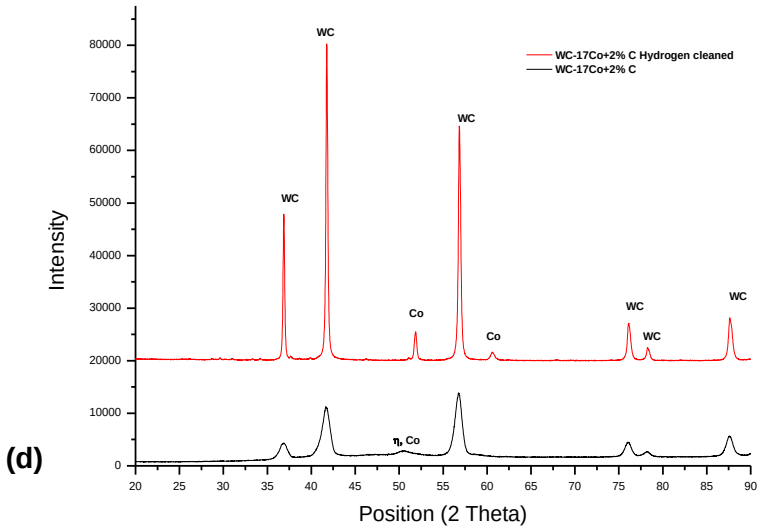

(d)

Figure 4- 18 (continued): XRD scans of the WC-Co coated samples before and after hydrogen cleaning: (c) WC-17Co and (d) WC-17Co+2%C (Co radiation).

Rietveld refinement of the WC-12Co coatings was done to determine if addition of carbon was effective. Table 4-5 shows the resulted from the Rietveld refinement showing that the addition of 2% carbon results in higher carbon content in the coatings.

Table 4-5: Results of the Rietveld refinement of the WC-12Co coatings to determine carbon enrichment (wt%).

	Co (Cub)	Co(hex)	W_6Co_6C	W_2C	WC
WC-12 Co pre H-cleaned	8.8± 3.9%	9.8±4.2%	6.6±1.2%	4.2±0.6%	70.6±4.2%
WC-12 Co H-cleaned	3.70± 1.5%	10.4±2.4%	7.9±0.8%	-	78.0±2.3%
WC-12Co+2%C pre H-cleaned	8.0±4.8%	5.3±3.6%	4.1±10%	-	81.9±4.5%
WC-12 Co+2%C H-cleaned	5.4±1.6%	7.4±2.3%	0.5±1.1%	-	86.8±2.9%

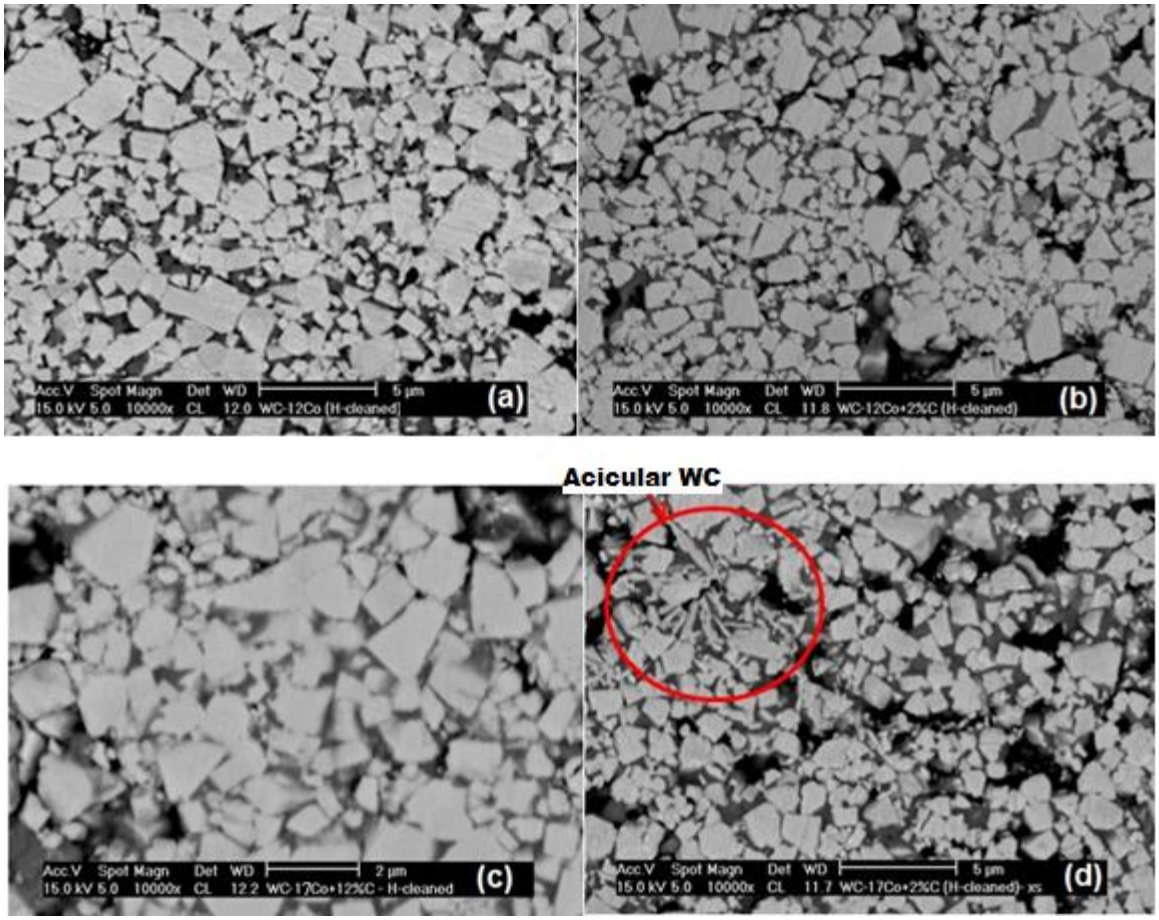

Figure 4-19: SEM-SEI microstructure of the hydrogen heat treated WC-Co coated samples on WC-Co substrates; (a) WC-12Co, (b) WC-12Co+2%C, (c) WC-17Co and (d) WC-17Co+2%C.

Chapter 5: Results of Wear Test & Wear Mechanisms

5.

This chapter describes the results, characterisation and discussion from the wear tests done on the coated substrates. The results include the heat treatment of the coatings, abrasive wear tests from the dry-sand rubber wheel test, the PGT test and hardness. The characterisation of the coated layers using XRD and SEM microstructural analysis of the wear scars is also covered.

5.1. Abrasive Wear Resistance

The coated samples used for the dry-sand rubber wheel wear tests were the WC-12Co, WC-12Co+2%C, WC-12Co+4%C, WC-12Co+6%C, WC-17Co, WC-17Co+2%C and WC-10Ni. The wear rate of the samples was tested before and after heat treatment.

5.1.1. Annealing Heat treatment

Samples from each batch were heat treated to determine the effect of annealing on the wear resistance of the coated layers. The coatings were heat treated in an argon environment at 700°C for 1 hour as described in Section 3.2.3. The phase analysis and microstructure of the annealed samples were determined. Figures 5-1 and 5-2 show the XRD results of the WC-12Co based, WC-17Co based and WC-Ni based coatings used for wear tests before and after the annealing heat treatment. The XRD results show that after annealing, the samples undergo decarburization of the WC-Co phases which results in the formation of W_2C and eta phases (η - Co_6W_6C). Re-crystallisation of the

stressed binder region (between 42-50 2°Theta) also occurs. Table 5-1 shows the phases of the annealed coatings compared to those of the as-sprayed samples.

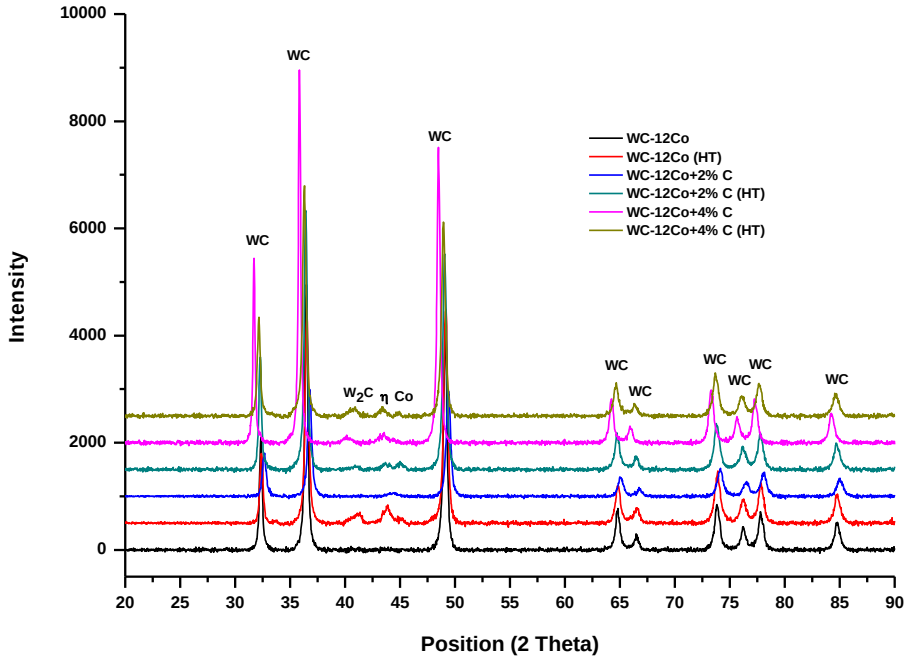

Figure 5-1: XRD scans of the WC-12Co-based coatings before and after heat treatment at 700°C for 1 hour in Ar gas (Cu-K_α radiation).

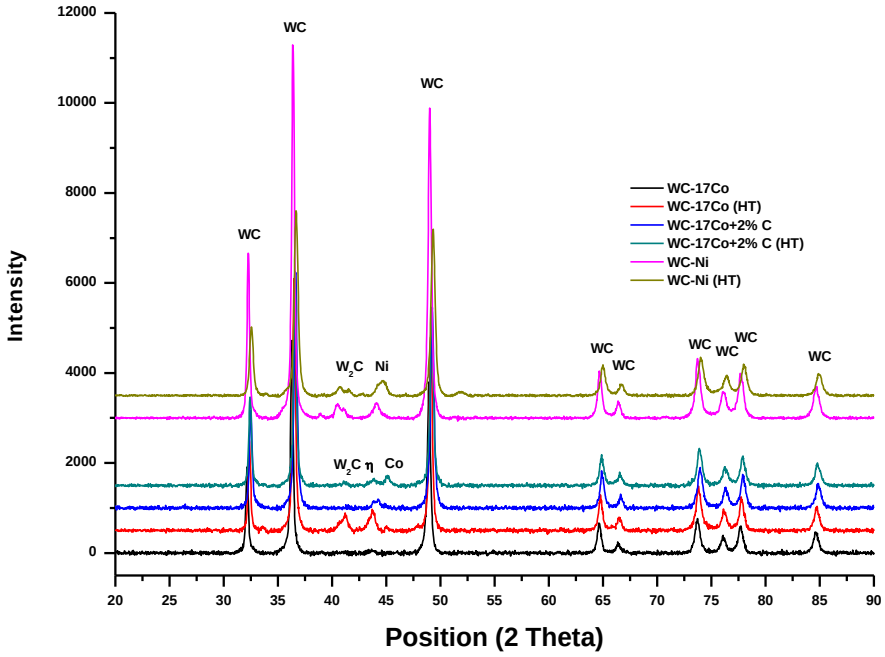

Figure 5-2: XRD scans of the WC-17Co-based and WC-Ni coatings before and after heat treatment at 700°C for 1 hour in Ar gas (Cu-K_α radiation).

Table 5-1: Composition of the coatings before and after heat treatment.

Coating	Phases (as-sprayed)	Phases (heat treated)
WC-12Co	WC	WC, W_2C, Co_6W_6C (η), Co
WC-12Co+2%C	WC	WC, W_2C, Co_6W_6C (η), Co
WC-12Co+4%C	WC, amorphous Co	WC, W_2C, Co_6W_6C (η), Co
WC-17Co	WC, amorphous Co	WC, W_2C, Co_6W_6C (η), Co
WC-17Co+2%C	WC, amorphous Co	WC, W_2C, Co_6W_6C (η), Co
WC-10Ni	WC, W_2C, Ni	WC, W_2C, Ni

The microstructures of the heat treated samples are shown in Figure 5-3. The results show evidence of a slight reduction in the binder phase between the WC grains in comparison to that of the as-sprayed coatings (Figure 4-9, Figure 4-10, Figure 4-14 and

Figure 5-3). Annealing of the samples improves the homogeneity of the microstructure and reduces the occurrence of voids and pores (Richert & Leszczynska-Madej, 2011). Table 5-2 shows the average particle size and phase analysis of the as-sprayed and heat treated samples. There was a slight grain growth in the WC particles (i.e. from 0.7µm to 1.2µm) compared to the as-received coatings although this increase is too insignificant to have any major effect on the properties of the coatings. The total area% of WC and binder phase remained fairly constant. The porosity in the heat treated samples compared to that of the as-sprayed samples (Table 4-4) showed a general decrease for the materials, indicating the redistribution of the phases during annealing.

Table 5-2: Particle size and phase analysis of as-sprayed and heat treated coated layers.

Sample:	Particle Size (µm)	Phase Analysis		% Porosity
		Area % WC	Area % Binder	
WC-12Co	0.8 ± 0.4	61.9 ± 2.3	34.8 ± 3.2	3.0 ± 0.8
WC-12Co+2%C	0.8 ± 0.5	55.7 ± 4.0	40.7 ± 4.6	3.7 ± 0.9
WC-12Co+4%C	0.7 ± 0.5	49.5 ± 2.3	42.2 ± 2.3	8.2 ± 0.1
WC-12Co+6%C	0.7 ± 0.5	62.04 ± 2.8	31.8 ± 2.4	6.2 ± 0.4
WC-17Co	0.8 ± 0.5	56.0 ± 6.0	33.2 ± 4.9	10.0 ± 2.1
WC-17Co+2%C	0.8 ± 0.5	48.5 ± 3.4	44.68 ± 0.3	6.9 ± 3.1
WC-10Ni	0.8 ± 0.4	68.9 ± 1.4	28.3 ± 1.6	2.8 ± 0.2
WC-12Co (HT)	0.8 ± 0.5	60.4 ± 2.3	37.8 ± 2.5	1.8 ± 0.5
WC-12Co+2%C (HT)	0.8 ± 0.5	63.4 ± 5.1	31.6 ± 3.4	5.0 ± 1.2
WC-12Co+4%C (HT)	0.9 ± 0.5	55.4 ± 2.2	40.4 ± 2.1	4.2 ± 0.1
WC-17Co (HT)	1.2 ± 0.6	67.8 ± 0.8	30.4 ± 0.4	1.8 ± 1.2
WC-17Co+2%C (HT)	1.1 ± 0.5	57.1 ± 1.0	39.1 ± 1.0	3.8 ± 1.0
WC-10Ni (HT)	1.09 ± 0.5	56.9 ± 3.5	40.0 ± 2.6	3.1 ± 0.9

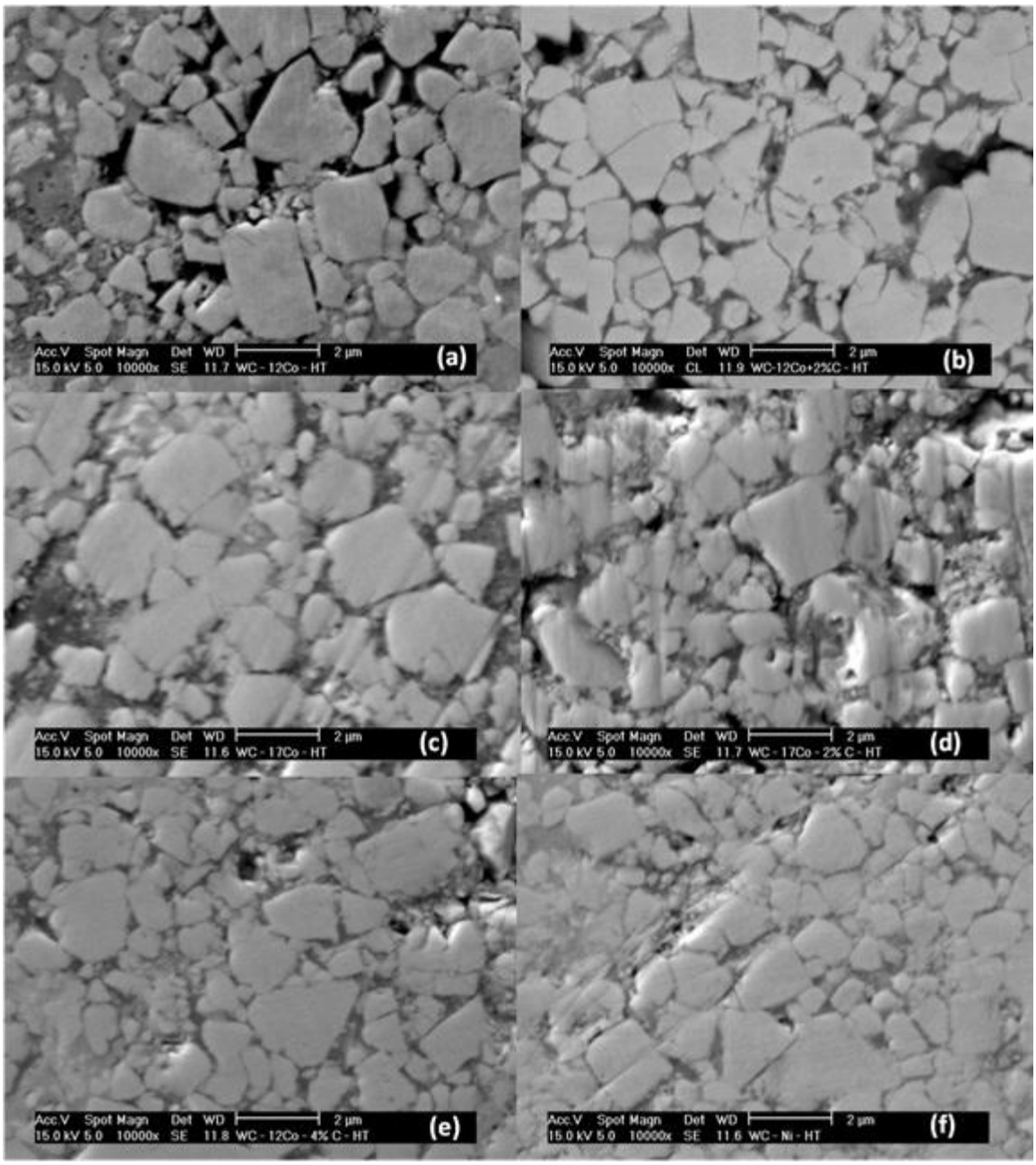

Figure 5-3: SEM-SEI micrographs of the annealed coatings; (a) WC-12Co(HT), (b) WC-12Co +2%C(HT) (c) WC-17Co(HT), (d) WC-17Co+2%C(HT), (e) WC-12Co+4%C(HT) and (f) WC-Ni(HT).

5.1.2. Dry-Sand Rubber Wheel Wear Test

The procedure for determining the wear using the dry-sand rubber wheel wear tests is described in Section 3.5.1. Two wear tests were carried out on the samples; a 30min test with mass loss measurements after 5min intervals and a full 30min tests with no intervals. Only the as-sprayed coatings were tested for both tests, the heat treated coatings were only tested using the full 30min test with no intervals.

5.1.2.1. As-Sprayed Coatings

The results for the 30min-5min interval tests using a 25N load for the non-annealed samples are shown in Figure 5-4 and 5-5 for the WC-12Co and WC-17Co materials respectively. The shape of the wear rate plot for the coatings shows an initial high wear rate for all samples within the first 5mins; this is due to roughness of the coating; the abrasive SiO_2 sand removes any peaks of the rough surface fast (it carries a higher load); any coating not adhered strongly to the substrate is also removed quickly. The wear rate drops generally to a constant wear rate after about 10-15mins to the end of the wear test time at 30min; lower mass loss is experienced when the sample is flat as the load is distributed over the whole surface. Any deviation from the trend could be caused by a malfunction in the flow rate of the SiO_2 sand during testing. This is due to blockages in the feed nozzle causing either a higher or lower feed rate resulting in higher or lower mass loss.

Except for the WC-12Co+6%C sample, the samples seemed to reach a constant wear rate. The results of the WC-12Co based coatings showed a slightly lower wear rate for the WC-12Co+2 and 4%C coatings than the WC-12Co coating, but a much higher wear rate for WC-12Co+6%C coating. The reason for the high wear rate of the WC-12Co+6%C

sample was the very thin coating which was removed quickly therefore resulting in the wear of the mild steel substrate (evidence of this can be seen in Figure 5-10 showing high amount of Fe). The WC-10%Ni sample showed the least wear rate. Similar results can be seen for the WC-17Co based coated samples, both the carbon enriched and Ni samples showed lower mass loss. The WC-17Co+2%C coating showed a larger mass loss over a longer period of time before decreasing (i.e. 15-20mins); this could be a result of the distribution of the WC particles within the coating. All the samples experienced substantial scatter in the results obtained caused by vibrations in the loading arm of the test rig.

The results were compared to that of work done on wear resistance of WC-Co materials by Machio et al. (Machio et al., 2005), shown in Figures 5-4 and 5-5 for WC-12Co and WC-17Co powders by initials CM. The results show that all samples produced (except WC-12Co+6%C) showed a much lower wear rate compared with the results from Machio et al. Although the coating compositions (WC-12Co and WC-17Co) were the same for the work done in this work and that of work done by Machio et al. (Machio et al., 2005), the spraying and wear parameters were different, giving altered results. Overall, the results showed very little change with increased carbon content (all in similar range); the 2%C enriched samples shows the best results. A low wear rate shows a good wear resistance, while a high wear rate shows a low or poor wear resistance.

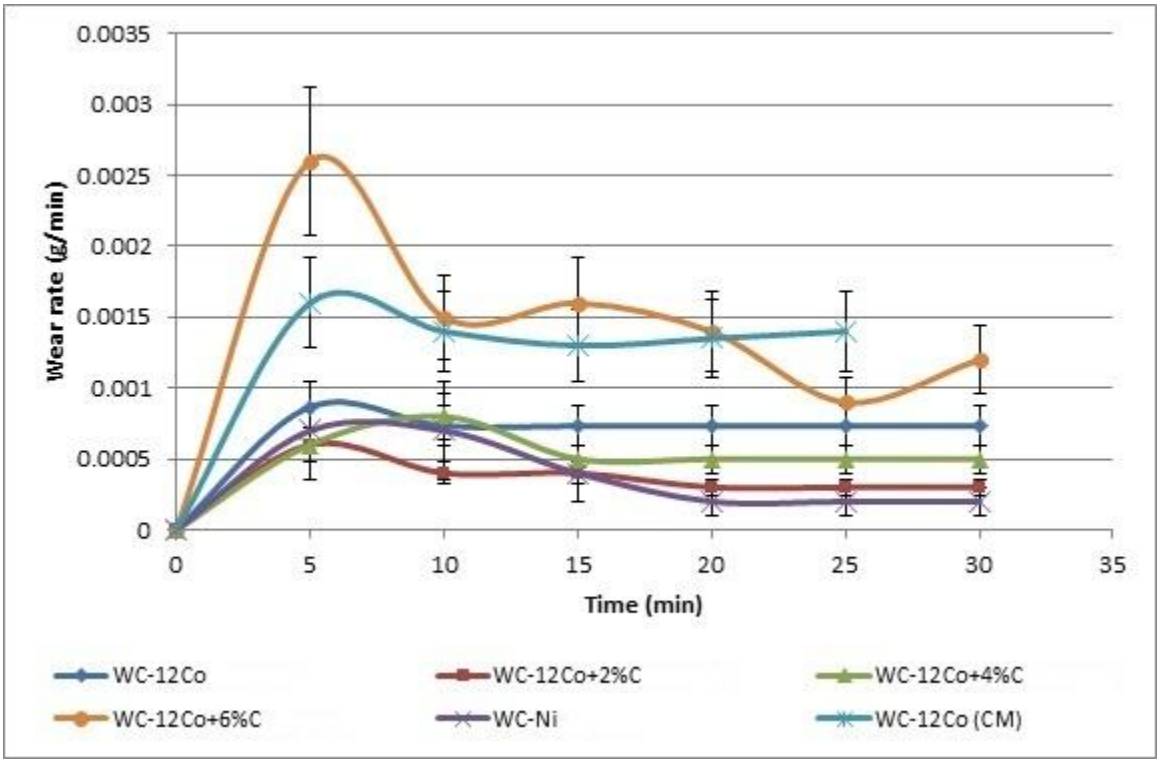

Figure 5-4: Wear resistance results of the WC-12Co, WC-12Co + 2, 4 & 6%C and WC-10Ni As-received coatings (WC-12Co (CM) data taken from (Machio et al., 2005)). The curves are the average of the 25 N 30min 5 interval measurements.

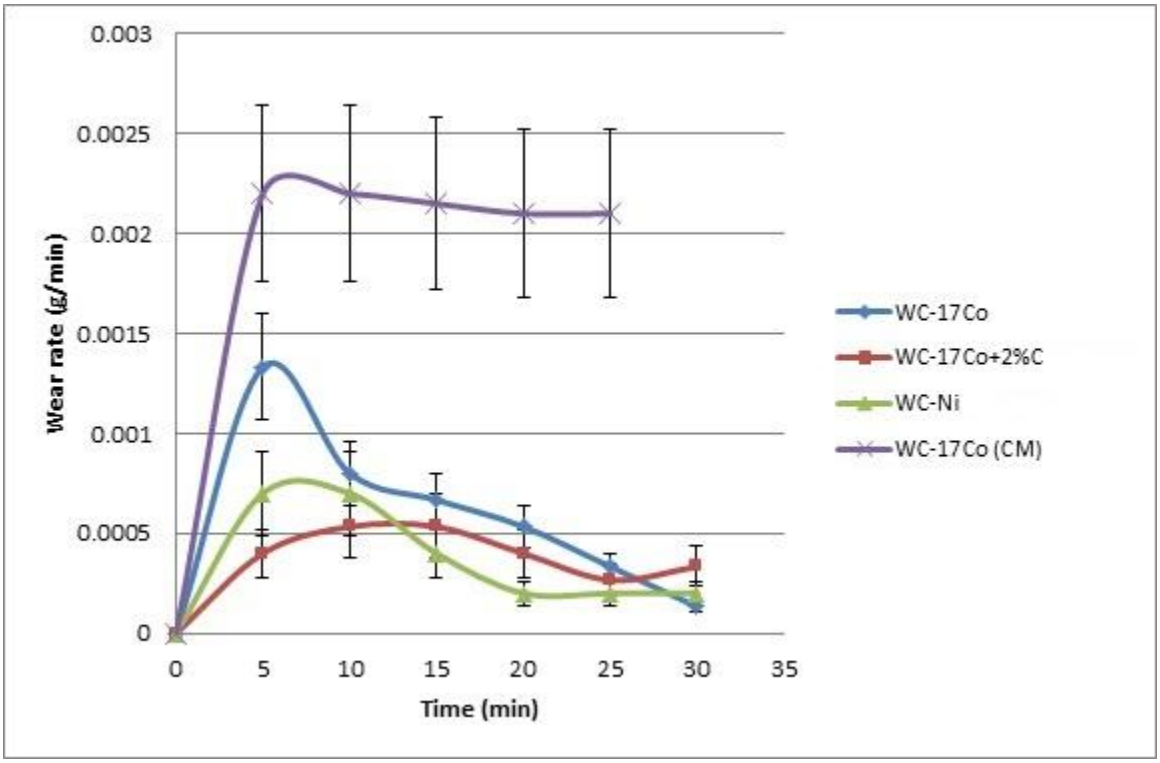

Figure 5-5: Wear resistance results of the WC-17Co, WC-17Co+2%C and WC-10Ni as-received coatings (WC-17Co (CM) data taken from (Machio et al., 2005)). The curves are the average of the 25 N 30min 5 interval measurements.

5.1.2.2. Heat treated Coatings

The results of the wear tests carried out for the full 30min was performed on both the as-sprayed (non-annealed) and annealed (HT) samples. The wear resistance results are shown in Figure 5-6. Most of the annealed samples showed a lower wear rate compared to that of the as-sprayed samples for most samples. The 2%C enriched samples (WC-12Co+2%C and WC-17Co+2%C) and the WC-10Ni material showed a slight increase in wear rate for the annealed sample. After annealing, the wear rate decreased compared to the as-sprayed samples due to the heat treatment effect on the residual stress; phase changes as well as void and pore reduction (Richert & Leszczynska-Madej, 2011).

Stewart et al. (Stewart et al., 1998) suggested that the lower residual stresses in the coatings will result in a reduced wear rate. The increased wear rate in the heat treated WC-17Co+2%C sample can be attributed to increased W_2C formation as well as the assumption that micro-cracking occurred in the microstructure although not shown. Likewise the increase in the wear rate of the WC-10Ni coating after annealing can also be caused by micro-cracking within the microstructure and changes in the residual stress state that could have occurred. Limited sample size can also affect the results producing large error discrepancies in the trends.

Literature (Nerz et al., 1992, Khan & Clyne, 1996 and Machio, 2005) suggests that the expected mass loss of the 17Co coatings should be higher than that of the 12Co materials as the amount of Co is higher. The higher the Co content, the softer the material and therefore the more likely the grain pullout and removal of the metal binder phase during abrasion wear. The WC-17Co coated sample had a similar wear rate to the equivalent WC-12Co coating if the errors are taken into account, while the WC-17Co+2%C had a higher wear rate than the equivalent WC-12Co+2%C coating. Higher amounts of W_2C and eta phases formed in the heat treated WC-17Co and WC-17Co+2%C coatings also contributed to the high mass loss.

The 2 and 4%C enriched samples showed the lowest overall wear rates for both as-received and heat treated. A decrease in the harder W_2C phases results in a decrease in wear resistance. Errors in results could be due to the limited sample size for each sample batch.

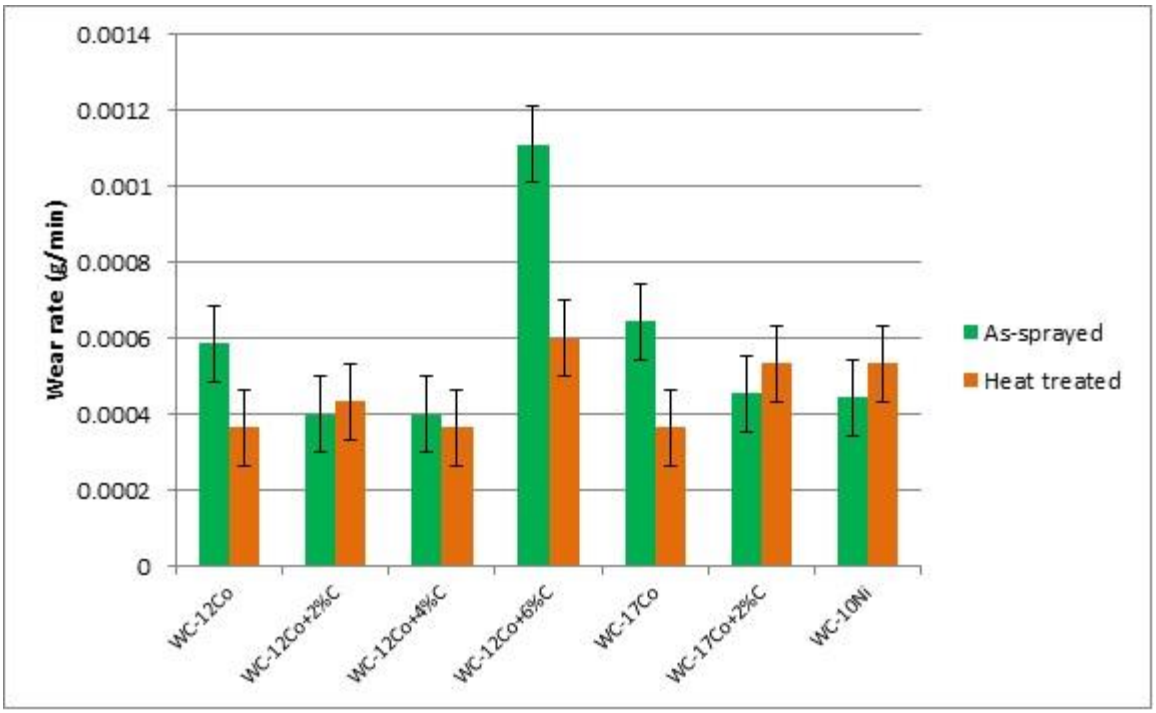

Figure 5-6: Wear resistance results of the annealed and non-annealed coatings.

5.1.3. Wear Surface

The worn surfaces of the as-sprayed WC-Co coatings on the mild steel can be seen in Figures 5-7 – 5-13. Here the samples are affected by various abrasive wear mechanisms such as cracking of the WC particles, pullout of the WC particles and loose WC particles surrounded by no binder phase (binder phase removal during the wear testing). In Figure 5-7 for the WC-12Co sample, all these wear mechanisms are observed. Figure 5-8 shows the images from the WC-12Co+2%C coatings; the results show cracking of the WC particles and a large amount of pullout resulting in Al_2O_3 being found by EDX. The Al_2O_3 is a result from the grit blasting process performed during the sample preparation of the substrates before coating to cause adhesion of coating to the substrate. Groove formation showing the direction of wear is evident in the WC-12Co+4%C coating (Figure 5-9). The groves were formed in the softer binder phase by either SiO_2 particles or from

debris from the removed WC particles. Figure 5-10 shows the wear surface of the WC-12Co+6%C coating, EDX shows evidence of Fe and Al from the steel substrate and grit blast layer. This indicates a high rate of mass removal from the sample. The WC-12Co+6%C sample had a coating thickness of approximately 58 µm, while the other coatings had a thickness of between 150-250 µm.

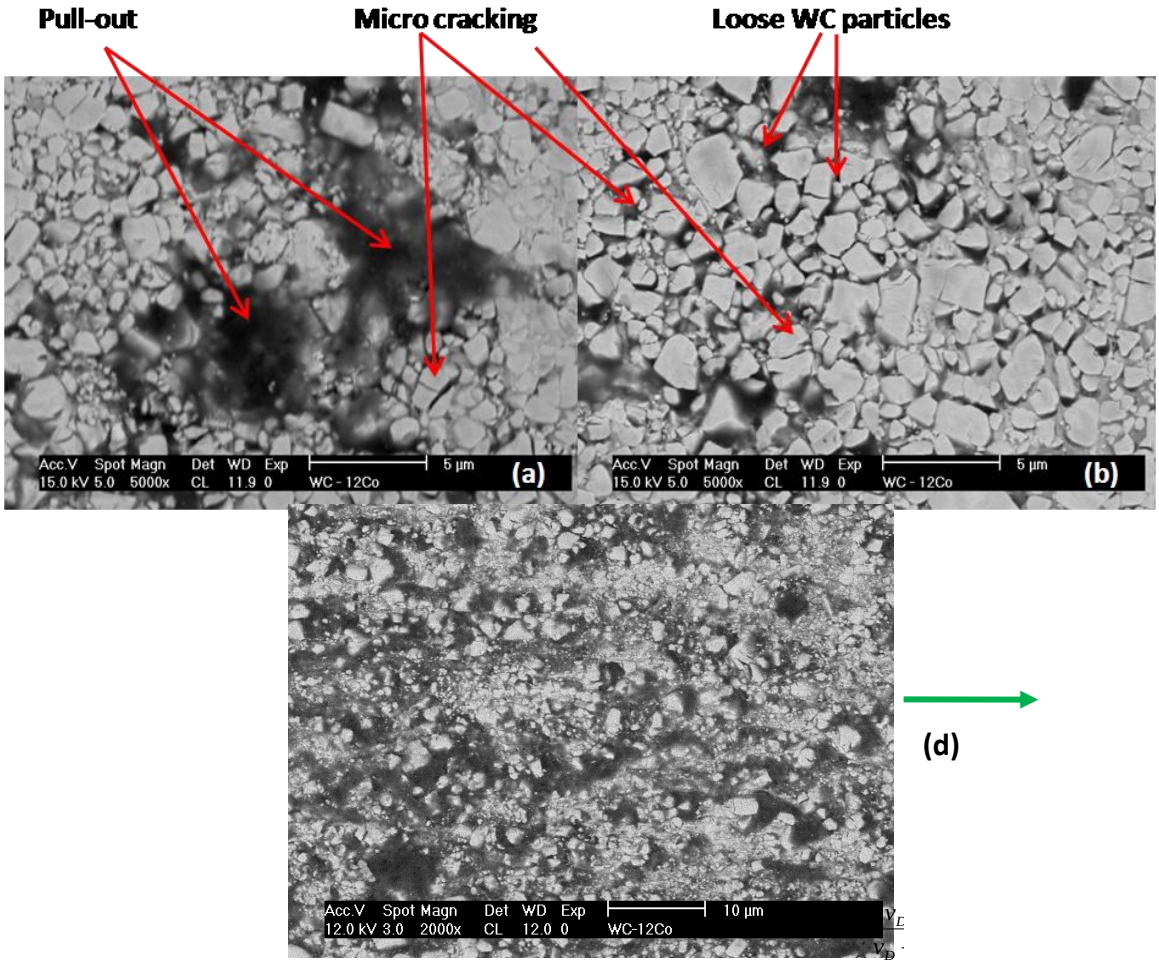

Figure 5-7: SEM-BSI micrographs of the worn surfaces for the WC-12Co coatings after 30mins test.

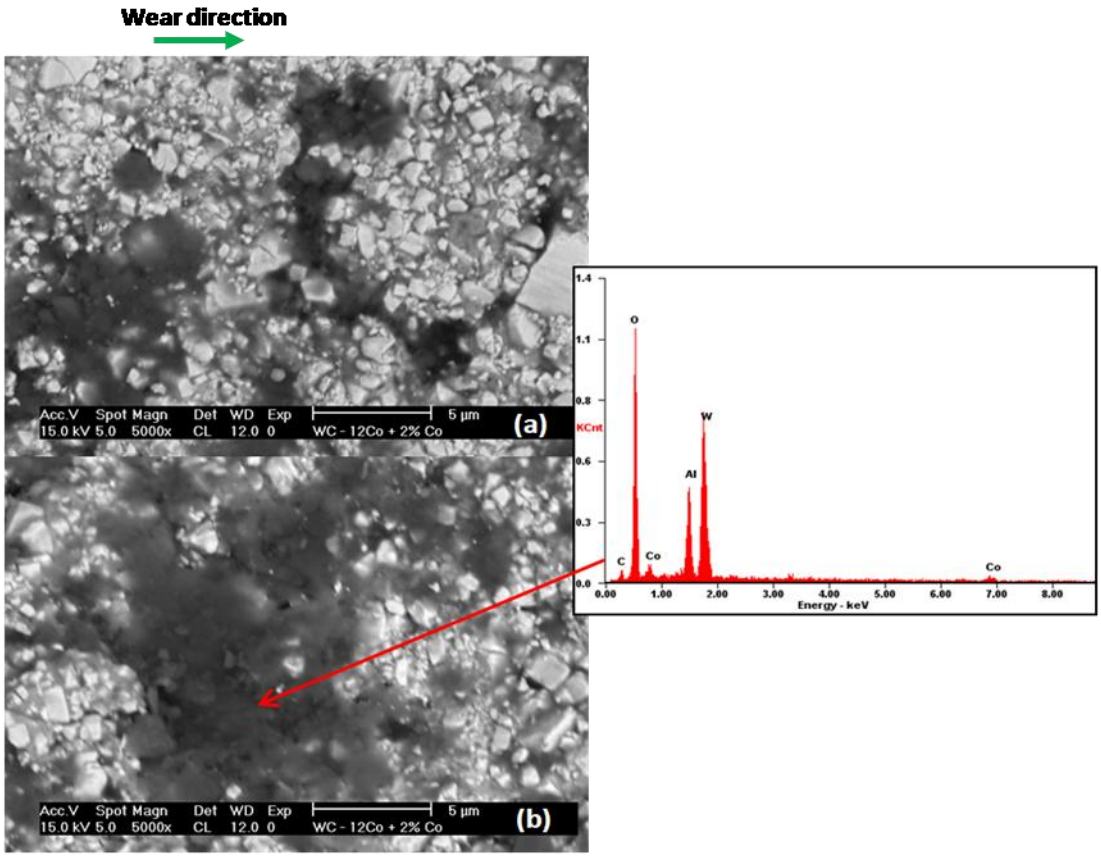

Figure 5-8: SEM-BSI micrographs of the worn surfaces for the WC-12Co+2%C coatings after 30mins test with EDS showing Al_2O_3 from the grit blast layer.

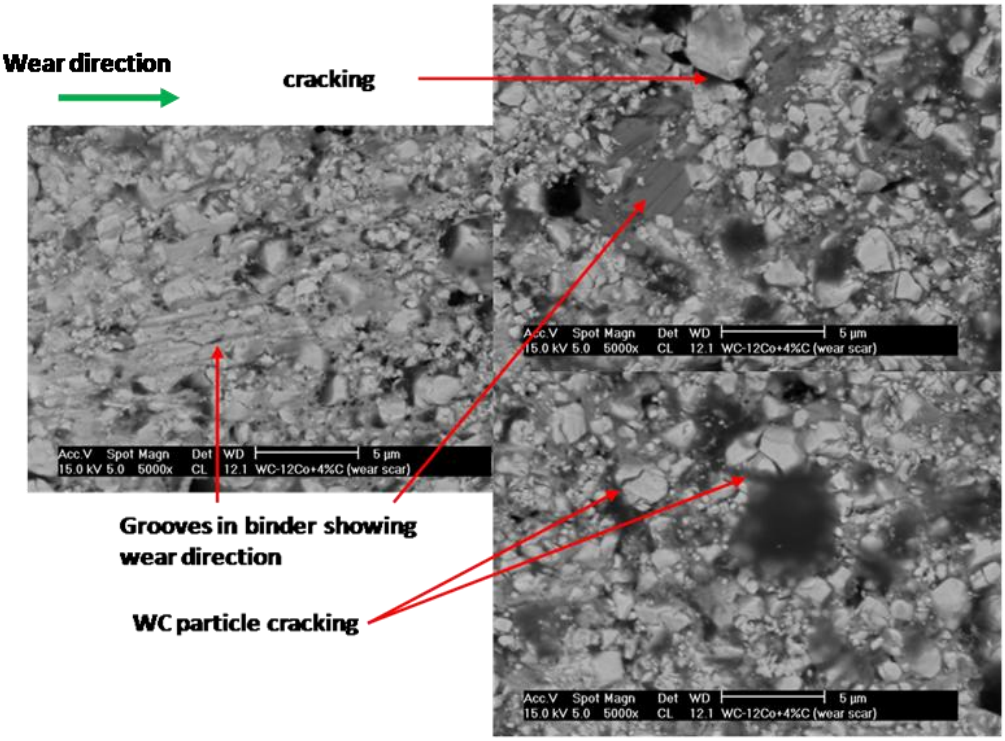

Figure 5-9: SEM-BSI micrographs of the worn surfaces for the WC-12Co+4%C coatings after 30mins test.

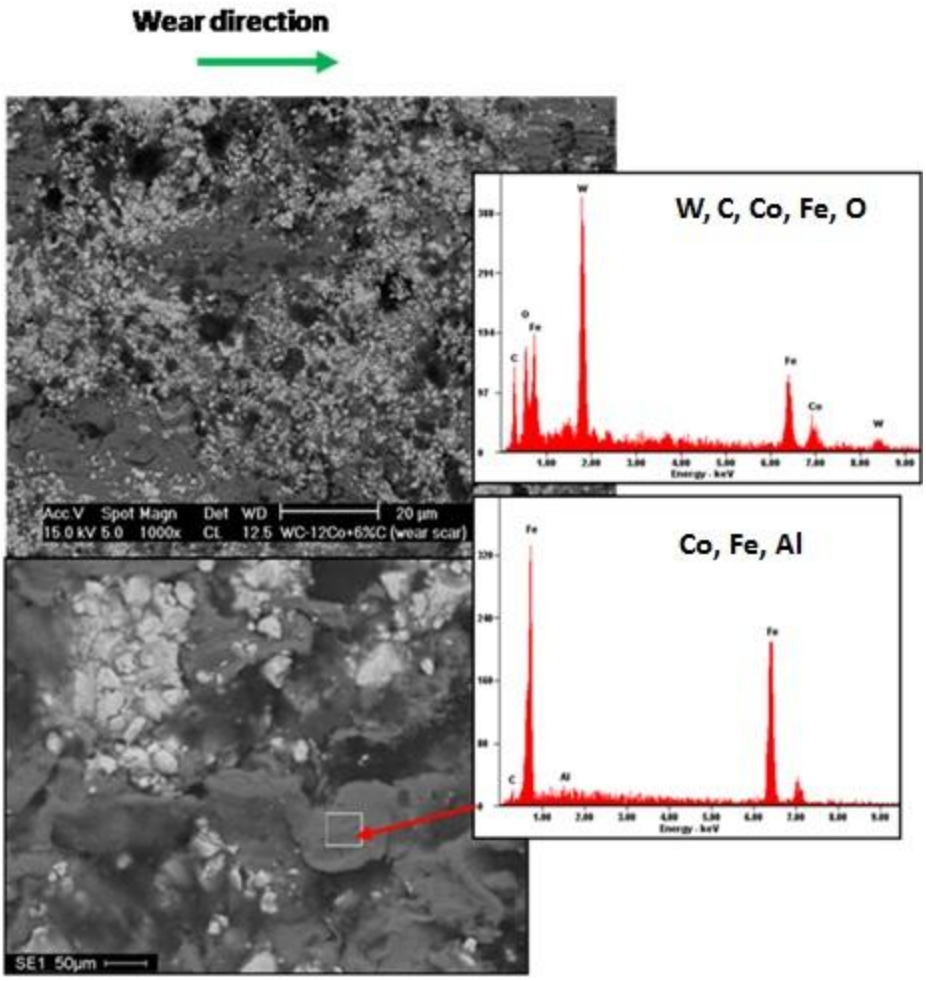

Figure 5-10: SEM-BSI micrographs of the worn surfaces for the WC-12Co+6%C coatings after 30mins test, with EDS showing Al_2O_3 and Fe from the grit blast layer and steel substrate.

Similar to that of the WC-12Co samples shown above, the wear of the as-sprayed WC-17Co coating (Figure 5-11) on the mild steel was affected by cracking of the WC particles, micro-cutting around the edges of the sample, adhesion of the WC-Co particles and pullout of the WC particles. The binder phase was removed during the wear testing, evident in the loose WC particles. Figure 5-12 shows SiO_2 was also found in the pull-out region of the WC-17Co+2%C sample, evidence that the SiO_2 sand has penetrated into the Al_2O_3 grit blast layer and embedded itself into the substrate.

Microcracking of the WC particles is highly evident in the wear surface of the WC-10Ni sample shown Figure 5-13.

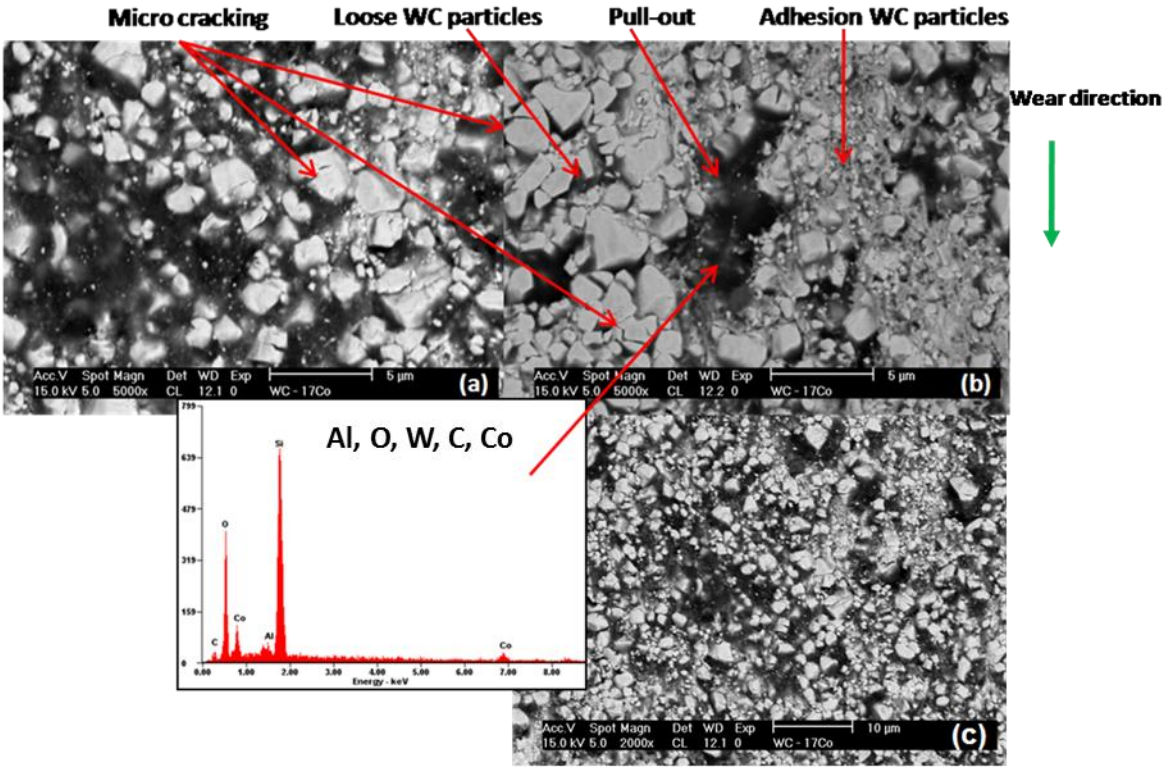

Figure 5-11: SEM-BSI micrographs of the worn surfaces for the WC-17Co coatings after 30mins test, EDS show SiO_2 and Al_2O_3 contamination from sand and grit blast layer.

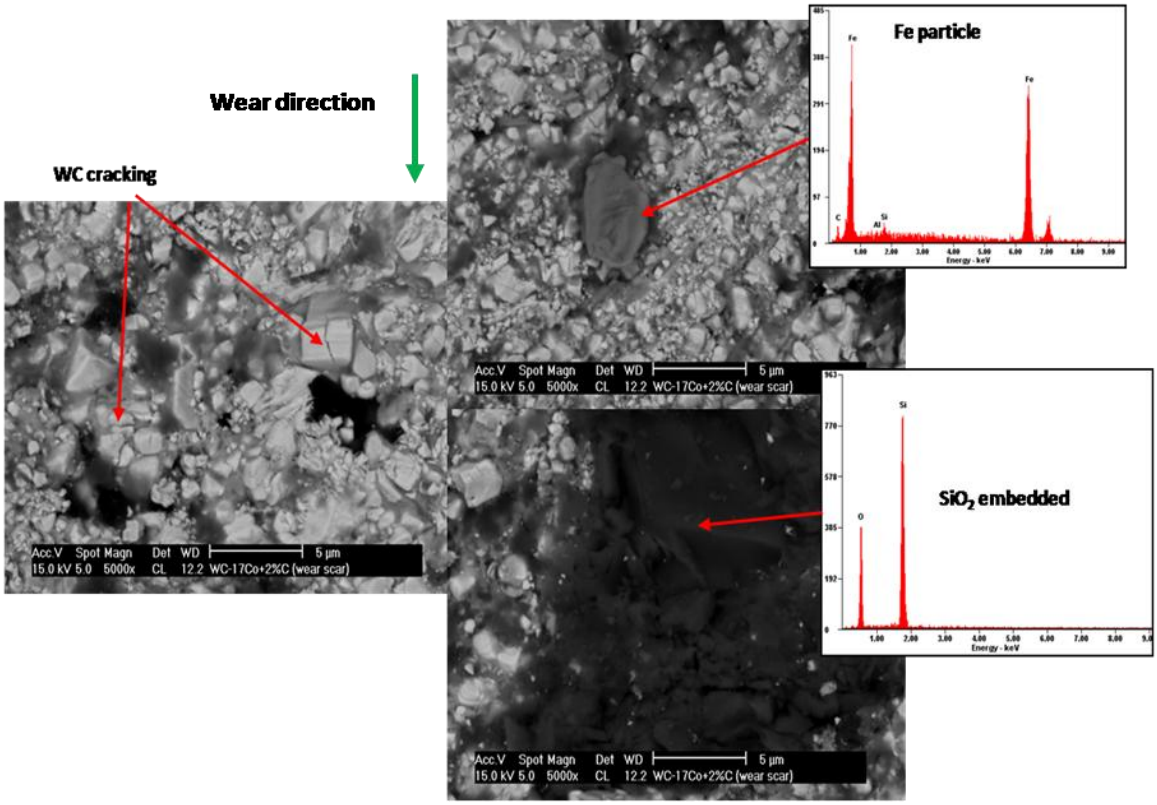

Figure 5-12: SEM-BSI micrographs of the worn surfaces for the WC-17Co+2%C coatings after 30mins test, EDS shows SiO_2 particles embedded into Fe substrate.

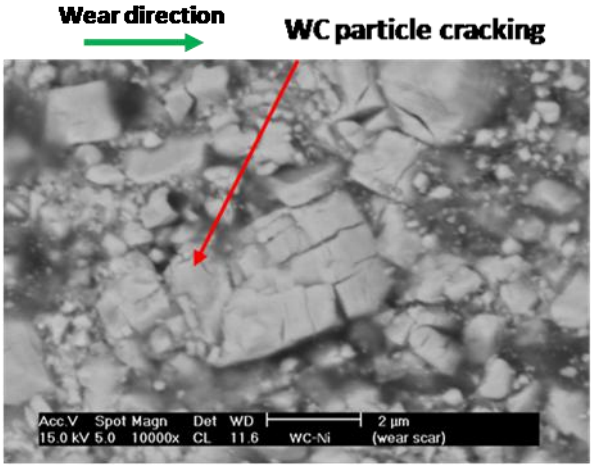

Figure 5-13: SEM-BSI micrographs of the worn surfaces for the WC-10Ni coating after 30mins test.

5.1.4. Hardness

The surface and cross-sectional hardness of the coatings was measured for both the as-sprayed and annealed samples. The hardness was measured using a micro Vickers hardness indenter with a load of 2kg for 10s. The results for the comparison between the surface and cross-sectional hardness of the as-sprayed coatings are given in Figure 5-14. The hardness values are in the range of 550 – 860 Hv. The low hardness values for the carbon enriched samples compared to the as-received WC-Co powder coatings is due to the higher porosity contents observed in the samples. The hardness values were comparable to that of work done by Yang et al. (Yang et al., 2003) who also showed hardness values in the range of 711 – 800 Hv (6.98 – 7.85 GPa), other authors measured much higher hardness values. Machio (Machio, 2005) quoted Hv(1kg) of 1106±23 and 1045±69 for WC-12Co and WC-17Co coatings respectively. Work done by Wayne and Sampath (Wayne & Sampath, 1992) quoted Knoop hardness (0.3kg) of 9.8±0.8 GPa and 10.4±0.2 GPa for WC-12Co and WC-17Co respectively.

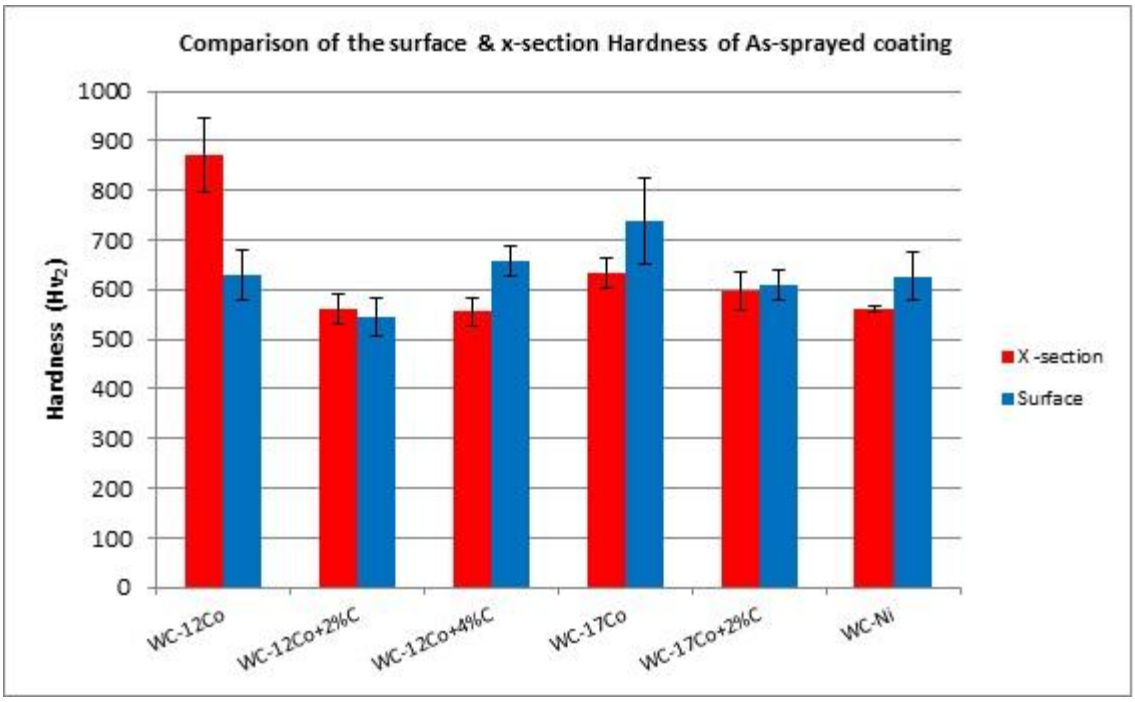

Figure 5-14: Comparison of the hardness measurements of the surface and cross-section of the as-sprayed coatings.

The surface and cross-sectional hardness was measured for both the as-sprayed and heat treated samples, the comparison is given in Figures 5-15 and 5-16 for surface and cross-section respectively. The hardness values for the surface was between 400 – 750HV, while the x-sectional was between 350 – 870HV. The two figures show similar trends where the hardness values of the heat treated samples are generally lower than that of the as-sprayed samples. The exceptions for the WC-12Co sample for the surface and WC-17Co and WC-Ni for the x-section the hardness values are very similar if errors are taken into account. The hardness values of the as-received coatings (WC-12Co and WC-17Co) for both the as-sprayed and heat treated samples are higher than those of the carbon enriched coatings (WC-12Co+2%C and WC-17Co+2%C).

Comparing the results of the hardness values with Co content the results should typically show that the hardness decreases with increasing Co content as the cobalt

phases are softer than that of the WC phase. The results in this work show an overlapping of the error bars for both sets of coatings, suggesting that the hardness values of the WC-17Co are not lower than WC-Co coatings. Deviations from the typical trend could be attributed to higher W_2C and eta phase formation compared to that of the WC-12Co samples; WC-17Co based samples also show reduced porosity levels (Table 5-2). Wayne and Sampath (Wayne & Sampath, 1992) showed an increase in hardness values of WC-12Co and WC-17Co as 9.8±0.8 GPa and 10.4±0.2 GPa respectively.

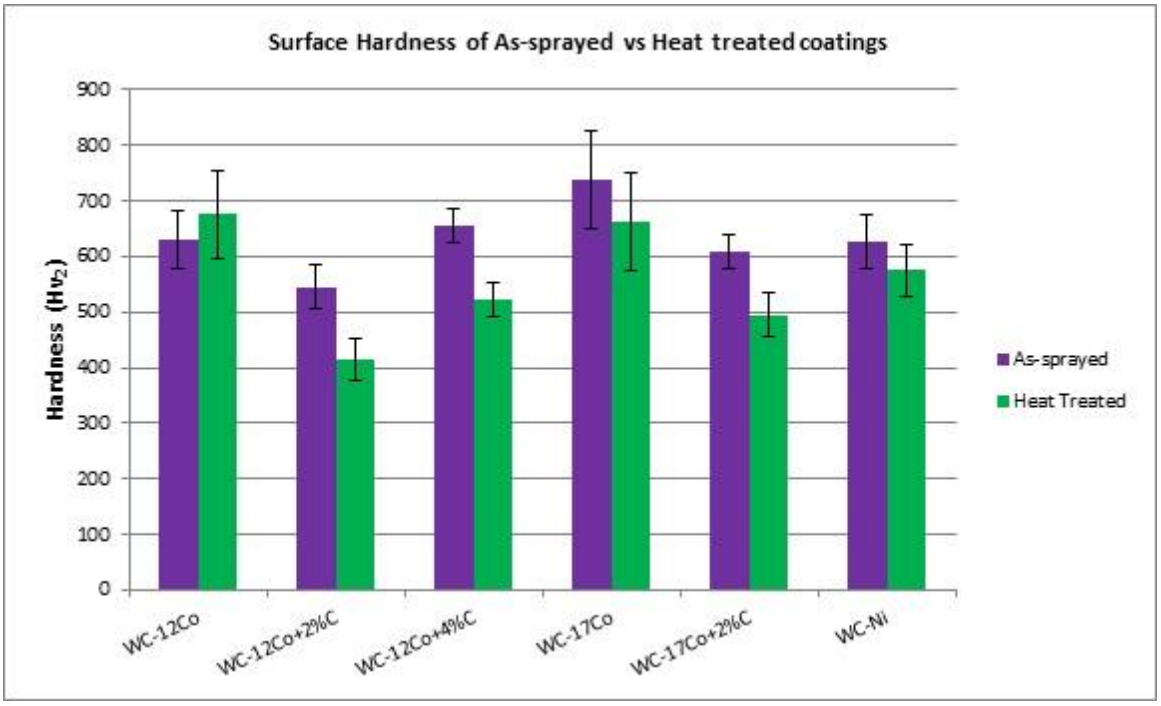

Figure 5-15: Comparison of the surface hardness measurements for the as-sprayed and heat treated coatings.

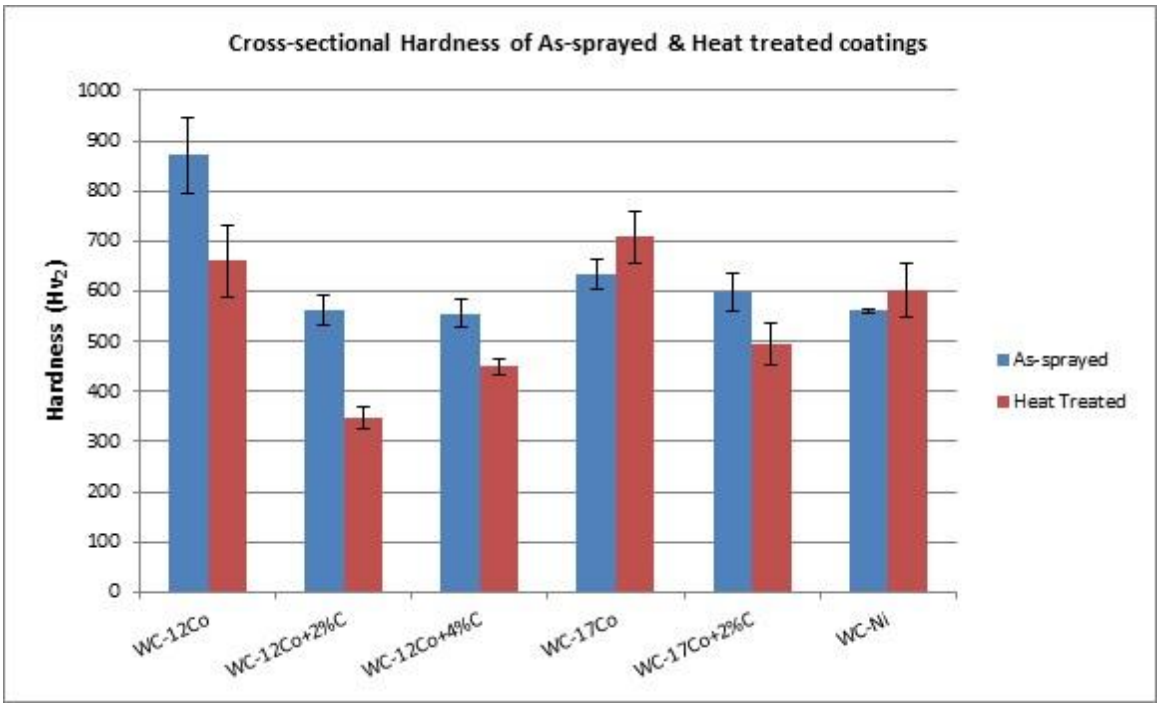

Figure 5-16: Comparison of the cross-sectional hardness measurements for the as-sprayed and heat treated coatings.

5.2. Discussion

Before discussing the effects of carbon content and annealing on the properties of the coatings it would be appropriate to mention that the thermal spraying process is a complex one. There is a large amount of factors and parameters which can affect the properties of the coatings. These factors make it increasingly difficult to directly compare results of coatings from other sources. Factors such as feedstock powders, spraying conditions and equipment, parameters and substrates can all lead to dramatic changes in the microstructure of the coatings. Each spray run could result in different phases formed, deposition rates and thicknesses, porosity levels and microstructure homogeneity. There is a vast amount of literature available on thermal spraying and the

effect on coatings with many authors showing contradicting results. The results depend on the microstructures produced during thermal spraying and provide more insight into the behaviour of coatings in general.

5.2.1. Effect of carbon content on the properties of the coatings

Feedstock powders have a huge impact on the resultant microstructure of a coating and therefore on the properties. In the case of addition of excess carbon in the starting WC-Co powder, although the carbon provides some relief for decarburization of the WC-Co powder, it can also affect the microstructure and properties.

During thermal spraying of WC-Co powders decarburization occurs, producing carbon deficient phases. The decarburization steps are given in Equation 2.17 – 2.19 (Section 2.3.2). Free carbon in the powders can potentially provide relief during thermal spraying. Instead of the WC-Co particles decomposing at high temperatures, undesired brittle phases such as W_2C or η eta phases (Co_XW_XC) can be formed; free carbon burns off forming CO or CO_2 gas.

Carbon surrounding the WC-Co particles is free to burn off during the thermal spraying process thereby reducing the amount of decarburization of the WC-Co particles. The free carbon reacts with oxygen, forming CO_2 or CO gas. However, the high velocity of impact of the particles could allow for free carbon to be trapped between the particle splats or carbon particles to appear between the WC-Co particle splats. The voids can lead to high porosity levels in the coating after spraying. Free carbon that is left and does not adhere strongly to the splats can also contribute to porosity and weaken the structure. The carbon burn off can also affect the deposition rate of the coatings, as

seen in this work. The higher the carbon content, the more difficult it is to deposit on to a substrate.

Decarburization of the WC-Co powders during HVOF spraying was reduced by the addition of 2wt%C (Figures 4-12 and 4-13) for the PCD samples. W_2C formation was reduced. Although XRD results were obtained from the same coating composition and from the same powder batch that was used to produce wear samples, these samples showed no evidence of W_2C and eta formation for either the as-received powder coatings (WC-12Co and WC-17Co) or the 2%C enriched as-sprayed coatings. This shows the composition variability of the spraying procedure. The cooling rate and kinetic impact of the particles on the substrate can cause variations in the composition produced. Samples with larger areas (wear samples) attained in a more equilibrium state compositions than the smaller sample coatings (PCD samples).

5.2.1.1. Wear and Hardness

From the results obtained above for the wear behaviour and hardness of the coated layers (Section 5.2.1), it can be seen that there was only a slight change in the wear results with addition of excess carbon, by removing some of the brittle W_2C and eta phases generated during spraying the wear resistance of the coatings with increasing carbon content increased slightly. Hardness on the other hand decreased. Porosity levels in the carbon enriched coatings also increased; this can also affect the hardness.

Overall, the wear resistance and hardness of the coatings produced were lower than expected. This would suggest that the carbon enrichment, although beneficial in reducing eta phase generation, showed no substantial improvement in the wear

resistance of the coatings and resulted in a decrease of the hardness. The dominant abrasive wear resistance mechanism is micro-cracking and micro-cutting abrasion.

5.2.2. Effect of annealing on the properties of the coatings

The effect of annealing on the properties of the coating were also studied, thermal heat treatment at any temperature may alter the stress state of the coating (Stewart et al., 1998). The annealing heat treatment is supposed to relieve stress build-up within the coating and to provide an improved microstructure. Coatings are considered to be in a metastable state and as mentioned earlier, heat treatment of the coatings can cause microstructure and phase compositional transformations, possibly by recrystallization of the matrix and pore and void reduction (Richert & Leszczynska-Madej, 2011). The compositional changes that can occur in the coatings consist of recrystallization of the amorphous Co region and decomposition of WC phase to W2C and other eta phases (η – Co6W6C). Recrystallization of the binder phase is said to occur between 600 - 853°C ((Nerz et al., 1992); (Li et al., 1996)). At the heat treatment temperature, plastic flow occurs in the coating and is responsible for changes in residual stress of the coating.

The heat treatment affects the decomposition of all the coatings produced by various degrees. All the coatings showed decomposition of the WC phase to W_2C and eta phases. The as-received coatings (WC-12Co and WC-17Co) showed the most decomposition. The carbon enriched coatings showed the least decomposition.

Heat treatment (hydrogen cleaning) was also done on the WC-Co coatings used in PCD sintering experiments. The heat treatment was carried out at 1100°C in H_2 gas for 1 hour. XRD results (Section 4.2.2 and Figure 4-18) show that no decomposition of the WC phase occurred. Any residual W_2C phase generated in the as-sprayed coatings after

spraying reverted back to the equilibrium WC phase (increased WC peak intensity). Recrystallization of the stressed binder region occurred to show well defined Co peaks. No property measurements were done on these samples.

5.2.2.1. Wear resistance

When looking at the effects of annealing on the wear resistance of the coatings, Asl (Asl et al., 2006) showed that the mass loss for heat treated samples should be higher than that of the as-sprayed coatings (Figure 2 18). Coversely, Kim (Kim et al., 2007) showed that heat treatment improved the wear resistance of the coating (Figure 5 17). The differences are affected by the phase composition of WC and eta phases generated.

From the results obtained in this study as described above, it can be seen that there are some contradictory results presented. Some of the samples (WC-12Co, WC-12Co+6%C, WC-17Co) showed a decreased in wear rate with annealing temperature, while other samples (WC-17Co+2%C and WC-Ni) showed an increase. It is noted that the WC-12Co+2%C and the WC-12Co+4%C samples show only negligible changes. Very few changes in the phase composition of the coatings was observed (i.e. for WC-12Co+4%C a similar amount of W_2C and Co was seen before and after annealing, similar with the WC-12Co+2%C where only a slight increase in eta phases were observed). The increase in wear rate for the WC-17Co+2%C and the WC-Ni samples can be attributed to a few factors such as an increase in W_2C and eta phase generation and cracking and binder dissolution within the WC. The decrease in the wear rate for the WC-12Co and WC-17Co samples can be attributed to factors such as a reduced stresses after annealing; this could result in less WC mass loss during wear testing as well as less binder removal during wear, although decomposition for these materials was much higher than that of the other coatings. Overall, the heat treatment provided better wear behaviour.

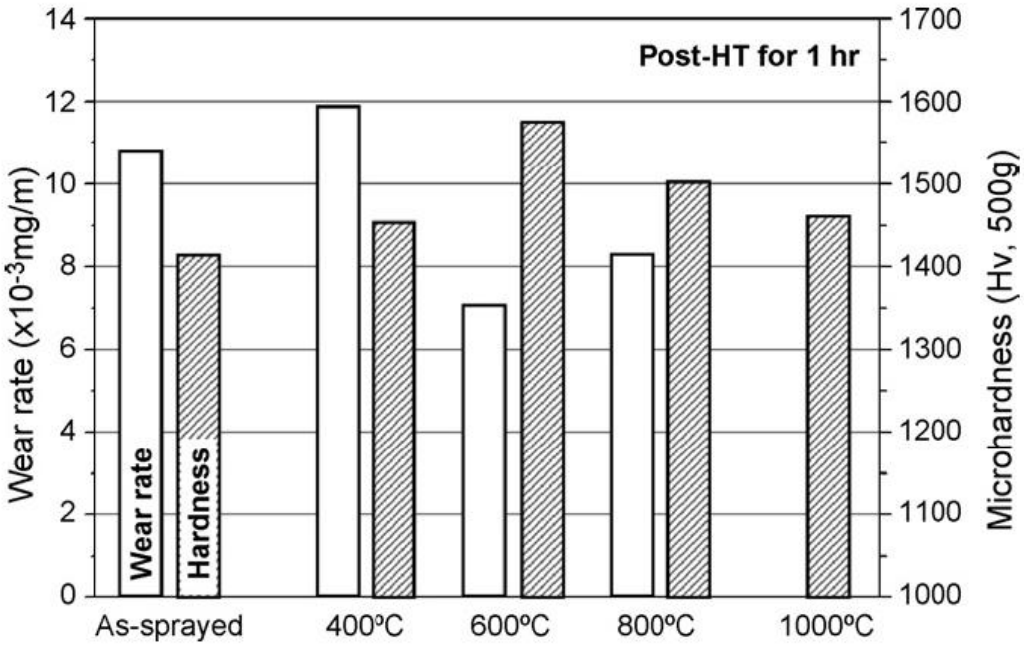

Figure 5-17: Abrasive wear rate and hardness of WC-Co nano-composite coatings (Kim et al., 2007).

5.2.2.2. Hardness

The results of the hardness values obtained after annealing could be explained by many influencing factors, such as level of porosity, WC grain size, residual thermal stresses and formation of various phases. The hardness of the as-sprayed coatings, although contradicted by some authors, can be typically higher than that of the heat treated samples. The heat treatment causes relief of thermal stress generated during spraying and change of phase composition. Authors such as Asl (Asl et al., 2006) (Figure 2 18) and Kim (Kim et al., 2007) (Figure 5-17) showed that after heat treatment, the hardness increases. During heat treatment (Asl et al., 2006), a greater amount of the WC and remaining amorphous phases are converted to W_2C or eta phases which are typically harder than WC. This could be counteracted by residual stresses, micro-cracking in the

material and increased WC grain size. In work done by Richert and Leszczynska-Madej (Richert & Leszczynska-Madej, 2011) on the annealing effects on WC-Co coatings, an improved homogeneous microstructure with fewer voids or pores was achieved but hardness values after annealing showed no significant increase. Stewart et al (Stewart et al., 1998) attributed the decrease in the hardness of the heat treated coatings above 700°C to gross micro-cracking within the sample, which would dominate any residual stress effects. There are a wide range of results reported, not all leading to improved hardness.

The WC grain size of the heat treated samples could also contribute to a slight decrease of hardness. The typical trend for polycrystalline materials hardness dependence on grain size can be seen in work done by Yang et al. (Yang et al., 2003). These authors studied the influence of WC grain size on hardness of WC-12Co HVOF coatings; hardness decreased with increasing WC grain size. In this study there was an increase in the WC grain size of the heat treated samples compared to that of the as-sprayed coatings (i.e. from 0.7 to 1.2μm shown in Table 4-4 and 5-2).

Porosity levels could also affect the hardness of the coating; higher porosity levels can lower the hardness. The carbon enriched coatings show a reduced amount of W_2C and eta phase generation, especially after heat treatment and an increase in Co re-crystallization. The heat treated samples showed higher W_2C and eta phase formation.

5.2.3. Comparison between Wear resistance and Hardness

A comparison was done between the wear resistance and the hardness of the coatings for both the as-sprayed and heat treated coatings. Figures 5-18 and 5-19 showed the results for the as-sprayed and heat treated coatings respectively.

Overall, the wear resistance was at the expense of the hardness of the coating. When the wear resistance was good (low wear rate) such as in WC-12Co+2 and 4%C, the hardness was low, similarly in the as-received coatings (WC-12Co and WC-17Co) good hardness values were counteracted by poor wear resistance (high wear rate).

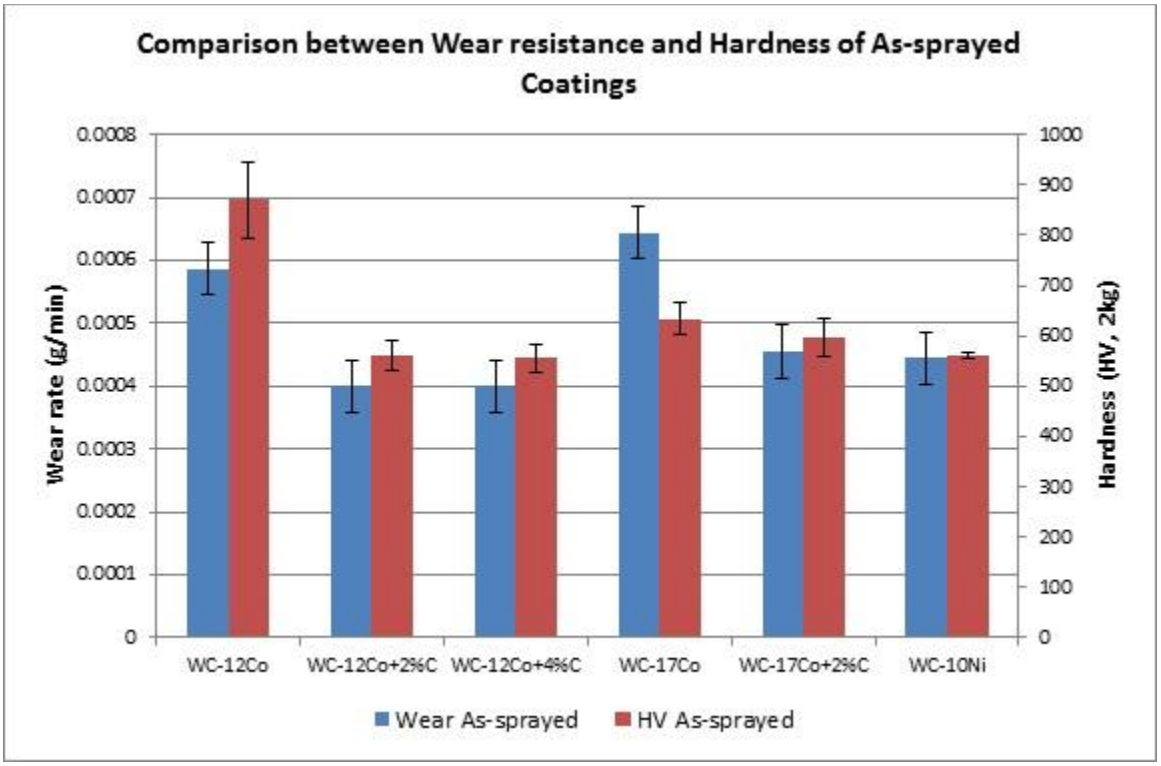

Figure 5-18: Comparison between the wear resistance and hardness of the as-sprayed coatings.

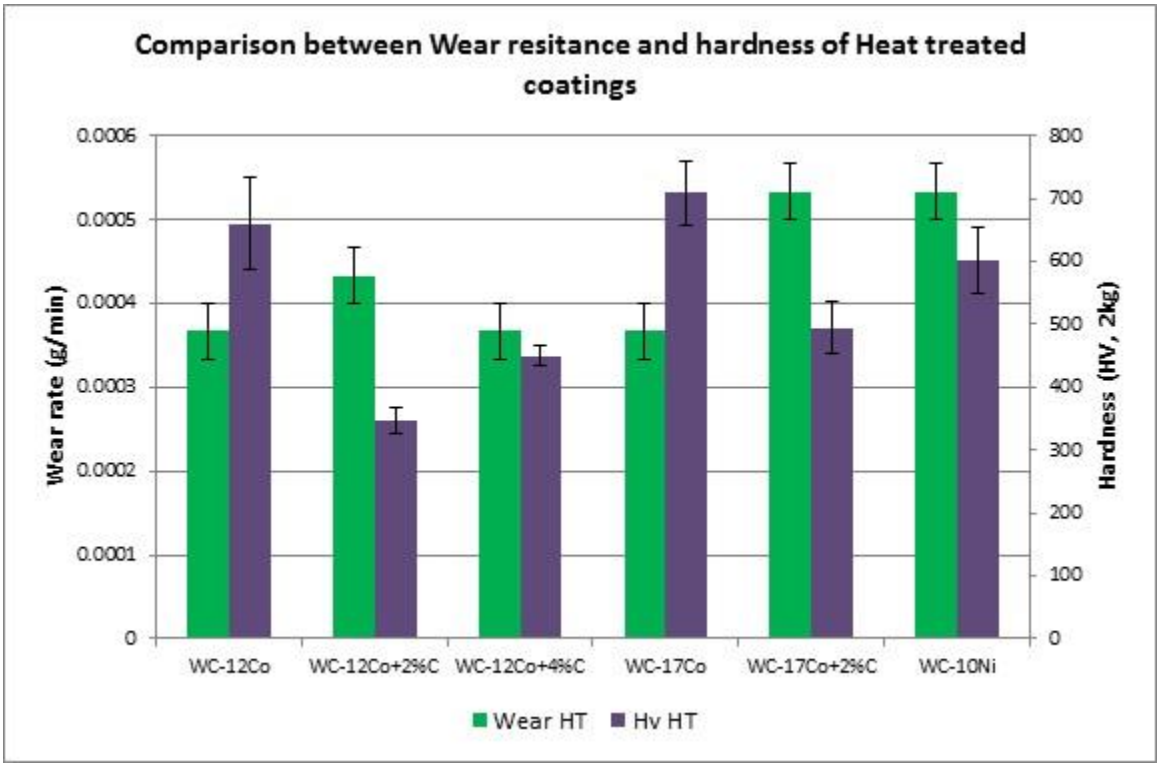

Figure 5-19: Comparison between the wear resistance and hardness of the heat treated coatings

Chapter 6: Results of PCD Sintering

6. Results

This chapter describes the results and characterisation achieved by sintering the carbon enriched WC-Co coated substrates and carbon enhanced carbide substrates with PCD at HPHT conditions using various diamond grain sizes. The characterisation includes SEM microstructural analysis, particle size distribution and image analysis of the diamond powders, WC substrate and sintered PCD samples.

6.1. Characterisation of Diamond powder & WC-Co substrate

6.1.1. Diamond powder

The diamond powders used in the PCD sintering are given in Section 3.1.1 in Table 3-2. Figure 6-1 shows the microstructure of the various diamond powders used, while the particle size distribution can be seen in Figure 6-2. The diamond powder batches are named according to the average particle size range; medium grade (MG), fine grade (FG-6) and ultra-fine grade (FG-0.5). The fine grade powder was used in most of the experiments and has an average particle size of 0.5 µm, hence as the nomenclature. Similarly the FG-6 was named for the average particle size. From Figure 6-1, it can be seen that the MG and FG-6 powder contain about 1 vol.% spheroidal (SP) Co particles. These tiny white particles help with sintering of the diamond. The FG-0.5 diamond powder does not contain any additional Co.

ADD PICTURE

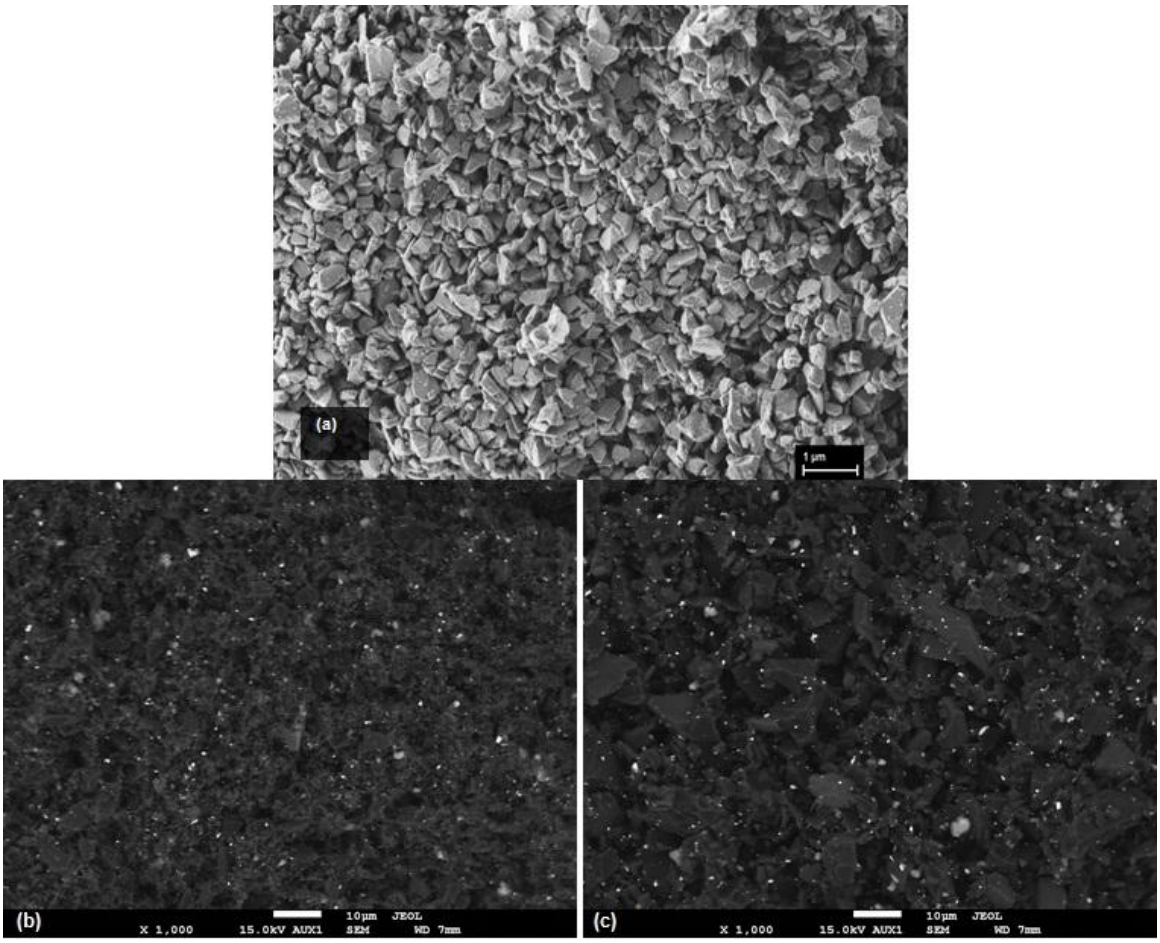

Figure 6-1: SEM-SEI micrograph of the various diamond powders (a) FG-0.5, 0.5µm fine grained diamond, (b) FG-6, 4-6µm fine grained diamond and (c) MG , 8 - 10µm medium grained diamond.

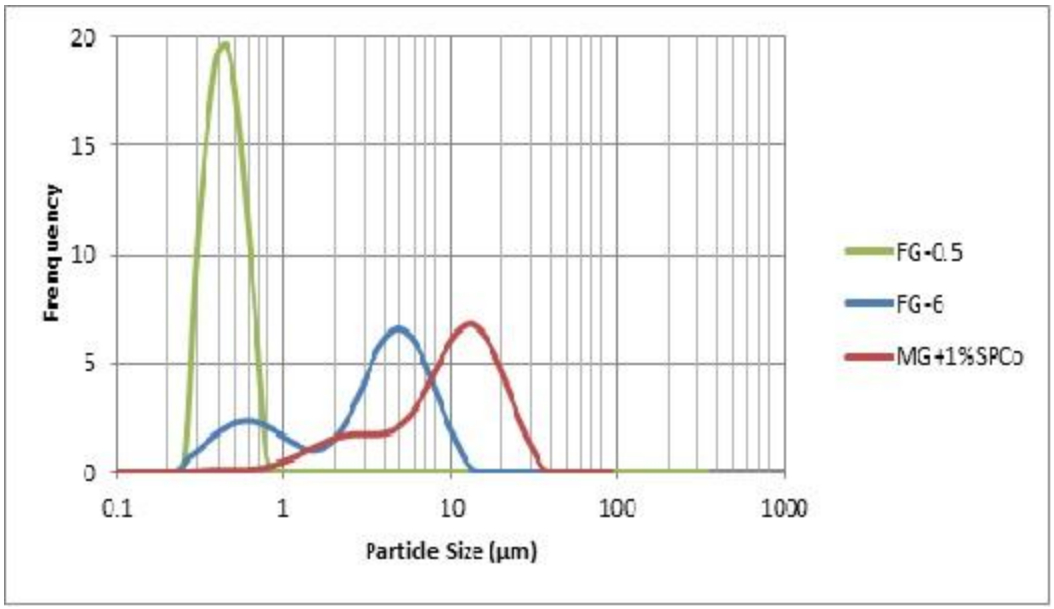

Figure 6-2: Particle size distribution of the various diamond powders.

6.1.2. WC-Co substrate

In PCD sintering a WC-13Co standard substrate is used as the Co metal infiltration source for facilitating diamond-diamond bonding. The microstructure of the standard WC-13Co substrate used in all PCD sintering samples is shown in Figure 6-3. The light phase and dark grey phase is WC and Co respectively as can be seen in the corresponding EDX spectrum. Image analysis of the WC-13Co substrate was done and the results are given in Table 6-1, showing that the WC particle size was in the range of 3.82 ± 1.41µm.

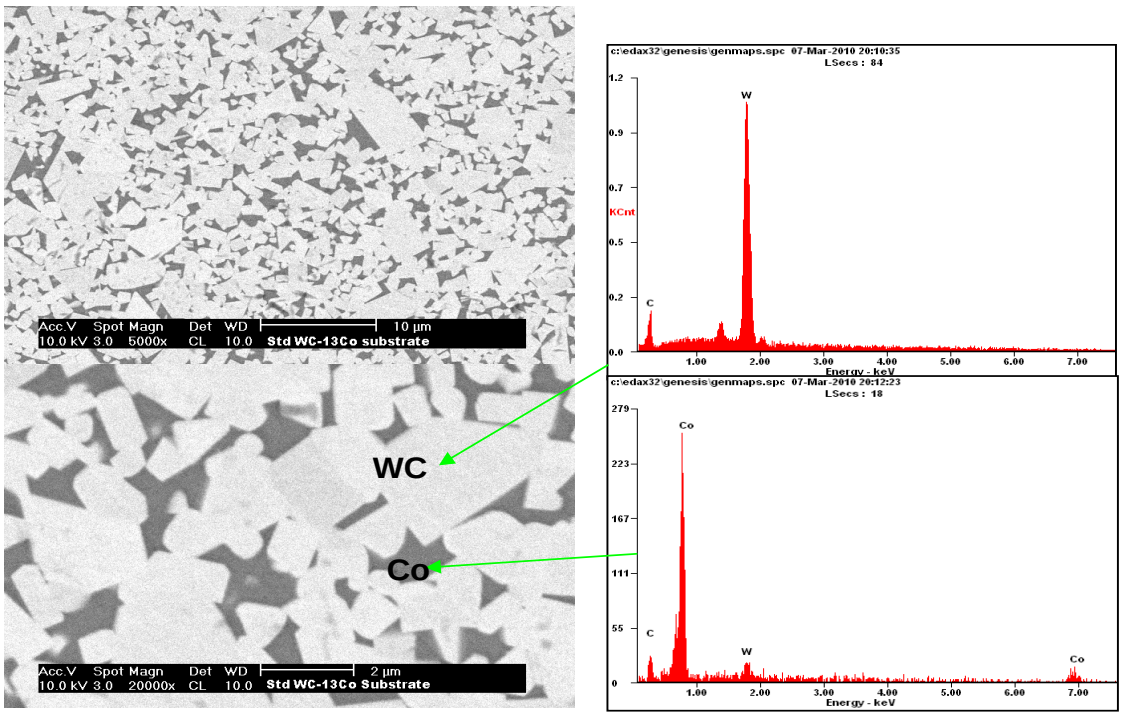

Figure 6-3: SEM-SEI micrographs and EDX of the WC-Co substrate used for PCD sintering.

Table 6-1: Image analysis results for WC-13Co standard substrate.

Property	Quantification
WC particle size (µm)	3.82 ± 1.41
Co pool size (µm)	1.05 ± 0.57
WC Content area (Area %)	85.96 ± 0.25
Binder Content (Area %)	14.04 ± 0.25
WC Mean Free Path (MFP) (µm)	2.37 ± 2.15
Binder Mean Free Path (MFP) (µm)	0.37 ±0.28
WC Contiguity (%)	50.3±1.10

6.2. PCD Sintering

Table 6-2 contains the sintering conditions of the different capsule runs and various diamond powders and corresponding substrates used. The various substrates used as described in Section 3.2 and 3.3 are given in Table 6 2 are:

- a standard WC-13Co substrate,
- carbon enriched coating,
- graphitized diamond/diamond enhanced substrates (GDEC/DEC),
- VC doped substrate

The sintering capsule runs:

- Capsule # 1 – 9 contained the 0 – 6%C coatings using various diamond powder grades (MG, FG-6 and FG-0.5),
- Capsule #10 – 14 contain the GDEC or DEC inter-layers and VC doped substrate sintered using different diamond powder grades (FG-6 and FG-0.5) and interlayer thickness and carbon content.
- A standard WC-13Co substrate was sintered in most capsules as a comparison.

Table 6-2: Samples and conditions of PCD capsule sintered at 1400°C.

Capsule	Conditions	Diamond Powder	Materials Densified
No.:	**Pressure (GPa)**	**Grain Size**	**Std / Coating / GDEC/DEC interlayer:**
Cap#1	5.6	MG	WC-12Co, WC-12Co+2%C, WC-17Co,WC-17Co +2%C coatings, std WC-13Co substrate
Cap#3	6.8	FG-0.5	WC-12Co, WC-12Co+2%C, WC-17Co, WC-17Co +2%C coatings, std WC-13Co substrate
Cap#4	6.8	FG-0.5	WC-12Co+4%C, WC-12Co+6%C, WC-17Co+4%C, WC-17Co +6%C coatings, std WC-13Co substrate
Cap#6	6.8	FG-0.5	WC-12Co, WC-12Co+2%C, WC-17Co, WC-17Co +2%C coatings, std WC-13Co substrate
Cap#7	6.8	FG-0.5	WC-12Co+4%C,WC-12Co+6%C, WC-17Co+4%C, WC-17Co +6%C coatings, std WC-13Co substrate
Cap#8	6.8	FG-6	WC-12Co, WC-12Co+2%C, WC-17Co, WC-17Co +2%C coatings, std WC-13Co substrate
Cap#9	6.8	FG-6	WC-12Co+4%C, WC-12Co+6%C, WC-17Co+4%C, WC-17Co +6%C coatings, std WC-13Co substrate
Cap#10	6.8	FG-0.5	10vol.% GDEC substrates – 0.1, 0.5, 1 & 2mm interlayer thickness and std WC-13Co substrate
Cap#11	6.8	FG-0.5	2.5 mm 10vol.% GDEC, Full 12.5 mm 10vol.% GDEC & 5, 10 & 15vol.% DEC 2.5mm interlayer
Cap#12	6.8	FG-6	2.5 mm 10vol.% GDEC, Full 12.5 mm 10vol.% GDEC & 5, 10 & 15vol.% DEC 2.5mm interlayer
Cap#13	6.8	FG-0.5	2, 3, 4, 5 and 6 mm 10vol.% GDEC inter-layers
Cap#14	6.8	FG-0.5	2 wt.% VC, 10vol.% 0.5µm DEC, 10vol.% 0.5µm DEC+2wt%VC interlayer

6.2.1. Standard WC-Co substrate

Samples were sintered using a conventional WC-13Co substrate described in Section 6.1.2. The following diamond powders were used; MG, FG-6µm and FG-0.5µm. The standard substrate was compared with the carbon enriched substrates and a VC doped substrate.

A – MG diamond powder

Initial PCD sintering tests were done using the medium grade (MG) PCD powder of 8-10µm particle size containing 1vol.% spherical Co. The sintering was done at 5.8GPa and 1400°C. These tests were done on a standard WC-13Co substrate and on the WC-Co and 2%C enriched coated substrates. The aim of this test was to determine if the Co pool region at the interface is reduced with increasing carbon content. Figure 6-4 shows the micrographs of the sintered PCD using a standard substrate WC-13Co (i.e. no coated layer) described above. The diamond particles (black phase) is surrounded by the Co pool (grey phase) with small particles of WC (light phase) in between. It is noted that for the standard substrate acicular grain growth of the WC particles was observed at the interface. Acicular grain growth of the WC is elongation of the WC particles, with the particles becoming needle-like. Large grain growth of the diamond is visible at the interface, resulting in grains of 15 – 20µm in size. The mean diamond particle size, Co pool size and binder content of the bulk PCD are given in Table 6-4, determined by image analysis described in section 3.7.3.1.

The Co pool size at the interface was measured from the PCD/substrate interface to the bottom of the densely packed diamond particles i.e. shown in Figure 6-4. The measured

Co pool size at the interface is 18 ± 2.3µm wide, summarized later in Table 6-5 (page 128). This table contains the results obtained for all MG samples sintered in Cap#1.

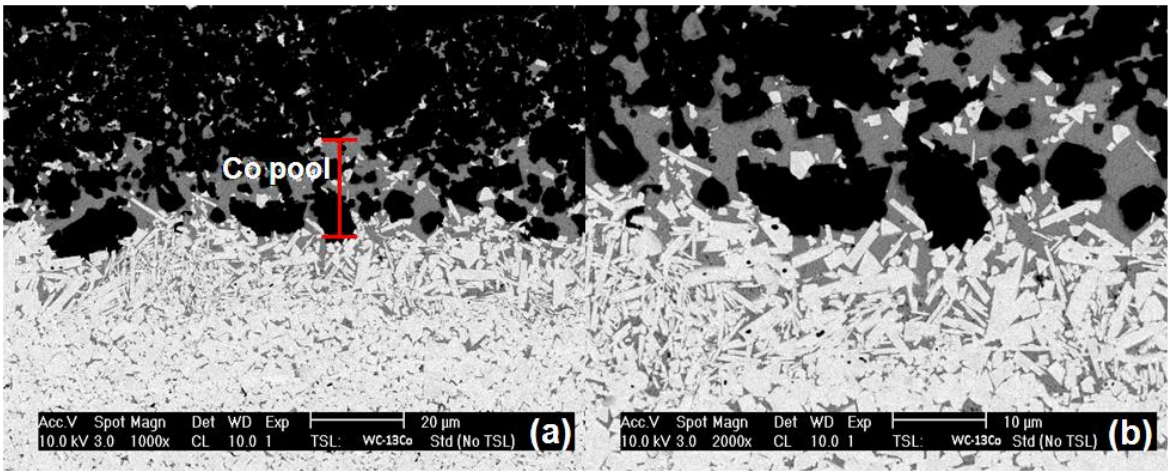

Figure 6-4: SEM-BSE micrograph of the interface of the MG diamond powder sintered PCD standard substrate.

B – FG-0.5µm fine grain diamond

Sintering of a fine grain 0.5µm (FG-0.5) diamond powder was performed to determine if the carbon enriched coated substrates would reduce grain growth at the interface. Samples were prepared and sintered at 1400°C and 5.6 – 6.8 GPa. It was found that the higher pressure produced better results; this is also the standard conditions used in industry to sinter fine grain PCD. Various capsules were run containing the different samples for UHPHT sintering.

Five samples were sintered using 0.5µm diamond on the standard WC-13Co substrates; these samples were sintered in capsule #3, 4, 6 and 7, all at the same sintering conditions. Sintering using 0.5µm diamond resulted in large AGG diamond crystals at the PCD to substrate interface; this can be seen in Figures 6-5 and 6-6. The large AGG region

is a result of the high chemical potential of the 0.5µm diamond particles which results in a significantly high driving force for grain growth. A remarkable difference in the thickness of the AGG region is evident between the five samples (Table 6-3). The average AGG thickness was determined using an optical microscope and measurement analysis software as described in Section 3.7.3.1. The thickness of the AGG region is summarized in Table 6-3. These AGG regions are excessive and are in the range between 238 - 1002µm. These large AGG regions consist of large diamond crystals inter-grown from the substrate interface and extending into the bulk PCD table. Each crystal is separated by Co with WC particles trapped due to re-precipitation.

Large "plumes" between 645 – 1342µm were also observed in many of the samples (Figure 6-13). "Plumes" are described as an extreme growth of diamond particles grown in a preferential direction and protruding out into the bulk PCD. The grains resulting from the plumes appear to grow on either side perpendicular to the plume; a Co pool separates the two growth directions. Cracks sometimes appear along the plume, it is still not known if a plume forms on a crack in the material during sintering or if a crack sometimes appears due to the formation of the plume during sintering.

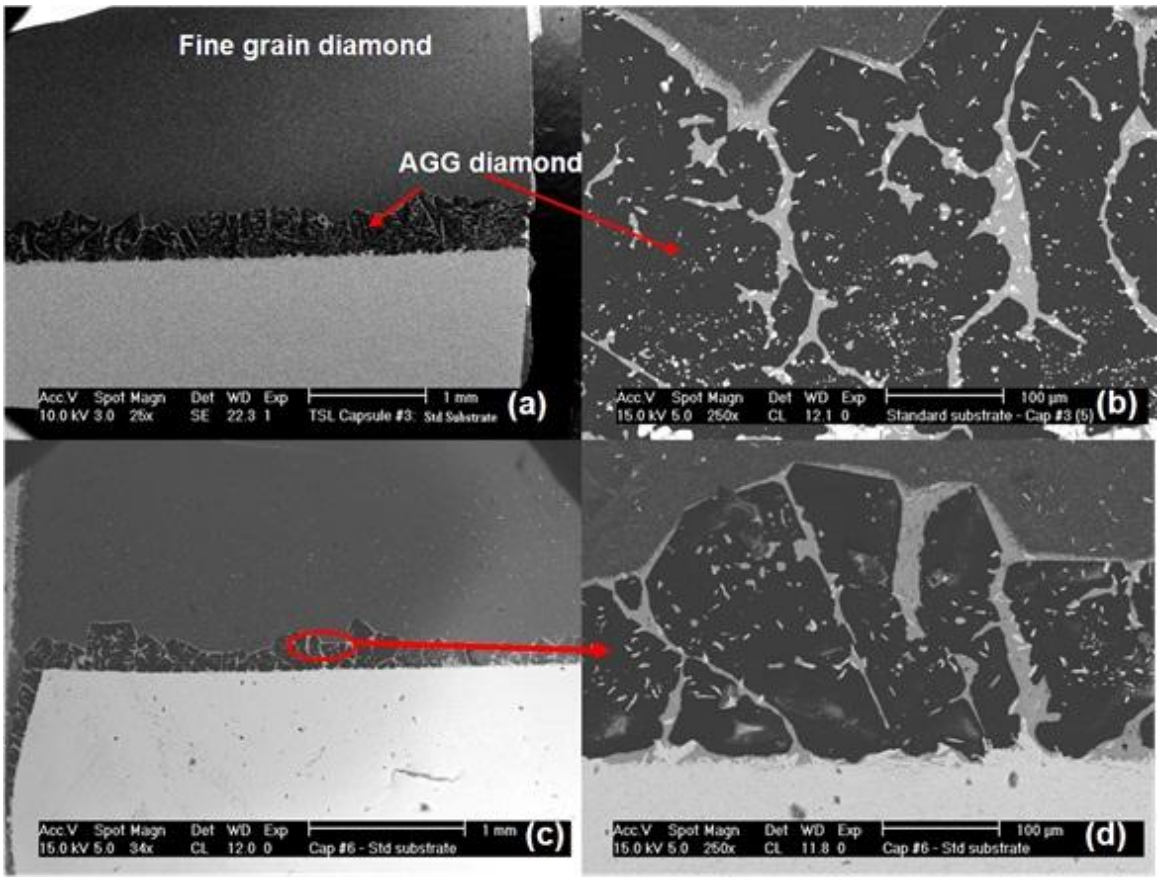

Figure 6-5: SEM-BSI micrographs of the interface of the FG-0.5µm diamond powder sintered PCD for the Standard WC-Co substrate from capsule #3 (a, b) and capsule #6 (c, d).

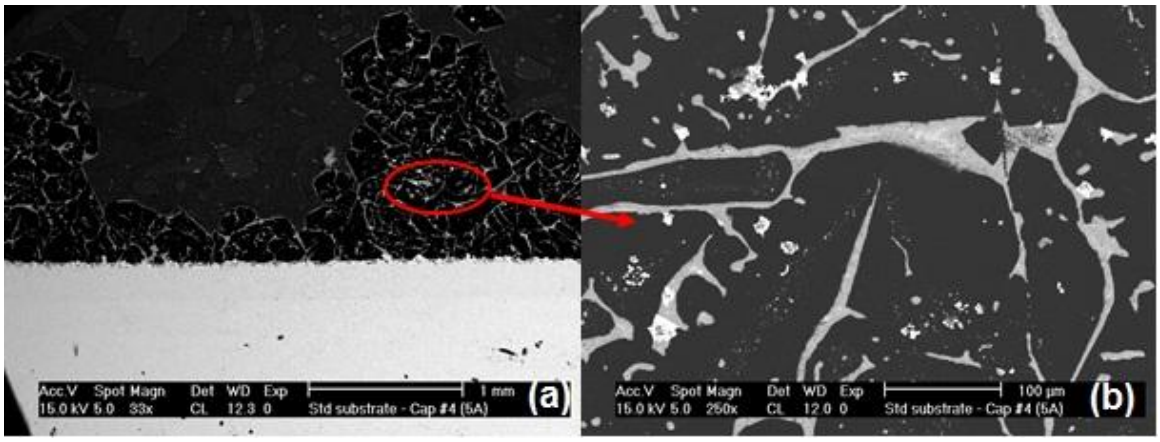

Figure 6-6: SEM-BSI micrographs of the interface of the FG-0.5µm diamond powder sintered PCD for the Standard WC-Co substrate from capsule #4.

Table 6-3: Thickness of abnormal grain growth region for MG diamond PCD samples on standard substrate.

Sintering run	AGG layer thickness (µm)	Plume thickness (µm)	Total thickness (µm)
Cap#3	387	1342	457
Cap#4	1002	1057	1015
Cap#6	238	-	238
Cap#7a	309	1205	393
Cap#7b	427	-	427

C - FG-6µm fine grain diamond

Since AGG is highly prevalent in the fine grade (FG-0.5) diamond samples, it was difficult to determine the effect the added carbon has on the amount of Co pooling. It was then necessary to look at the effect carbon had on Co pooling at the interface when a coarser diamond powder was used. This was a fine grained (FG-6) diamond powder with a multimodal particle size distribution of about 0.5-6 µm. Since this material has some fine grain particles (0.5 µm) and slightly coarser particles (4-6 µm), the driving force for grain growth is low therefore AGG should not have appeared. The Co pool at the interface would therefore be more prominent.

Two samples were sintered using the FG-6µm diamond powder on a standard WC-13Co substrate; each sample was sintered at the same sintering conditions but in a different capsule run (cap #8 and #9). The results obtained are shown in Figure 6-7; here no AGG of the diamond was evident at the interface. This can be attributed to the larger grain size of the diamond which results in a lower driving force for grain growth. Similar to that of the MG-8µm diamond sample, Co pool formation was evident at the interface. The Co pool thickness was measured to be 21.2±2.4µm and 28.4±2.0µm for cap #8 and

#9 respectively (summarized in Table 6-9). Acicular grain growth of the WC was evident in the samples from Cap#9. Image analysis of the bulk sintered PCD of the MG and FG-6µm diamond samples are given in Table 6-4.

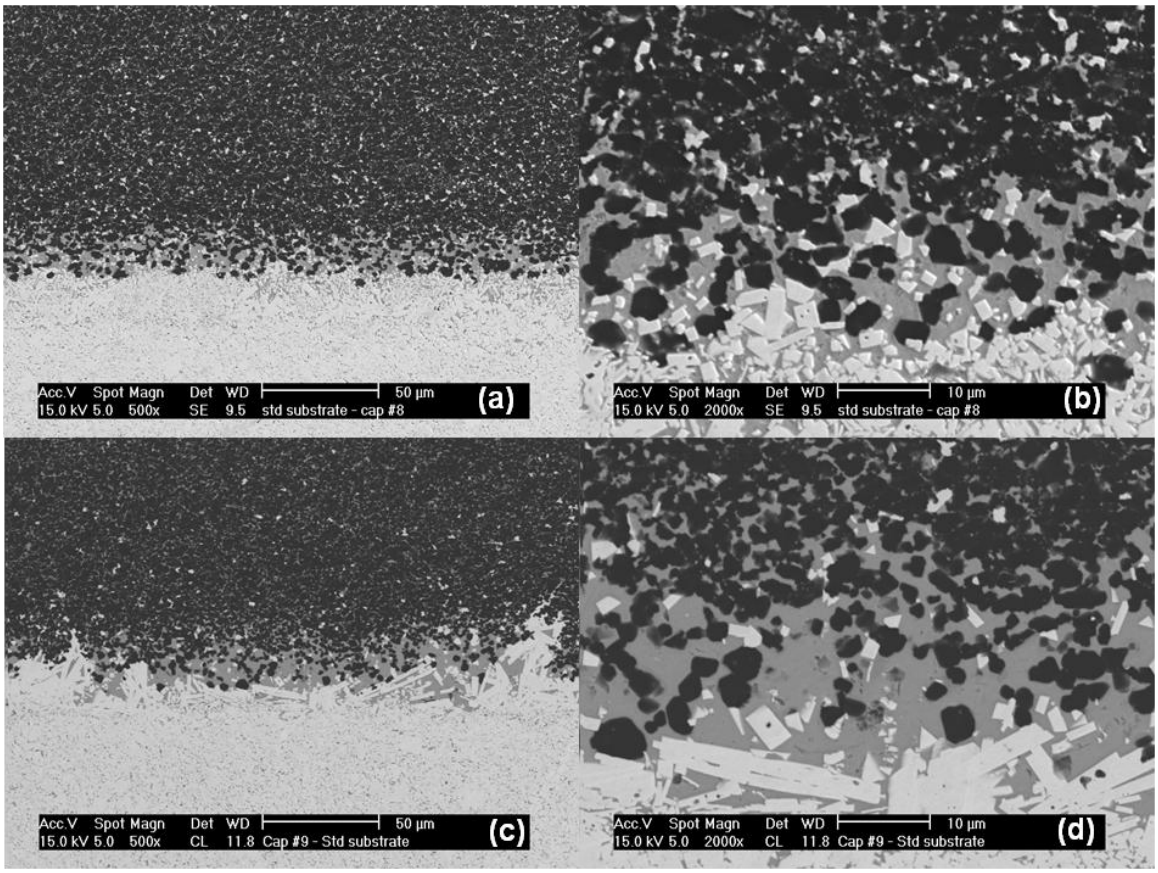

Figure 6-7: SEM-BSI micrographs of the interface of the FG-6 sintered PCD for the standard WC-13Co substrate from Cap#8 (a, b) and Cap#9 (c, d), the dark phase is diamond, grey phase is Co and light phase is WC.

Table 6-4: Image analysis results of the diamond layer sintered on a WC-Co standard substrate using MG and FG-6µm PCD.

Property	MG	FG-6µm Cap #8	FG-6µm Cap #9
Diamond particle size (µm)	10.3 ± 3.8	4.2 ± 1.1	4.0 ± 1.2
Co pool size (µm)	1.9 ± 0.9	1.3 ± 0.7	1.3 ± 0.6
Diamond Content (Area %)	90.8 ± 0.4	88.1 ± 0.3	87.3 ± 0.6
Binder Content (Area %)	9.2 ± 0.4	11.9 ± 0.3	12.7 ± 0.6
Diamond Mean Free Path (MFP) (µm)	7.0 ± 7.6	3.5 ± 3.5	3.1 ± 3.1
Co Mean Free Path (MFP) (µm)	0.8 ± 0.6	0.5 ± 0.4	0.5 ± 0.4
Diamond Contiguity (%)	58.7 ± 1.6	60.1 ± 2.1	59.5 ± 1.7
WC particle size (µm)	0.5 ± 0.3	0.4 ± 0.3	0.3 ± 0.2
WC Content (Area %)	1.4 ± 0.2	4.8 ± 1.3	1.8 ± 0.4

6.2.2. Carbon Enriched Substrates

Carbon enriched substrates were produced to suppress or eliminate AGG of the 0.5µm diamond. Two types of carbon enriched substrates were produced; carbon enriched thermally sprayed WC-Co coatings on standard WC-Co substrate and diamond/graphite enhanced WC-Co substrates. The extra carbon in the substrate acts to prevent Ostwald ripening of the diamond and reduce the carbon solubility difference between the infiltrating Co melt and the diamond PCD table. The results of the testing of this theory are described below.

6.2.2.1. Carbon Enriched Thermally Sprayed Coatings

As described in Section 3.2, carbon enriched thermally sprayed WC-Co coatings were sprayed on standard WC-Co substrates; these coatings were sintered with various

diamond powders (MG, FG-6µm and FG-0.5µm). The various coatings compositions, diamond powders used and sintering conditions are described in Table 6-2.

A – MG diamond

A initial PCD sintering test (cap #1) was done using the medium grade PCD powder of 8-10µm (MG) containing 1vol.% spherical Co as stated in Section 6.2.1. The sintering was done at 5.8GPa and 1400°C. The aim was to determine the effect the carbon enriched coating has on the grain growth and Co pool formation. Typically, no AGG was expected in this material, as is evident in the standard WC-13Co substrate. Similar to the standard substrate, Co pool formation was expected. Only the 0 – 2%C coatings for both the WC-12Co and WC-17Co powders were sintered. Micrographs of these samples can be seen in Figures 6-8 and 6-9. These images show well sintered materials. The 2%C enriched samples in Figure 6-8 c & d and Figure 6-9 c & d show very little acicular grain growth of the WC particles as compared to the non-carbon enriched (WC-12Co and WC-17Co) samples and that of the standard WC-13Co shown in Figure 6-4. This could suggest that a small amount of carbon enrichment can prevent acicular grain growth from occurring.

The Co pooling at the interface was measured to range between 21-23µm, and shown in Table 6-5. These changes were insignificant. Image analysis results of the bulk PCD are given in Table 6-6. Diamond grains at the interface in the Co pool appeared slightly larger than the diamond particles in the bulk. The Co pool acted as a source for re-precipitation of dissolved C, thus grains in this region appeared to be larger than in a region where there is little Co pooling.

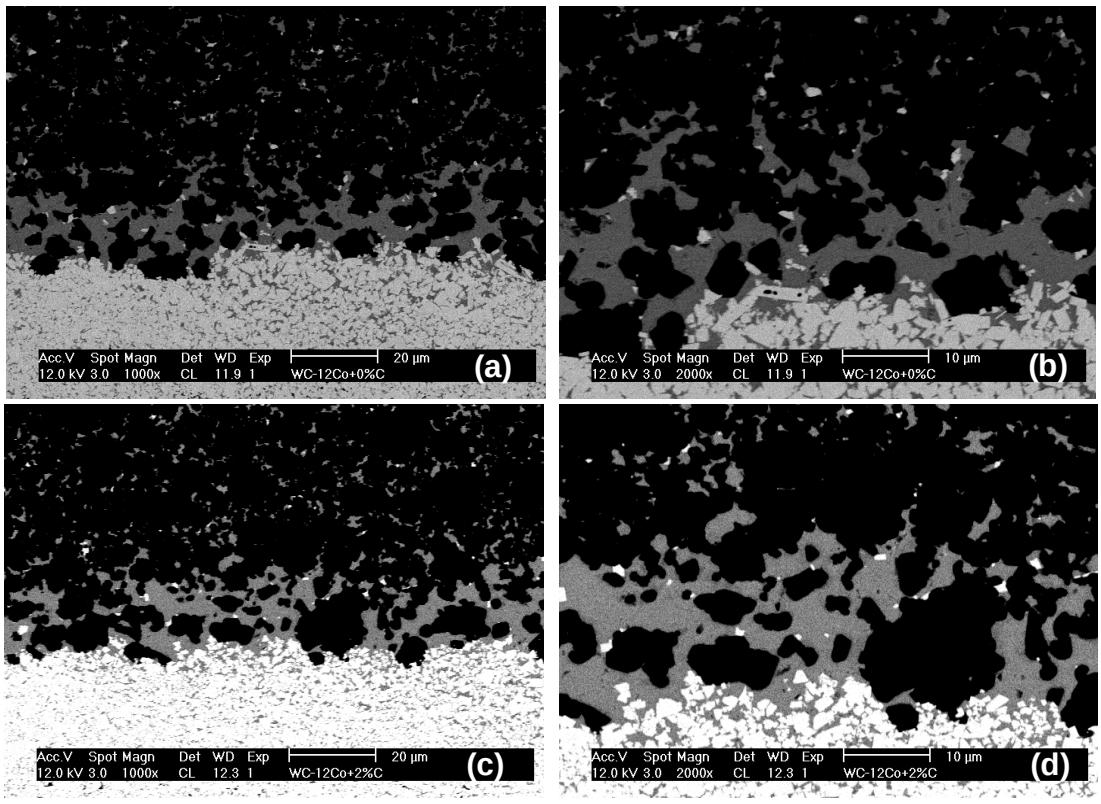

Figure 6-8: SEM-BSI micrographs of the interface of the MG diamond sintered PCD for the WC-12Co samples: (a & b) WC-12Co coated layer and (c & d) WC-12Co+2%C coated layer (cap#1).

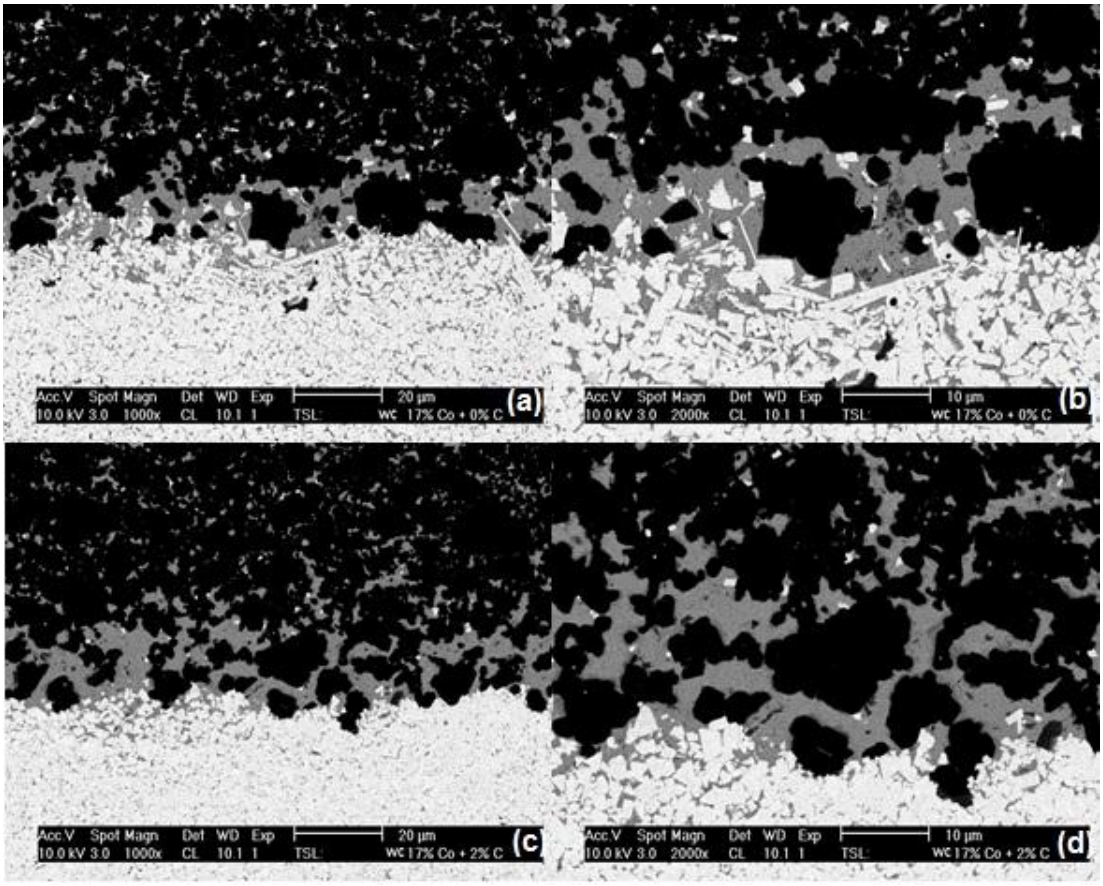

Figure 6-9: SEM-BSI micrographs of the interface of the MG diamond sintered PCD for the WC-17Co samples: (a & b) WC-17Co coated layer and (c & d) WC-17Co+2%C coated layer (cap#1).

Table 6-5: Cobalt pool size of Medium grade (MG) PCD samples (cap#1).

Material	Co pool size (µm)
Std WC-13Co substrate	18.0 ± 2.3
WC-12Co	22.9 ± 1.8
WC-12Co+2%C	23.2 ± 1.5
WC-17Co	20.4 ± 1.6
WC-17Co+2%C	22.7 ± 2.4

Table 6-6: Image analysis results of medium grade (MG) PCD samples (cap #1).

Property	WC-12Co	WC-12Co+2%C	WC-17Co	WC-17Co+2%C
Diamond particle size (µm)	9.9 ± 3.9	9.8 ± 3.4	10.3 ± 3.8	10.6 ± 4.1
Co pool size (µm)	2.0 ± 1.0	2.0 ± 1.0	2.00 ± 1.1	2.2 ± 1.1
Diamond Content (Area %)	89.8 ± 0.4	90.7 ± 0.7	90.9 ± 0.4	89.7 ± 0.3
Binder Content (Area %)	10.2 ± 0.4	9.4 ± 0.7	9.1 ± 0.4	10.4 ± 0.3
Diamond Mean Free Path (MFP) (µm)	6.2 ± 6.9	6.8 ± 7.4	7.3 ± 8.0	6.8 ± 7.7
Co Mean Free Path (MFP) (µm)	0.8 ± 0.6	0.8 ± 0.6	0.8 ± 0.6	0.8 ± 0.6
Diamond Contiguity (%)	53.7 ± 1.5	57.7 ± 2.4	57.9 ± 1.5	56.7 ± 0.9
WC particle size (µm)	0.5 ± 0.4	0.6 ± 0.4	0.5 ± 0.3	0.6 ± 0.4
WC Content (Area %)	3.0 ± 0.3	2.8 ± 0.5	0.6 ± 0.1	2.7 ± 0.6

B – FG-0.5µm fine grain diamond

Sintering of a fine grain 0.5µm (FG-0.5) diamond powder was performed to determine if the carbon enriched coated substrates would reduce grain growth at the interface. Samples were prepared and sintered at 1400°C and 6.8 GPa. It was found that the higher pressure produced better results; this is also the standard conditions used in industry to sinter fine grain PCD. Various capsules were produced containing the different samples for UHPHT sintering, 0, 2, 4 and 6%C coated layers were sintered with a standard substrate for reference.

Two sets of capsules were sintered for the 0 – 2%C samples (cap #3 and #6) and two for the 4 – 6%C samples (cap #4 and #7) with the standard WC-Co substrate as a reference. 0.5µm diamond was used for the PCD layer. Sintering was done at 1400°C and 6.8GPa. The microstructure of the 0 – 6%C enriched substrates using 0.5µm FG diamond samples

are shown in Figures 6-10 – 6-15; the results show that all the samples experienced large AGG of the diamond particles at the substrate to PCD interface. Large plume formation was also evident in some materials (i.e. Figure 6-11c, Figure 6-13c and Figure 6-15c).

Table 6-7 and Table 6-8 give the results of the AGG thickness measurements for the 0-2%C (range between 200 - 750µm) and 4-6%C coatings (range between 200 - 1000 µm) respectively The results show that there is only a slight decrease in the AGG for the 2%C enriched coating compared to the as-received sprayed powders and the standard substrate for both capsule runs. This shows promising results; i.e. Carbon enrichment can potentially decrease AGG of fine grained PCD. Overall the 4 and 6%C samples show a higher amount of AGG than that of the 2%C coatings.

Although sintering conditions for both cap #3,#6 and cap #4,#7 were the same (i.e. 1400°C and 6.8GPa), from the results in the above Table 6-7 and 6-8 and figures 6-11 – 6-15, it follows that there is a high variability in the results. The results from cap #6 were much lower than that of cap #3 for most samples. Similarly with the results of cap #4 and #7. The high variability shows how unstable the fine grained diamond can be, and how sensitive the system is to other parameters (oxygen content, impurities and press conditions such as non-uniform heating distribution in the press, leading to uneven melting fronts during sintering).

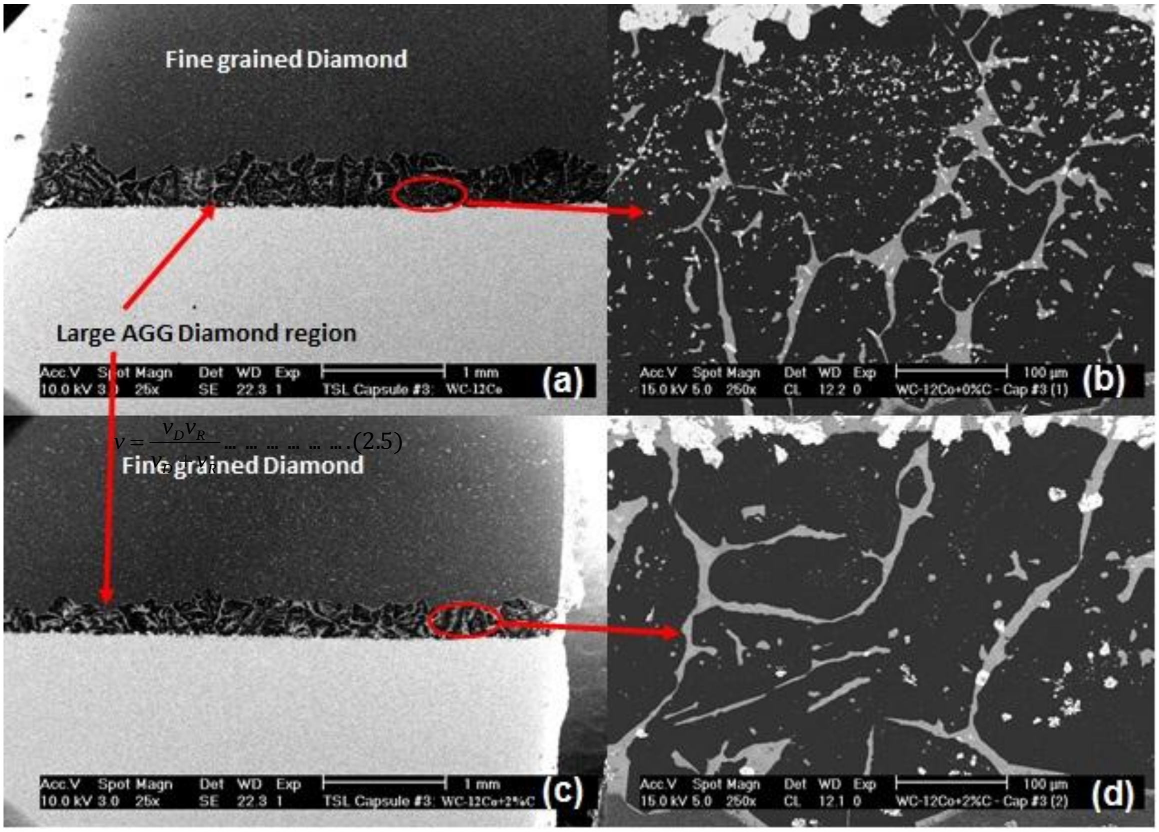

Figure 6-10: SEM-BSI micrographs of the interface of the FG-0.5µm diamond sintered PCD for the WC-12Co samples Cap#3: (a & b) WC-12Co coated layer and (c & d) WC-12Co+2%C coated layer.

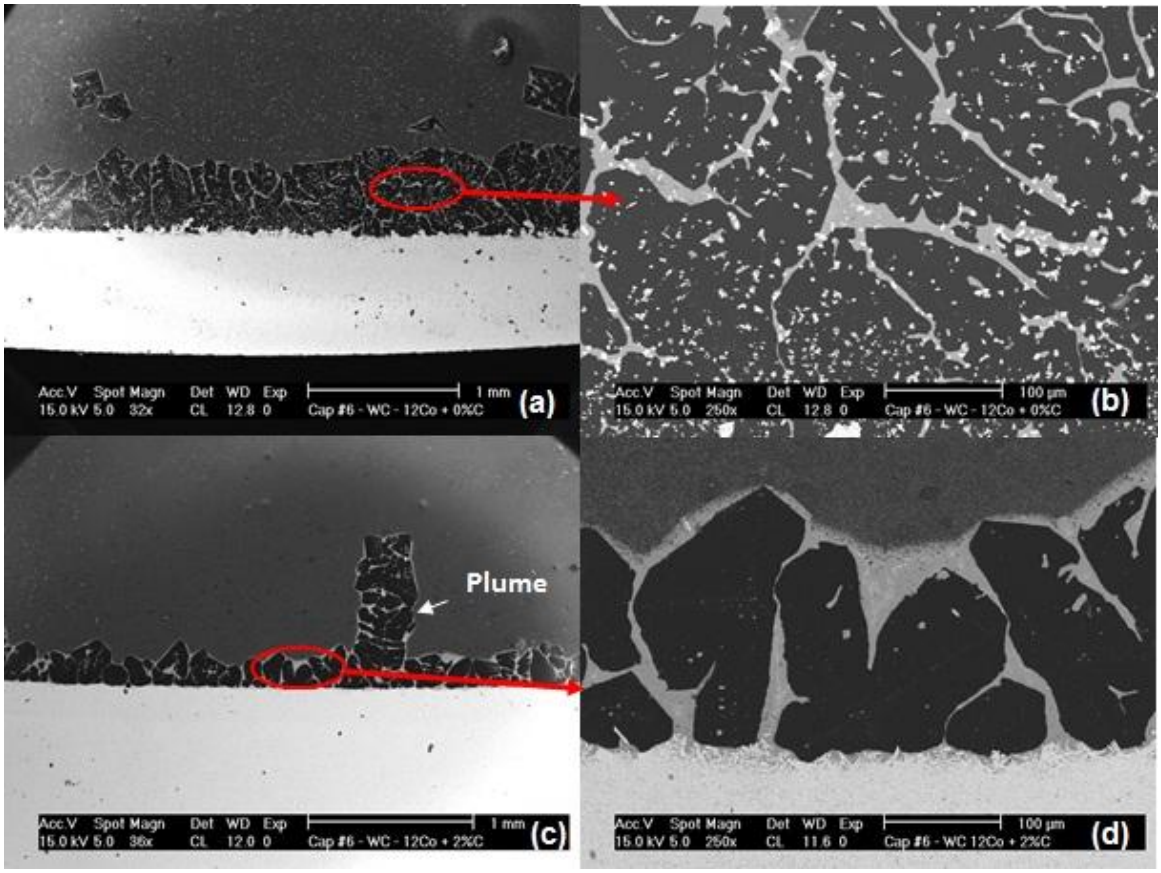

Figure 6-11: SEM-BSI micrographs of the interface of the FG-0.5µm diamond sintered PCD for the WC-12Co samples Cap#6: (a & b) WC-12Co coated layer and (c & d) WC-12Co+2%C coated layer.

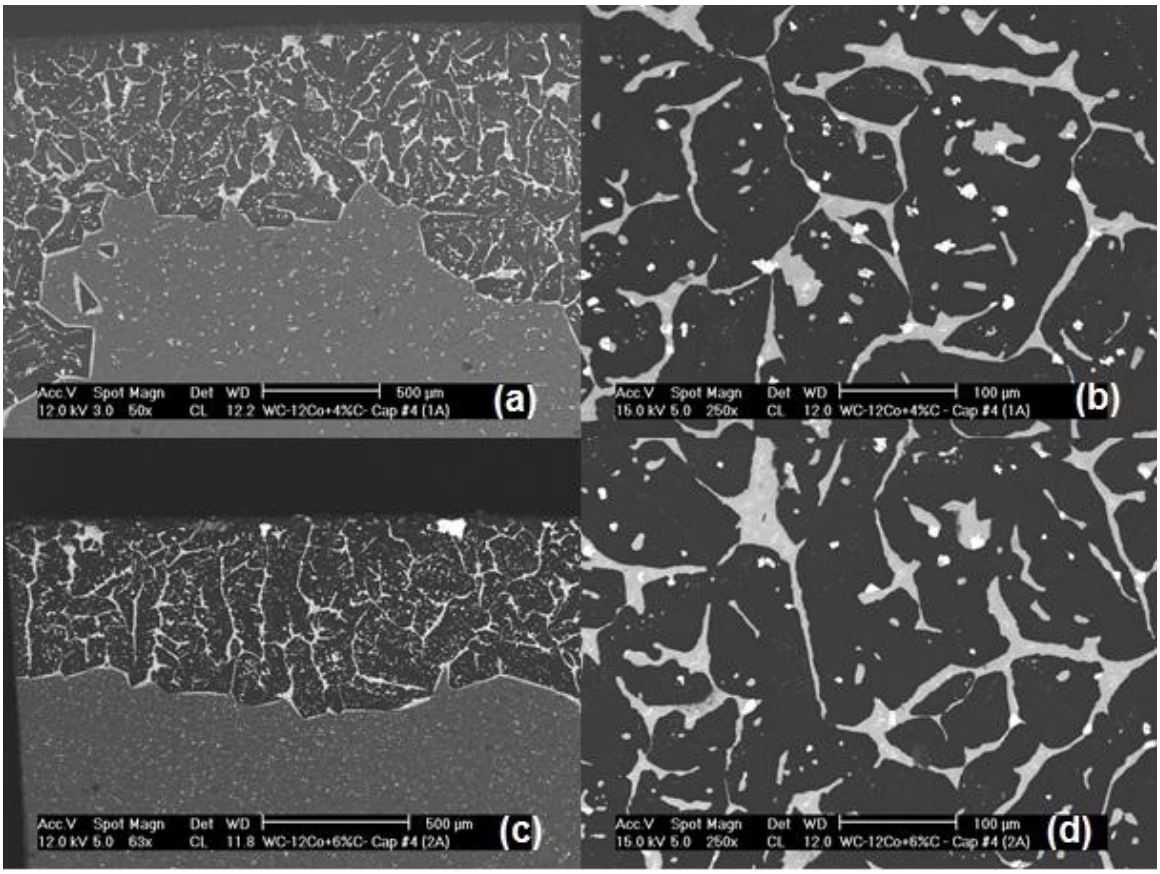

Figure 6-12: SEM-BSI micrographs of the interface of the FG-0.5µm diamond sintered PCD for the WC-12Co samples: (a & b) WC-12Co+4%C coated layer and (c & d) WC-12Co+6%C coated layer.

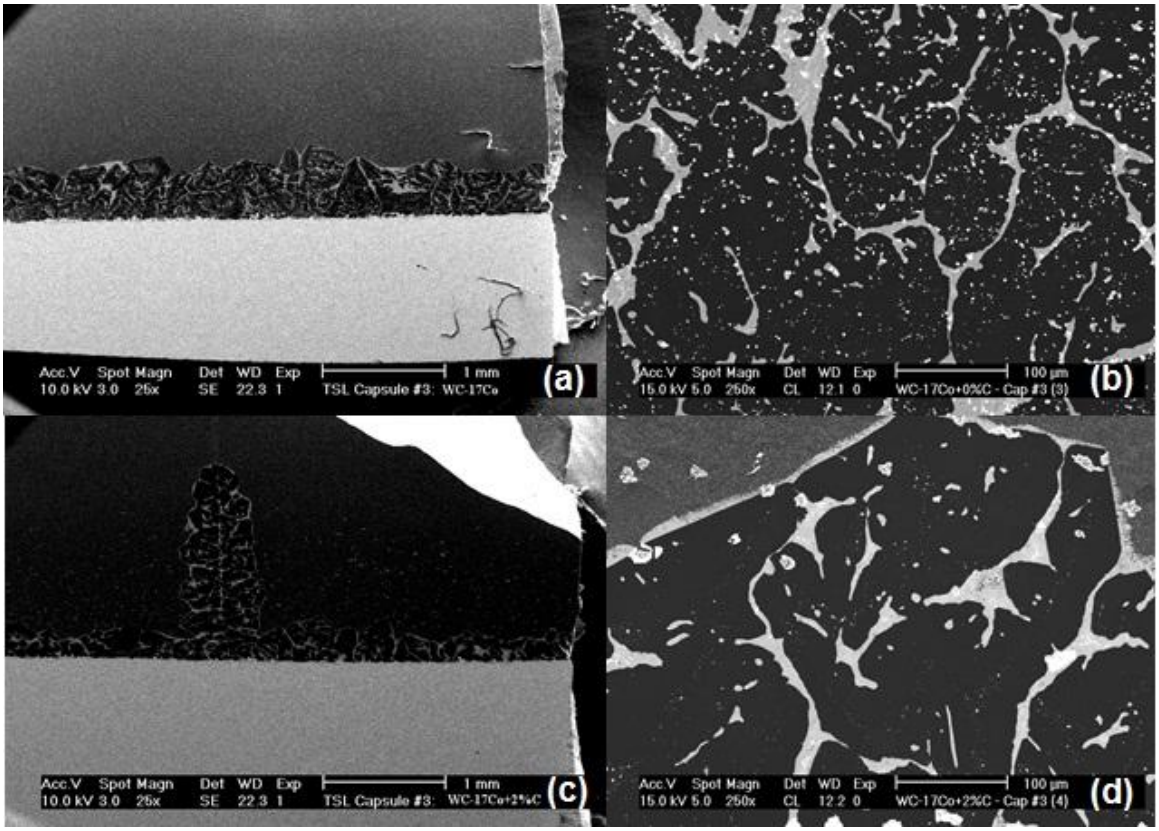

Figure 6-13: SEM micrographs of the interface of the FG-0.5µm diamond sintered PCD for the WC-17Co samples Cap#3: (a & b) WC-17Co coated layer and (c & d) WC-17Co+2%C coated layer (cap#3).

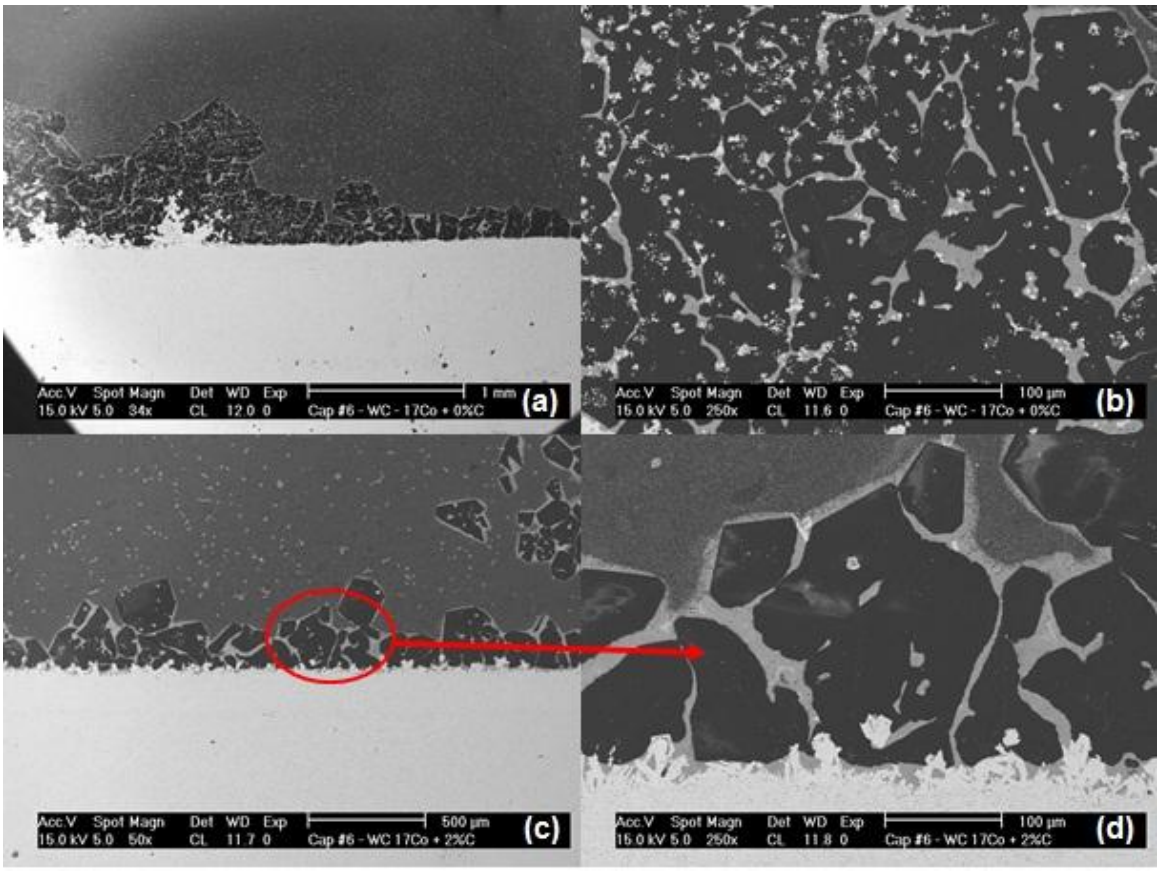

Figure 6-14: SEM-BSI micrographs of the interface of the FG-0.5µm diamond sintered PCD for the WC-17Co samples Cap#6: (a & b) WC-17Co coated layer and (c & d) WC-17Co+2%C coated layer (Cap#6).

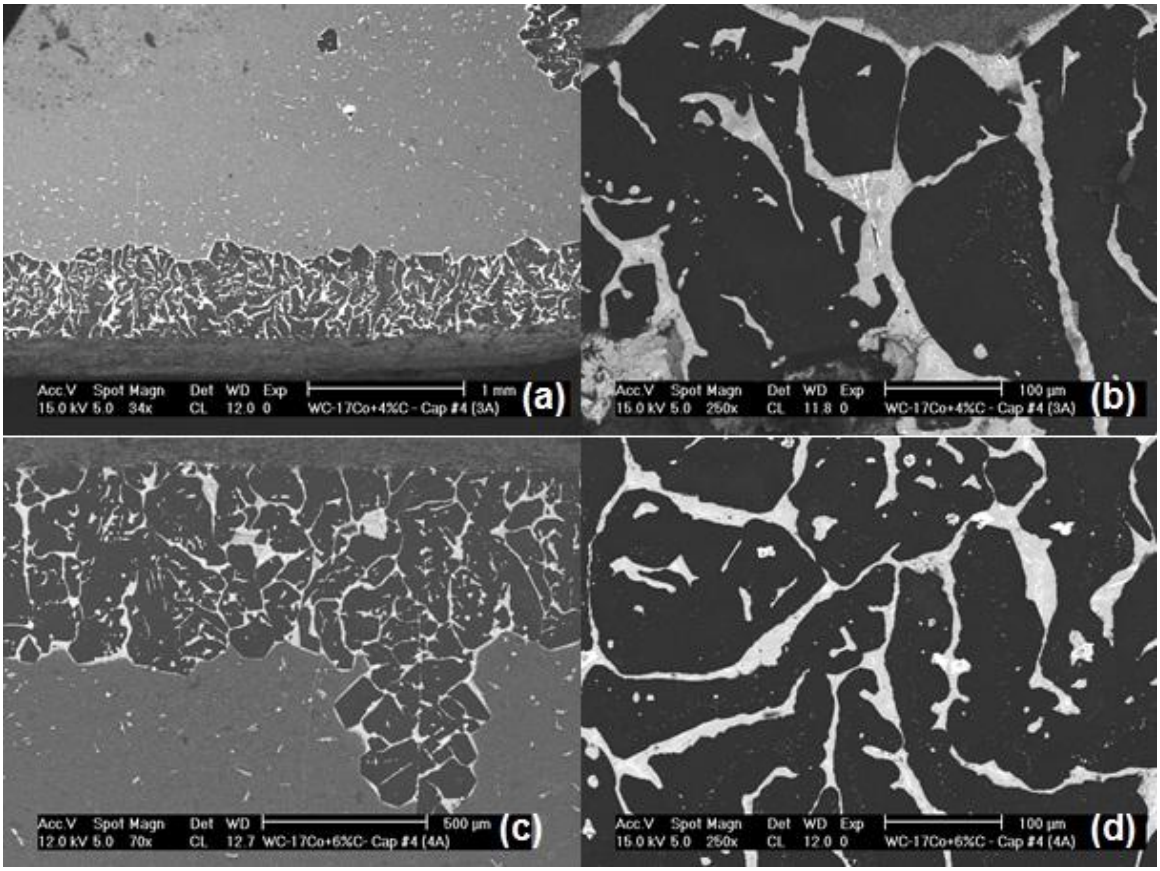

Figure 6-15: SEM-BSI micrographs of the interface of the FG-0.5µm diamond sintered PCD for the WC-17Co samples: (a & b) WC-17Co+4%C coated layer and (c & d) WC-17Co+6%C coated layer (Cap#4).

Table 6-7: Thickness of the AGG region for the 0 – 2%C coatings in Cap #3 and #6 using FG-0.5µm diamond.

Material	AGG layer thickness (µm)		Plume size (µm)		Total AGG layer thickness (µm)	
	Cap #3	Cap #6	Cap #3	Cap #6	Cap #3	Cap #6
WC-12Co	434	518	1978	-	590	518
WC-12Co+2%C	328	202	-	1907	328	389
WC-17Co	717	570	-	1475	717	751
WC-17Co+2%C	281	489	1966	-	385	489
Std substrate	387	238	1342	-	457	238

Table 6-8: Thickness of the AGG region for the 4 - 6%C coatings in Cap #4 and #7 using FG-0.5µm diamond.

Material	AGG layer thickness (µm)		Plume size (µm)		Total AGG layer thickness (µm)	
	Cap #4	Cap #7	Cap #4	Cap #7	Cap #4	Cap #7
WC-12Co+4%C	969	577	2148	-	1286	577
WC-12Co+6%C	622	238	-	-	622	238
WC-17Co+4%C	-	-	-	-	-	-
WC-17Co+6%C	606	366	894	-	645	366
Std substrate A	1002	309	1057	1205	1015	393
Std substrate B	-	427	-	-	-	427

C – FG-6µm fine grain diamond

As described above in Section 6.2.1, a fine grained (FG-6) diamond powder was used to determine the effect the carbon content of the sprayed coatings has on Co pool formation at the interface. The 0 – 2%C and 4 – 6%C samples from the WC-12Co and WC-17Co powders were sintered in cap#8 & 9 respectively with each capsule containing a standard WC-13Co substrate for comparison. The samples were sintered at the same conditions as the fine grained (FG0.5) samples: 1400°C and 6.8GPa. Figures 6-16 and 6-17 show the microstructure of the 0 – 2%C and 4 – 6%C samples respectively. No AGG is evident as predicted. The Co pool size of the sintered FG-6µm PCD samples is given in Table 6-9. The results show the Co pool thickness was between 21 - 29µm. The Carbon enriched samples had a larger Co pool thickness than the as-received powder coatings and the standard substrate. This would suggest that there would be a larger grain growth for the Carbon enriched samples. From the image analysis results for both cap#8 and #9 given in Table 6-10 and 6-11, the diamond particle size ranged between 3.8 –

4.4µm with a binder content of 11.4 – 12.9%. The results indicate that the diamond particles had not grown compared to that of the starting powder.

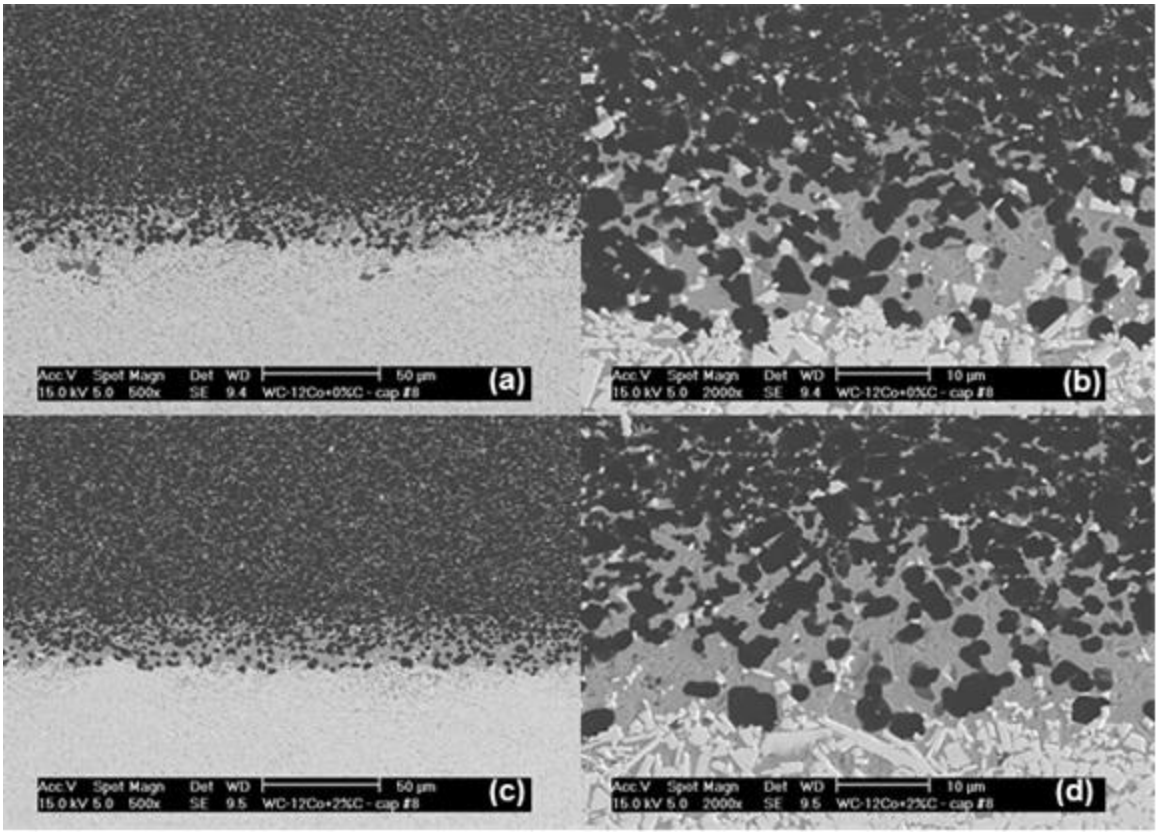

Figure 6-16: SEM-BSI micrographs of the interface of the FG-6µm diamond sintered PCD for the WC-12Co + 0 – 2%C enriched WC-Co substrate from Cap #8.

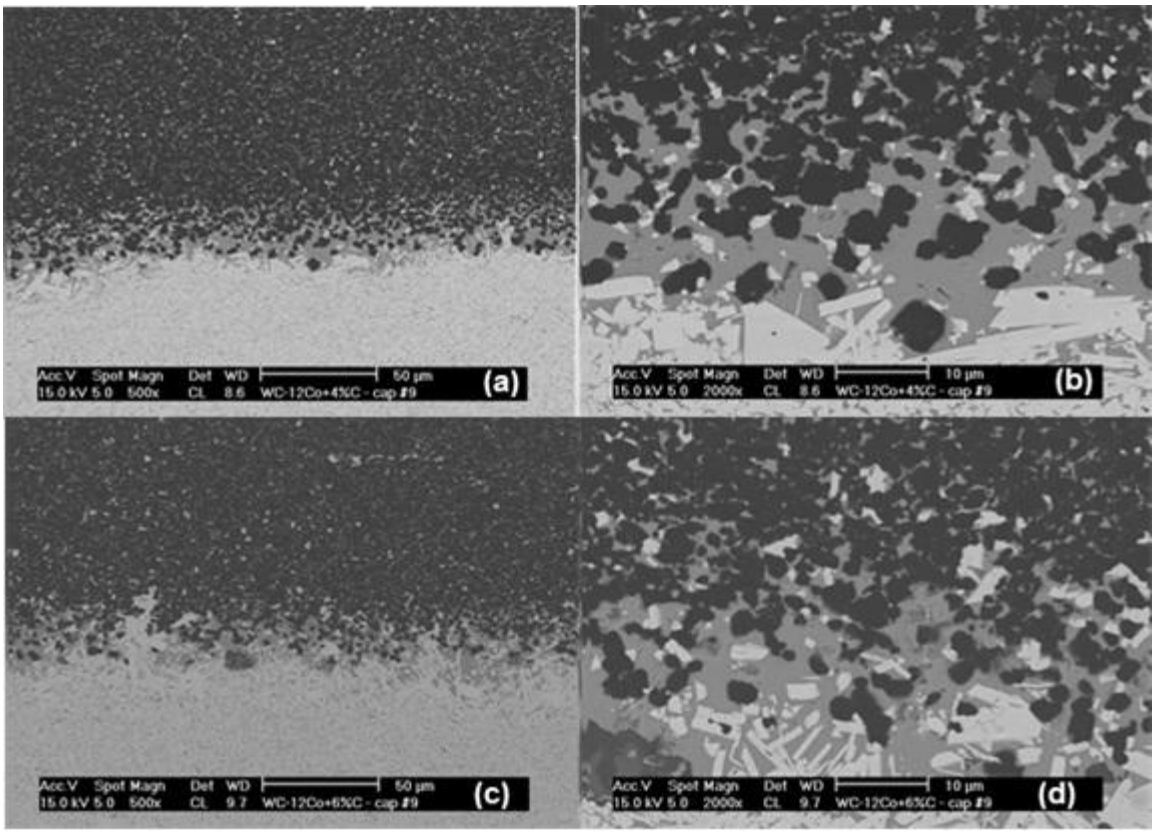

Figure 6-17: SEM-BSI micrographs of the interface of the FG-6µm diamond sintered PCD for the WC-12Co+ 4 - 6%C enriched WC-Co substrate from Cap #9.

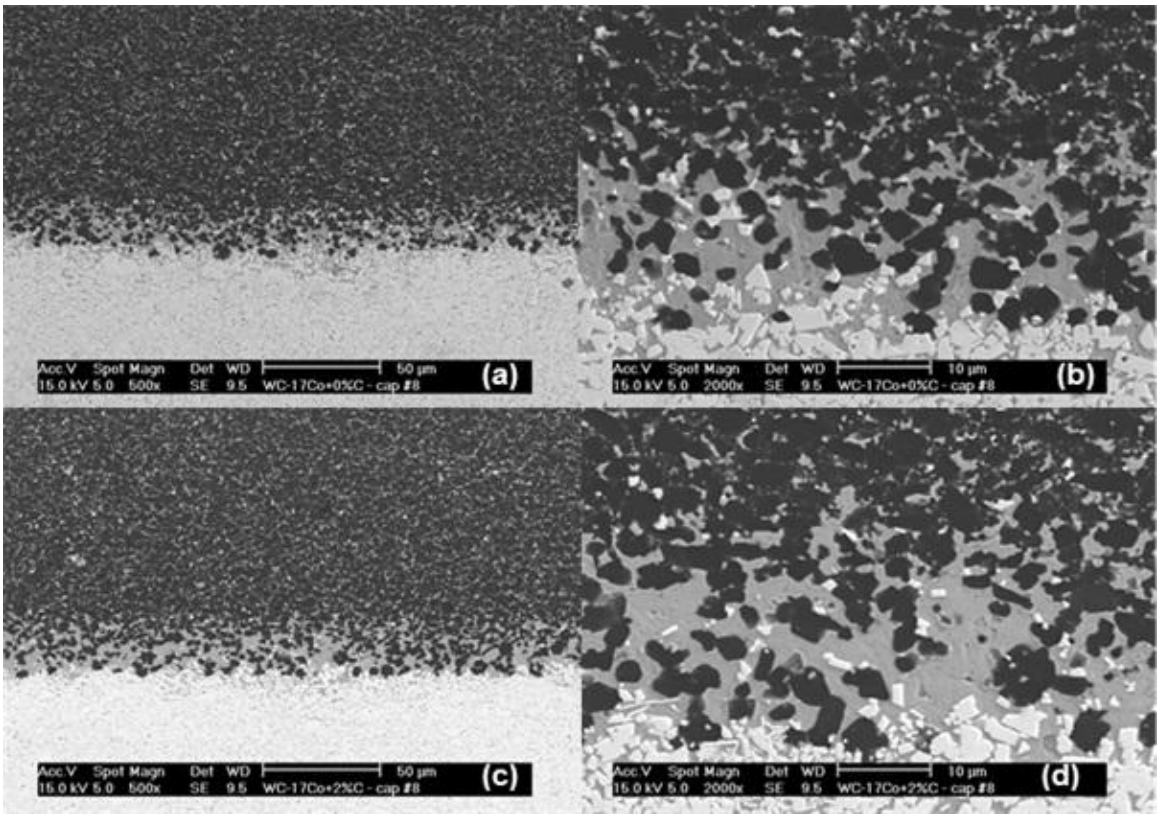

Figure 6-18: SEM-BSI micrographs of the interface of the FG-6µm diamond sintered PCD for the WC-17Co + 0 – 2%C enriched WC-Co substrate from Cap #8.

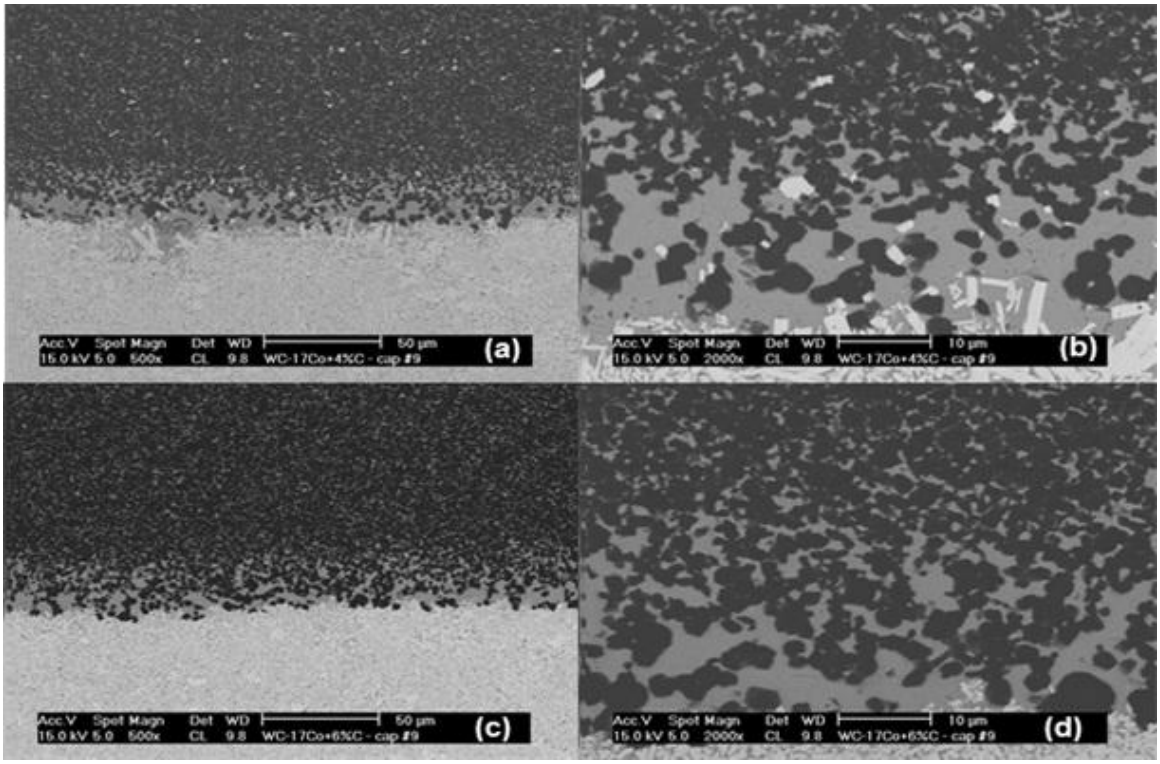

Figure 6-19: SEM-BSI micrographs of the interface of the FG-6µm diamond sintered PCD for the WC-17Co+ 4 - 6%C enriched WC-Co substrate from Cap #9.

Table 6-9: Cobalt pool size of the FG-6µm diamond PCD samples in Cap #8 and #9.

Material	Co pool size (µm)
Cap #8: WC-12Co + 0%C	22.3±2.0
Cap #8: WC-12Co + 2%C	26.4±1.4
Cap #8: WC-17Co + 0%C	23.8±1.9
Cap #8: WC-17Co + 2%C	25.6±1.6
Cap #8: WC-13Co	21.2±2.4
Cap #9: WC-12Co + 4%C	26.1±1.4
Cap #9: WC-12Co + 6%C	22.5±3.1
Cap #9: WC-17Co + 4%C	26.0±3.1
Cap #9: WC-17Co + 6%C	27.8±1.7
Cap #9: WC-13Co	28.4±2.0

Table 6-10: Image Analysis results of the FG-6µm diamond PCD samples from Cap #8 TSL coatings.

Property	WC-12Co	WC-12Co+2%C	WC-17Co	WC-17Co+2%C
Diamond particle size (µm)	4.4 ± 1.3	4.2 ± 1.2	4.2 ± 1.2	4.2 ± 1.2
Co pool size (µm)	1.4 ± 0.8	1.4 ± 0.8	1.3 ± 0.6	1.3 ± 0.7
Diamond Content (Area %)	88.1 ± 0.4	87.6 ± 0.6	87.8 ± 0.5	87.1 ± 0.5
Binder Content (Area %)	11.9 ± 0.4	12.5 ± 0.6	12.2 ± 0.5	12.9 ± 0.5
Diamond Mean Free Path (MFP) (µm)	3.8 ± 3.8	3.4 ± 3.4	3.4 ± 3.4	3.2 ± 3.2
Co Mean Free Path (MFP) (µm)	0.5 ± 0.5	0.5 ± 0.4	0.5 ± 0.4	0.5 ± 0.4
Diamond Contiguity (%)	61.5 ± 1.6	58.4 ± 1.5	58.7 ± 1.4	55.5 ± 2.0
WC particle size (µm)	0.4 ± 0.3	0.2 ± 0.2	0.3 ± 0.2	0.3 ± 0.2
WC Content (Area %)	2.4 ± 0.9	1.2 ± 0.1	2.8 ± 0.4	3.0 ± 0.3

Table 6-11: Image Analysis results of the FG-6µm diamond PCD samples from Cap# 9 TSL coatings.

Property	WC-12Co	WC-12Co+2%C	WC-17Co	WC-17Co+2%C
Diamond particle size (µm)	4.3 ± 1.2	3.9 ± 1.1	3.8 ± 1.2	3.8 ± 1.3
Co pool size (µm)	1.4 ± 0.8	1.4 ± 0.8	1.2 ± 0.6	1.3 ± 0.7
Diamond Content (Area %)	88.6 ± 0.7	88.6 ± 0.4	87.5 ± 0.5	87.3 ± 0.4
Binder Content (Area %)	11.4 ± 0.7	11.4 ± 0.4	12.5 ± 0.5	12.7 ± 0.4
Diamond Mean Free Path (MFP) (µm)	3.5 ± 3.6	3.4 ± 3.4	3.2 ± 3.1	3.1 ± 3.0
Co Mean Free Path (MFP) (µm)	0.5 ± 0.4	0.5 ± 0.4	0.5 ± 0.4	0.5 ± 0.4
Diamond Contiguity (%)	60.9 ± 1.5	61.9 ± 1.7	58.9 ± 1.4	60.0 ± 1.4
WC particle size (µm)	0.4 ± 0.4	0.7 ± 0.5	0.2 ± 0.1	0.3 ± 0.2
WC Content (Area %)	1.3 ± 0.5	1.5 ± 0.4	0.8 ± 0.2	1.0 ± 0.3

6.2.2.2. Diamond/Graphite Enhanced Carbide Substrates

The graphitized-diamond enhanced carbide (GDEC) and diamond enhanced carbide (DEC) substrates used at Element Six (Pty) Ltd, South Africa and described in Chapter 3.3

were used to reduce AGG of fine grain PCD. The diamond/graphitized diamond in the substrate interlayer is analogous to a carbon enriched thermally sprayed coating on a WC-Co substrate and acts as the source of carbon to prevent/suppress Ostwald ripening in fine grain PCD. This method of carbon enriching the WC-Co substrate was used as it provided a more manageable method of determining the carbon content in the substrate, as this was predetermined during substrate production.

Four capsules were sintered using the GDEC/DEC substrates. These include cap #10 - #13, outlined in Section 6.2, in Table 6-2. The graphitized-diamond enhanced carbide (GDEC) substrate contained a graphitized diamond content of 10 vol.%, thickness of the substrates ranged between 0.1mm – 6mm (referred to as interlayers) and a full substrate thickness of 12.5 mm. Samples sintered were in cap #10, #11, #12 and #13. The DEC substrates had compositions of diamond powder of 5, 10 and 15 vol.%. The thickness of the DEC interlayer was about 2.5 mm. Samples sintered were in cap #11 and #12. Diamond powders used were FG-0.5µm and FG-6µm. This was to determine the effect of excess carbon content on the grain growth of the diamond and Co pool formation at the interface.

A – FG-0.5µm Fine grain diamond

GDEC interlayer

A 0.5µm diamond powder was sintered onto the GDEC interlayers with a standard WC-Co substrate backing at standard sintering conditions of 1400°C and 6.8 GPa. An initial sintering run (cap #10) was done using the 10 vol.% GDEC substrate interlayer of thickness 0.1, 0.5, 1 and 2mm and a standard WC-13Co substrate as a reference. The microstructures of the 0.5µm PCD graphite enhanced carbide (GDEC) layers are shown

in Figures 6-20 – 6-21, while the results obtained for the reference standard WC-Co substrate sintered in the same capsule as the GDEC layers is shown in Figure 6-22. As can be seen from the microstructures (Figures 6-20 – 6-22), all the samples experienced AGG. The thickness of the AGG regions for each layer thickness was measured and can be seen in Table 6-12 (ranging between 430 - 1488µm). These results are very large and unexpected. Another capsule (cap #11) was sintered using a 10vol.% GDEC interlayer of 2.5mm and a full 12.5mm substrate at the same standard sintering conditions (1400°C and 6.8GPa), Figure 6-23 shows the microstructure for these two samples. The results show that the 2.5 mm thick 10vol.% GDEC interlayer showed a slight reduction in diamond grain growth (i.e. AGG located locally along the interface), 10-15% of the interface surface area resulted in no AGG diamond. The full 12.5mm GDEC substrate showed no evidence of large AGG at the interface. This was a very promising result, suggesting that there was a sufficient amount of excess carbon in the infiltrating Co metal to allow saturation and thus suppress the conditions for Ostwald ripening, thus proving the theory that excess carbon in the substrate can potentially eliminated AGG in fine 0.5µm PCD. The Co pooling at the interface was very prominent and the thickness was measured to be about 60 ± 5 µm. The diamond grains at the interface of the full GDEC substrate consisted of a range of particle sizes between 0.5 - 10µm, most of the grains were small below 5µm. There were a few grains at the interface which had grown to 5-10µm. In the region of these larger grains, there was clear evidence that there are no or very few smaller diamond particles surrounding the larger particles (green oval in Figure 6-23d). These grains are much larger than 0.5µm and have undergone normal grain growth.

A study of the microstructure of the 10 vol.% GDEC layer after sintering as shown in Figure 6-24, revealed that there was a conversion of the graphite to diamond during sintering and that diamond is still evident in the layer after sintering. The converted diamond particles appear to be in the range of 2 – 20µm. The diamond particles were

clustered together which can be called polycrystalline diamond clusters (PCDC). These clusters consisted of interlocked superhard diamond particles closely surrounded by WC particles. The clusters were irregular in shape (i.e. did not form faceted diamond particles). This helped in preventing pullout of the diamond particles from the substrate. Cobalt metal particles can also be trapped inside or around these clusters, seen by the grey phase present in the diamond clusters.

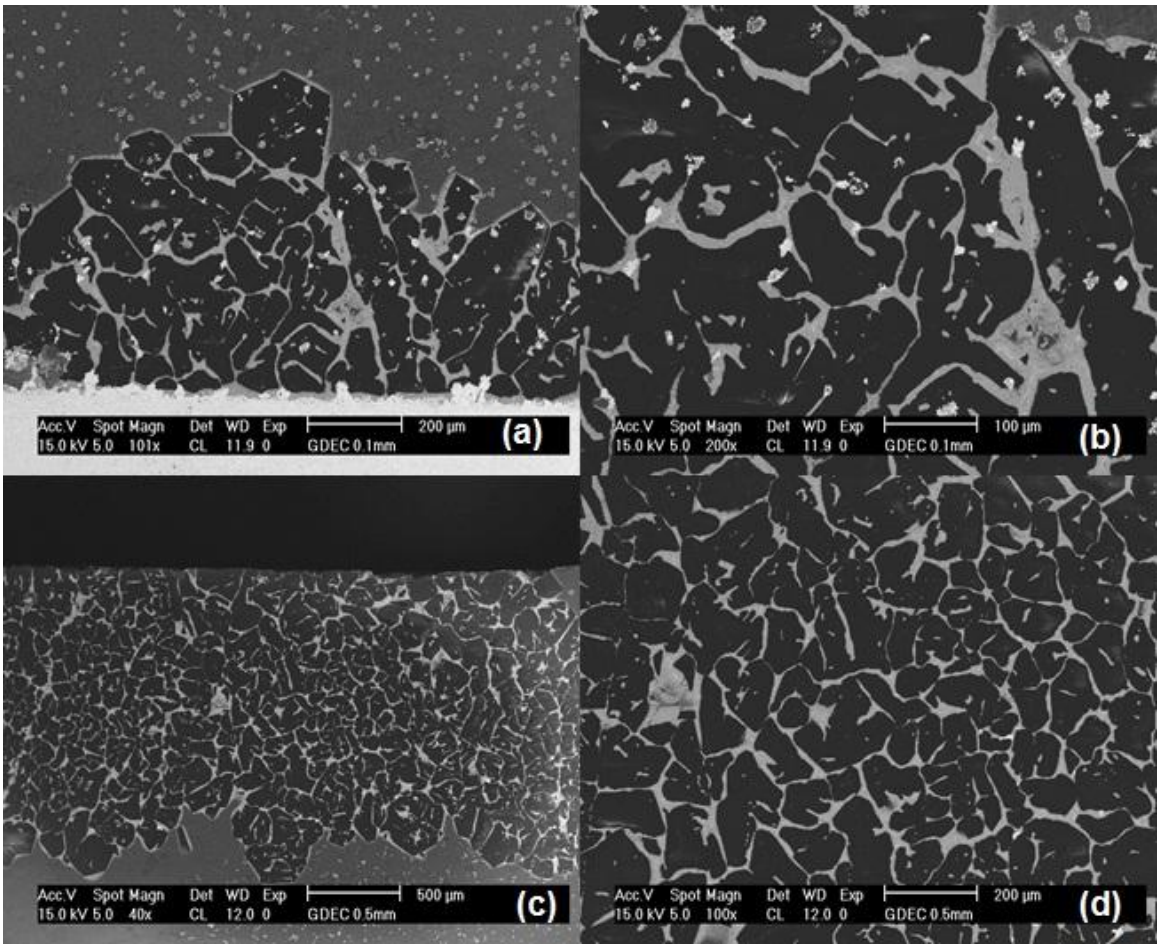

Figure 6-20: SEM-BSI micrographs of the sintered FG-0.5µm diamond PCD of the graphite enhanced carbide (GDEC) samples; (a & b) 0.1 mm layer and (c & d) 0.5 mm layer.

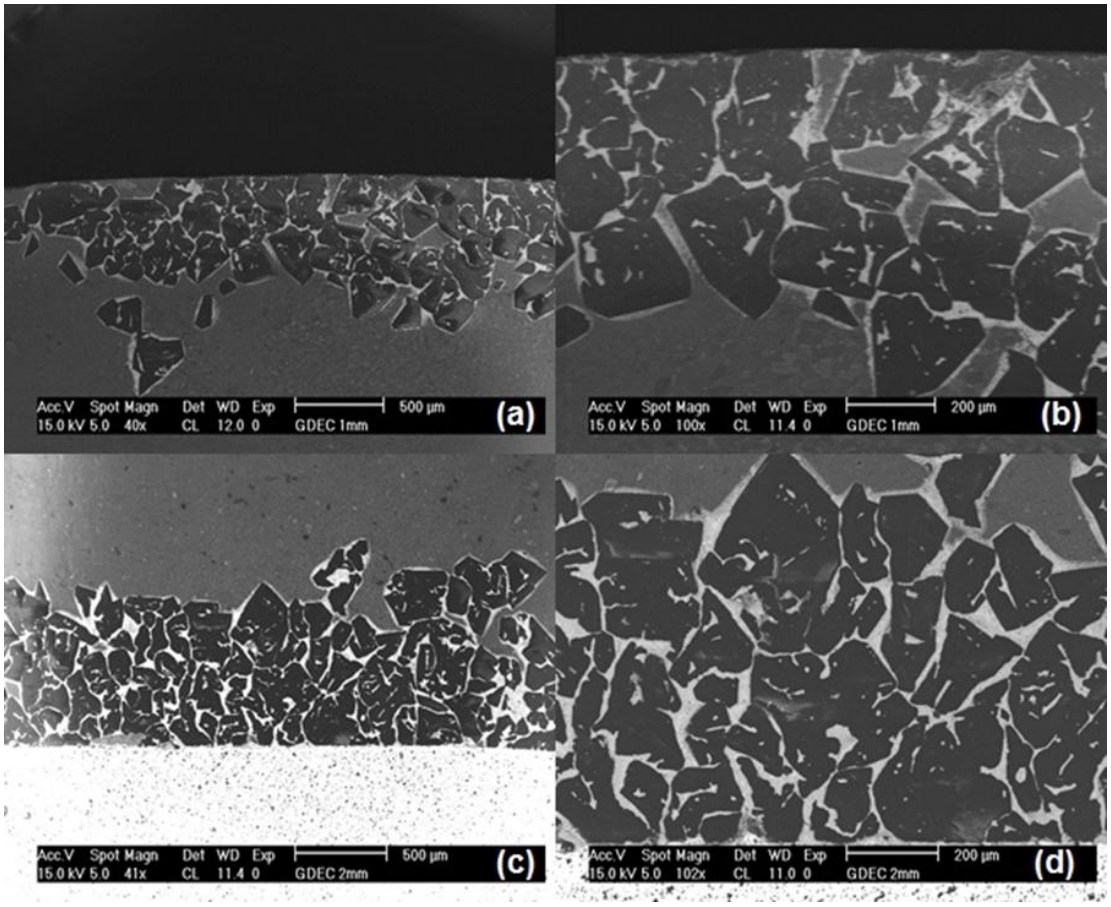

Figure 6-21: SEM-BSI micrographs of the sintered FG 0.5µm diamond PCD of the graphite enhanced carbide (GDEC) samples; (a & b) 1 mm layer and (c & d) 2 mm layer.

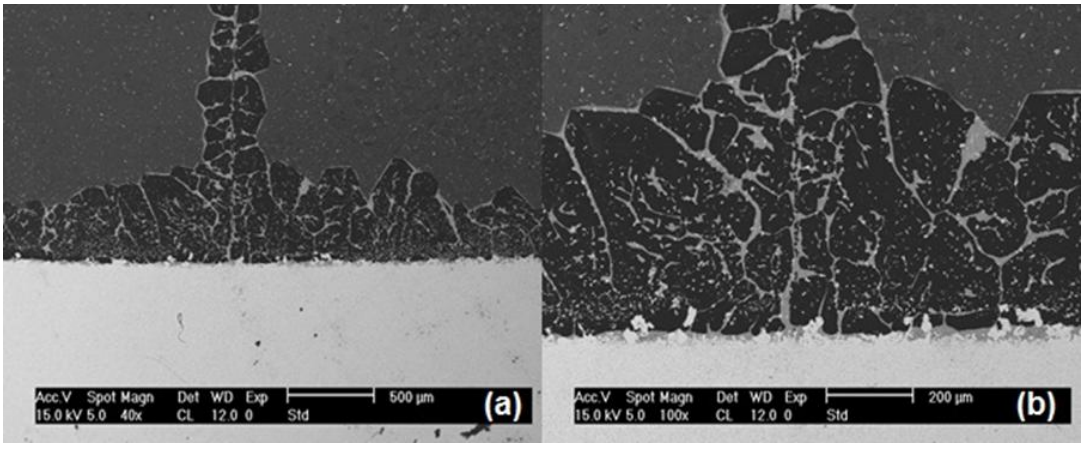

Figure 6-22: SEM-BSI micrographs of the reference standard WC-Co sample sintered with the graphite enhanced carbide with FG-0.5µm diamond.

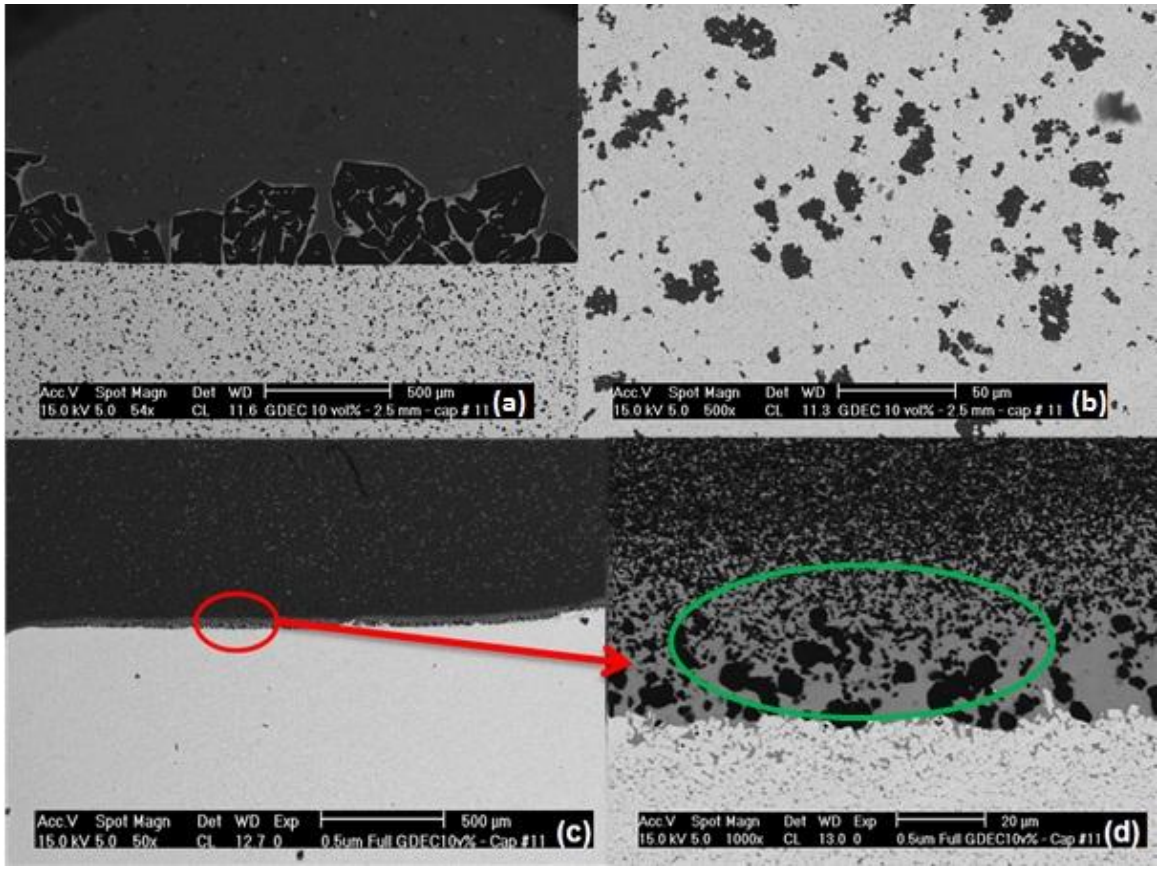

Figure 6-23: SEM-BSI micrographs of the microstructure of the sintered FG-0.5µm diamond PCD graphite-diamond enhanced carbide (GDEC) samples; (a & b) 2 mm 10vol.%GDEC (cap#11) and (c & d) full 12mm 10vol.% GDEC substrate (cap#11).

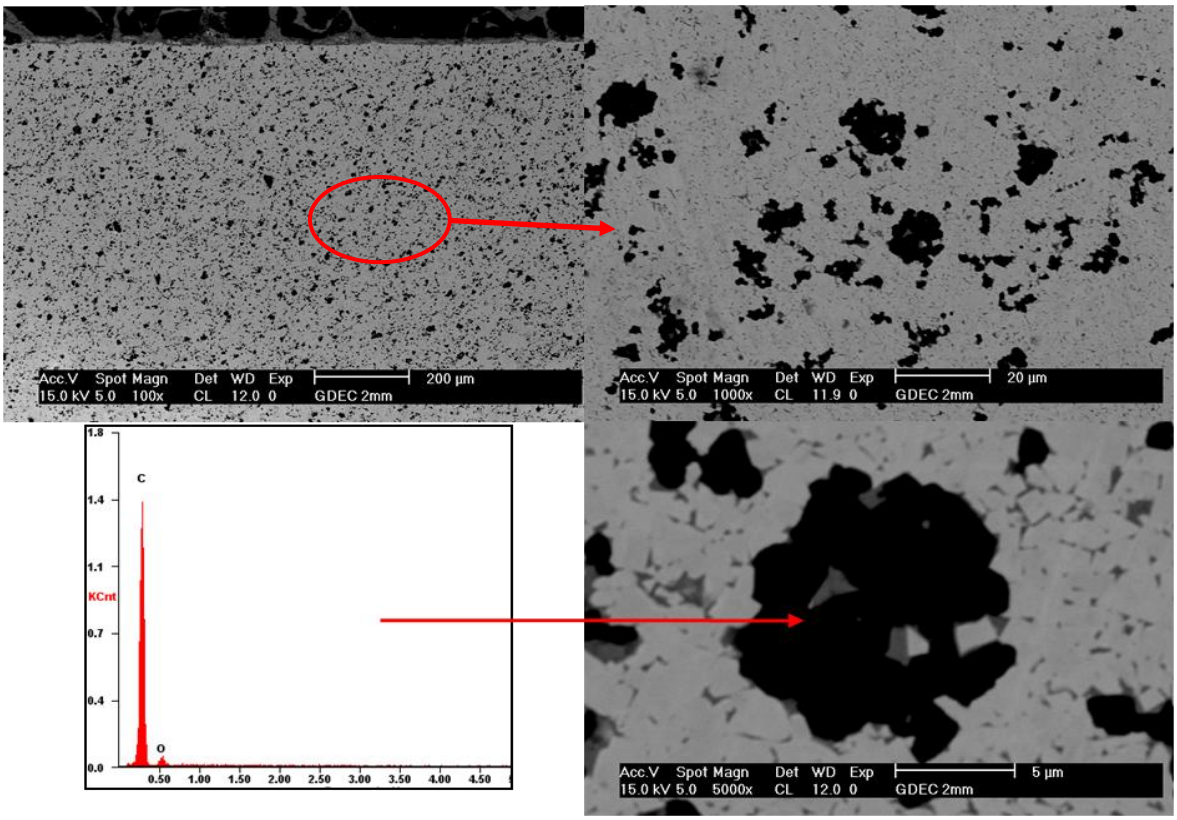

Figure 6-24: SEM-BSI micrographs of the microstructure of the graphite-diamond enhanced carbide (GDEC) 2mm layer after sintering, EDX analysis shows clusters are carbon based (i.e. diamond).

Table 6-12: Thickness of the AGG region of the graphite-diamond enhanced carbide (GDEC) samples (Cap#10 and #11).

Material	AGG thickness (µm)	Plume thickness (µm)	Total AGG thickness (µm)
Cap#10 - 0.1 mm GDEC	489.8	-	489.8
Cap#10 - 0.5 mm GDEC	1488.3	-	1488.3
Cap#10 – 1.0 mm GDEC	575.5	-	575.5
Cap#10 – 2.0 mm GDEC	955.6	-	955.6
Std WC-Co substrate	429.4	705.7	465.7
Cap#11 – 2.5 mm GDEC	288.3	-	288.3
Cap#11 – full 12mm GDEC	**No AGG**	-	**No AGG**
Cap#11 – 2.5 mm 5wt.% DEC	566.5	-	566.5
Cap#11 – 2.5 mm 10wt.% DEC	233.3	-	233.3
Cap#11 – 2.5 mm 15wt.% DEC	376.8	-	376.8

Following the promising results of the full 10vol.% GDEC substrate, it was decided to try to determine the minimum thickness of the GDEC interlayer which would result in no AGG of the 0.5μm diamond. With this in mind, Cap #13 was prepared using a the FG0.5μm diamond and the 10vol.% GDEC interlayer with varying thicknesses of 2, 3, 4, 5 and 6 mm. The samples were sintered using the standard sintering conditions of 1400°C and 6.8GPa. The microstructure of these samples is shown in Figures 6-25 and 6-26. All materials sintered showed AGG at the interface. The thicknesses of the AGG regions were measured and the result is given in Table 6-13.

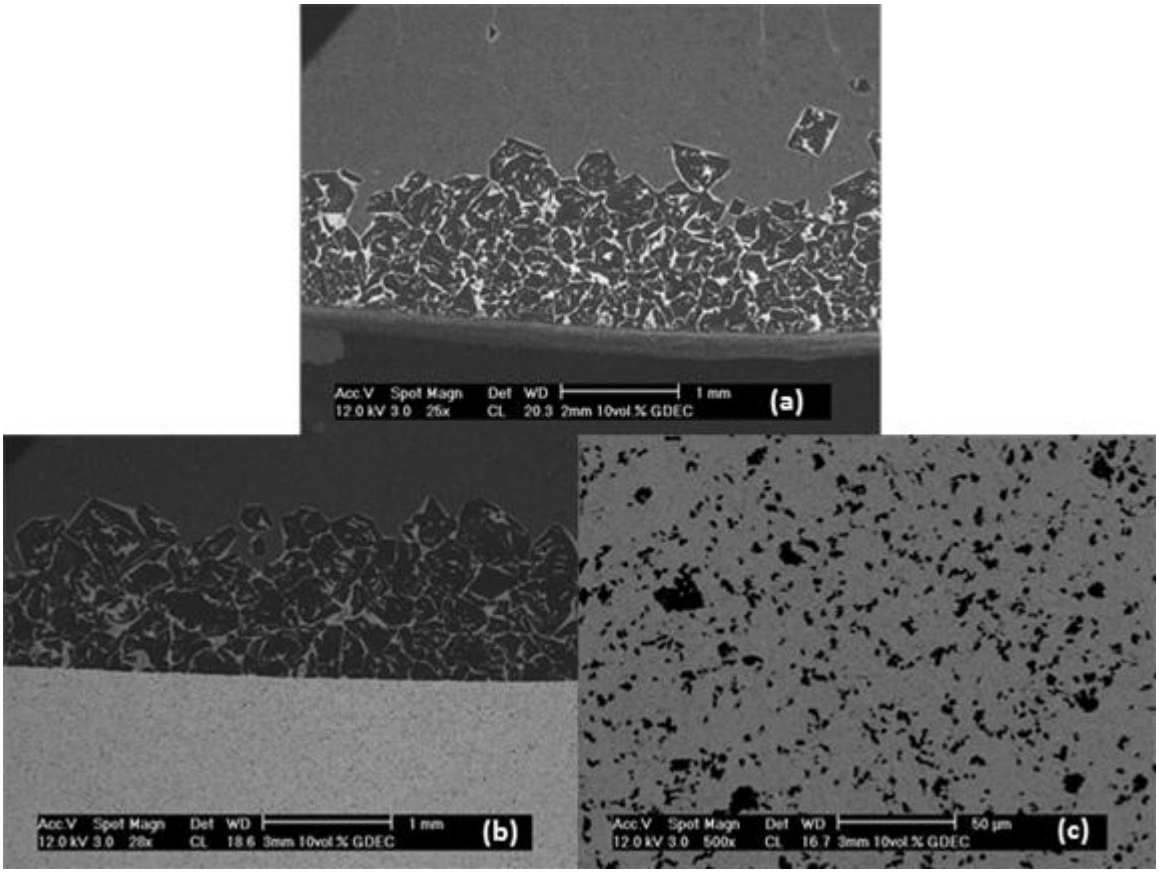

Figure 6-25: SEM-BSI micrographs of the microstructure of the sintered 0.5μm PCD graphite-diamond enhanced carbide (GDEC) samples; (a) 2 mm 10vol.% GDEC (cap#13); (b) 3mm 10vol.% GDEC (cap#13) and (c) substrate of the 3mm 10vol.% GDEC layer, showing clusters of diamond particles.

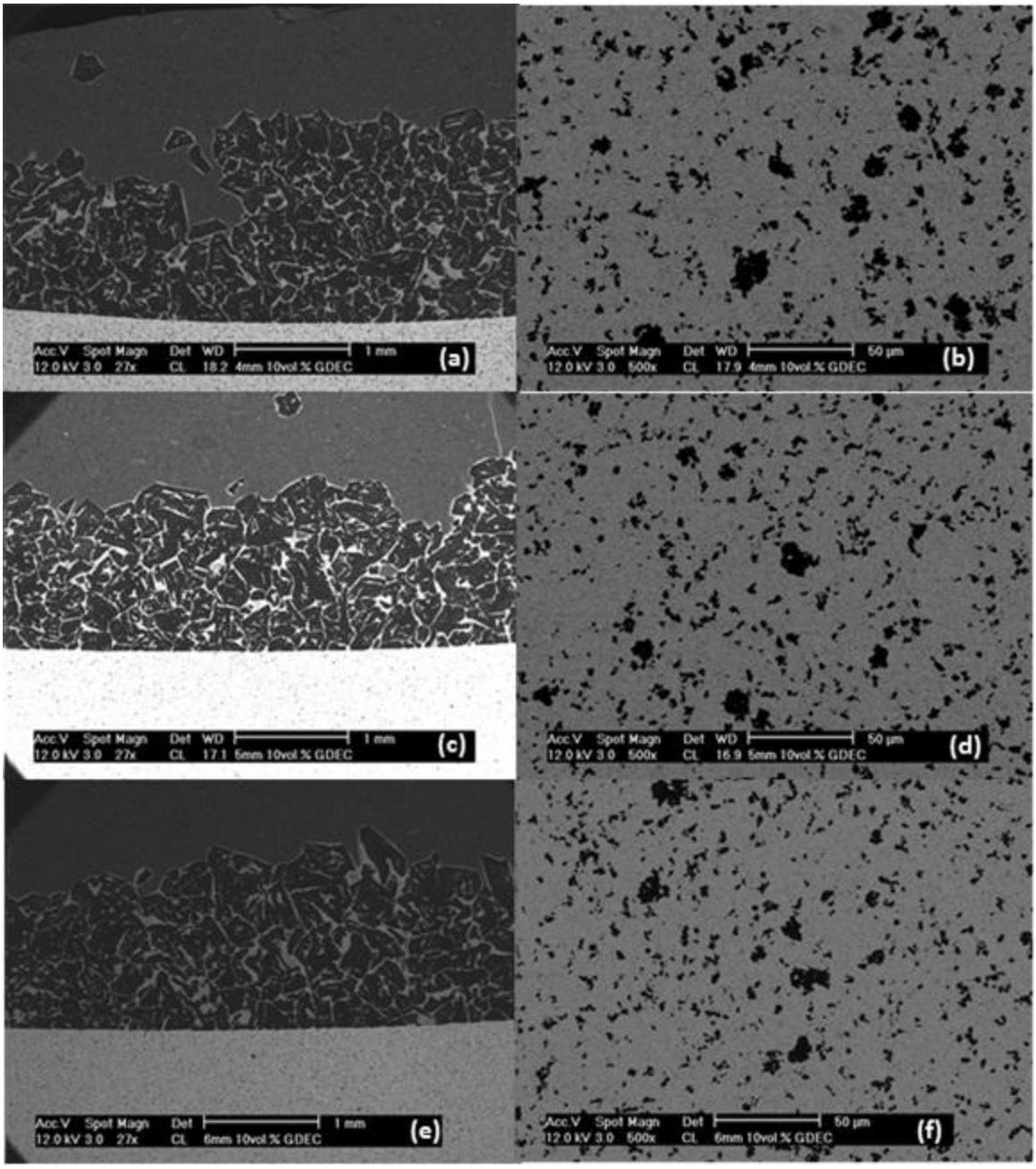

Figure 6-26: SEM-BSI micrographs of the microstructure of the sintered 0.5µm PCD graphite-diamond enhanced carbide (GDEC) samples; (a & b) 4 mm 10vol.% GDEC (cap#15); (c & d) 5mm 10vol.% GDEC (cap #15) and (e & f) 6mm 10vol.% GDEC (cap #15). Images b, d and f show the microstructure of the substrates for each material respectively.

Table 6-13: Results of AGG the graphite-diamond enhanced carbide (GDEC) samples for Cap#13.

Material	AGG thickness (µm)	Total AGG thickness (µm)
Cap#13 – 2mm 10vol.% GDEC	1027.4	1027.4
Cap#13 – 3mm 10vol.% GDEC	1231.1	1231.1
Cap#13 – 4mm 10vol.% GDEC	1383.7	1383.7
Cap#13 – 5mm 10vol.% GDEC	1471.5	1471.5
Cap#13 – 6mm 10vol.% GDEC	1273.1	1273.1

DEC inter-layers

Samples were sintered in capsule (cap #11) with the three variations of DEC compositions with a 0.5 µm diamond layer. Figure 6-27 shows the micrographs of the sintered 0.5 µm PCD on DEC substrates. The results produced were unsatisfactory as evidence of large AGG diamond grains were found throughout all the samples. The AGG region was in the region of 233 – 567µm (Table 6-12). No trend was observed with increasing diamond content. The substrates showed evidence of residual diamond particles. These increased with increasing initial diamond concentration and they were 2 - 30µm in size.

B - FG-6µm fine grain diamond

A capsule (cap #12) was sintered using the FG-6µm diamond powder with the 2.5mm and full 12.5mm 10vol.% GDEC substrates and the 2mm DEC inter-layers with varying diamond contents of 5, 10 and 15%. The results of are shown in Figures 6-28 and 6-29 for the GDEC and DEC inter-layers respectively. The microstructure of the sintered GDEC samples showed that there was no abnormal grain growth in any of the samples as

expected. The full 12.5mm GDEC substrate showed a well sintered material with no Co pooling at the interface, while the 2.5mm 10vol.% GDEC sample had only a small Co pool of approximately 10µm. Acicular grain growth of the WC particles was also evident in Figure 6-28b, while no acicular WC particles were found in the full 12.5 mm GDEC substrate. Large diamond particle clusters could be seen in the substrate near the interface. These were formed by the reconversion of the graphitized-diamond to diamond clusters during sintering. Table 6-14 shows the results of the image analysis done on the PCD layer near the interface of the GDEC samples from cap#12; the results showed similar diamond particle size, Co pool size and binder contents of approximately 4.2µm, 1.3µm and 13%.

The microstructure of the sintered DEC samples shown in Figure 6-29 showed a similar trend to the GDEC substrates (i.e. no AGG and no Co pooling evident at the interface). Some residual diamond particles could be seen in the substrate and connected to the diamond layer. Image analysis of the bulk PCD near the interface shown in Table 6-15 revealed that the diamond particle size, Co pool size and binder content was very similar (4.0, 13-1.6 and 56% respectively).

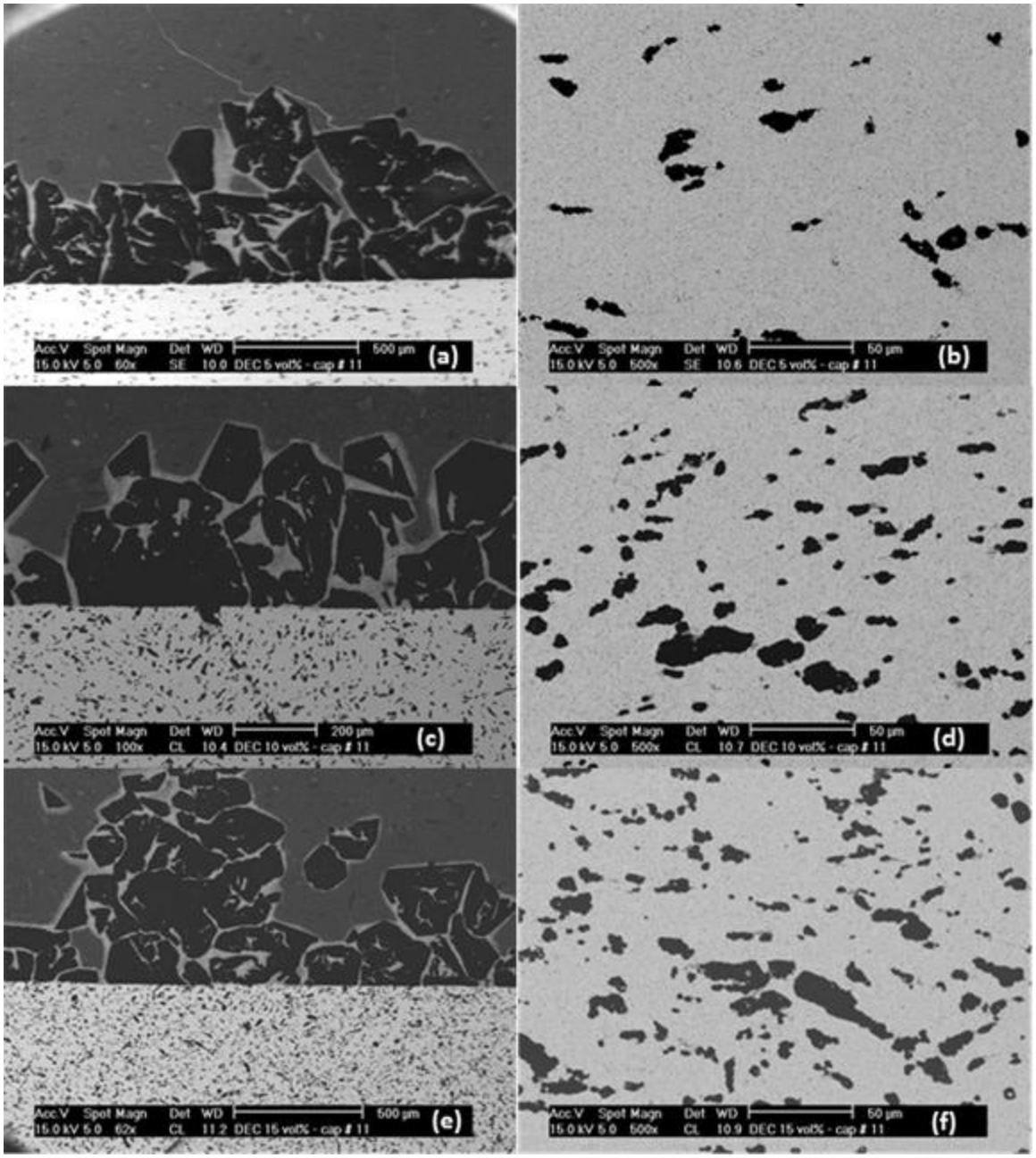

Figure 6-27: SEM-BSI micrographs of the microstructure of the sintered FG-0.5µm diamond PCD diamond enhanced carbide (GDEC) samples; (a & b) 5vol.% DEC, (c & d) 10vol.% DEC and (e & f) 15vol.% DEC substrate from Cap#11. Images b, d & f show the microstructure of the substrates respectively.

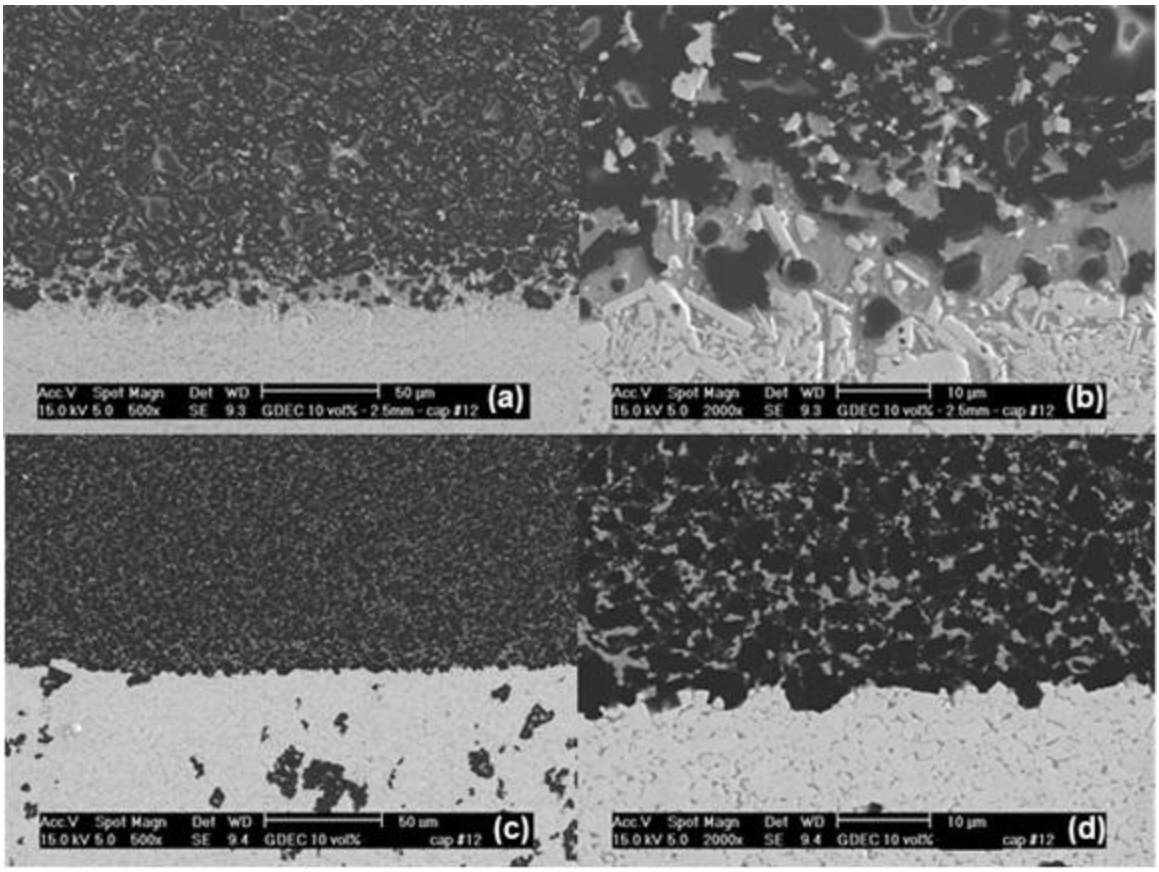

Figure 6-28: SEM-BSI micrographs of the microstructure of the sintered FG-6µm diamond PCD graphite-diamond enhanced carbide (GDEC) samples; (a & b) 2.5 mm 10vol.% GDEC (cap#12) and (c & d) full 12mm 10vol.% GDEC substrate (cap#12).

Table 6-14: Image Analysis results of the FG-6µm diamond PCD samples from Cap#12 GDEC inter-layers.

Property	2.5mm 10vol.% GDEC	Full 10vol.% GDEC
Diamond particle size (µm)	4.2 ± 1.3	4.0 ± 1.0
Co pool size (µm)	1.3 ± 0.8	1.3 ± 0.7
Diamond Content (Area %)	87.0 ± 1.3	87.2 ± 0.5
Binder Content (Area %)	13.0 ± 1.3	12.8 ± 0.5
Diamond Mean Free Path (MFP) (µm)	4.3 ± 4.4	3.0 ± 3.0
Co Mean Free Path (MFP) (µm)	0.7 ± 0.6	0.5 ± 0.4
Diamond Contiguity (%)	58.5 ± 2.9	54.4 ± 1.2
WC particle size (µm)	0.3 ± 0.3	0.4 ± 0.3
WC Content (Area %)	1.5 ± 0.7	6.0 ± 0.4

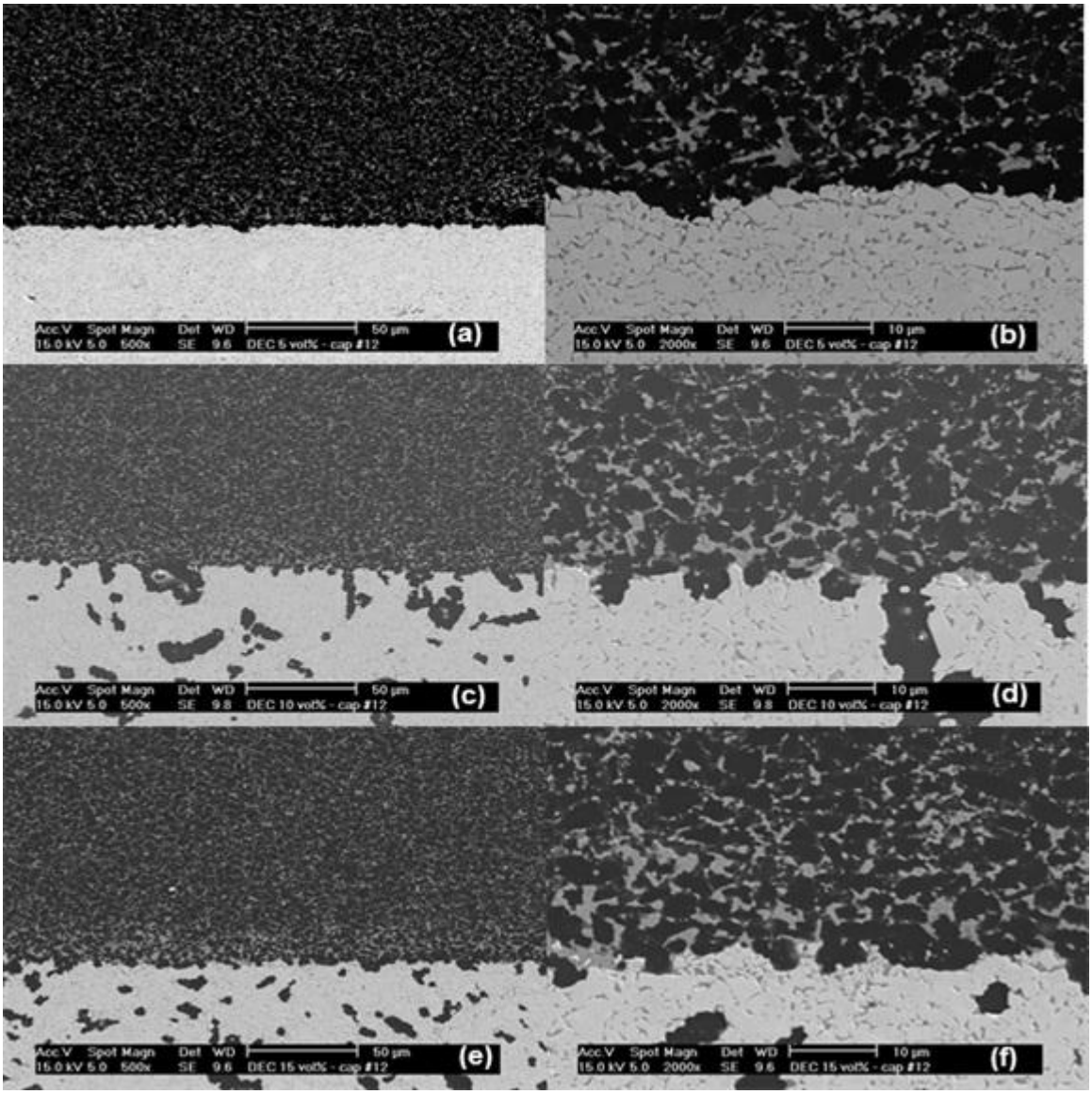

Figure 6-29: SEM-BSI micrographs of the microstructure of the sintered FG-6µm diamond PCD diamond enhanced carbide (DEC) samples; (a & b) 5vol.% DEC, (c & d) 10vol.% DEC and (e & f) 15vol.% DEC substrate from Cap#12.

Table 6-15: Image analysis results of the FG-6µm diamond PCD samples from Cap #12 DEC inter-layers.

Property	5vol.% DEC	10vol.% DEC	15vol.% DEC
Diamond particle size (µm)	4.1 ± 1.1	4.1 ± 1.1	4.0 ± 1.1
Co pool size (µm)	1.3 ± 0.7	1.5 ± 0.9	1.6 ± 1.2
Diamond Content (Area %)	86.6 ± 0.5	85.7 ± 0.8	86.2 ± 0.7
Binder Content (Area %)	13.4 ± 0.5	14.3 ± 0.8	13.8 ± 0.7
Diamond Mean Free Path (MFP) (µm)	3.5 ± 3.1	2.9 ± 2.8	3.0 ± 3.1
Co Mean Free Path (MFP) (µm)	0.5 ± 0.4	0.5 ± 0.4	0.5 ± 0.4
Diamond Contiguity (%)	54.1 ± 1.3	51.2 ± 2.0	53.3 ± 1.0
WC particle size (µm)	0.4 ± 0.3	0.3 ± 0.2	0.4 ± 0.3
WC Content (Area %)	6.7 ± 0.6	4.0 ± 0.3	6.8 ± 1.0

0.5µm DEC interlayer

AGG was still highly evident in the GDEC and DEC inter-layers sintered using the FG-0.5µm diamond shown in Figure 6-30. The AGG was located in regions locally along the interface and not throughout the whole substrate interface (48% of substrate free of AGG). A sufficient amount of carbon was evident in the substrates (i.e. there was a high amount of residual diamond in inter-layers after sintering). This would suggest that there is a sufficient amount of carbon available for saturation. The problem would be the kinetics of the system. Since the Co melt infiltrated from the bottom of the substrate up into the PCD layer, there was insufficient time for the Co melt to sufficiently saturate itself with carbon from the diamond in the substrate as the size of the diamond could be too large (i.e. diamond particles 10 – 20µm). These large diamond particles had a lower chemical potential for dissolution within the melt, therefore slowing down the saturation rate. To enhance the kinetics of the dissolution of diamond into the Co melt, a carbon source with a higher chemical potential for dissolution is needed. A fine grain diamond powder such as the FG0.5µm is highly reactive as is evident in the results above by the formation of AGG diamond regions at the interface.

A 0.5µm diamond powder was added to WC-12Co powder and spark plasma sintered (SPS) (Section 3.6) to produce a diamond enhanced substrate with an increased kinetics for dissolution and thus saturation of the infiltrating Co melt. The diamond content in the substrate was 10vol.%. An interlayer of 3mm was sintered onto FG0.5 µm diamond powder under standard sintering conditions (Cap#14). Figure 6-30 shows the microstructure of the sintered 0.5µm PCD with a 10vol.% 0.5µm diamond interlayer. The image shows that AGG was observed at the interface, although there were regions where fine grain diamond was found at the interface indicating that AGG grain growth was limited to only a few grains. The result of the AGG thicknesses is given in Table 6-16 and is compared to the effects an addition of a grain growth inhibitor (2wt% VC) has on the grain growth of the diamond. The substrate showed fine grain diamond surrounding areas of WC-Co clusters; this was due to the large particles of the agglomerated WC-Co powders which were used (i.e. thermal spraying WC-12Co powder, Section 4.1.1). The diamond particles and Co phase formed barriers between the WC-Co clusters.

Table 6-16: Results of AGG the 0.5µm diamond enhanced carbide samples for Cap#14.

Material	AGG thickness (µm)	Total AGG thickness (µm)
Cap#14 – 3mm 10vol.% 0.5µm interlayer (SPS)	452.1	452.1
Cap#14 – 3mm 10vol.% 0.5µm +2wt%VC interlayer (SPS)	588.3	588.3

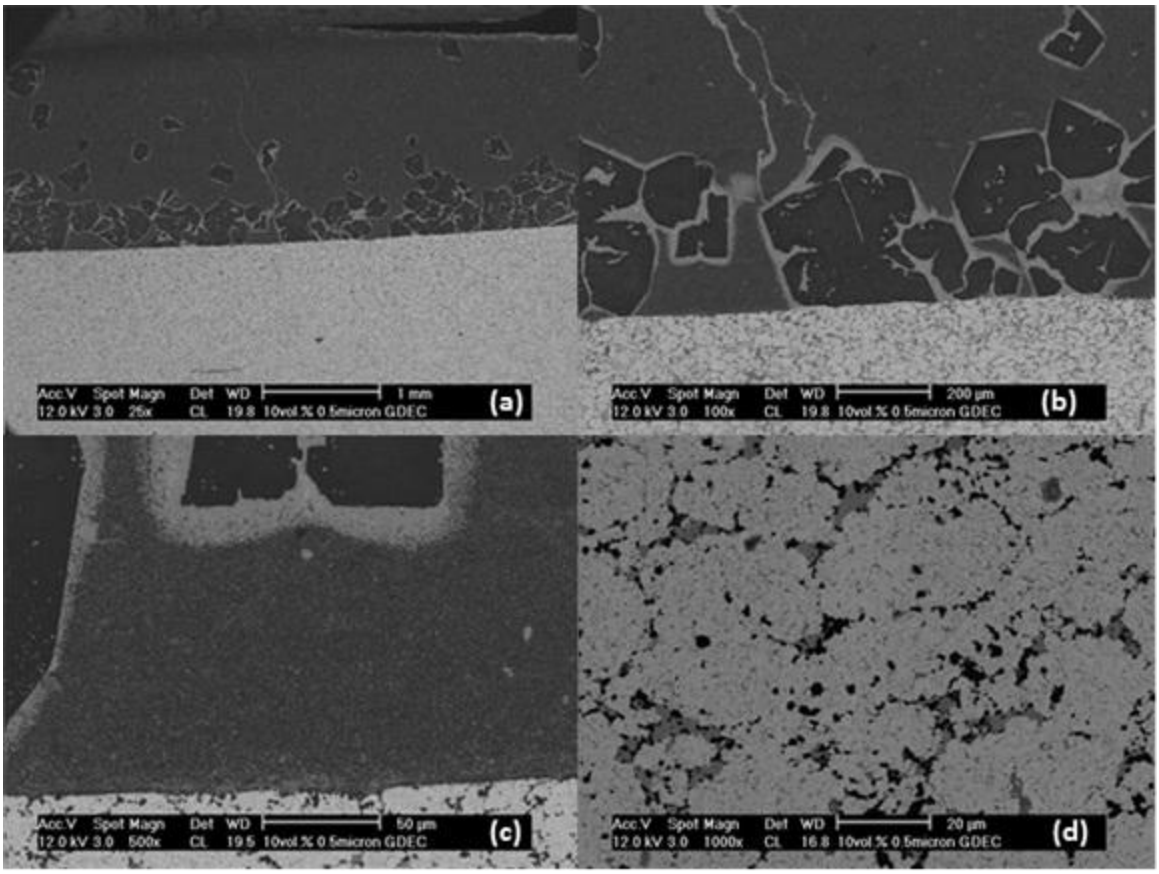

Figure 6-30: SEM-BSI microstructure of the sintered FG0.5µm PCD on a 0.5µm diamond enhanced interlayer (Cap#14); showing (a &b) AGG at interface, (c) area of fine grain at interface and (d) interlayer containing 0.5µm diamond.

6.2.3. Grain growth inhibitors

Experiments were conducted where VC was added to the WC-Co substrate as a grain growth inhibitor. VC has a high affinity for carbide formation and would form more stable carbides when in contact with a carbon source. This could form VC adsorption on the diamond, thus reducing the grain growth.

A WC-Co interlayer sample doped with 2wt%VC was produced by spark plasma sintering (SPS) (Section 3.3) and sintered with the FG0.5µm diamond at the standard sintering conditions (in Cap #14). The results are shown in Figure 6-31; the microstructure showed no AGG present at the interface and the diamond particle remained small (<1µm). EDS analysis shows V in the PCD near the interface, in the substrate and at the interface. Areas of Co and VC pooling at the interface were observed. The concentration of V decreased away from the interface. Areas of high and low density packing of the diamond particles were also observed in the bulk PCD; this suggests areas of inhomogeneous packing and agglomeration.

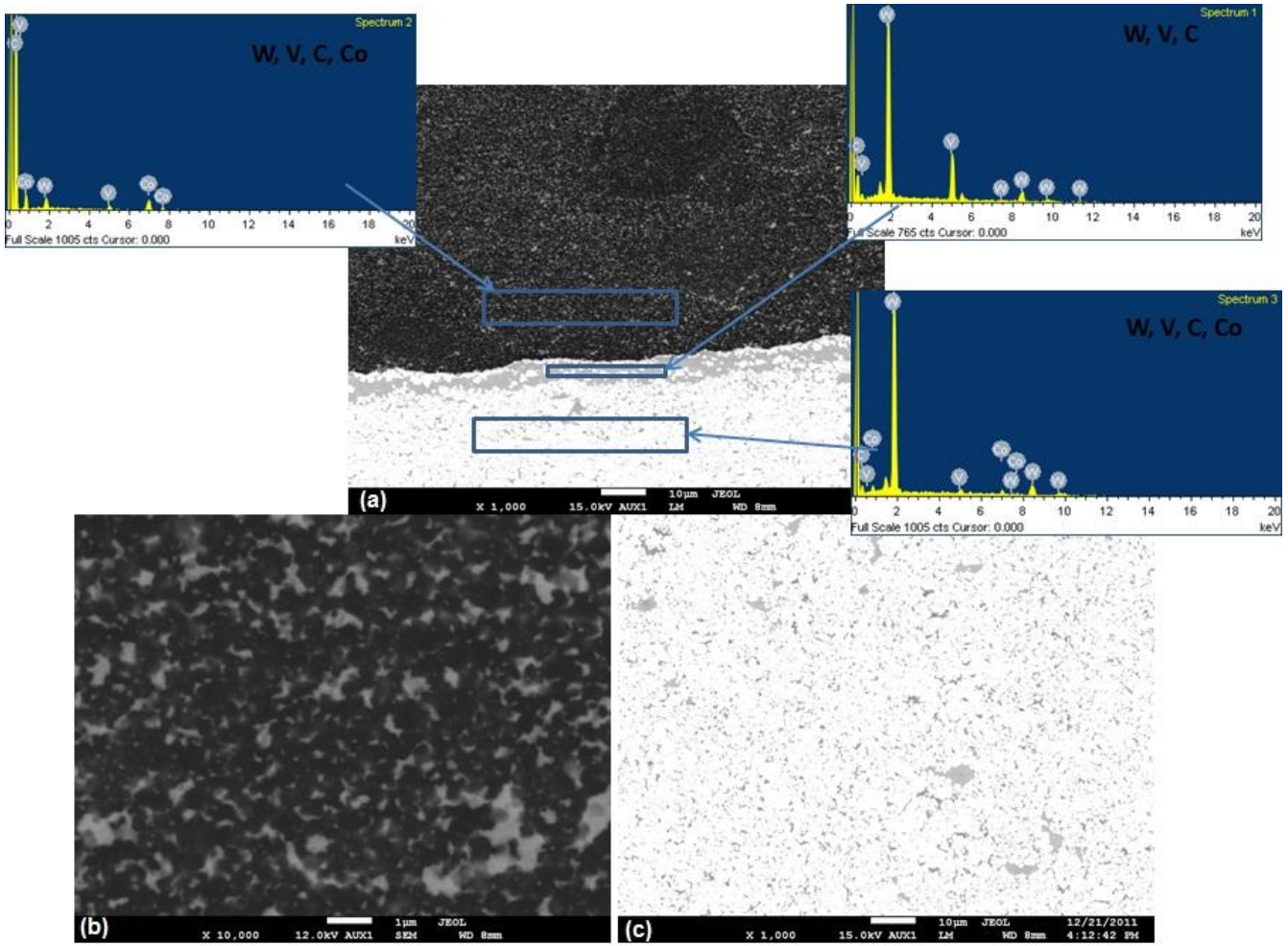

Figure 6-31: SEM-BSI micrograph of the microstructure of the sintered 0.5µm PCD on the 2wt.%VC doped substrate (Cap#14); showing (a) No AGG at interface, VC pooling (b) fine grain diamond and (c) interlayer containing 2wt.%VC.

Due to the potential grain growth inhabitation of the VC, a WC-Co sample interlayer was produced using 10vol.% 0.5µm diamond powder + 2wt%VC powder, then SPS sintered. A 0.5µm diamond PCD layer was then sintered on to the interlayer at the standard sintering conditions. The results of the microstructure and AGG thickness are given in Figure 6-32 and Table 6-16. The microstructure showed AGG at the interface. Similar to the 0.5µm GDEC substrate earlier, the substrate showed 0.5µm diamond particles surrounding the clusters of WC-Co particles, where the diamond, Co and VC formed a barrier between the particles.

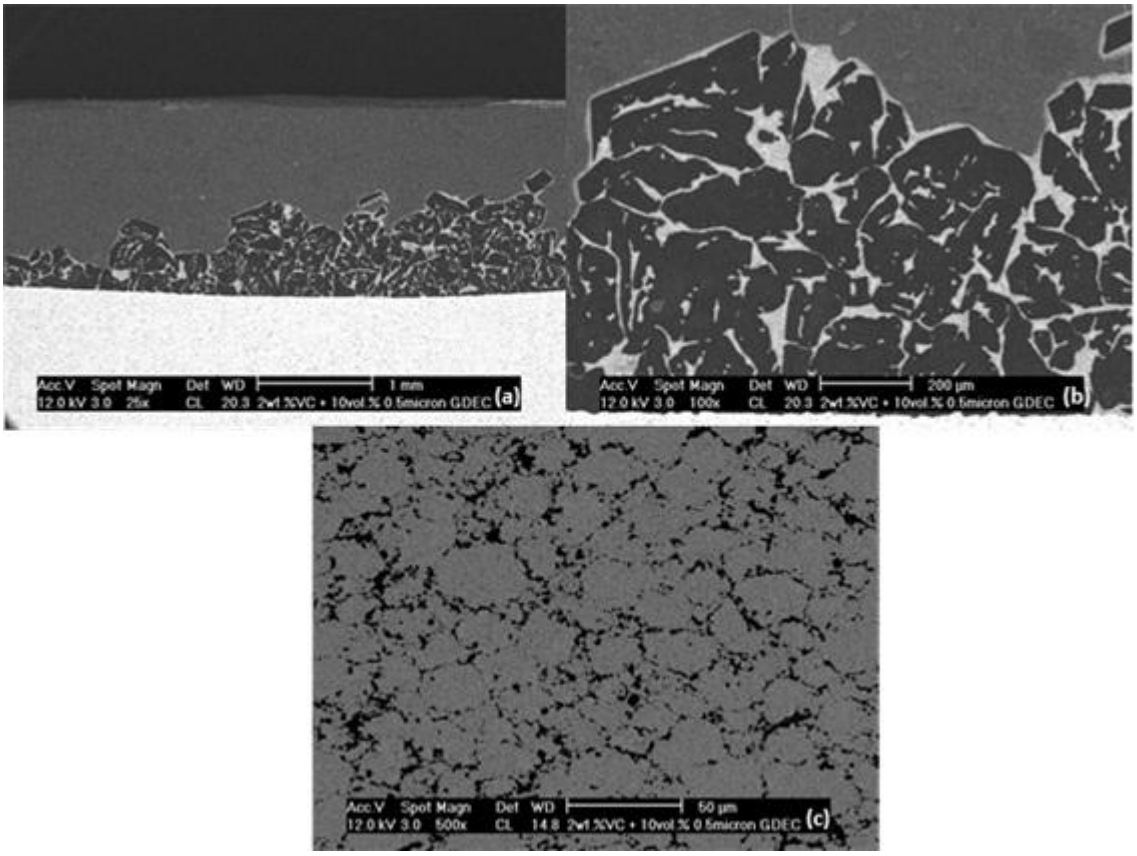

Figure 6-32: SEM-BSI micrograph of the microstructure of the sintered 0.5µm PCD on the 10vol.% 0.5µm diamond + 2wt.%VC doped substrate (Cap #14); showing (a & B) AGG region at the interface and (c) interlayer containing 0.5µm diamond and VC.

6.2.4. Summary

An overall summary of the major features for each sample sintered in this project is given in Tables 6-17 and 6-18 for the coated layers and the diamond enhanced carbide and VC doped substrates respectively.

Table 6-17: Summary of the results from sintered PCD of coated layer samples.

Sample	Cap#1	Cap#3	Cap#4	Cap#6	Cap#7	Cap#8	Cap#9
WC-12Co	P, CG, No AGG	UFG, AGG	-	UFG, AGG	-	FG, No AGG, P	-
WC-12Co+2%C	P, CG, No AGG	UFG, AGG	-	UFG, AGG	-	FG, No AGG, P	-
WC-12Co+4%C	-	-	UFG, AGG	-	UFG, AGG	-	FG, No AGG, P, Ac
WC-12Co+6%C	-	-	UFG, AGG	-	UFG, AGG	-	FG, No AGG, P, Ac
WC-17Co	P, CG, No AGG, Ac	UFG, AGG	-	UFG, AGG	-	FG, No AGG, P	-
WC-17Co+2%C	P, CG, No AGG	UFG, AGG	-	UFG, AGG	-	FG, No AGG, P	-
WC-17Co+6%C	-	-	UFG, AGG	-	UFG, AGG	-	FG, No AGG, P
WC-13Co	P, CG, No AGG, Ac	UFG, AGG	UFG, AGG	UFG, AGG	UFG, AGG	FG, No AGG, P	FG, No AGG, P

Table 6-18: Summary of results from sintered PCD of Carbon enriched & VC doped substrates.

Sample	Cap#10	Cap#11	Cap#12	Cap#13	Cap#14
10vol.% GDEC – 0.1 mm	UFG, AGG, No RDS	-	-	-	-

P – Co pooling at the interface
CG – Course grain diamond (MG)
UFG – Ultra Fine grain diamond (FG-0.5µm)
AGG – Abnormal grain growth of diamond at the interface
FG – Fine grain diamond (FG-6µm)
Ac – Acicular grain growth of WC particles
RDS – Residual diamond left in substrate

10vol.% GDEC – 0.5 mm	UFG, AGG,	-	-	-	-
10vol.% GDEC – 1 mm	UFG, AGG	-	-	-	-
10vol.% GDEC – 2-2.5 mm	UFG, AGG, RDS	UFG, AGG, L, RDS	FG, No AGG, No RDS, Ac	UFG, AGG, RDS	-
10vol.% GDEC – 3 mm	-	-	-	UFG, AGG, RDS	-
10vol.% GDEC – 4 mm	-	-	-	UFG, AGG, RDS	-
10vol.% GDEC – 5 mm	-	-	-	UFG, AGG, RDS	-
10vol.% GDEC – 6 mm	-	-	-	UFG, AGG, RDS	-
Full 10vol.% GDEC	-	UFG, No AGG, P, RDS	FG, No AGG, No P, RDS	-	-
5vol.% DEC	-	UFG, AGG, RDS	FG, No AGG, No P, No RDS	-	-
10vol.% DEC	-	UFG, AGG, RDS	FG, No AGG, No P, RDS	-	-
15vol.% DEC	-	UFG, AGG, RDS	FG, No AGG, No P, RDS	-	-
10vol.% 0.5µm DEC	-	-	-	-	UFG, AGG, L, RDS
2wt.%VC interlayer	-	-	-	-	UFG, No AGG, V pooling
2wt.%VC+10vol.% 0.5µm DEC	-	-	-	-	UFG, AGG, RDS

6.2.5. Paarl-Granite Turning (PGT) Test

Wear tests were done on two PCD sintered samples using a Paarl Granite Turning (PGT) test outline in Section 3.4.2. The two PCD samples tested were a standard MG PCD layer on WC-13Co (cutter 5 STD) and a standard MG PCD layer on a coated WC-17Co+2%C substrate (Cutter 4). The results of the 10min PGT test are given in Figure 6-33. Figure 6-33 shows the volume of rock removal per millimetre of wear scar. This shows that the sample with the standard substrate (cutter #5) performed better than that of the coated substrate (cutter #4). The bar chart shows three distinct regions indicating the minimum (blue), mean (maroon) and maximum (yellow) values. This showed that the standard

L – AGG located locally along the interface
V pooling –VC pooling at the interface

Cutter 5 had a wider range of values than the WC-17Co+2%C Cutter 4. The results are still within the normal testing range for PCD materials given by the red and green lines. The red line shows the lower end value (0.1 x 10^3 m^3/mm wear scar) for good performance of a PCD cutter, while the green line (which should be above 0.2 x 10^3 m^3/mm wear scar) shows the upper end for the good performance range for a PCD cutter. Values above the green line show excellent wear performance. Both cutters showed acceptable performance behaviour. Figure 6-34 shows the wear scars of the cutter 5 and 4, cutter 4 showed a deeper wear scar compared to that of the standard cutter 5, thus indicating that the standard cutter 5 performed better than the WC-17Co+2%C cutter 4. Since the performance behaviour of only one sample per set was tested, these results give only an indication of the performance behaviour. Although this result challenges the initial idea that an increase wear resistant coated substrate can help improve the wear resistance of the PCD material it should not crush the idea. Many various spraying problems could have influenced the result, including thickness of the coated layer and homogeneity. For true performance behaviour more samples would have to be tested.

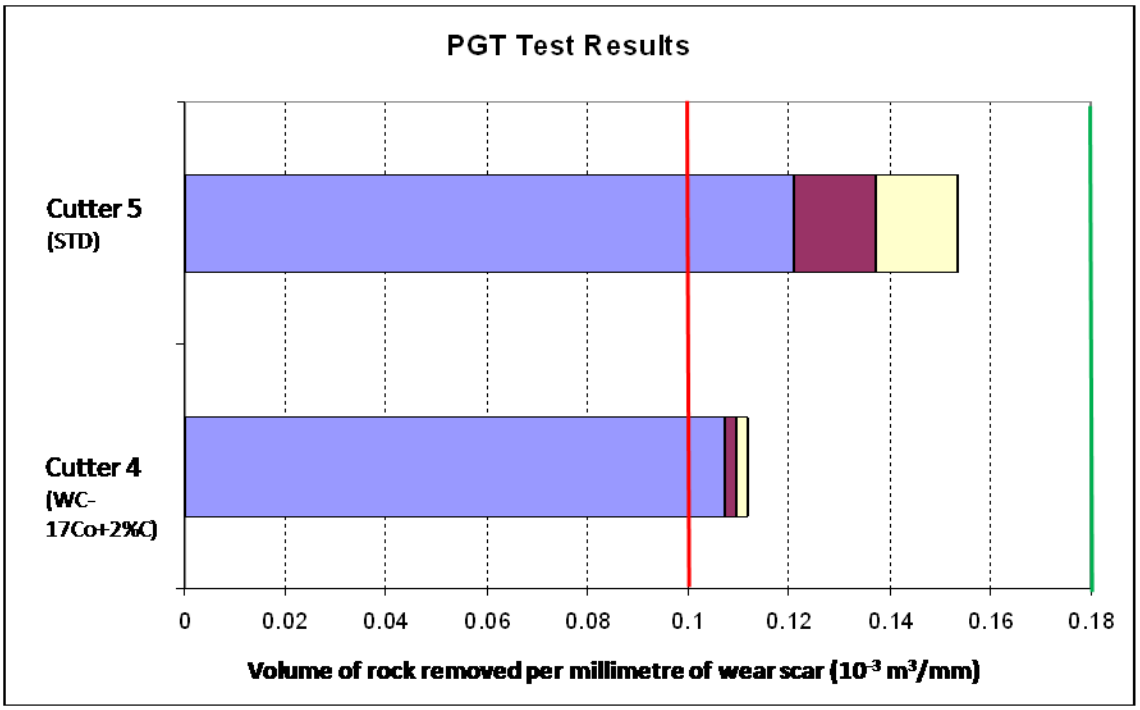

Figure 6-33: Results of the PGT 10 min test showing the volume removal of rock per distance of the wear scar.

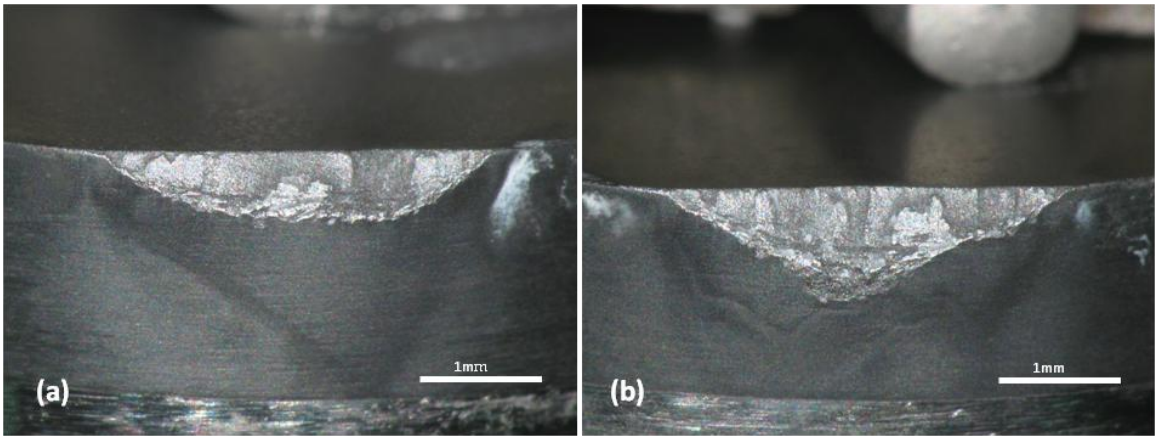

Figure 6-34: Optical images of the wear scar for the (a) Standard PCD cutter (Cutter #5) and (b) WC-17Co+2%C coated substrate PCD cutter (Cutter #4).

Chapter 7: Discussion of PCD Sintering & Grain Growth

7.

7.1. Reproducibility of results

7.1.1. Comparison of AGG within the same sintering conditions

A comparison of the results for the sintered FG-0.5µm diamond samples is given in Figure 7-1, showing the differences between the measured AGG of the various capsule runs using the FG-0.5µm diamond sintered at the same HPHT sintering conditions. It was observed that although these samples were sintered at the same sintering conditions, the amount of AGG evident at the interface varied substantially in each material set. This could be seen especially for the standard WC-13Co samples sintered in four different capsule runs (#3, 4 , 6 & 7), where the results differed greatly. In cap#7, the results of the two substrates were similar. It is therefore easier to compare the trend of samples within the same capsule and compare that trend with the trend of a different capsule, but with the same sample set and conditions. For example, for the coated samples the AGG increased from cap#3 to cap#6, while the standard WC-13Co decreased. It is noted that the 2%C enriched coatings showed an overall lower AGG formation.

Sintering of PCD under HPHT conditions was variable even under constant conditions; there are various factors that can influence/affect the sintering of PCD. These factors include oxygen content, impurities, press conditions and unequal melting fronts during sintering which can change the conditions and precipitate non-normal grain growth. Due to the high reactivity of the fine grained diamond particles, even small variations could cause a substantial change in the growth rate. This has to be taken into account during

the discussion of the growth experiments. Only if conditions are determined, where small changes do not change the grain growth very much, a stable production of such materials is possible.

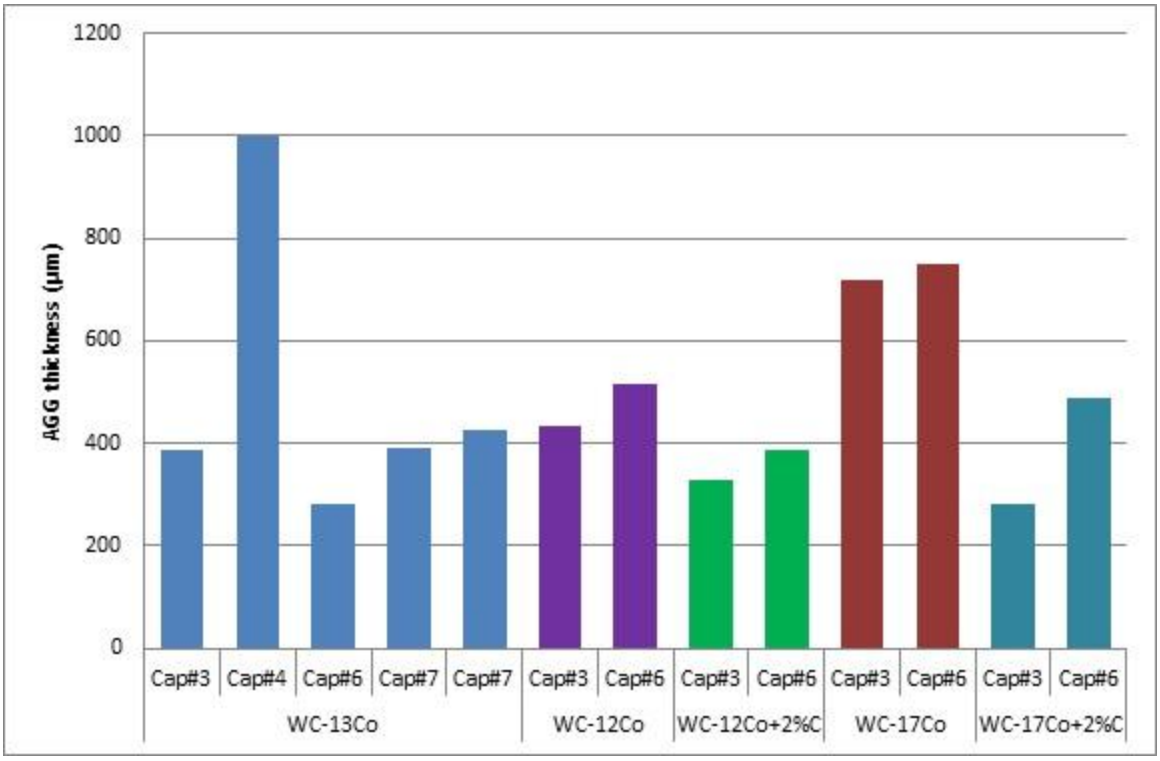

Figure 7-1: Comparison of the AGG thickness of FG-0.5 diamond on various substrates in different capsule runs at the same sintering conditions (6.8 GPa and 1400°C).

7.1.2. Comparison of Co pooling formation

For the powders with larger grain size (MG & FG-6µm), AGG of the diamond particle did not occur. However, Co pool formation at the interface was evident. Co-pool formation also existed in fine grain diamond materials (FG-0.5 µm), but was insignificant compared to that of the AGG formation. The amount of Co pooling at the interface could indicate how the Co metal affected grain growth of the diamond. The smaller the Co pool

thickness, the less impact the Co had on the diamond grain growth. A smaller Co pool resulted in less carbon dissolution to cause saturation (i.e. less dissolution of diamond particles was needed). For larger Co pool formation, more carbon was needed to saturate the Co melt; therefore more diamond dissolution took place setting up Ostwald ripening conditions. This can indicate the amount of carbon saturation of the infiltrating melt. Figure 7-2 shows the comparison of the Co pool thickness for the coated layers sintered for the MG and FG-6µm diamond samples. There was a negligible difference in the Co pooling in cap #1 (MG diamond) for the various samples. The Co pool thickness was higher for the higher Co content samples (i.e. 17Co). The Co pooling in cap #8 & 9 for the FG-6 µm diamond were similar to that of cap #1 using the MG diamond. The carbon enriched coated samples had a larger Co pool than the as-received samples. There was no significant difference between the Co pool formation of the 4 and 6%C enriched samples compared to that of the 2%C samples.

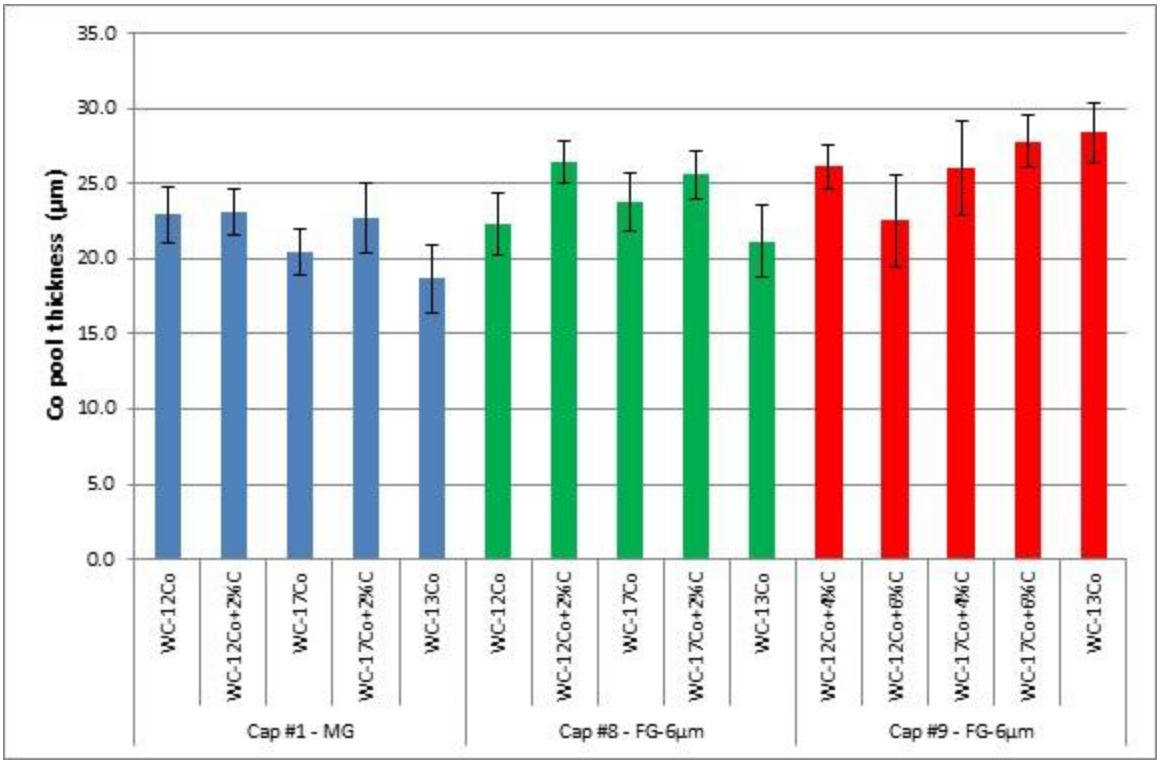

Figure 7-2: Comparison of the Co pool thickness for MG and FG-6µm diamond for coated samples, for different substrates.

7.2. Grain growth mechanisms in PCD

Literature on grain growth theory described in Section 2.2.1 had shown that the conditions for abnormal grain growth to occur during liquid phase sintering if the grain growth is interfacial reaction controlled. Strong evidence for interfacial reaction controlled mechanism was the existence of faceted grains. The growth of the faceted grains is layer by layer; while grain growth of non-faceted grains (i.e. spherical) grows by diffusion controlled mechanisms (Chapter 2.2).

It is evident in fine grained PCD materials that the grains were highly faceted, Figure 7-3. Here both the large AGG grains and the fine grains are faceted. The abnormal grain growth of the fine grain diamond during sintering is so quick (i.e. has a high driving force for growth) that the WC particles were trapped inside the Co pool between and inside the diamond grains. Figure 7-4 shows the SEM micrographs of the various phases present in a PCD material. Both the fine grained diamond particles and the AGG diamond particles were present. WC and Co particles were trapped within the AGG diamond grains. Figure 7-5 shows the EDX analysis of the binder phase indicating the Co and WC phases. The image shows that the WC particles grew within the Co phase. This is a result of the re-precipitation of the WC phase from the saturated molten Co metal upon cooling.

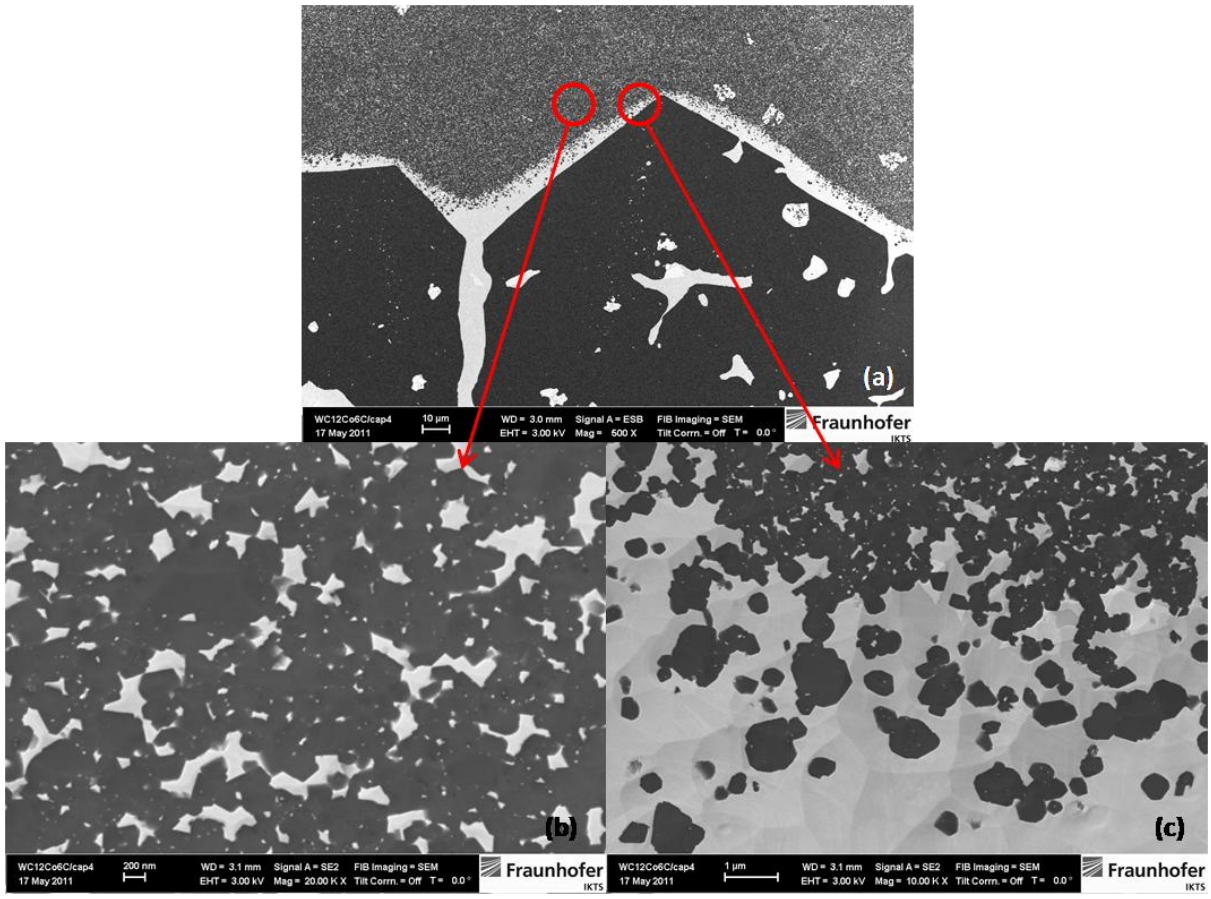

Figure 7-3: SEM-BSI image of faceted grains in 0.5 m fine grain sintered diamond (a) large AGG faceted grains, (b) fine faceted grains in bulk layer and (c) fine faceted grains in Co pool, the Co and WC phases are the dark grey and light grey phases respectively.

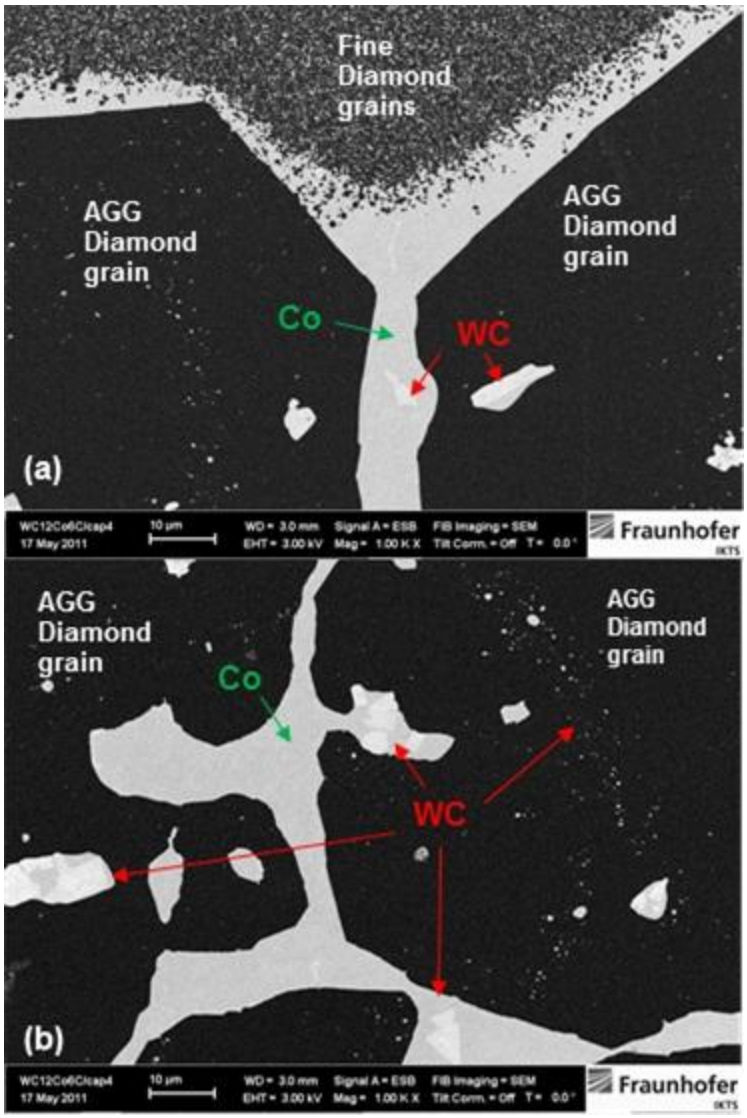

Figure 7-4: SEM-BSI micrographs of re-precipitation of WC in Co binder between the exaggerated diamond grains.

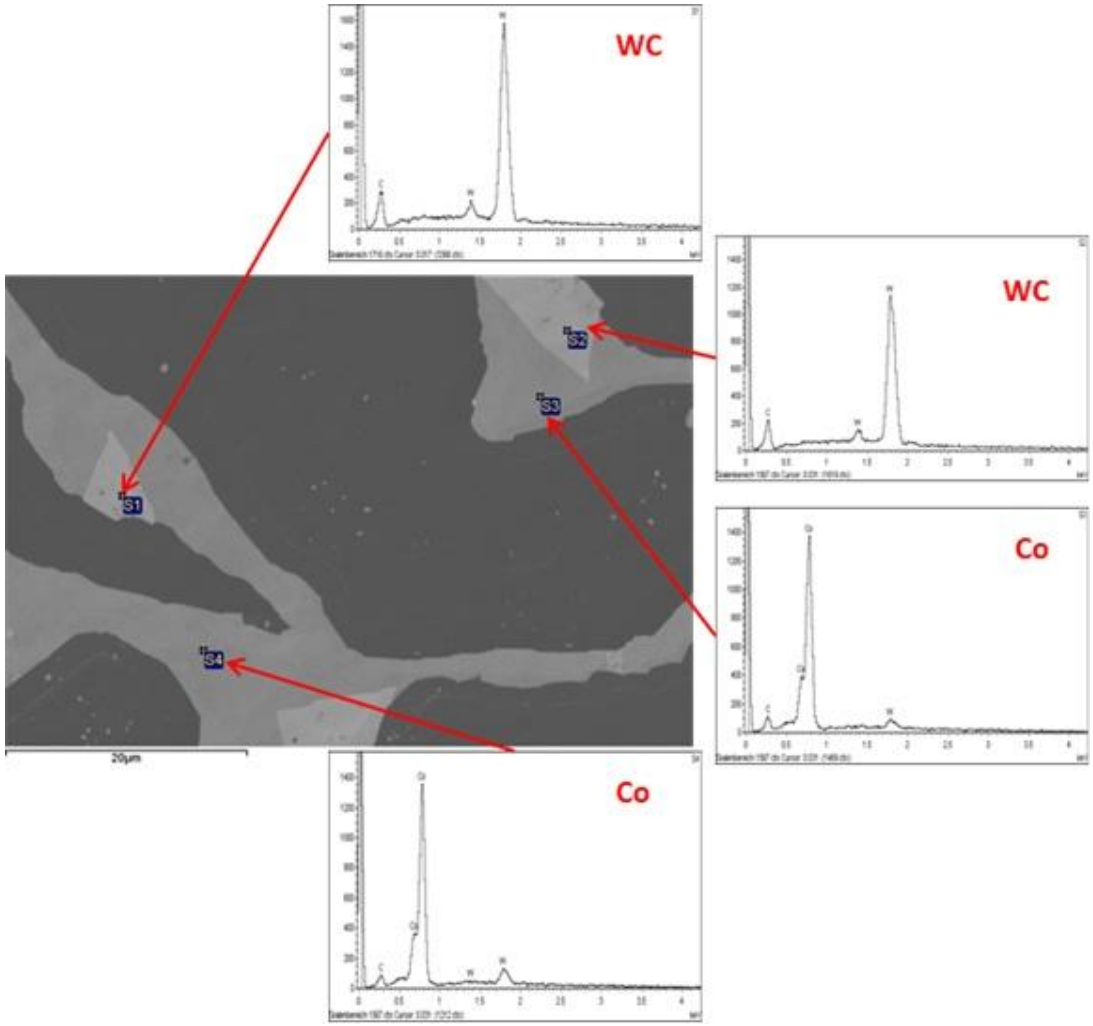

Figure 7-5: EDS analysis of the phases within the binder (WC and Co phases).

When analysing the AGG region it was difficult to determine how large each AGG diamond grain was or if it was made up of several smaller grains grown together. Image analysis of the AGG diamond region was tried; results proved unsuccessful as the IA programme took the tiny re-precipitated WC grains that were trapped in the AGG diamond grains to be barriers/grain boundaries, therefore dividing the large AGG diamond grains into much smaller particles, giving incorrect data. Due to this reason it was important to determine how the grains were growing. To do this SEM investigation was done on the WC-12Co+6%C sample from cap #4. Electron back scattered diffraction (EBSD) was carried out on the sample to determine the orientation of the diamond grains. This is shown in Figures 7-6 – 7-7, where the diamond grain orientation is indicated in various colours differentiating the various *hkl* normal directions of the diamond grains, the colour codes corresponding to the various *hkl* directions of the diamond grains are shown in the insert of Figure 7-7. From Figure 7-7, it can be seen that the diamond grains grew in various directions. The grain boundary and approximate grain size of some of the grains can be seen.

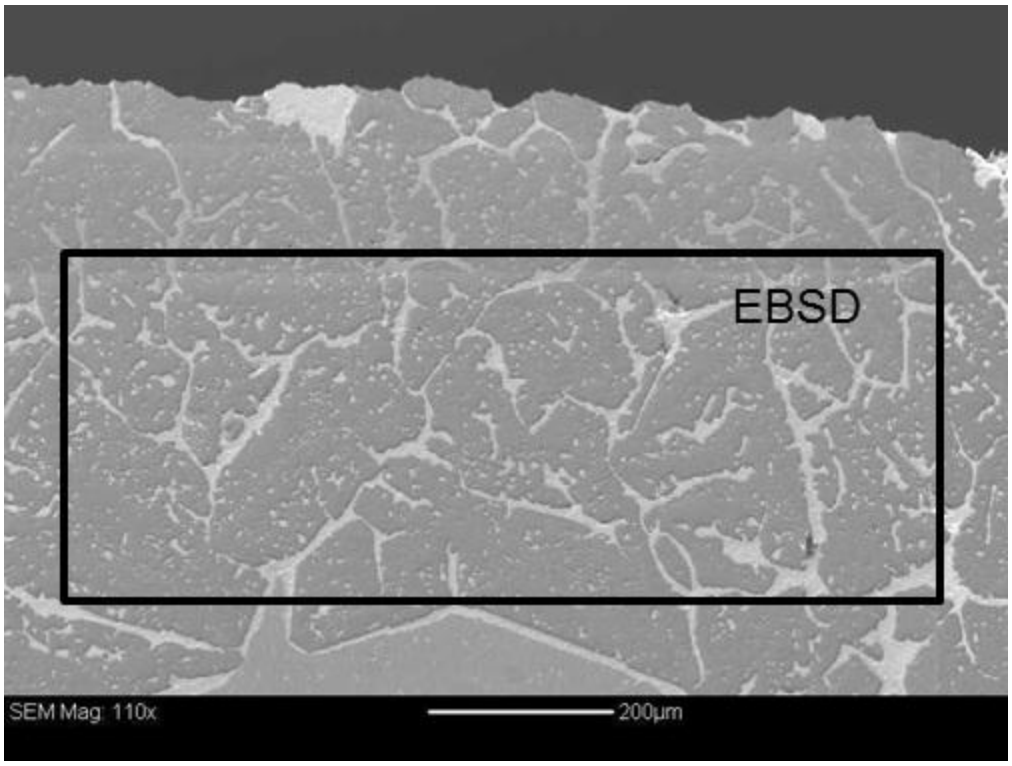

Figure 7-6: SEM-SEI micrograph of the AGG diamond region in WC-12Co+6%C from cap#4.

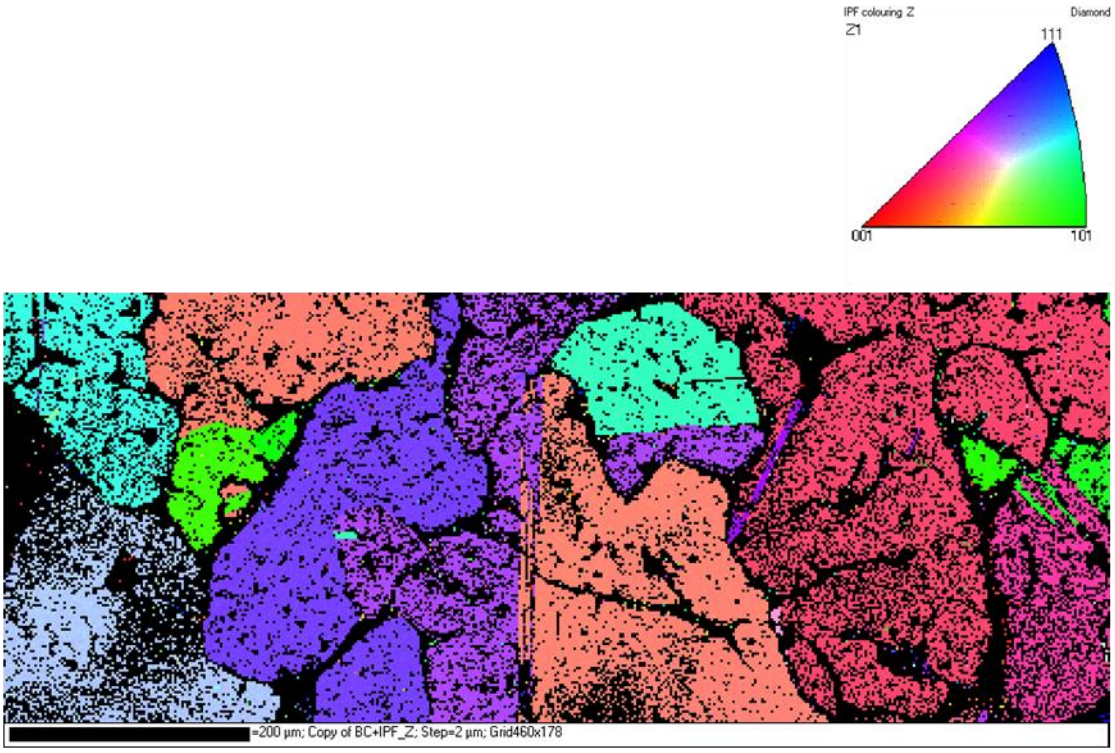

Figure 7-7: EBDS image showing the exaggerated diamond grains, each colour corresponds to the different hkl normal direction (colour codes in insert), the red colour shows the diamond grains grown in the 001 direction, blue in the 111 direction and green in the 101 direction.

The dominant growth faces of diamond is the {100} for cube shaped diamond and the {111} for octahedral-shaped morphology (Yarbrough & Messier, 1990). The fast growing faces usually "grow out" and disappear leaving the slow growing faces. The preferential growth of diamond is in the fast growing diamond direction; [100] and [110] directions. The {111} facets are the slowest growing faces, which usually results in the {111} facets remaining after growth. Shin (Shin et al., 2004) showed that the largest facets of the AGG diamond were the {111} planes (Figure 0-9). This would imply that AGG diamond particles shown in Figure 7-8 indicate the fast growth direction {100} facets (blue arrow), slow growing {111} facets (red arrow) and carbon flux direction (green arrow) (although this was not determined in this study). The selected diamond grains grow in the

direction of the incoming carbon flux. Twinning of diamond crystals can be found in the {111} planes (Shin et al., 2004). No twinning can be seen in these images.

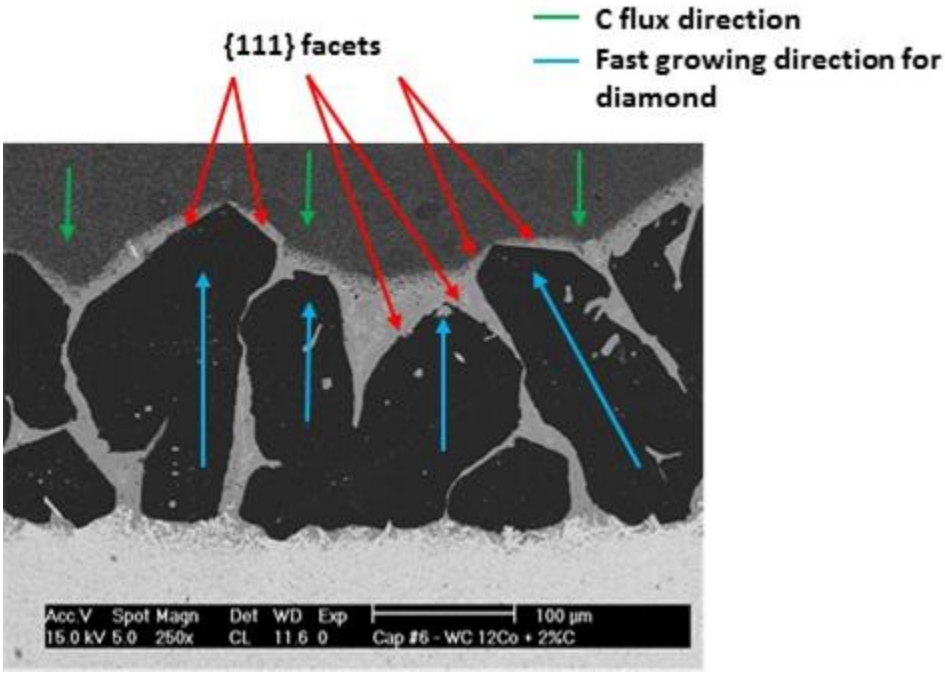

Figure 7-8: SEM-BSI image of AGG showing the typical growth directions of diamond.

7.2.1. Factors Eliminating Abnormal Grain Growth in PCD materials

There are two main ways to avoid the formation of AGG in PCD: changing the interfacial energy (γ_{sl}) of the diamond in the melt and controlling the oversaturation of the melt.

By changing the interfacial energy of the diamond particles, a change in the grain growth mechanism occurs. A smaller interfacial energy is needed to facilitate a reduction in grain growth. Small additions of active elements such as (Cr, V, BN etc…) can be potentially used to lower the interfacial energy of the diamond particles and change them from atomically smooth to atomically rough surfaces (i.e. from faceted to spherical particles). Spherical shapes have an isotropic surface energy, which implies an

atomically rough (or diffuse) interface. The atom attachment or detachment at a rough interface is sufficiently rapid to maintain a local equilibrium (Park et al., 1996). Spherical particles follow the diffusion controlled growth mechanism where the growth rate is linearly proportional to the driving force and no AGG can occur. A calculation was made to determine the effect changing the interfacial energy had on the solubility curve (Figure 7-9) (Section 7.2.2 has the calculation information and data). The solubility curve shifted to the left when the interfacial energy of the system was lowered.

Control of the oversaturation of the carbon in the melt is another way to eliminate AGG. In this case the carbon concentration in the Co melt is controlled and manipulated to reduce the driving force for grain growth of the faceted particles. This project dealt with controlling the carbon content in the Co solution during sintering to produce a carbon saturated melt and the effect this has on fine diamond grain growth.

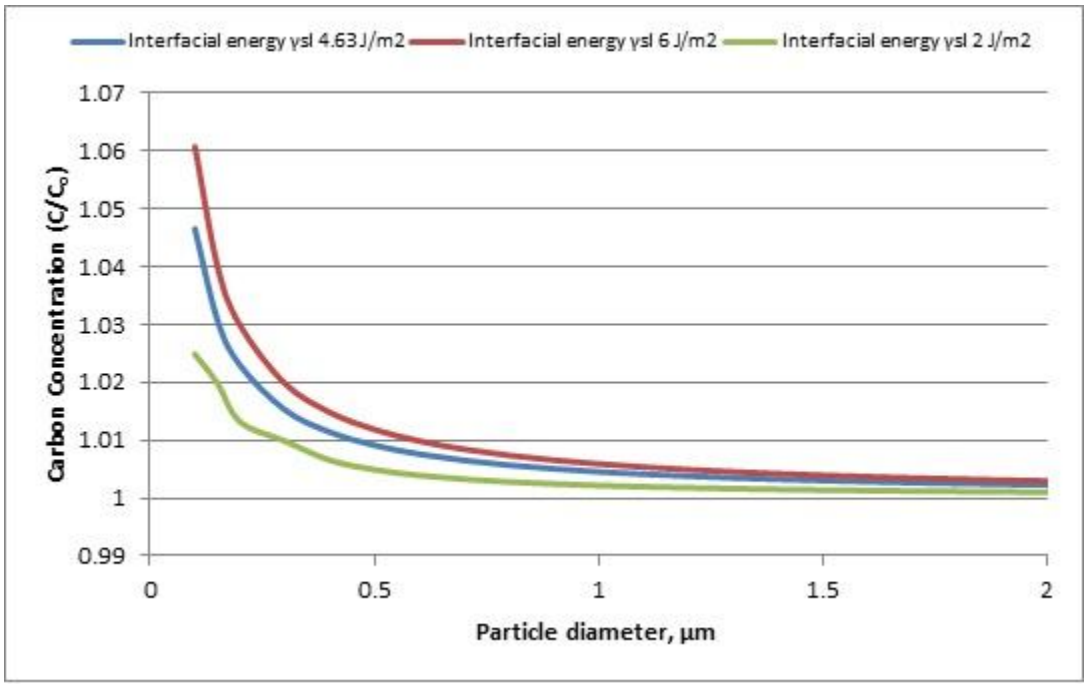

Figure 7-9: Calculated values of the change in the diamond solubility curve with change in diamond interfacial energy.

7.2.2. Carbon Content in the Co solution as a function of the substrate composition and diamond grain size

There are two factors that can affect the carbon solubility in the Co melt in PCD sintering. These factors are

- Change of the carbon concentration due to the composition of the substrate (i.e. standard WC-Co versus WC-Co + excess carbon),
- Change of the solubility with grain size of the diamond particles.

The concentration of carbon in the Co melt in the WC-Co substrates depends on the phase composition. The concentration of the melt from the WC-Co substrate was determined using an isopleth from the WC-Co phase diagram at high pressure (55kbar ∽ 5.5GPa) and temperature (1773K ∽1500°C) generated through data in Thermo-Calc (Element Six Pty Ltd, database), Figure 7-10. This isopleth was used as it provided the closest dataset to the conditions used in this project (1400°C and 6.8GPa). The concentration of the carbon and W in the WC-Co substrate for both the standard and the carbon saturated cases were determined. The carbon concentration in the material with stoichiometric composition of WC-Co is 2.8wt%, whereas the concentration in the material with WC-Co and diamond is 3.5wt%. These data were then compared to thermodynamic data for the same WC-Co system at ambient pressure (1bar) and various temperatures (1350 - 1600°C) from FACTSAGE (Factsage 5.5, Them fact and 6TT-Technology). Figure 7-11 shows a comparison of the carbon concentration in the melt for both 1 bar and 55kbar conditions. From Figure 7-11, a similar trend at 1 bar and 55kbar can be seen although slightly shifted. The differences can be a result of the different datasets used and not only by pressure differences (i.e. 1bar data is more recent). There is a carbon solubility change from unsaturated to saturation of the melt of approximately 20%.

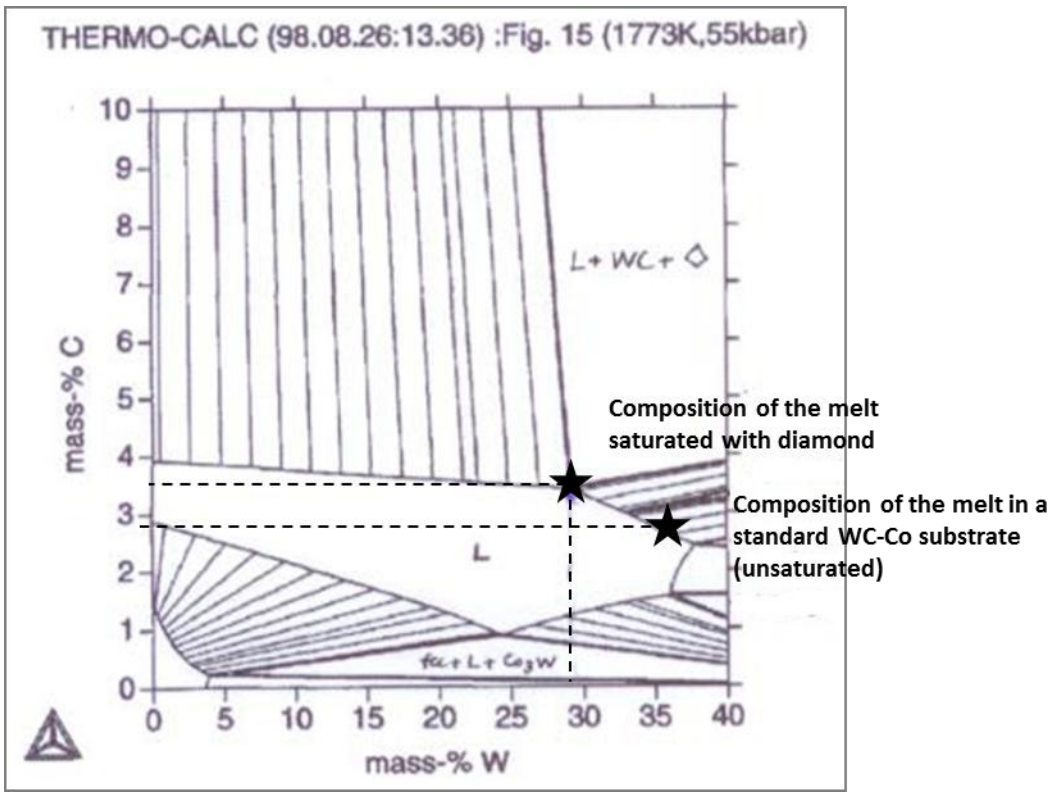

Figure 7-10: Thermodynamic calculated WC-Co isopleths at 1773K and 55kbar (Element Six (Pty) Ltd. database).

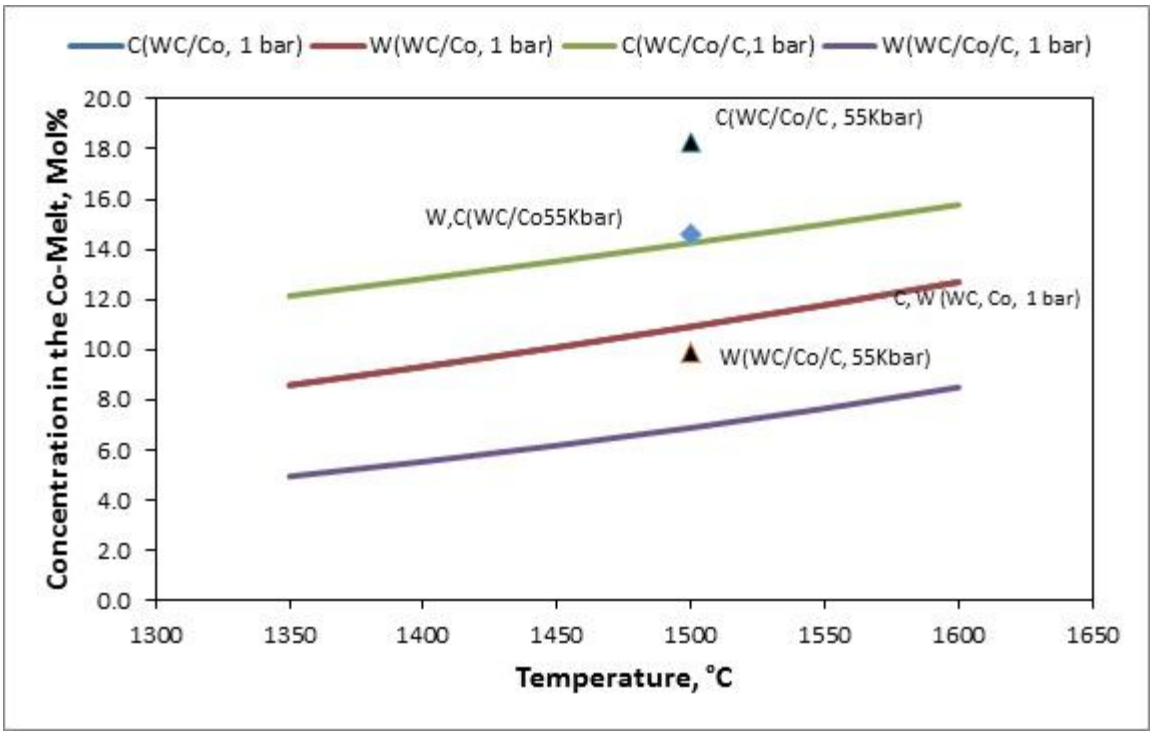

Figure 7-11: Comparison of the concentrations of C and W in the Co melt at 1 bar and 55kbar.

The change in the solubility of the melt with diamond grain size was also calculated using the Gibbs/Thompson equation (below) from Equation 2.3 in Section 2.2.1 and data on the interfacial energy of diamond in Co determined by V. Andreyev (Andreyev, 1994) listed in Table 7-1.

$$C = C_O exp\left[\frac{4\gamma_{sl}\Omega}{kT}\frac{1}{r}\right] \ldots\ldots\ldots\ldots\ldots (2.3)$$

The interfacial energy data used were determined for 6.5 GPa and 1970K (Andreyev, 1994). Using Equation 2.3 and approximating the particle shape for a sphere, the solubility curve for diamond in the Co melt was calculated: Figure 7-12. This shows that there is a strong dependence of the solubility on the grain size of the diamond only below 0.2 – 0.3µm and less so at 1-2µm, as initially stated in literature (Akaishi, M., 1991; Hong et al., 1988). At 0.1µm the diamond has only a 6% higher solubility

compared to that of infinite larger grains. This therefore suggests that the carbon concentration in the melt is affected more by the saturation in the melt from the substrate than the grain size.

Table 7-1: Solubility data for diamond-Co melt.

Parameters	Values	Conditions
Interfacial Energy, γ_{sl} (Andreyev, 1994)	4.63 J/m^2	6.5 GPa and 1970 K
Molar Volume, V_m	3.4 x 10^{-6} m^3/mol	
Gas Constant, R	8.314 J/(mol. K)	
Temperature, T	1670 K	

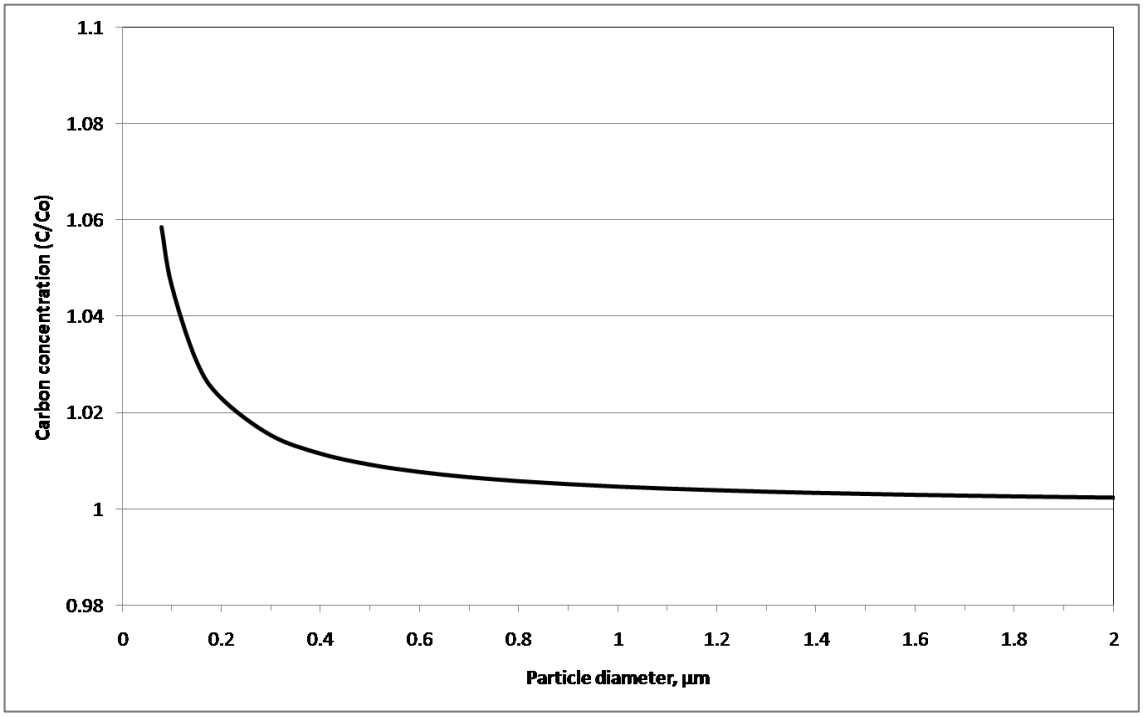

Figure 7-12: Solubility curve of diamond in the Co melt.

A comparison can be made from data for the carbon concentration line for the unsaturated WC-Co (Figure 7-11) and the WC-Co + diamond saturated curve (Figure 7-12), shown in Figure 7-13. Here it can be seen the 20% difference in the solubility

(ΔC_1). From this it can see that even for 0.5µm diamond the effect of the substrate is more pronounced than that of the grain size. This suggests that AGG in 0.5µm diamond is more intensely dependent on the solubility change in the melt than the size effect of the particles.

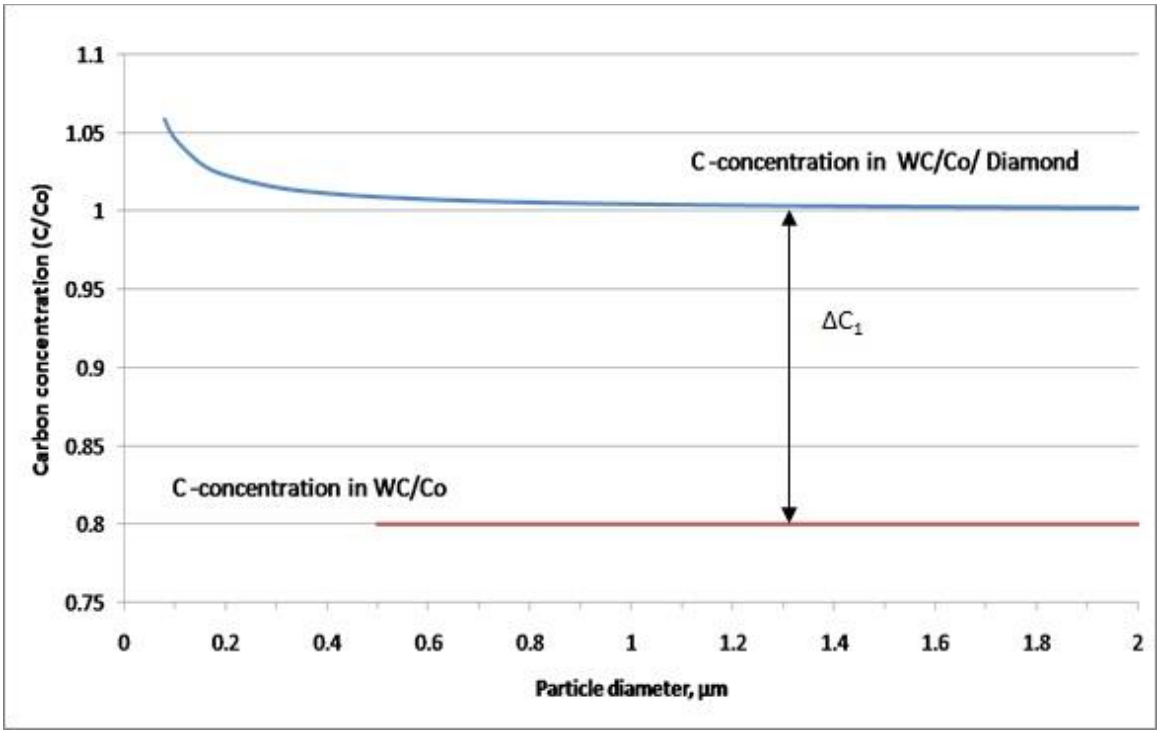

Figure 7-13: Carbon concentration in WC-Co and WC-Co-diamond substrates.

Evidence of the effect of solubility change in the melt on grain growth can be seen in work done on electrophoretic deposition (EPD) of diamond laminates produced by Džepina (Džepina, 2012). In this work, alternating diamond laminates of 2µm and 0.5µm were produced by EPD and HPHT sintered under the same conditions (1400°C and 6.8GPa). The interface between the alternating laminates is shown Figure 7-14. There was no evidence of AGG observed between the two layered structures; this supports the calculated curves. If the grain size effect had a more pronounced effect, the 0.5µm

diamond particles at the interface between the layers would have resulted in a higher amount of grain growth than experienced.

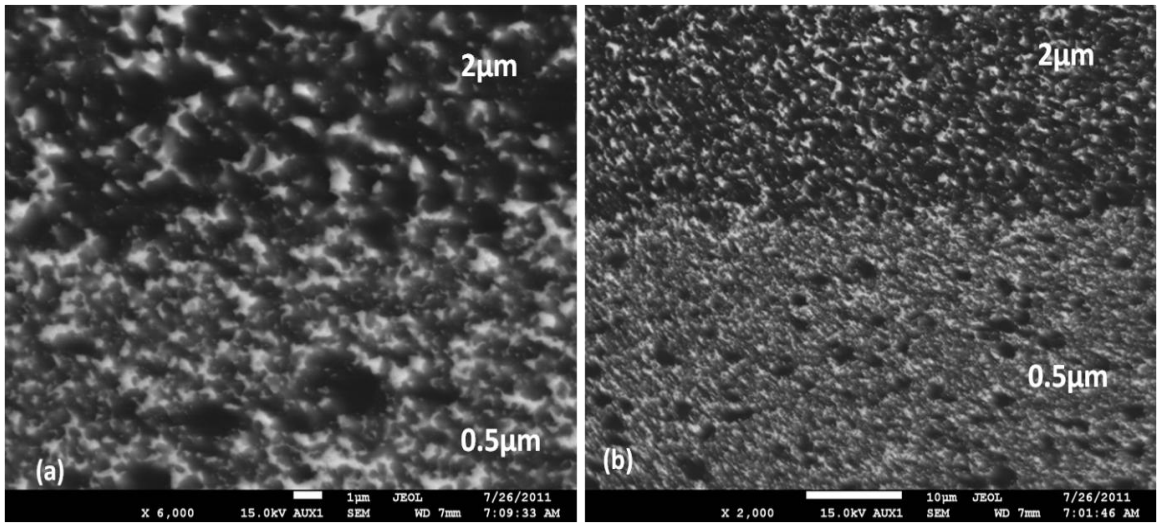

Figure 7-14: SEM-BSI images for 0.5 and 2µm diamond EPD laminates sintered at 1400°C and 6.8GPa (Džepina, 2012), (a) shows the boundary between the two diamond layers (b).

7.2.3. Effect of substrate on the grain growth & Co pooling during sintering

In this project, the two substrate types used were the standard WC-Co substrate and the WC-Co + excess C substrate (analogous to GDEC/DEC substrate). The effect of the type of substrate on the grain growth and Co pooling during sintering is discussed.

7.2.3.1. Grain Growth

The model for grain growth of PCD is shown schematically in Figure 7-15 for both the conventional and the WC-Co + excess carbon substrates.

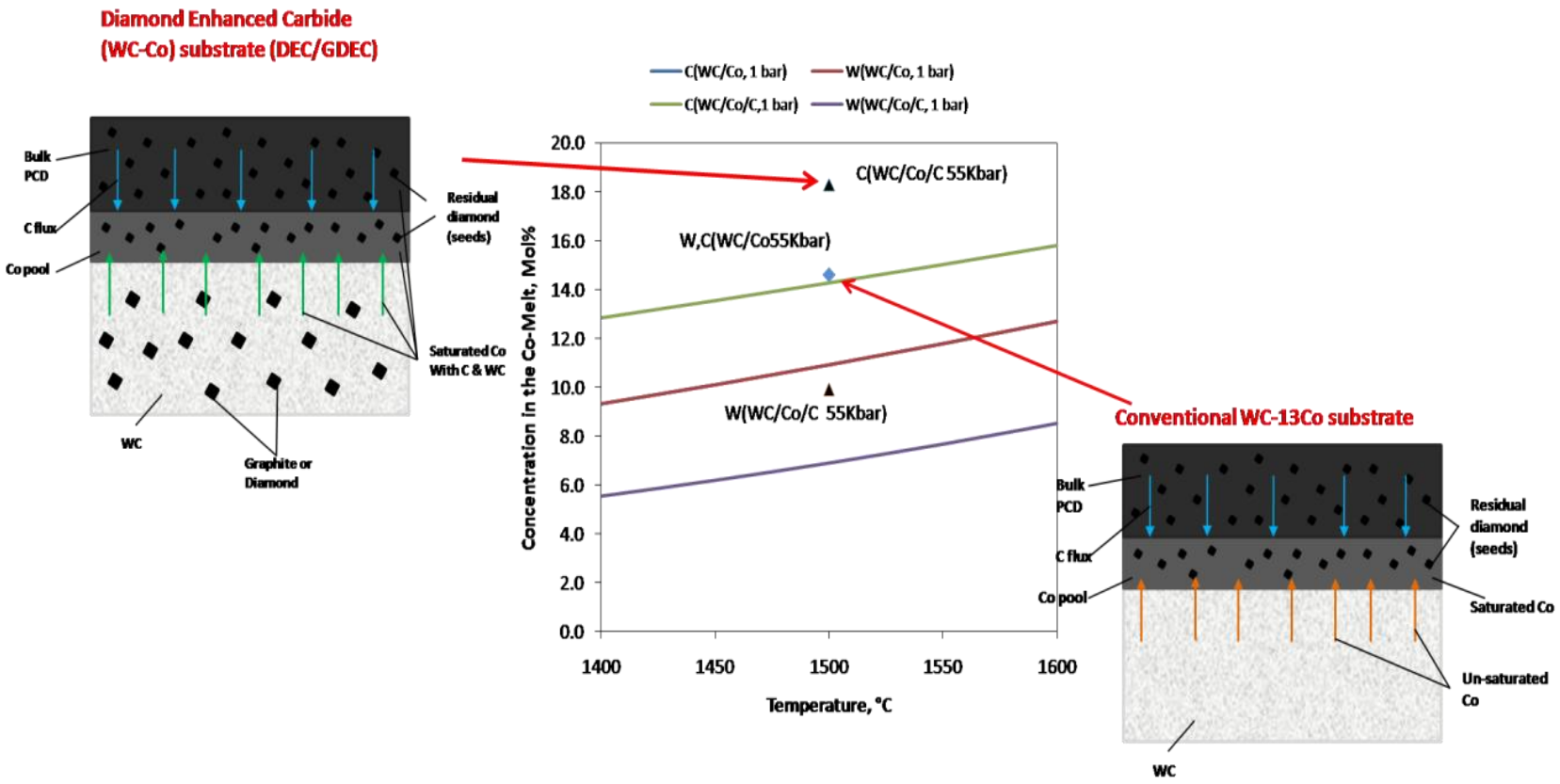

Figure 7-15: Schematic diagram for a standard WC-Co substrate and DEC substrate during sintering and the corresponding carbon concentration in the melt.

7.2.3.2. Conventional WC-Co substrate

Also the case of a WC-Co substrate in contact with the micron diamond powder and sintered under HPHT conditions the following occurs. During sintering the cobalt metal melts, the Co melt infiltrates from the substrate (orange arrows) into the micron diamond powder (refer to Figure 7-15). For a conventional WC-Co substrate, the Co melt has a low carbon content (un-saturated). This sets up a carbon sink in the Co metal between the substrate and the PCD layer (very high carbon content). The Co metal will readily dissolve the layer of fine micron diamond adjacent to the interface. The fine grained tail particles are most reactive and will dissolve first leaving residual coarse grained particles as residual seed crystals once the Co metal is saturated with carbon. The Co metal infiltrates into the bulk PCD. Grain growth of the residual diamond particles is then established by re-precipitation of carbon from the Co melt.

The bulk PCD particles remain small and well bonded, while diamond particles are grown in the Co pool adjacent to the interface. These diamond particles are larger than in the bulk as they are surrounded by a saturated Co metal. Tungsten from the substrate also dissolves into the Co melt; some of the carbon dissolved in the Co metal reacts with the W in solution and precipitates out WC on to WC particles at the interface or inside the Co in the PCD layer. The fast growing direction of the WC in the Co pool is away from the interface into the Co metal, these particles can grow as small faceted particles or long needle-like particles (acicular growth).

Figure 7-16 shows a schematic representation of the factors affecting the grain growth from a standard WC-Co substrate during sintering. For the standard WC-Co substrate, the change in the carbon concentration between the unsaturated Co melt and the PCD layer is given by ΔC_1 for grain sizes >1µm. For grain sizes <1µm, the change is slightly

higher (i.e. for 0.5µm $\backsim \Delta C_2$). Dissolution of the fine grains near the interface will result in a shift in the mean particle size distribution to lower values and a broadened distribution (Figure 7-16b), resulting in the size effect on the solubility playing a larger role in AGG formation, especially for finer particle size distributions. For 0.5µm diamond particles the mean particle size distribution moves to much lower values than 0.5µm near the interface, due to the particle dissolution of the grain (under saturated ΔC_1). As described in Section 2.2.1, the driving force for growth (Δg) is dependent on the change in the critical radius (r*) (grain with zero growth rate, i.e. neither grows nor shrinks) and the effective mean particle (r) and given below (Kang et al., 2009; Park et al., 1996].

$$\Delta g = 2\gamma_{sl} V_m \left(\frac{1}{r*} - \frac{1}{r} \right) \quad \text{.....( )}$$

For a broad particle size distribution, (1/r* -1/r) is large, the driving force for growth is large. Similarly if the particle size distribution is narrow, (1/r* -1/r)) is small, the driving force is low.

The change in the particle size distribution of the diamond particles sintered onto the standard WC-Co substrate affects the driving force for grain growth; this can be seen in Figures 7-16b and 7-16c. Before dissolution the driving force for grain growth is below the critical driving force (Δg_c) (i.e. narrower particle size distribution), after dissolution of the diamond particles within the melt the grain size distribution broadens (Figure 7-16b). There is now a larger difference between the mean particle size and lower mean particle size. The large change in the grain size shifts the change in carbon solubility to higher values, $>\Delta C_2$, this in turn shifts the driving force past Δg_c in the range where the interfacial reaction curve becomes dominant and AGG is prevalent and grain growth occurs at an exponential rate.

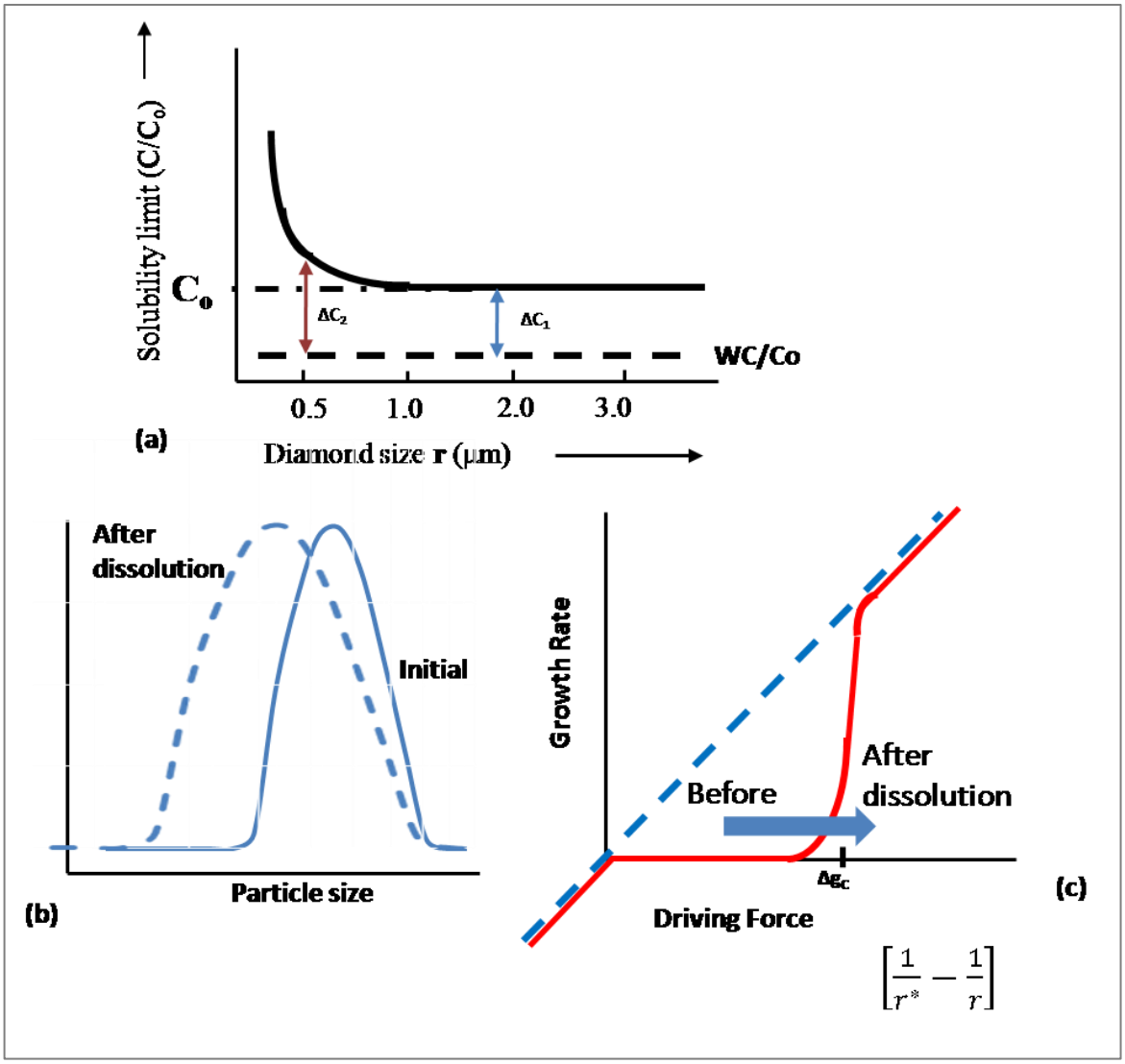

Figure 7-16: Schematic representation of the grain growth formation for standard WC-Co substrate (a) solubility, (b) grain size effect and (c) driving force.

7.2.3.3. WC-Co + excess C

In the case of a WC-Co substrate with excess carbon (i.e. DEC), the model for grain growth is similar to that of the conventional substrate. The Co melts during sintering

and infiltrates the diamond layer. The excess carbon in the substrate acts as an extra carbon source to saturate the infiltrating Co metal, thus reducing the driving force for grain growth of the fine grained diamond particles. The closer the change in the saturation level of the carbon in the Co metal is to the diamond solubility curve line (equilibrium carbon solubility limit, C_o), the lower the driving force for grain growth of the fine tail particles. Since a saturated Co melt has the same concentration as the carbon solubility limit Co, there is little to no driving force for grain growth. The infiltrating Co metal saturated with carbon is then swept towards the PCD table, at the interface there is no need for the Co metal to dissolving the first fine grained diamond particles it comes into contact with reducing the conditions for Ostwald ripening (i.e. lower driving force for growth). The Co metal infiltrates (orange arrows in Figure 7-15) into the bulk PCD materials until fully infiltrated, normal grain growth conditions are established. Here the bulk PCD consists of fine grained diamond particles grown together.

For grain growth from a substrate saturated with carbon, like the DEC substrates, very little to no dissolution of the diamond particles at the interface occurs. Figure 7-17 is a schematic representation of the factors affecting the grain growth. For a carbon saturated melt, the concentration of carbon is equivalent to the equilibrium carbon concentration C_o. For a diamond grain size greater than 1µm the carbon solubility in the melt is near to that of C_o, for a diamond grain size less than 1µm the carbon solubility is slightly higher (i.e. for 0.5µm $\backsim\Delta C_3$). The change in the concentration for a DEC substrate is much smaller than that for the standard WC-Co substrate ($\Delta C_3 << \Delta C_2$ & ΔC_1). The driving force for grain growth is also much lower. During sintering, dissolution of the diamond particles is minimal; resulting in only a slight shift in the mean particle size distribution to lower values and the width of the particle size distribution remains similar (Figure 7-17b). There is nearly no change in the driving force, below the critical driving force (i.e. $<\Delta g_c$). The driving force will remain below Δg_c as shown in Figure 7-17c,

resulting in no AGG formation. This is strongly dependent on the kinetics of dissolution of the diamond particles in the DEC substrate.

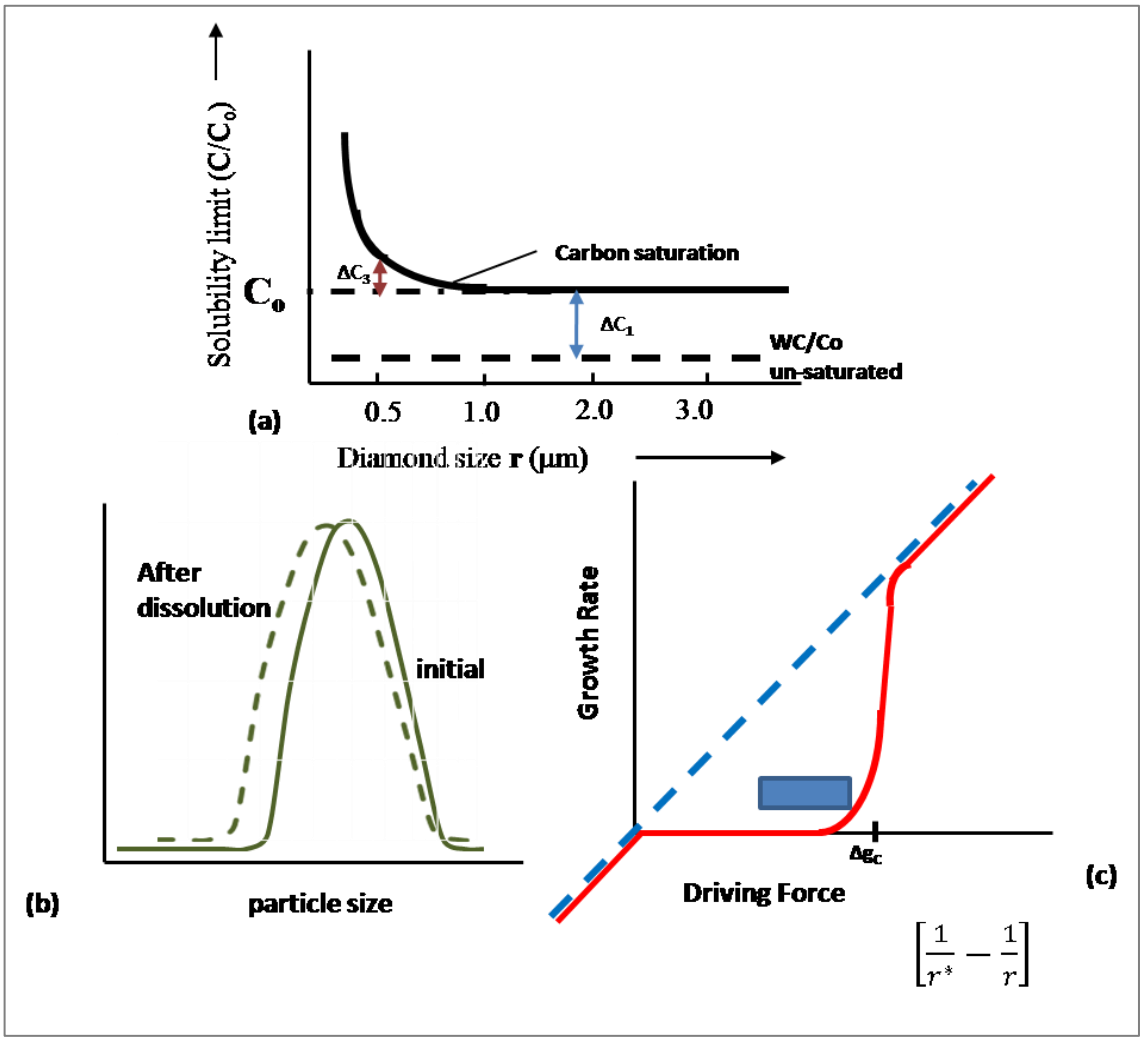

Figure 7-17: Schematic representation of the grain growth formation for WC-Co + excess C (DEC) substrate (a) solubility, (b) grain size effect and (c) driving force.

7.2.3.4. AGG dependence on Carbon content in the substrate

From the theory discussed in Section 7.2, the carbon content in the substrate is an important factor influencing the grain growth. To show the effect excess carbon in the substrate samples has on the abnormal grain growth, the relative excess carbon in the layer compared to that of the diamond was determined The relative excess carbon content was calculated by taking the volume of excess carbon added to the layer and dividing by the volume of diamond in the PCD table, (i.e. Volume excess carbon in layer/Volume PCD layer (%)). The volume of the excess carbon was calculated by multiplying the concentration of carbon by the volume of the coating or interlayer (the interlayer is a layer of the DEC/GDEC substrate backed on a standard WC-Co substrate). The volume of excess carbon takes into account all available added carbon into substrate which can saturate the cobalt melt and infiltrate into the PCD layer. Experimentally, the volume of the PCD table consisted of a 18 mm disc with a thickness of 2 – 3mm.

A comparison of the AGG thickness and relative carbon content of the coated layers (0, 2, 4 and 6%C) and standard WC-13Co substrate for the FG-0.5µm diamond samples was determined (

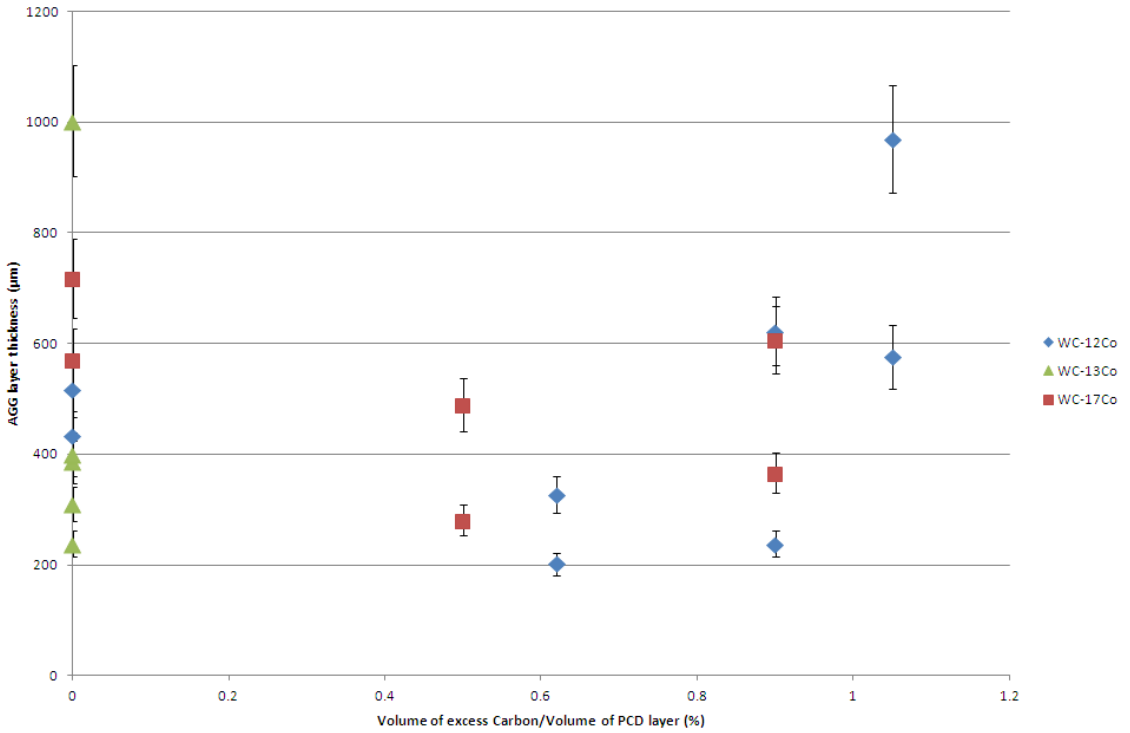

Figure 7-18). The standard WC-13Co and 0%C coatings had a 0% relative excess carbon (i.e. no added carbon), while the 2, 4 and 6%C coatings had a relative excess carbon in the region of 0.5 – 0.63%, 0.9% and 0.9-1.0% for the carbon enriched coatings respectively. These depended on the thickness of the coated layer and PCD table. The results show that the materials with the overall lowest AGG thickness were the 2%C enriched samples (equivalent to 0.63% excess C and 0.5% excess C) for both the 12Co and 17Co coatings respectively.

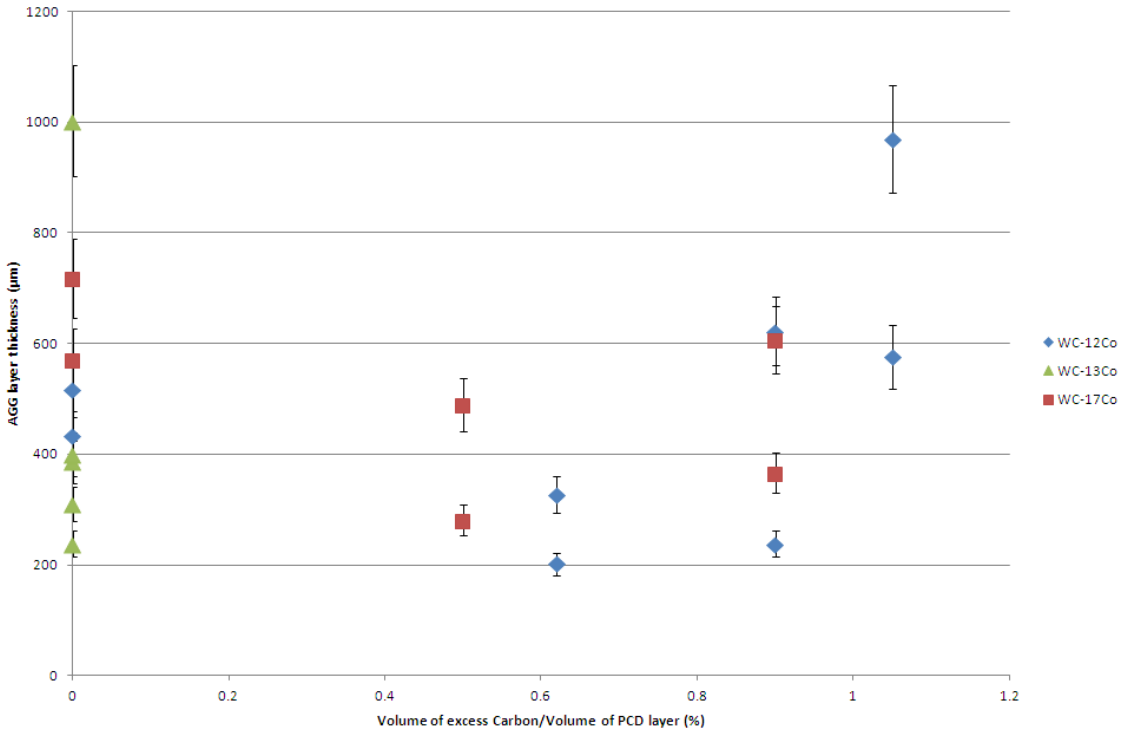

Figure 7-18: Comparison of the AGG with relative excess carbon in the coated layers for FG-0.5µm diamond (10% error).

Similarly, the AGG thickness and relative carbon content of the various DEC/GDEC layers were also determined, Figure 7-19. The results show that the at a relative excess carbon content of 41.7% (full 10vol.% GDEC), no AGG was evident in the materials. This also shows the vast difference between the effect of the carbon contents on the AGG region of the coatings, GDEC/DEC interlayers and full GDEC substrate; the high excess content of the full GDEC substrate resulted in a high enough saturation to prevent AGG of the fine grain diamond.

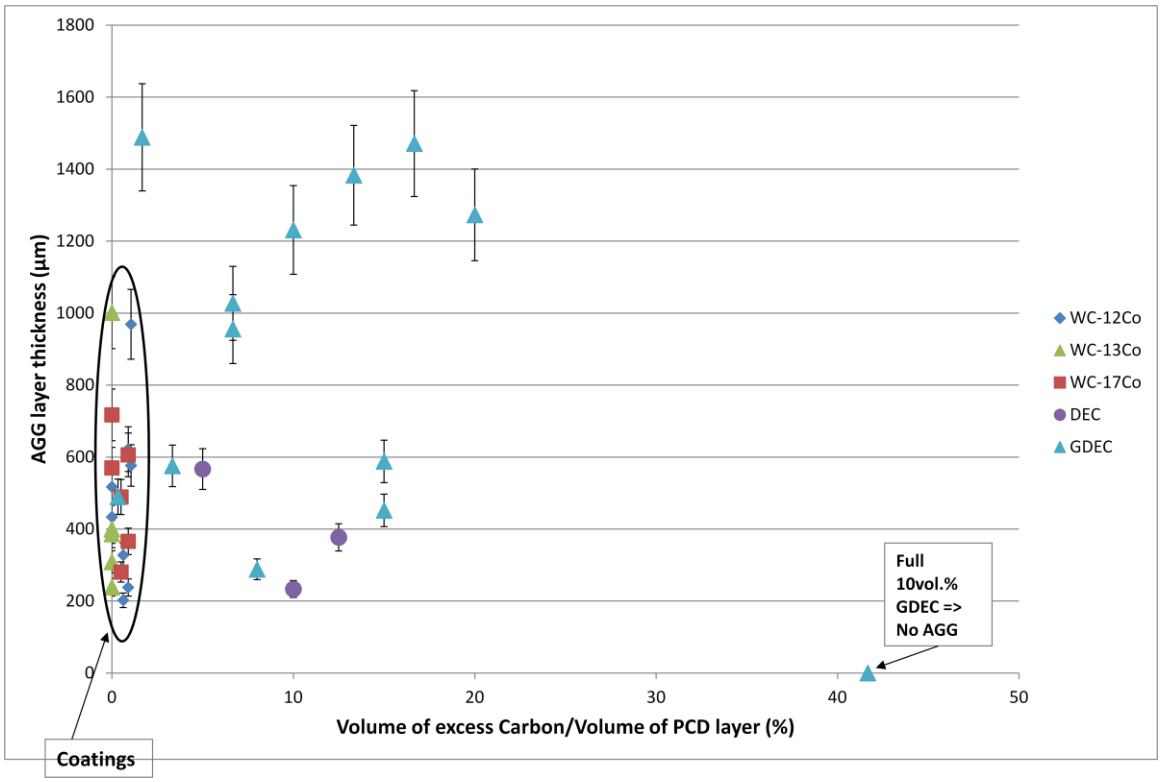

Figure 7-19: Comparison of the AGG with relative excess carbon in the coated and DEC/GDEC layers for FG-0.5µm diamond (10% error).

The micrographs of the DEC/GDEC substrates (Section 6.2.2.2) show that in the substrate a high amount of carbon was left. Therefore, the overall concentration of excess carbon in the substrate was not the appropriate value for controlling AGG. The existence of excess of carbon in the substrate suggests that the solution kinetics was not high enough to achieve full saturation during the infiltration of Co into the diamond layer. Therefore the AGG was plotted against the thickness of the carbon enriched layer (Figure 7-20); the thickness of the carbon enriched layer after PCD sintering showed very little change.

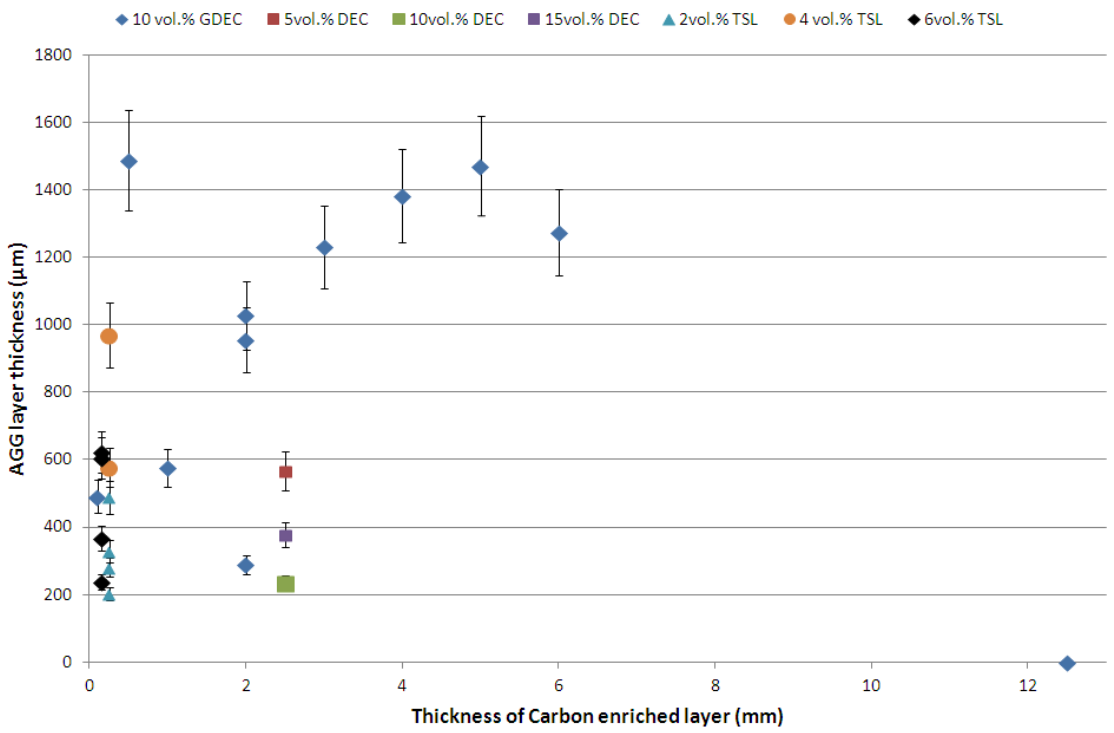

Figure 7-20: Comparison of the AGG thickness to the thickness of the Carbon enriched layers (10% error), (TSL – Thermal sprayed layers/coatings).

7.2.3.5. Effect of dissolution in DEC/GDEC substrate

Results shown in Section 6.2.2.2 on both the GDEC and DEC substrate showed AGG at the interface, even in samples carrying 5 - 15vol.% excess carbon in the form of diamond particles, Figure 7-21. Optical/SEM images of the DEC layers after sintering showed retained excess carbon (Figure 7-22). The DEC/GDEC layer thickness before and after sintering was measured; the layer thickness in all samples decreased slightly. In Figure 7-23, the dotted line shows the boundary point at which the amount of carbon in the interlayer remained constant. For data is below the dotted line, there was a reduction in the DEC layer thickness after sintering, suggesting that some of the carbon from the substrate was dissolved into the melt during sintering.

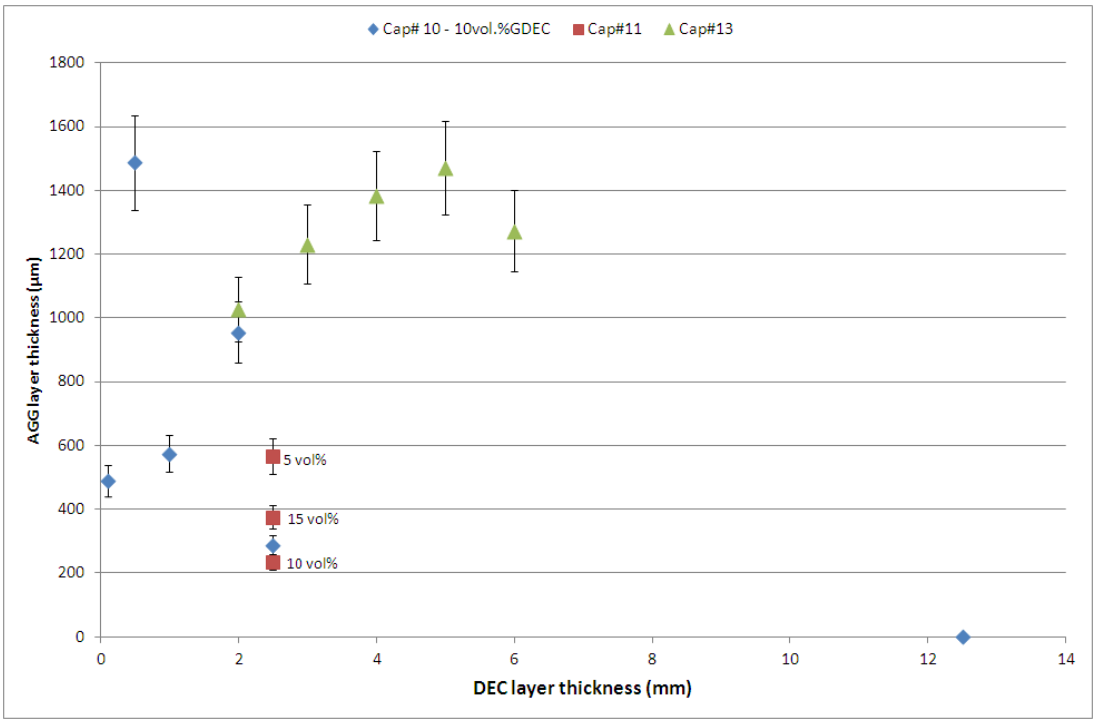

Figure 7-21: DEC layer thickness and effect of AGG thickness (10% error).

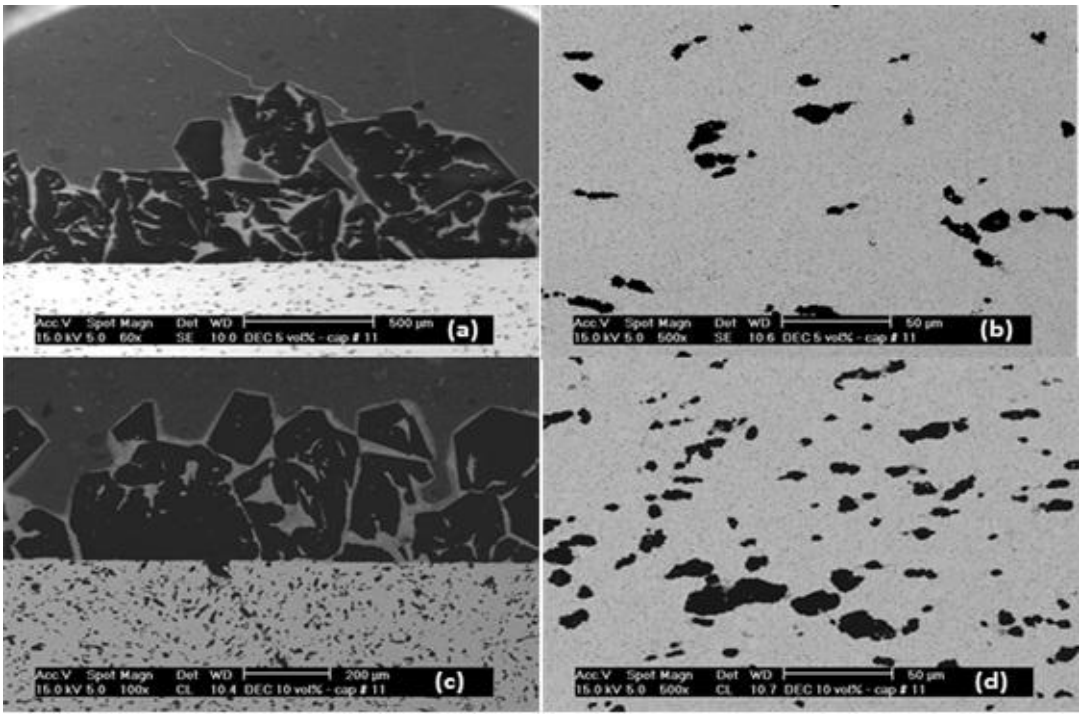

Figure 7-22: SEM-BSI images of the DEC substrates after sintering showing a high amount of carbon remaining.

Even in the 5vol.% DEC inter-layer, there was enough carbon remaining after sintering. By theory, only a very low amount of carbon in the DEC (1vol.% or less) is required for saturation of the melt. Remaining carbon in the DEC substrate after sintering suggests that there was enough carbon available to cause saturation of the melt, but AGG formation suggests insufficient saturation of the melt. This would mean that there was a kinetics effect on the dissolution of carbon in the interlayer during sintering. The particle size of the diamond in the DEC/GDEC layers were determined to be about 10 - 25µm. The particles may have been too large for sufficient dissolution during sintering to cause saturation of the melt. This would suggest that the kinetics of dissolution of carbon/diamond in the substrate needed to be increased for the DEC substrate to suppress AGG formation. Smaller grain size particles can be used to increase the kinetics of dissolution.

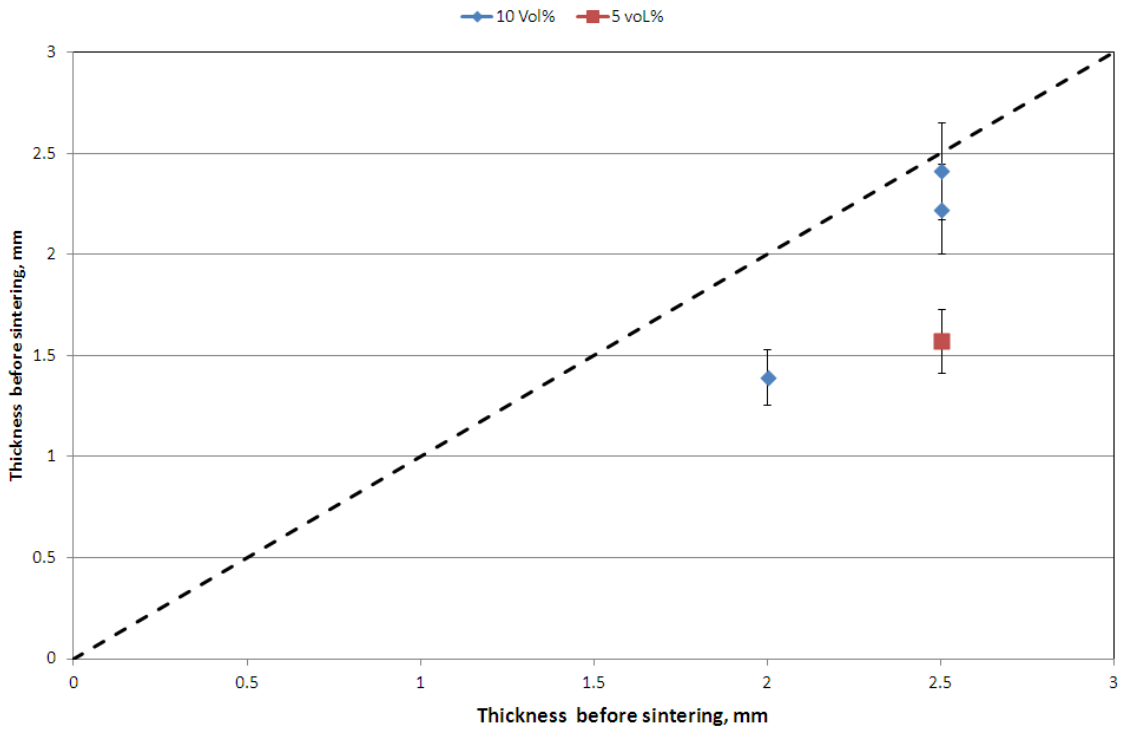

Figure 7-23: Comparison of the DEC/GDEC thickness before and after sintering (10% error).

7.2.3.6. WC-Co substrate with diamond particles of a similar size as the PCD

A similar particle size distribution of the diamond in the DEC substrates to that used for the PCD was used to increase the kinetics of dissolution and subsequent saturation of the melt (i.e. increased dissolution kinetics results in increased saturation). A schematic representation of the factors affecting the grain growth during sintering of the similar particle size diamond in the DEC substrate is shown in Figure 7-24. For similar sized diamond particles in the DEC substrate, there is an increase in over-saturation of the carbon in the Co melt above the carbon saturation line/curve (blue dotted line in Figure 7-24a) corresponding to the mean grain size r* of the C inclusions. Therefore the larger diamond particles will be in contact with an oversaturated melt, whereas the mean particle size will be in contact with a saturated melt. This means that the larger particles will grow slightly, the mean particles will not significantly change and the small particles will dissolve. Taking into account the calculated values from Figure 7-12, a homogeneous grain growth would be expected for mean grain sizes ≥ 0.1 – 0.2 µm, additionally the Co pooling would be suppressed. No dissolution of the diamond particles at the interface occurred. The particle size distribution of the diamond powders will shift to slightly coarser values (Figure 7-24b), with very little change in the mean distribution. This results in nearly no change in the driving force for growth (i.e. $<<\Delta g_c$), allowing the diamond particles to remain small (Figure 7-24c).

Although the concept of the use of similar size diamond in the substrate to that of the PCD layer is an innovative idea in increasing the kinetics of carbon dissolution in Co melts to reduce AGG formation, the execution of this showed less than satisfactory results as shown in Section 6.2.2.2 (Figure 6-30). AGG was noted in the samples sintered. The diamond particles in the substrate were strongly aggregated, this would mean that the effective grain size would be larger than 0.5µm (Figures 6-30 – 6-32),

resulting in insufficient dissolution for saturation. AGG occurred on a local scale along the interface (i.e. AGG as suppressed in areas along the interface). This shows that the concept has merit.

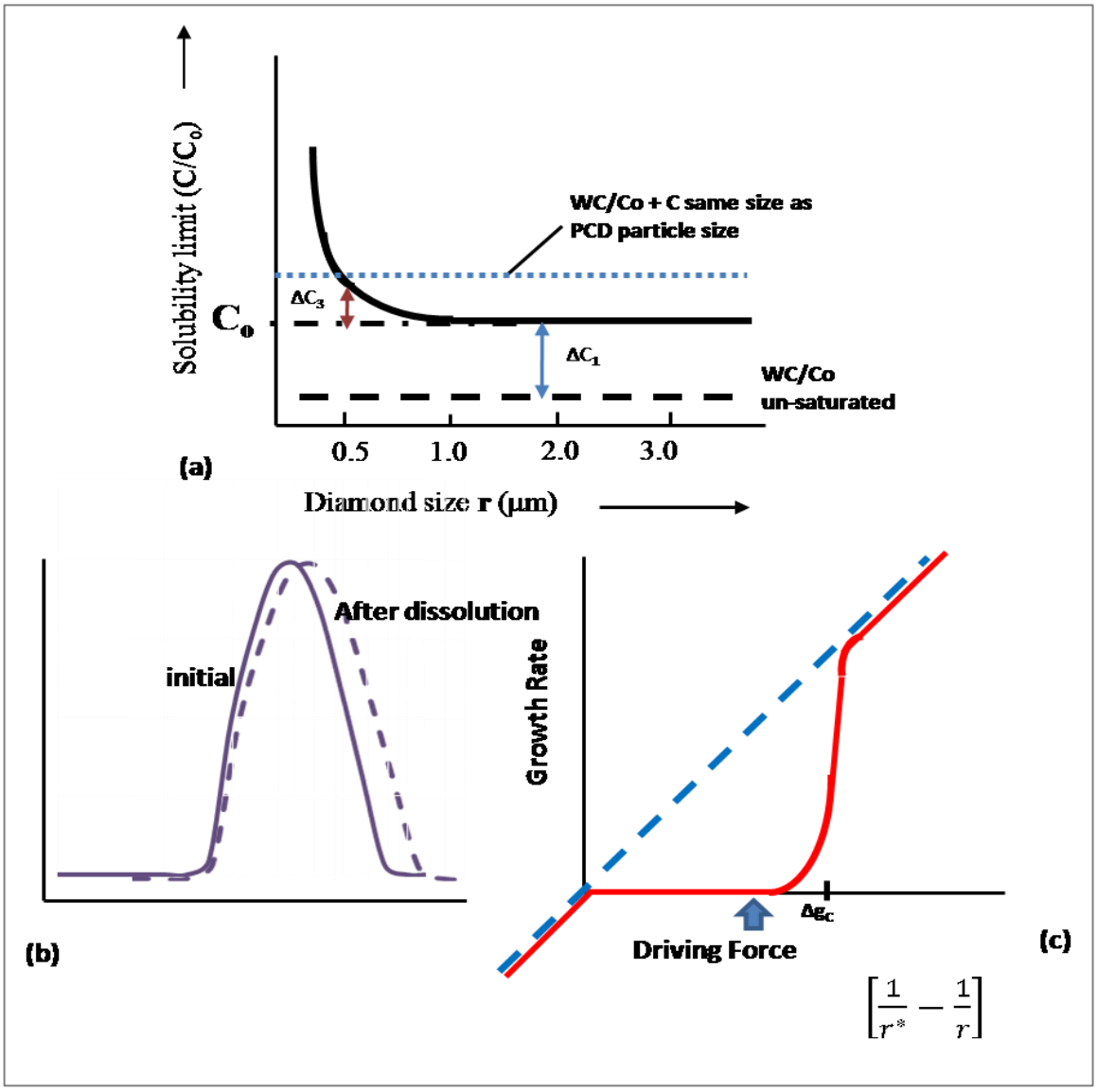

Figure 7-24: Schematic representation of the grain growth formation for similar size diamond DEC substrate (a) solubility, (b) grain size effect and (c) driving force.

7.2.3.7. Co-pool formation

Figure 7-15 shows the point for a conventional WC-Co substrate, unsaturated in carbon. During sintering the Co melt at the interface is not saturated with carbon, once the Co melt infiltrates into the PCD layer dissolution of the diamond particles at the interface occurs rapidly. This causes Co pool formation at the interface to be nearly independent of the grain growth and irrespective of the grain size of the material. Evidence of this can be seen in the comparison between the Co-pool formation with carbon content in Figure 7-2 and Figures 7-25 – 6-26. The SEM images shown in Figures 7-27 and 7-28 for MG and FG-6 µm sintered samples show evidence of the Co pool formation at the interface. Co-pool formation is stronger in the lower diamond size materials, due to the faster dissolution of the diamond near the interface and the slightly higher equilibrium concentration. For larger grain sizes, the dissolution will take place over a larger area and therefore is not as pronounced. Similar results were seen for the carbon-enriched coated substrates where there is an insufficient amount of carbon in the layers for saturation so the samples acted like the standard substrate.

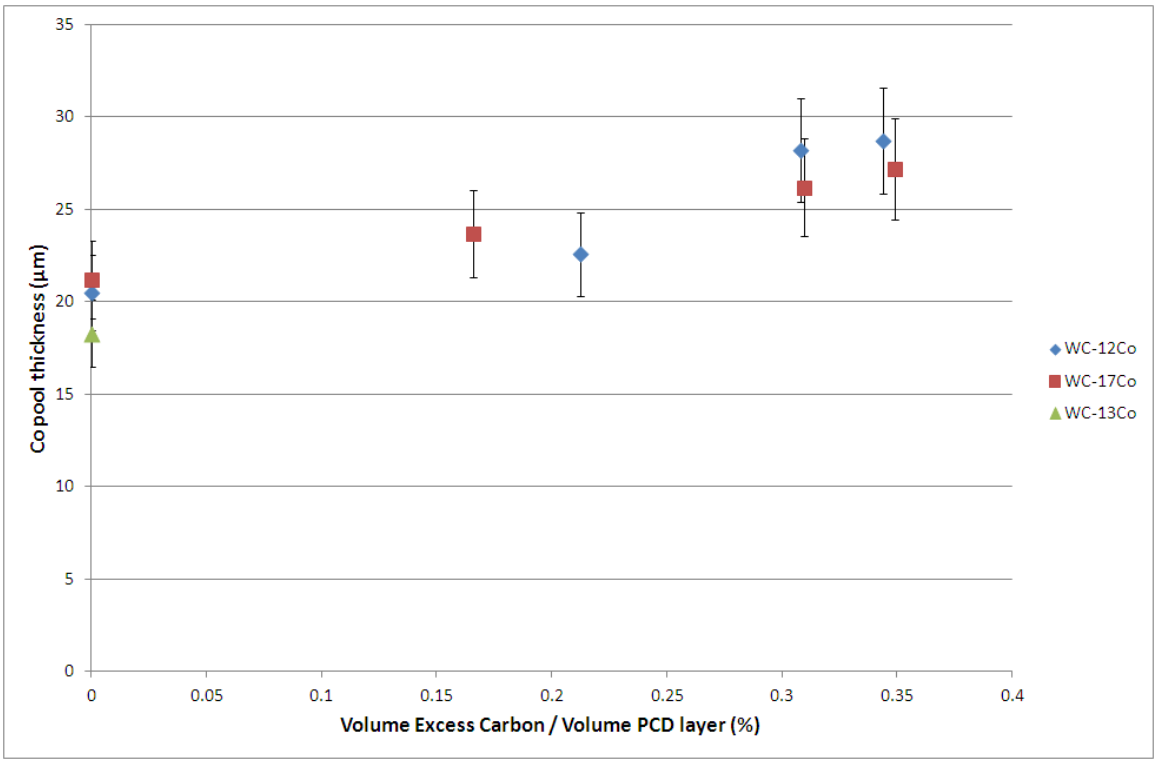

Figure 7-25: Comparison of the Co-pool thickness with relative excess carbon in the coated layer for FG-6µm diamond samples (10% error).

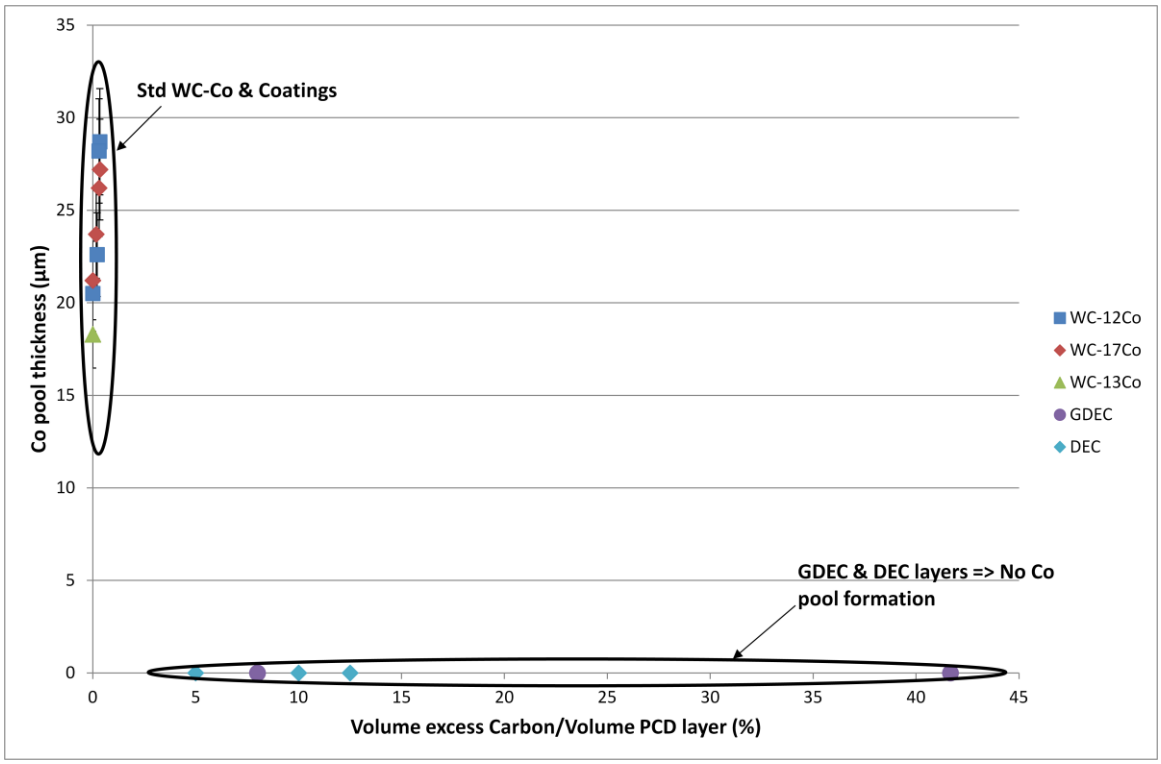

Figure 7-26: Comparison of the Co-pool thickness with relative excess carbon in the coated and DEC/GDEC layer for FG-6µm diamond samples (10% error).

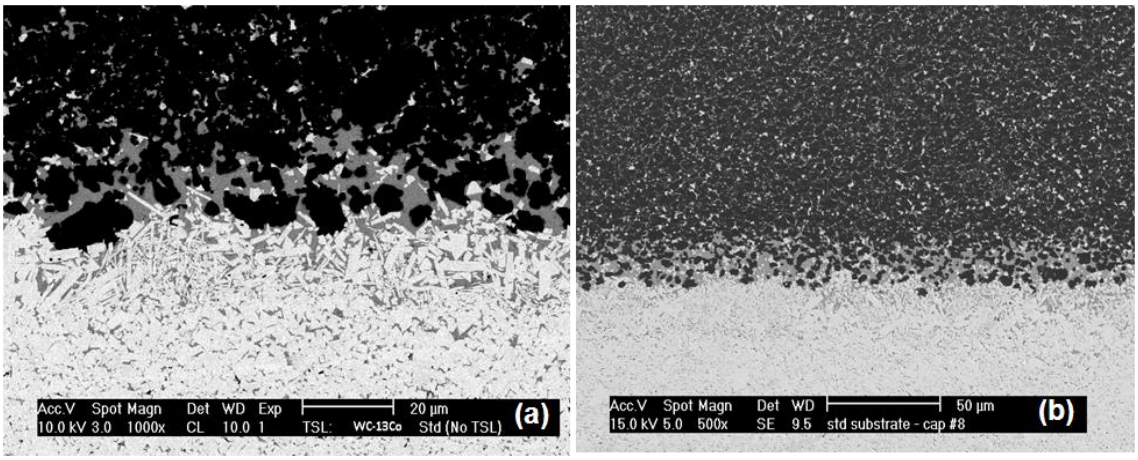

Figure 7-27: SEM-BSI showing Co-pool formation in standard WC-Co substrate for (a) MG diamond powder and (b) FG-6µm diamond powder.

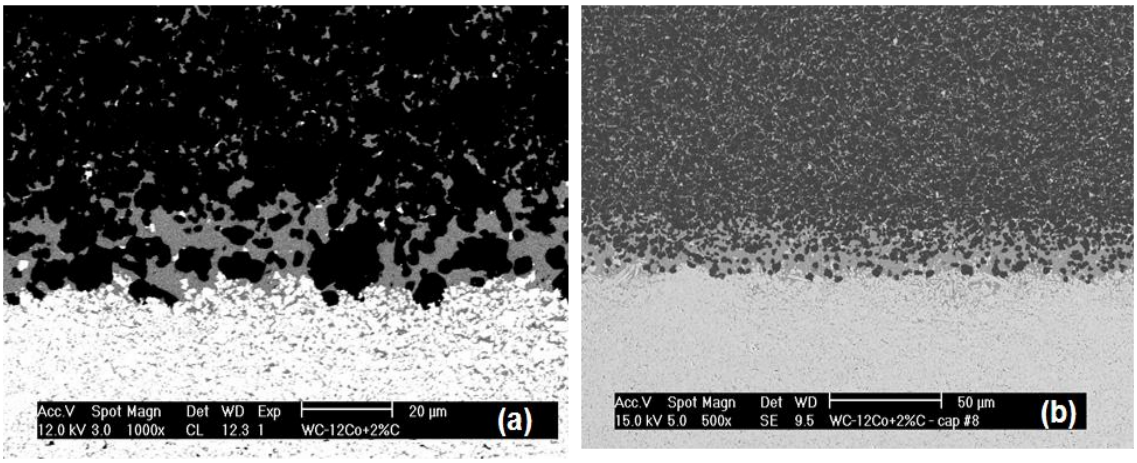

Figure 7-28: SEM-BSI showing Co-pool formation in a WC-12Co+2%C coated sample for (a) MG diamond powder and (b) FG-6µm diamond powder.

For the DEC substrate, Figure 7-15 shows a schematic diagram of the DEC substrate during sintering, corresponding to the point at which the carbon in the melt is saturated. During sintering, the Co melt at the interface becomes saturated with carbon by dissolving the diamond particles in the substrate; once the Co melt infiltrates into the PCD layer little to no further drive for dissolution of the diamond particles at the interface occurs (i.e. already saturated). This causes no Co pool formation at the interface. Evidence of this can be seen in Figure 7-29, where the FG-6µm diamond grain size was used with various DEC or GDEC substrate inter-layers, no Co-pool formation was apparent.

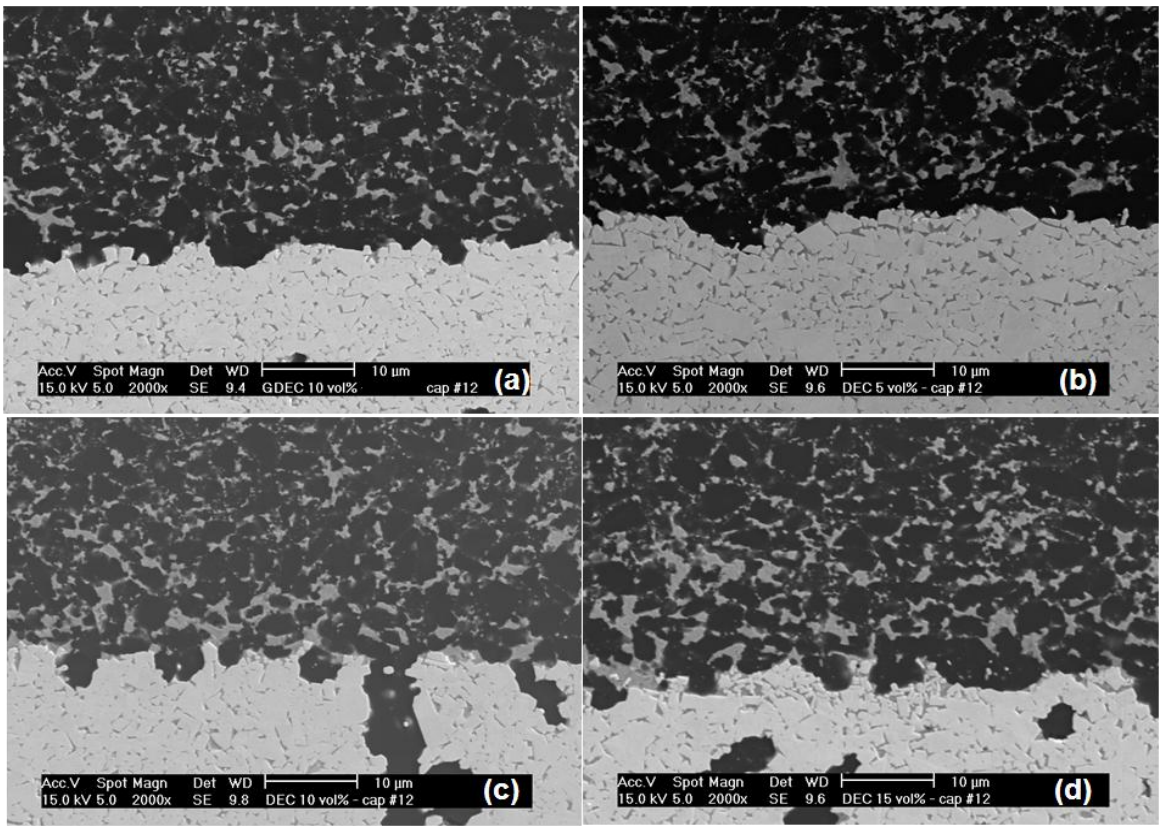

Figure 7-29: SEM-BSI showing the interface of FG-6µm diamond powder sintered on various WC-Co + excess C substrate/inter-layers (a) 10vol.% GDEC, (b) 5vol.% DEC, (c) 10vol.% DEC and (d) 15vol.% DEC, showing no Co-pool formation.

7.2.3.8. Effect of changing interfacial energy on AGG formation

As explained previously (Section 2.2.4 above) changing the interfacial energy of the diamond particles results in a change in the growth mechanism. Small additions of grain growth inhibitors such as VC, Cr_2C_3 and cBN can be used to change the solid/liquid interfacial energy and or block active sites for growth. The shape of the particle grains can change from faceted to spherical/rounded. Rounded particles undergo diffusion related grain growth (i.e. follow a linear dependence on the grain growth with driving force, blue dotted line in Figure 2-5). This process is more controllable than interfacial

reaction controlled growth. There is very literature available relating to the effect VC has on diamond grain growth, the exception being the patent WO 2011/042566A1 by Israelsson et al. (Israelsson et al., 2011). This patent suggested that refractory metal or metal carbides from the group (Ti, V, Cr, Zr, Nb, Mo, Hf and Ta) can reduce the abnormally large diamond grains in fine grain diamond. There is much literature on the effect VC and other grain growth inhibitors have on WC-Co systems (Sun et al., 2011; Lei & Wu, 2009; Choi et al., 2000). VC has a high solubility and mobility in the Co phase and is thus the most effect grain growth inhibitor for WC-Co systems.

As described previously AGG of faceted materials like WC-Co and diamond occurs due to 2D nucleation controlled coarsening. From the theory of 2D nucleation given in Section 2.2.1, the rate of 2D nucleation interfacial controlled grain growth (Equation 2.7) is dependent on various parameters. One of the largest parameters is the step/edge free energy (σ). Small changes in the edge energy will result in noticeable changes in the driving force for growth. Choi (Choi et al., 2000) explained that the addition of VC to the WC-Co system will result in increased edge energy of the WC crystal thereby increasing the 2D nucleation energy barrier. When the edge energy increases, the formation of nuclei is retarded, thereby decreasing the rate of material transfer. The number of growing grains also decreases dramatically because the driving force is significantly high to overcome the 2D nucleation energy barrier allowing for suppression of AGG of the WC grains. This theory can also be applied to diamond grain growth. The addition of Cr as a grain growth inhibitor would be more effective, Cr dissolves more readily in Co, it therefore is more intensively transported to the diamond-Co interface.

Additionally the solid/liquid interfacial energy can be changed with additions of grain growth inhibitors. The interfacial energy of a system is lowered by additions of grain growth inhibitors such as VC. Figure 7-30 shows a schematic representation of the effect of lowering the interfacial energy on the solubility and therefore the driving force for

grain growth of the diamond. By lowering the interfacial energy of the diamond, the solubility curve shifts to the left, lowering the driving force for growth. A calculation was made to determine the effect of changing the interfacial energy on the solubility curve. Increasing the interfacial energy of the diamond particles resulted in increasing the solubility curve, therefore increasing the solubility change and driving force for growth. On the other hand, a decrease in the diamond interfacial energy decreases the solubility curve and shifts it to lower grain size values resulting in lower driving forces for grain growth.

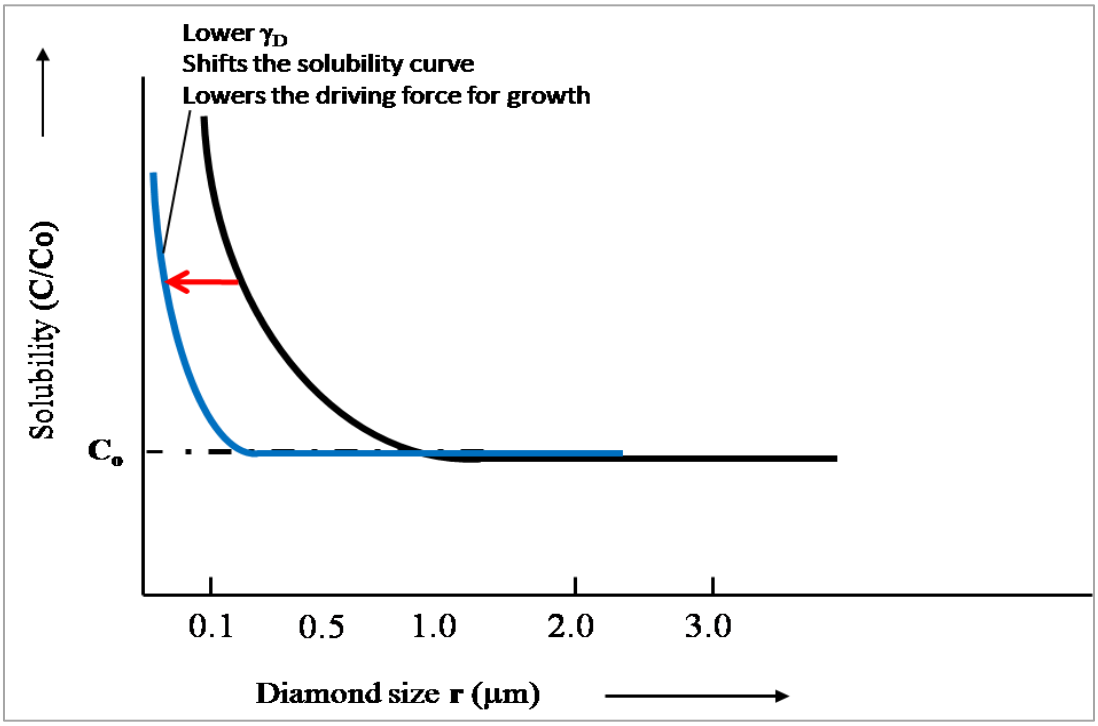

Figure 7-30: Schematic diagram showing the effect lowering the interfacial energy of the diamond on the solubility and driving force for grain growth.

Lowering the interfacial energy of the diamond particles by introducing a grain growth inhibitor (VC) was shown in Section 6.2.3 to be very effective. Additions of 2wt%VC to the substrate interlayer showed no AGG formation in 0.5µm fine grained PCD. It was not

possible to measure the change in interfacial energy of the diamond with the addition of VC, but this change must have been significant enough to shift the solubility curve to values where the driving force for growth was low. The particle size and shape of the diamond crystals near the interface remained small (<<1µm) and were still faceted, shown in Figure 7-31. This result confirms the suggestion by Israelson et al. (Israelsson et al., 2011) that the small addition of VC can decrease the abnormally large diamond grains in fine grain PCD. It eliminates large grain growth completely.

Addition of VC formed a (W,V)C pool (2-3µm thick) at the interface instead of a Co pool. This was due to the VC in the WC-Co dissolving in the high Co content, being attracted towards the diamond table, the V meets the diamond particles and readily bonds with excess carbon; and therefore precipitates out as VC at the interface displacing Co. EDX results showed that the VC content in the substrate decreased with increasing distance away from the interface, most of the VC was concentrated in the VC pool at the interface.

The addition of VC to the 0.5µm diamond GDEC layer had no real effect of the grain growth of fine grain PCD. This was because the driving force of the 0.5µm diamond particles inside the interlayer was too high compared to the effect of the VC (i.e. the transportation of the VC to the diamond interface was not fast enough).

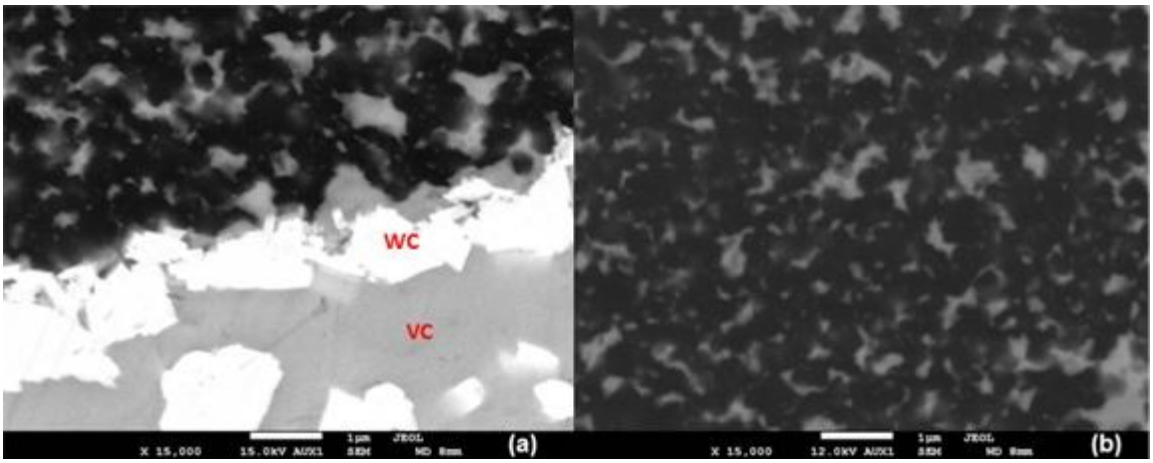

Figure 7-31: SEM-BSI images of the interface of the sintered 0.5µm diamond on the 2wt% VC doped substrate showing (a) interface and (b) fine grain diamond.

Chapter 8: Summary

A summary of the results from the numerous experiments done on carbon enrichment of WC-Co powders, wear tests and PCD sintering were the following:

1. Carbon enrichment of WC-Co powders were possible using a phenolic resin precursor followed by pyrolysis. Carbon enriched powders of 2, 4 and 6wt%C were produced. Carbon enrichment of powders above 2wt% required a multi-stage process of C enrichment and pyrolysis. Carbon adhered to the surface of the WC-Co particles.

2. Thermal spraying was used to produce carbon enriched WC-Co coatings from the carbon enriched WC-Co powders. The higher the carbon content, the more problems resulted in the spraying of the coatings. These problems included high amounts of carbon burn off, low deposition thickness and a lack of retained carbon in coatings. Quantification of the amount of carbon retained in the coated layers was difficult to determine.

3. Eta phase (η - $Co_xW_xC_z$) and decarburized WC phase (W_2C) generation was suppressed during spraying of the carbon enriched powders, especially in the 2wt%C samples. Higher carbon values the effect was counteracted by spraying and deposition problems.

4. Wear resistance of the as-sprayed and carbon enriched coated layers was good, and carbon enriched 2%C samples showed improved wear resistance.

5. The wear of annealed WC-Co coatings at 700°C for 1 hour was analysed, the results showed that decomposition of the phases in the coatings occurred; W_2C and η (eta phases) were generated. Crystallization of the amorphous Co region also occurred. Heat treatment of WC-Co coatings used in PCD sintering at 1100°C in H_2 for 1 hour caused W_2C to revert back to WC and recrystallization of Co phase occurred (i.e. formation of a pure WC/Co phase).

6. The wear resistance of the heat treated coatings showed lower values than that of the as-sprayed region for most coatings.

7. The worn surfaces of the as-sprayed coatings were analysed, showing that the abrasive wear mechanisms affecting the coatings were removal of the binder phases, micro-cracking of the WC particles and pull-out of the WC particles.

8. Hardness values were in the region of 400 – 850 HV, lower than some values quoted in literature. High porosity levels in the coatings could have affected the measured results. The heat treated coatings showed lower hardness values compared to the as-sprayed coatings, which is contradictory to some authors.

9. The correlation between wear and hardness of the coatings were opposite, good wear resistance was associated with in low hardness, and similarly, coatings with good hardness showed low wear resistance for both the as-sprayed and heat treated conditions.

10. Overall, the 2%C enriched coating produced the best results in terms of good wear resistance.

11. A model was produced to potentially reduce or eliminate abnormal grain growth of diamond particles in fine grained PCD (0.5μm). The model was based on

reducing carbon gradient between the WC-Co substrate and the diamond PCD layer. The proposed model suggested that by increasing the carbon content (until saturated or near saturation) of the infiltrating Co metal during HPHT sintering before reaching the PCD layer will potential reduce the driving force for grain growth of the diamond based on the Gibbs/Thompson effect. The method of increasing the carbon content of the infiltrating Co melt was by increasing the carbon content of the WC-Co substrates. The proposed method of increasing the carbon content of the WC-Co substrate was to add a carbon enriched layer between the WC-Co and the PCD layer. The carbon enriched layer was produced by HVOF thermally spraying a carbon enriched WC-Co powder onto the WC-Co substrate.

12. PCD sintering using the carbon enriched coated layers had no real affect in reducing or eliminating diamond abnormal grain growth. Lack of retained carbon in coatings resulted in insufficient carbon to saturate the infiltrating Co metal, thus reducing the driving force for grain growth. Wear results on coated PCD were good but did not surpass the standard PCD cutter.

13. Graphitized-diamond and diamond enhanced carbides (GDEC and DEC) were used to modify the infiltrating Co metal to reduce/suppress abnormal grain growth of fine grained (0.5μm) diamond. Interlayers of the GDEC and DEC substrates with various diamond contents were used.

14. A range of different thickness (0.5 – 12.5mm) of the 10vol.% GDEC inter-layers were studied. AGG was visible in most 0.5μm PCD samples, suggesting insufficient carbon saturation of the Co melt.

15. A full 12.5mm 10vol.% GDEC substrate was successful in eliminating abnormal grain growth of the diamond at the substrate/PCD interface of the 0.5µm PCD sample. This proved the proposed model that by saturating the Co metal with carbon before reaching the PCD layer will eliminate abnormal grain growth in 0.5µm fine grained PCD.

16. Various concentrations of the DEC (5-15vol.%) were also studied. AGG was evident in all 0.5µm PCD materials.

17. Addition of 10vol.% 0.5µm diamond GDEC to the inter-layer encourages increased dissolution rates of the diamond by increasing the kinetics. Although results showed that in some areas AGG was prevented, not all AGG was eliminated. This could suggest that the kinetics of solution was not fast enough to saturate the infiltrating Co melt to facilitated grain growth suppression.

18. Additions of VC (2wt%) into the WC-Co substrate lowers the interfacial energy of diamond resulting in no AGG occurring at the interface. Diamond grains remained small (<< 1µm). This confirmed the suggestion made by Israelsson et al. (Israelsson et al., 2011), patent WO 2011/042566A1, that small additions of VC can decrease large abnormal grains in fine grain PCD.

19. Sintering of PCD materials at high pressure and high temperature (HPHT) conditions was very problematic. Very small changes in process conditions had a substantial effect of the outcome, especially in highly reactive systems such as fine grained diamond. Even within the same sintering run (i.e. same capsule) the conditions can differed, producing different results.

20. Electron back-scattered diffraction (ESBD) analysis of AGG regions showed various grain orientations of the large grown diamonds.

21. There are two main ways of avoiding the formation of AGG in faceted materials such as PCD: control of the oversaturation of the melt and changing the interfacial energy (γ_{sl}) of the diamond in the melt.

22. Two factors that can affect the carbon solubility of the melt in PCD sintering are: (a) changing the composition of the substrate (i.e. standard WC-Co versus WC-Co + excess carbon), and (b) changing the carbon solubility with grain size of the diamond particles.

23. From calculated data of the carbon solubility in the melt, there was a strong dependence of the solubility on the grain size of diamond only below 0.2-0.3µm. Data showed that the carbon concentration in the melt was affected more by the saturation in the melt from the substrate than the grain size (even at 0.5µm diamond grain size). Evident in alternate diamond laminates (2µm and 0.5µm diamond) produced by EPD (Džepina, 2012), no AGG was observed between the two layers.

24. A model was developed to compare the grain growth and Co pool formation of PCD with conventional WC-Co substrate and WC-Co carbon enriched substrate.

25. In conventional WC-Co substrates, the infiltrating Co melt was unsaturated, generating a carbon sink between substrate and PCD layer. Fine grain particles dissolve readily into the Co melt saturating the melt, by Ostwald ripening conditions of larger particles tended to grow. The change in carbon concentration between the unsaturated Co melt and the PCD layer was determined (ΔC_1 for grain size > 1µm and ΔC_2 for grain size ~ 0.5µm). The shift in the mean particle distribution to lower values (dissolution of fine grains), resulted in an increased driving force for grain growth beyond the critical driving

force for interfacial reaction. Grain growth occurred exponentially and AGG became prevalent.

26. In carbon enriched WC-Co substrates (i.e. coatings and DEC substrates), the Co melt is saturated with carbon, the carbon solubility was equivalent to the equilibrium solubility limit (C_o) (diamond solubility curve). The change in carbon concentration, $\Delta C_3 << \Delta C_2$ and ΔC_1, therefore lowering the driving force for grain growth. A saturated Co melt required no dissolution of fine grain diamond particles (i.e. minimal shift in the mean particle size distribution - eliminating the conditions for Ostwald ripening). Driving force remained below the critical driving force (Δg_c), resulting in no AGG formation and normal grain growth conditions occurred.

27. Conditions for carbon enriched substrates were dependent on the kinetics of dissolution of carbon into the melt. Slow kinetics resulted in insufficient dissolution to cause saturation, giving in Ostwald ripening conditions. Kinetics was increased by introducing similar size particles in the substrate to PCD layer (i.e. 0.5µm PCD, 0.5µm or less diamond particles in substrate).

28. Similar size particles results in an oversaturated melt (i.e. carbon concentration above the carbon saturation curve). The larger grains were in contacted with an oversaturated melt, growing slightly. No significant change in the mean particle size occurred, resulting in no change in the driving force for growth (i.e. $<<\Delta g_c$) allowing the fine grain particles to remain small.

29. Co pool formation in conventional WC-Co substrates (i.e. un-saturated) occurred at the interface between the PCD layer and the WC-Co substrate independently of grain growth and irrespective of the diamond grain size. Evidence was seen of Co pool formation in MG (8µm) and FG-6µm (6µm)

diamond samples. Co pool formation was more dominant in lower grain size materials due to faster dissolution rates near interface.

30. Co pool formation in carbon enriched substrates (i.e. DEC) was prevented due to the saturation of the Co melt. Little to no dissolution occurred at the interface, resulting in no Co formation. This was seen in DEC substrates sintered with FG-6µm diamond.

31. Change of interfacial energy of the diamond particles can also reduce the driving force for grain growth and thus eliminated AGG in fine grain materials. Grain growth inhibitors such as VC were can be used to change the interfacial energy of diamond particles. Decreasing the interfacial energy resulted in a shift of the solubility curve to lower grain sizes (i.e. to the left).

Chapter 9: Conclusions and Recommendations

The conclusions drawn from this project outlined in the summary above, as indicated in the introduction (chapter 1) the aim of this project was to reduce or eliminate abnormal grain growth of fine grained polycrystalline diamond by manipulation of the infiltrating cobalt melt. The Co melt was changed by altering the saturation of carbon in the melt, by producing a carbon enriched layer acting as a barrier between the substrate (WC-Co) and the PCD layer. The carbon enriched layer was produced by carbon enrichment of a WC-Co thermal spray powder, which was subsequently sprayed onto a substrate (WC).

It was also hypothesized that the addition of carbon to the WC-Co powder can potentially also decrease the amount of WC decarburisation which takes place during thermal spraying by acting as a reducing agent to form CO_2 instead of decarburisation of WC. This decrease in decarburization of WC would result in a decrease in eta phases and potential increase the wear resistance of the coating in wear coating applications. The results obtained suggest that the carbon enrichment of WC-Co powders and subsequence thermal spraying of powders on to a substrate can be achieved; however, limitations exist in production. Producing a completely homogeneous carbon enriched thermal sprayed layer is difficult and subjected to limitations which include high free carbon in the powders which decreases thermal spraying efficiency and thus deposition rate, affecting decarburization. Good hardness and wear resistance can be achieved to but is subjected to variations in coating homogeneity. Although these carbon enriched WC-Co coatings can be made, the viability in making them does not result in the expected hypothetical results, i.e. a well-defined decrease in eta phase generation and a substantial increase in wear resistance.

Limited carbon enrichment of coated substrates subsequently has an effect on the desired use of the coating, i.e. to act as a carbon source to manipulate the Co infiltrant and thus decrease grain growth in fine grain PCD manufacture. Test results confirmed this limitation by having to significant effect on abnormal grain growth reduction. Eliminating the use of carbon enriched thermally sprayed coatings as an option for infiltrant manipulation.

A subsequent procedure such as GDEC and DEC substrates were used to manipulate the infiltrant. These substrates having high carbon content although in the form of graphite/ graphitized diamond were also analysed and proved to be more effective depending on the dissolution kinetics of the carbon source during sintering. Fast dissolution of graphite/diamond was required to effectively saturate the Co infiltrant before reaching the diamond layer. A full 10vol.%GDEC substrate showed no AGG at the interface, which resulted from longer time and faster dissolution of the graphitised diamond at the bottom of the substrate where the Co starts to infiltrating from so that when reaching the PCD layer the Co melt is already completely saturated with carbon. Models were derived and summarized above (chapter 8) showed the differences in saturation effects of various substrates. Finer grain size graphitized diamond in a WC-Co layer was also tested and although did not result in the required results in this project should not be over looked as a potential carbon source for future PCD grain growth experiments. Potentially finer particles of carbon are highly reactive and will result in faster dissolution and therefore saturation of the molten infiltrant.

Another method of grain growth reduction was also evaluated, although not initially hypothesised in this study is grain growth inhibitors. A strong grain growth inhibitor in WC-type materials (VC) was tested and proved very effective in eliminating grain growth of fine grain PCD. A brief model was suggested on the effect the grain growth inhibitor has on the saturation of the Co infiltrant. Additional examination of

strong carbide formers and their effect on diamond grain growth and Co saturation needs to be analysed.

Further study on diamond grain growth and the elimination of AGG in fine grained diamond materials is essential in providing future knowledge. Recommendations for future work are given below.

Recommendations

Proposed further studies into eliminating abnormal grain growth in fine grained PCD can be done to further the PCD grain growth model. Suggested work could include modifying the diamond crystals by adding a grain growth inhibitor either to the initial diamond powder of the WC-Co substrate. Finer grain sized diamond particles (<0.5µm) can be added to the substrate to facilitate faster dissolution kinetics, to improve saturation of the infiltrating Co melt. The use of grain growth inhibitors such as Cr_2C_3 has to be investigated; the Cr dissolves more in Co in comparison to VC, which will result in a more intense and faster transportation to the diamond-Co interface, thereby facilitating reduced driving force for grain growth. Another addition that can be assessed at to improve sintering of fine grain diamond is Ni, Ni-Cu alloys or Ti. Ni and Ti sinter diamond at lower rates than Co. The use of Ti(C, N) doped WC or cermets can also be of potential use. These materials lower the interfacial energy of diamond crystals, therefore reducing the driving force for grain growth. By shifting the solubility curve of diamond and passivating the diamond particles, these additives can potentially allow for the production or manufacture of finer PCD materials, even to the nano scale, without large abnormal grain growth issues.

References

Akaishi, M., 1991. Synthesis of fine-grained Polycrsytalline diamond Compact and its Microstructure. Journal of the American Ceramics Society, 74(1), pp.5-10.

Akaishi, M., 1991. Synthesis of fine-grained Polycrsytalline diamond Compact and its Microstructure. Journal of the American Ceramics Society, 74(1), pp.5-10.

Andreyev, A.V., 1994. The wetting and bonding of diamond films by high melting point metals in the range of diamond thermodynamic stability. Diamond and Related Materials, 3, pp.1262-64.

Ardell, A.J, 1972. The effect of volume fraction on particle coarsening: Theoretical considerations. Acta Metallurgica, 20, pp.61-71.

Asl, S.K., Heydarzadeh Sohi, M., Hokamoto, K. & Uemura, M., 2006. Effect of heat treatment on wear behaviour of HVOF thermally sprayed WC-Co coatings. Wear, 260, pp.1203-08.

ASTM G65-04, 2010. Standard test method for measuring abrasion using the dry/rubber wheel apparatus. In Annual Book of ASTM Standards Volume 03.02. Philadelphia: ASTM.

ASTM, 1987. Standard Terminology Relating to Wear and Erosion, Annual Book of Standards. ASTM.

Belnap, J.D, 2009. Thermally-stable polycrystalline diamond materials and compacts, US 2009/0114454 A1.

Chapman, R.A. & Davies, G.J., 2002. Nucleation and superaturation in diamond synthesis. Element Six (Pty) Ltd Internal Research Report.

Choi, K., Hwang, N.M. & Kim, D.-Y., 2000. Effect of VC addition on microstructural evolution of WC-Co alloy: mechanism of grain growth inhibition. Powder Metallurgy, 43(2), pp.168 - 172.

Davies , G.J., Mfuma, L.M. & Peters, G.S., 2002. Model for the formation of Polycrystalline diamond products (PCD) interface structures. Element Six (Pty) Ltd Internal Research Report.

Davies, J.R., 2004. Handbook of thermal spray technology. ASM International.

Davies, G.J., 2009. Private Correspondence. Element Six (Pty) Ltd.

Davies, G.J. & Myburgh, J.L., 2008. Carbon enrichment technique for PCD raw materials.

Element Six (Pty) Ltd Internal Research Report.

de Villiers Lovelock, H.L., 1998. Powder/Processing/Structure Relationships in WC-Co Thermally Spray Coatings: A Review of Published Literature. Journal of Thermal Spray Technology, 7(3), pp.357-73.

Dorfman, M., DeFalcon, J. & Karthikeyan, J., 2000. Tunsten carbide-cobalt coatings for industrial applications. in Thermal spray: Surface Engineering via applied research. Proceeding of the 1st ITSC, Montreal Canada, May 2000, C Berndt ed., ASM International, pp.471 - 478.

Džepina, B., 2012. Electrophoretic (EPD) of diamond/diamond laminates. MSc Dissertation: Unversity of the Witwatersrand.

German, R., 1996. Sintering Theory and Practice. New York: Wiley & Sons.

GordonEngland, 2011. [Online] Available http://www.gordonengland.co.uk/wear.htm.

Hall, H.T., 1969. Science, 169, pp.868-69.

Hong, S.M. et al., 1988. Behaviour of Cobalt infiltration and abnormal grain growth during sintering of diamond on Co substrate. Journal Material of Science, 23, pp.3821-26.

Hong, S., Akaishi, M., Osawa, T. & Yamaoka, S., 1991. Synthesis of fine grained polycrystalline diamond compacts. New Diamond Science and Technology, pp.155-60.

Howse, H.J. & van Wyk, P., 1998. The application of thermal spray coatings for combating slurry erosion in centrifugal pumps. in: Proceedings of the 6th International Tribology Conference of South Africa Institute of Tribology/SAIT, pp.27 - 33.

Israelsson, G.J., Hannersjo, K.E. & Schelin, P.E.H., 2011. Patent WO 2011/ 042566 A1.

Kang, S-J L., 2005. Sintering: Densification, Grain Growth and Microstructure. Oxford: Elsevier Butterworth Heinmann.

Kang, M.-K., Kim, D.-Y. & Hwang, N.M., 2002. Ostwald ripening of angular grains dispersed in a liquid phase by 2D nucleation and AGG. Journal of the European Ceranics Society, 22, pp.603-12.

Kang, S.-J.L., Lee, M.-G. & An, S.-M., 2009. Microstructural evolution during sintering with control of the interface structure. Journal of the Americal Ceramics Society, 92(7), pp.1464-71.

Katzman, H. & Libby, W.F., 1971. Science, 172, pp.1132-34.

Khan, M.S.A. & Clyne, T.W., 1996. Microstructure and abrasive resistance of plasma sprayed cermets. Thermal Spray: Practical Solutions for Engineering Problems, pp.113-22.

Kim, J.H., Baik, K.H., Seong, B.G. & Hwang, S.Y., 2007. Effect of post-spraying threatment on wear resistance of WC-Co nano-composite coatings. Material Science and Engineering A, 449-451, pp.876-79.

Lei, Y. & Wu, E., 2009. Sintering characteristics and microstructure of WC-Co-VC/Cr3C2 ultrafine cemented carbides. Rare Metals, 28(5), pp.482-86.

Lifshitz, I.M. & Slyozov, V.W., 1961. Kinetics of precipitation from supersaturated solid solutions. Journal of Physical Chemistry Solids, 19(1-2), pp.35-50.

Li, C.-J., Ohmori, A. & Harada, Y., 1996. Effect of powder structure on the structure of thermally sprayed WC-Co coatings. Journal of Materials Science, 31, pp.785-94.

Machio, C.N., 2005. Preparation, charaterization and testing of WC-VC-Co HP/HVOF Theraml Spray Coatings. PhD Thesis: University of the Witwatersrand.

Machio, C.N., Akdogan, G., Witcomb, M.J. & Luyckx, S., 2005. Performance of WC-VC-Co thermal spray coatings in abrasive and slurry erosion tests. Wear, 258, pp.434 - 442.

Metco, S., 2011. Thermal Sparying. [Online] Available at: www.sulzermetco.com [Accessed 2011].

Mukhopadhyay, D.K. & Bertagnolli, K.E., 2011. Control of exaggerated WC grain growth at diamonf-substrate interface of polycrstalline diamond cutter (PDC). International Journal Refractory Metal and Hard Materials, 29, pp.361-64.

Naidoo, K., 2010. Composite diamond abrasive compact WO 2010/020962 A2.

Nerz, J., Kushner, B. & Rotolico, A., 1992. Microstructural evolution of tungsten carbide-cobalt coatings. Journal of Thermal Spray Technology, 1(2), pp.147-52.

Nic, M., Jirat, J. & Kosata, B., 2006-. Ostwald ripening. Online ed ed. IUPAC Compendium of Chemical Technology.

Ozbayraktar, S., 1995. PCD Sintering Model. Element Six (Pty) Ltd Internal Research Report.

Park, Y.J., Hwang, N.M. & Yoon, D.Y., 1996. Abnormal growth of faceted (WC) grains in a (Co) liquid matrix. Metallurgical and Materials Transactions A, 27A, pp.2809-19.

Perry, J.M., Hodgkiess, T. & Neville, A., 2000. Some aspects of the erosion and corrosion behaviour of a WC-Co-Cr HVOF sprayed coating. in Thermal spray: Surface Engineering. via applied research. Proceedings of 1st ITSC, Montreal Canada, May 2000, C Berndt ed., ASM International, pp.1033 - 1038.

Poeton, 2011. [Online] Available at: http://www.poeton.co.uk/w1/p-solver/erosive.htm. [September 2011]

Richert, M. & Leszczynska-Madej, B., 2011. Effect of annealing on the microstructure of HVOF deposited coatings. Journal of Achievements in Materials and Manufacturing Engineering., 46(1).

Riedel, R., 2000. Handbook of Ceramic Hard Materials. Wiley-VCH.

Salagaram, T., 2007. PhD Thesis: Application of the Anisotropic Coarsening Theory to the Liquid-Phase sintering of Si3N4. University of KwaZulu-Natal.

Santana, Y.Y., Renault, P.O., Sabastiani, M. & Barber, 2008. Characterization and residual stresses of WC-Co thermally sprayed coating. Surface & Coating Technologies, 202, pp.4560-65.

Shin, T.J., Oh, J.O., Oh, K.H. & Lee, D.N., 2004. The mechanism of abnormal grain growth in polycrystalline diamond during high pressure and high temperature sintering. Diamond and Related Materials, 13, pp.488-94.

Smith International, I., 1995. Daimond and cBN cutting tools, US 5441 817.

Stevenson, A.N.I. & Hutchings, I.M., 1996. Development of the dry/rubber wheel abrasion test. Wear, 195, pp.232-40.

Stewart, D.A., Shipway, P.H. & McCartney, D.G., 1998. Influence of heat treatment on the abrasive wear behaviour of HVOF sprayed WC-Co coatings. Surface and Coating Technology, 105, pp.13-24.

STLE, 2011. Society of tribologists and lubrication Engineers, Basics on Wear. [Online] Available at: http://www.stle.org/resources/lubelearn/wear/default.aspx [Accessed 2011].

Stromberg, H.D. & Stephans, D.R., 1970. Sintering of Diamond at 1800-1900°C and 60-65kBar, Journal of the American Ceramics Society, 49(2), pp.1030-32.

Sun, L., Yang, T., Jia, C. & Xiong, J., 2011. VC, Cr3C2 doped ultrafine WC-Co cemented carbides prepared by spark plasma sintering. International Journal of Refractory Metals and Hard Materials , 29, pp.147 - 152.

Wagner, C., 1961. Theory of precipitate change by redissolution. Z. Electrochem., 65, pp.581-91.

Wang, Q., Chen, Z.H. & Ding, Z.X., 2009. Performance of abrasive wear of WC-12Co coatings sprayed by HVOF. Tribology International, 42, pp.1046-51.

Wayne, S.F. & Sampath, S., 1992. Structure/Property Relationships in Sintered and Thermally Sprayed WC-Co. Journal of Thermal Spray Technology, 1(4), pp.307-15.

Wentorf, 1973. Patent SAP 7315038.

Yang, Q., Senda, T. & Ohmori, A., 2003. Effect of carbide grainsize on microstructure and sliding wear behavior of HVOF-sprayed WC-12%Co coatings. Wear, 254, pp.23-34.

Yarbrough, W.A. & Messier, R., 1990. Current issues and problems in the chemical vapor deposition of diamond. Science, 247, pp.688-96.

Yazu, S., 1997. Powders Powder Metall., 44, p.897.

Yu, H.C., Li, S. & Hu, E., 1994. Sintering of ultrafine diamond particles under high temperature and high pressure. Diamond and Related Materials, 3, pp.222-26.

Zhang, Y. et al., 2009. High pressure and high temperature sintering of fine grained PCD using bi-layered assembly. High Pressure Research, 29(2), pp.325-34.

APPENDIX A: Raman Carbon Analysis of Coatings

As the Raman spot size is less than 1µm, it is only possible to analyse a very small area of each sample. 64 positions in an 8x8 array covering an area of 100 x 100 µm were examined for each sample. The spectra are shown below.

WC 12% Co

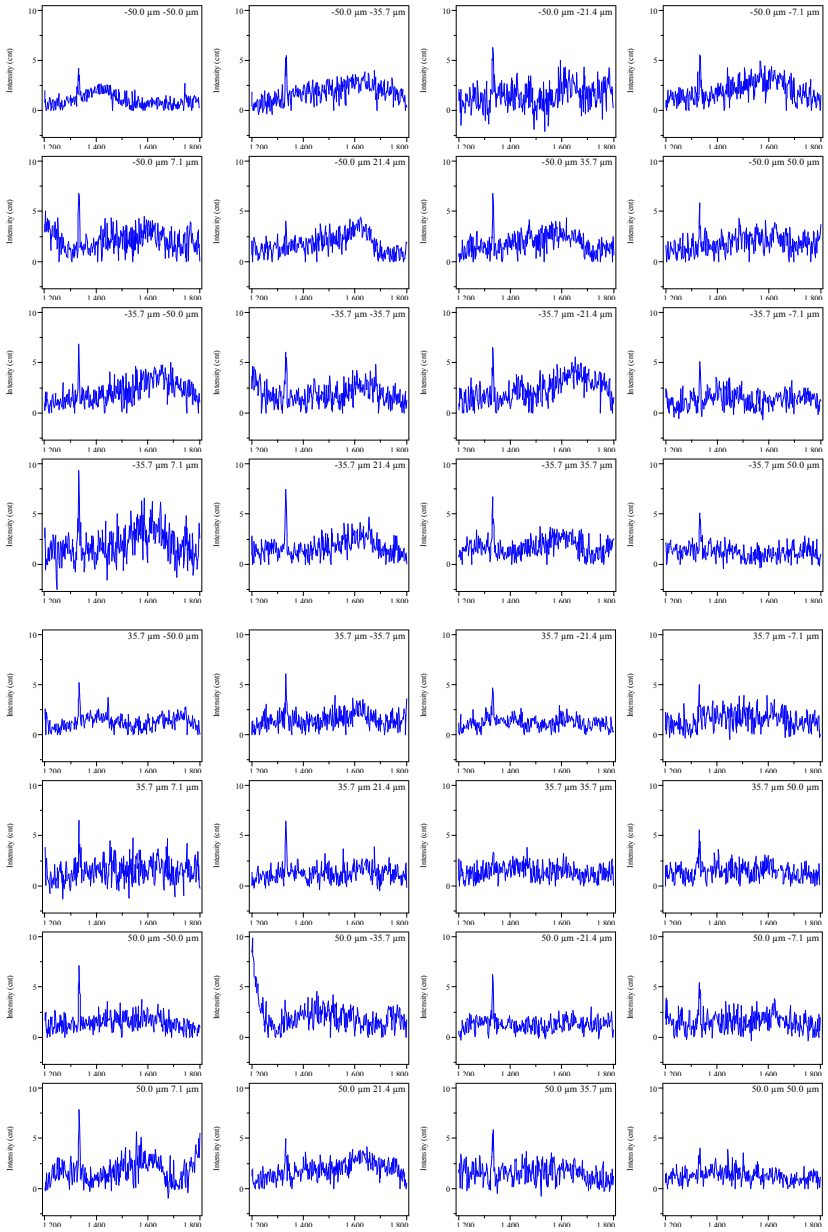

WC 12% Co 2% C

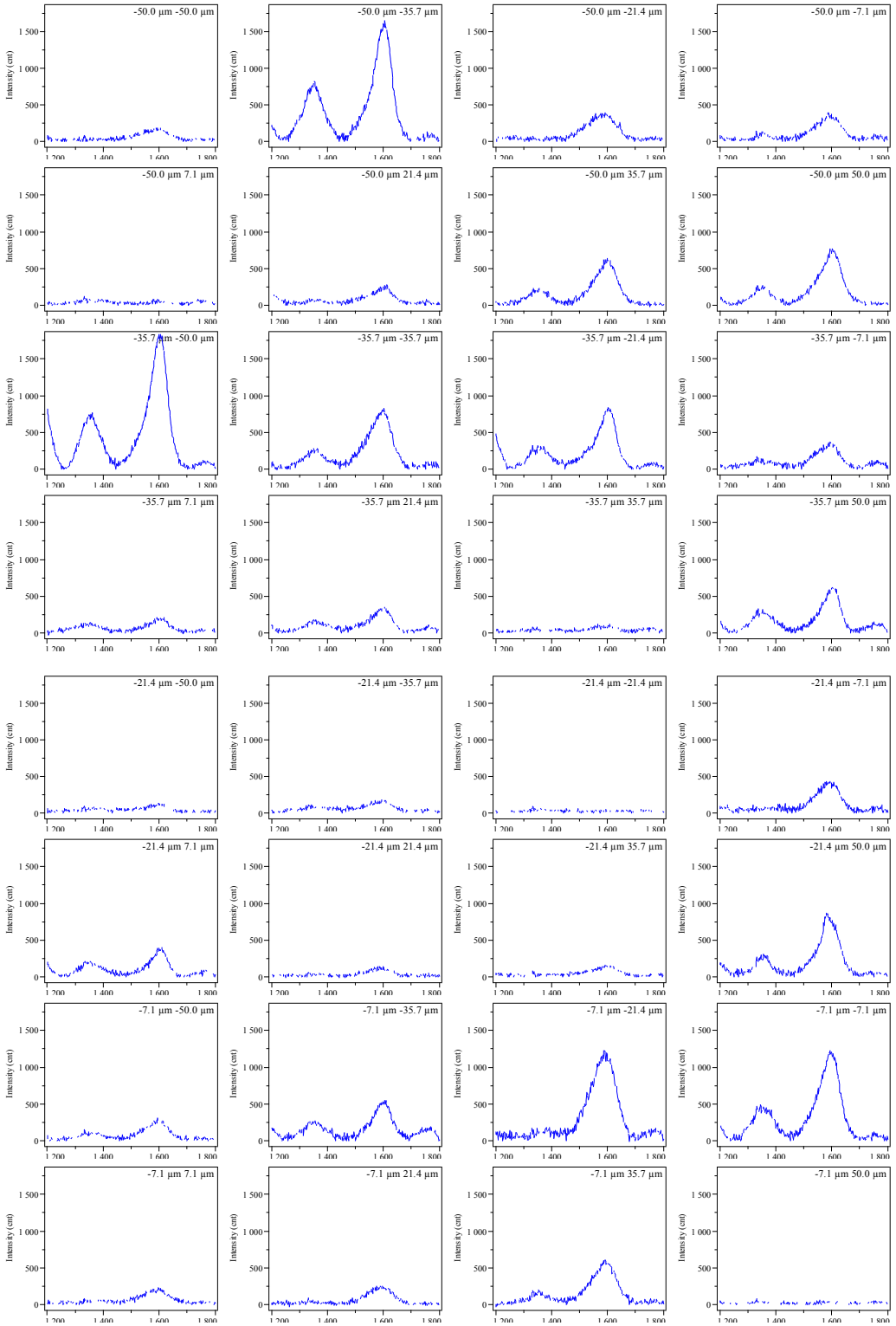
-50.0 µm -50.0 µm
-50.0 µm -35.7 µm
-50.0 µm -21.4 µm
-50.0 µm -7.1 µm
-50.0 µm 7.1 µm
-50.0 µm 21.4 µm
-50.0 µm 35.7 µm
-50.0 µm 50.0 µm
-35.7 µm -50.0 µm
-35.7 µm -35.7 µm
-35.7 µm -21.4 µm
-35.7 µm -7.1 µm
-35.7 µm 7.1 µm
-35.7 µm 21.4 µm
-35.7 µm 35.7 µm
-35.7 µm 50.0 µm
-21.4 µm -50.0 µm
-21.4 µm -35.7 µm
-21.4 µm -21.4 µm
-21.4 µm -7.1 µm
-21.4 µm 7.1 µm
-21.4 µm 21.4 µm
-21.4 µm 35.7 µm
-21.4 µm 50.0 µm
-7.1 µm -50.0 µm
-7.1 µm -35.7 µm
-7.1 µm -21.4 µm
-7.1 µm -7.1 µm
-7.1 µm 7.1 µm
-7.1 µm 21.4 µm
-7.1 µm 35.7 µm
-7.1 µm 50.0 µm
Intensity (cnt)
0
500
1 000
1 500
1 200
1 400
1 600
1 800

WC 12% Co 4% C

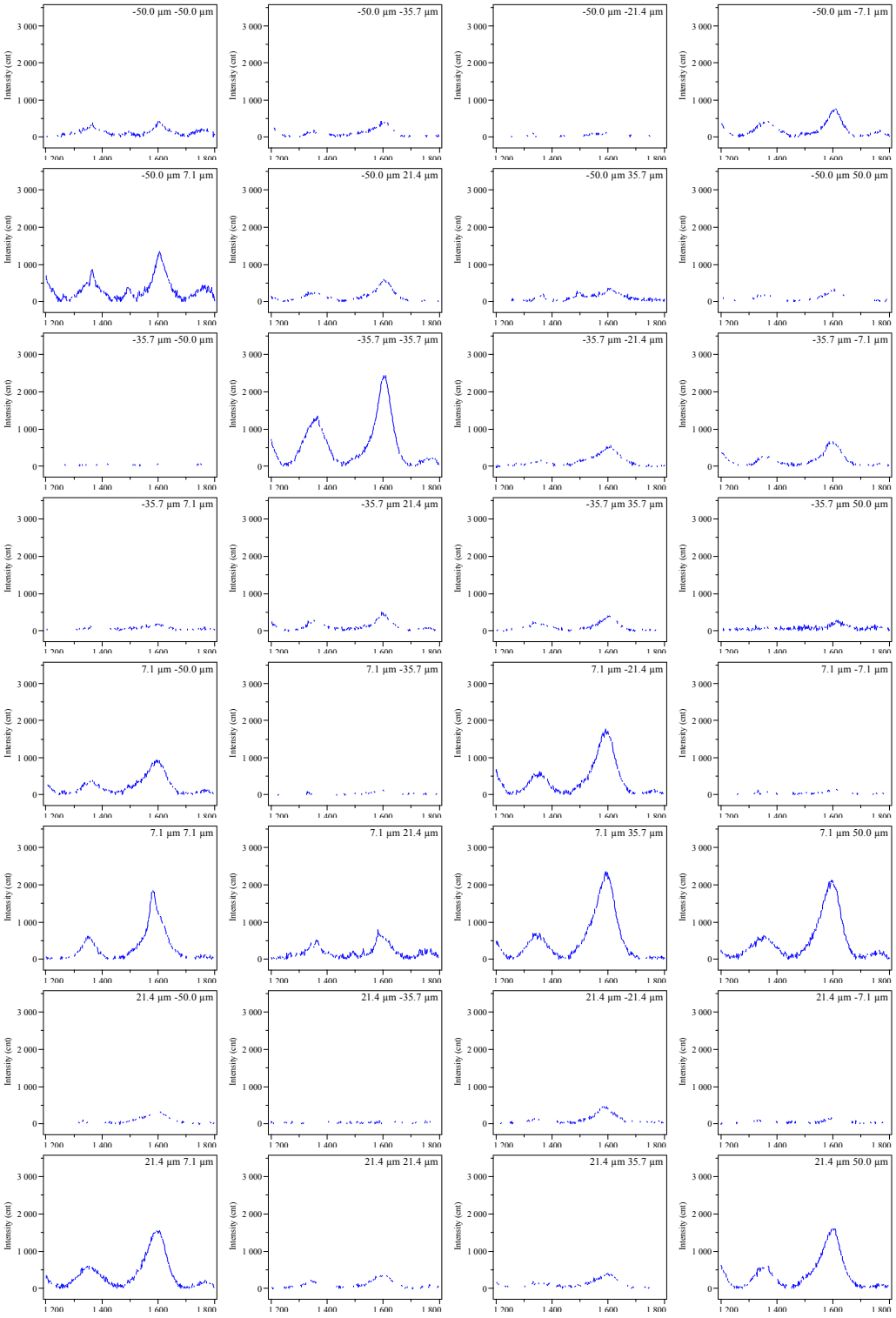
-50.0 µm -50.0 µm
-50.0 µm -35.7 µm
-50.0 µm -21.4 µm
-50.0 µm -7.1 µm
-50.0 µm 7.1 µm
-50.0 µm 21.4 µm
-50.0 µm 35.7 µm
-50.0 µm 50.0 µm
-35.7 µm -50.0 µm
-35.7 µm -35.7 µm
-35.7 µm -21.4 µm
-35.7 µm -7.1 µm
-35.7 µm 7.1 µm
-35.7 µm 21.4 µm
-35.7 µm 35.7 µm
-35.7 µm 50.0 µm
7.1 µm -50.0 µm
7.1 µm -35.7 µm
7.1 µm -21.4 µm
7.1 µm -7.1 µm
7.1 µm 7.1 µm
7.1 µm 21.4 µm
7.1 µm 35.7 µm
7.1 µm 50.0 µm
21.4 µm -50.0 µm
21.4 µm -35.7 µm
21.4 µm -21.4 µm
21.4 µm -7.1 µm
21.4 µm 7.1 µm
21.4 µm 21.4 µm
21.4 µm 35.7 µm
21.4 µm 50.0 µm
Intensity (cnt)
0
1 000
2 000
3 000
1 200
1 400
1 600
1 800

WC 12% Co 6% C

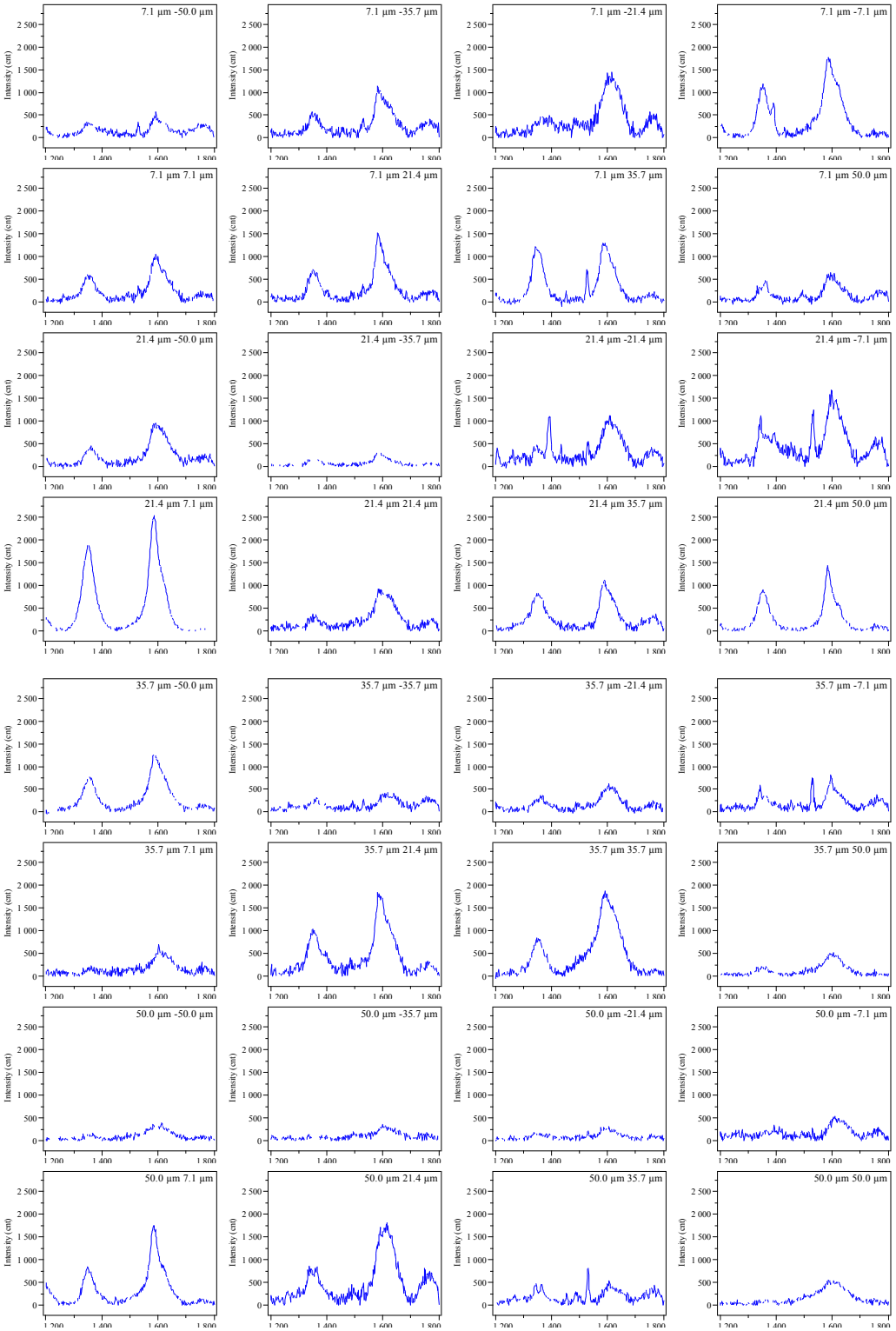
7.1 µm -50.0 µm
7.1 µm -35.7 µm
7.1 µm -21.4 µm
7.1 µm -7.1 µm
7.1 µm 7.1 µm
7.1 µm 21.4 µm
7.1 µm 35.7 µm
7.1 µm 50.0 µm
21.4 µm -50.0 µm
21.4 µm -35.7 µm
21.4 µm -21.4 µm
21.4 µm -7.1 µm
21.4 µm 7.1 µm
21.4 µm 21.4 µm
21.4 µm 35.7 µm
21.4 µm 50.0 µm
35.7 µm -50.0 µm
35.7 µm -35.7 µm
35.7 µm -21.4 µm
35.7 µm -7.1 µm
35.7 µm 7.1 µm
35.7 µm 21.4 µm
35.7 µm 35.7 µm
35.7 µm 50.0 µm
50.0 µm -50.0 µm
50.0 µm -35.7 µm
50.0 µm -21.4 µm
50.0 µm -7.1 µm
50.0 µm 7.1 µm
50.0 µm 21.4 µm
50.0 µm 35.7 µm
50.0 µm 50.0 µm
Intensity (cnt)

WC 17% Co

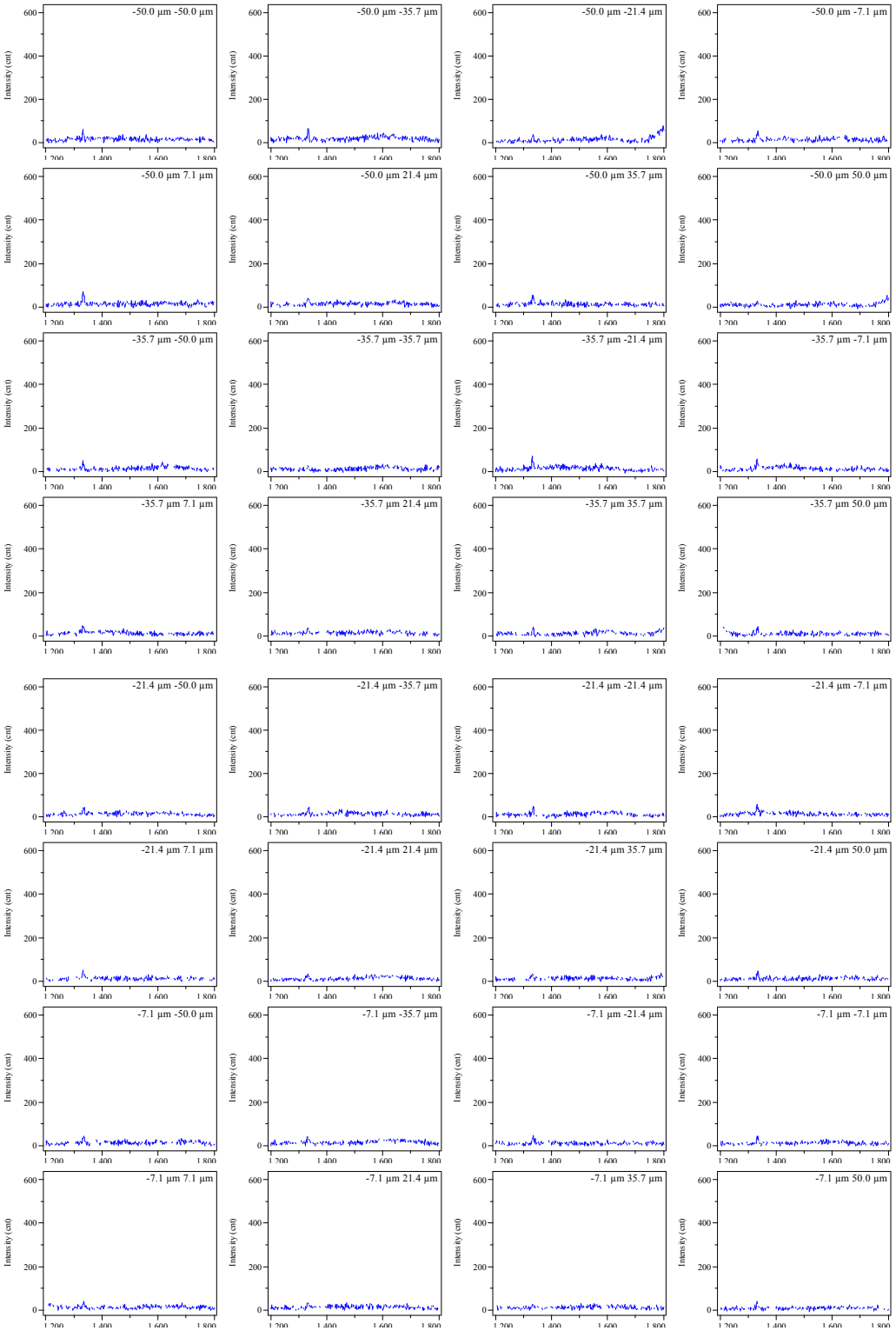
-50.0 µm -50.0 µm
-50.0 µm -35.7 µm
-50.0 µm -21.4 µm
-50.0 µm -7.1 µm
-50.0 µm 7.1 µm
-50.0 µm 21.4 µm
-50.0 µm 35.7 µm
-50.0 µm 50.0 µm
-35.7 µm -50.0 µm
-35.7 µm -35.7 µm
-35.7 µm -21.4 µm
-35.7 µm -7.1 µm
-35.7 µm 7.1 µm
-35.7 µm 21.4 µm
-35.7 µm 35.7 µm
-35.7 µm 50.0 µm
-21.4 µm -50.0 µm
-21.4 µm -35.7 µm
-21.4 µm -21.4 µm
-21.4 µm -7.1 µm
-21.4 µm 7.1 µm
-21.4 µm 21.4 µm
-21.4 µm 35.7 µm
-21.4 µm 50.0 µm
-7.1 µm -50.0 µm
-7.1 µm -35.7 µm
-7.1 µm -21.4 µm
-7.1 µm -7.1 µm
-7.1 µm 7.1 µm
-7.1 µm 21.4 µm
-7.1 µm 35.7 µm
-7.1 µm 50.0 µm
Intensity (cnt)

WC 17% Co 2% C

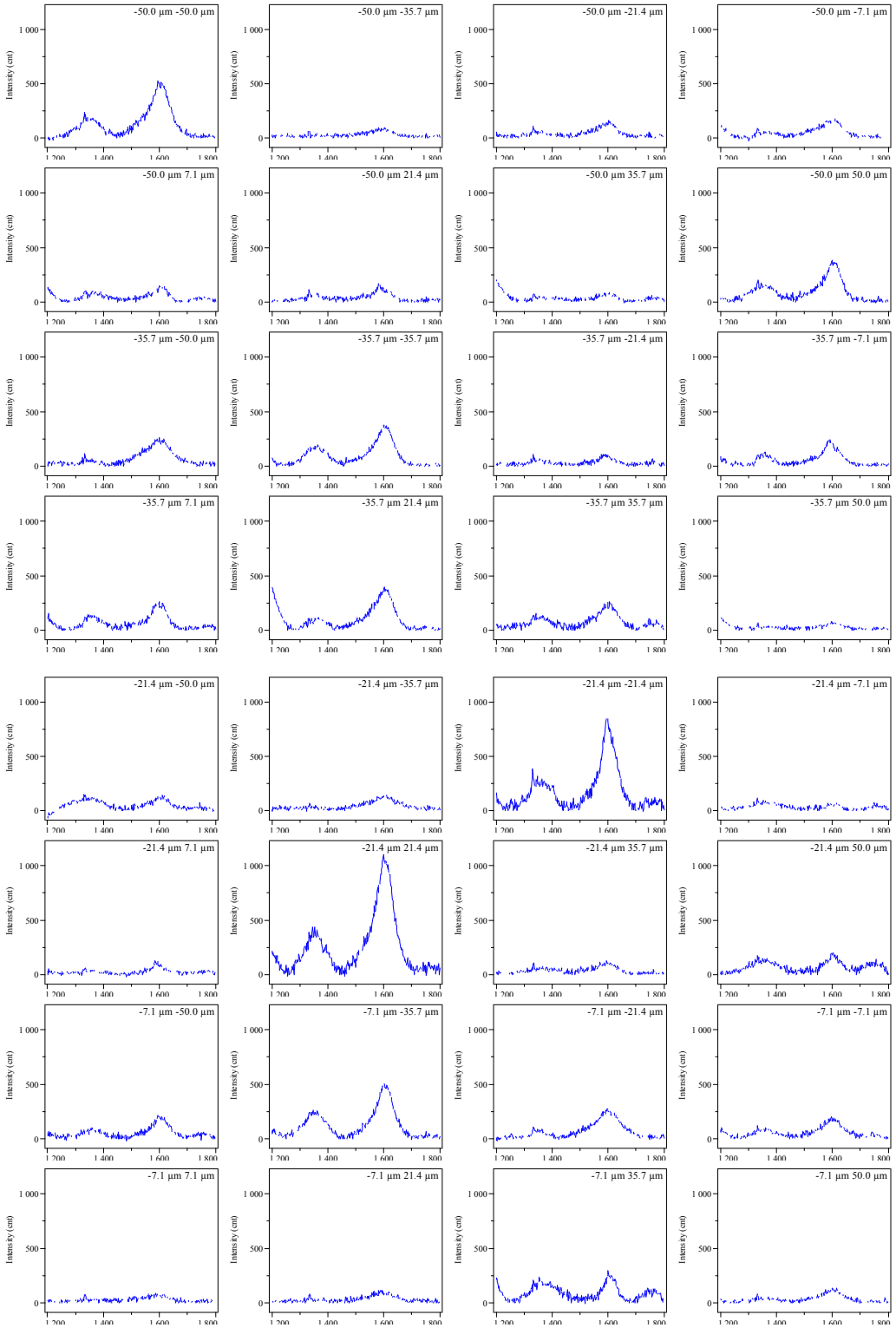
-50.0 µm -50.0 µm
-50.0 µm -35.7 µm
-50.0 µm -21.4 µm
-50.0 µm -7.1 µm
-50.0 µm 7.1 µm
-50.0 µm 21.4 µm
-50.0 µm 35.7 µm
-50.0 µm 50.0 µm
-35.7 µm -50.0 µm
-35.7 µm -35.7 µm
-35.7 µm -21.4 µm
-35.7 µm -7.1 µm
-35.7 µm 7.1 µm
-35.7 µm 21.4 µm
-35.7 µm 35.7 µm
-35.7 µm 50.0 µm
-21.4 µm -50.0 µm
-21.4 µm -35.7 µm
-21.4 µm -21.4 µm
-21.4 µm -7.1 µm
-21.4 µm 7.1 µm
-21.4 µm 21.4 µm
-21.4 µm 35.7 µm
-21.4 µm 50.0 µm
-7.1 µm -50.0 µm
-7.1 µm -35.7 µm
-7.1 µm -21.4 µm
-7.1 µm -7.1 µm
-7.1 µm 7.1 µm
-7.1 µm 21.4 µm
-7.1 µm 35.7 µm
-7.1 µm 50.0 µm
Intensity (cnt)
1 000
500
0
1 200
1 400
1 600
1 800

WC 17% Co 4% C


-50.0 µm -50.0 µm
-50.0 µm -35.7 µm
-50.0 µm -21.4 µm
-50.0 µm -7.1 µm
-50.0 µm 7.1 µm
-50.0 µm 21.4 µm
-50.0 µm 35.7 µm
-50.0 µm 50.0 µm
-35.7 µm -50.0 µm
-35.7 µm -35.7 µm
-35.7 µm -21.4 µm
-35.7 µm -7.1 µm
-35.7 µm 7.1 µm
-35.7 µm 21.4 µm
-35.7 µm 35.7 µm
-35.7 µm 50.0 µm
-21.4 µm -50.0 µm
-21.4 µm -35.7 µm
-21.4 µm -21.4 µm
-21.4 µm -7.1 µm
-21.4 µm 7.1 µm
-21.4 µm 21.4 µm
-21.4 µm 35.7 µm
-21.4 µm 50.0 µm
-7.1 µm -50.0 µm
-7.1 µm -35.7 µm
-7.1 µm -21.4 µm
-7.1 µm -7.1 µm
-7.1 µm 7.1 µm
-7.1 µm 21.4 µm
-7.1 µm 35.7 µm
-7.1 µm 50.0 µm
Intensity (cnt)
40 000
30 000
20 000
10 000
0
1 200
1 400
1 600
1 800

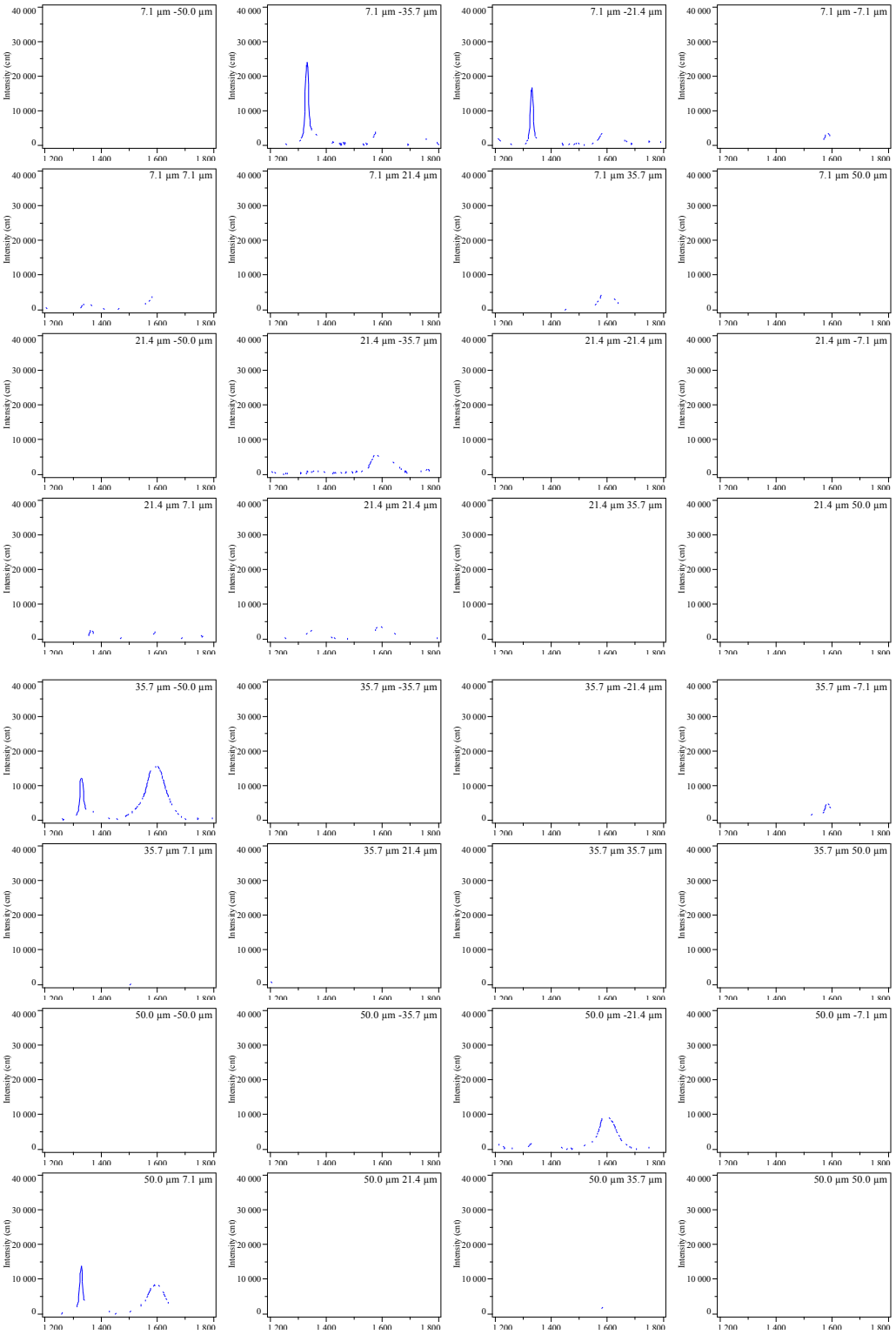
7.1 µm -50.0 µm
7.1 µm -35.7 µm
7.1 µm -21.4 µm
7.1 µm -7.1 µm
7.1 µm 7.1 µm
7.1 µm 21.4 µm
7.1 µm 35.7 µm
7.1 µm 50.0 µm
21.4 µm -50.0 µm
21.4 µm -35.7 µm
21.4 µm -21.4 µm
21.4 µm -7.1 µm
21.4 µm 7.1 µm
21.4 µm 21.4 µm
21.4 µm 35.7 µm
21.4 µm 50.0 µm
35.7 µm -50.0 µm
35.7 µm -35.7 µm
35.7 µm -21.4 µm
35.7 µm -7.1 µm
35.7 µm 7.1 µm
35.7 µm 21.4 µm
35.7 µm 35.7 µm
35.7 µm 50.0 µm
50.0 µm -50.0 µm
50.0 µm -35.7 µm
50.0 µm -21.4 µm
50.0 µm -7.1 µm
50.0 µm 7.1 µm
50.0 µm 21.4 µm
50.0 µm 35.7 µm
50.0 µm 50.0 µm
Intensity (cnt)
40 000
30 000
20 000
10 000
0
1 200
1 400
1 600
1 800

WC 17% Co 6% C

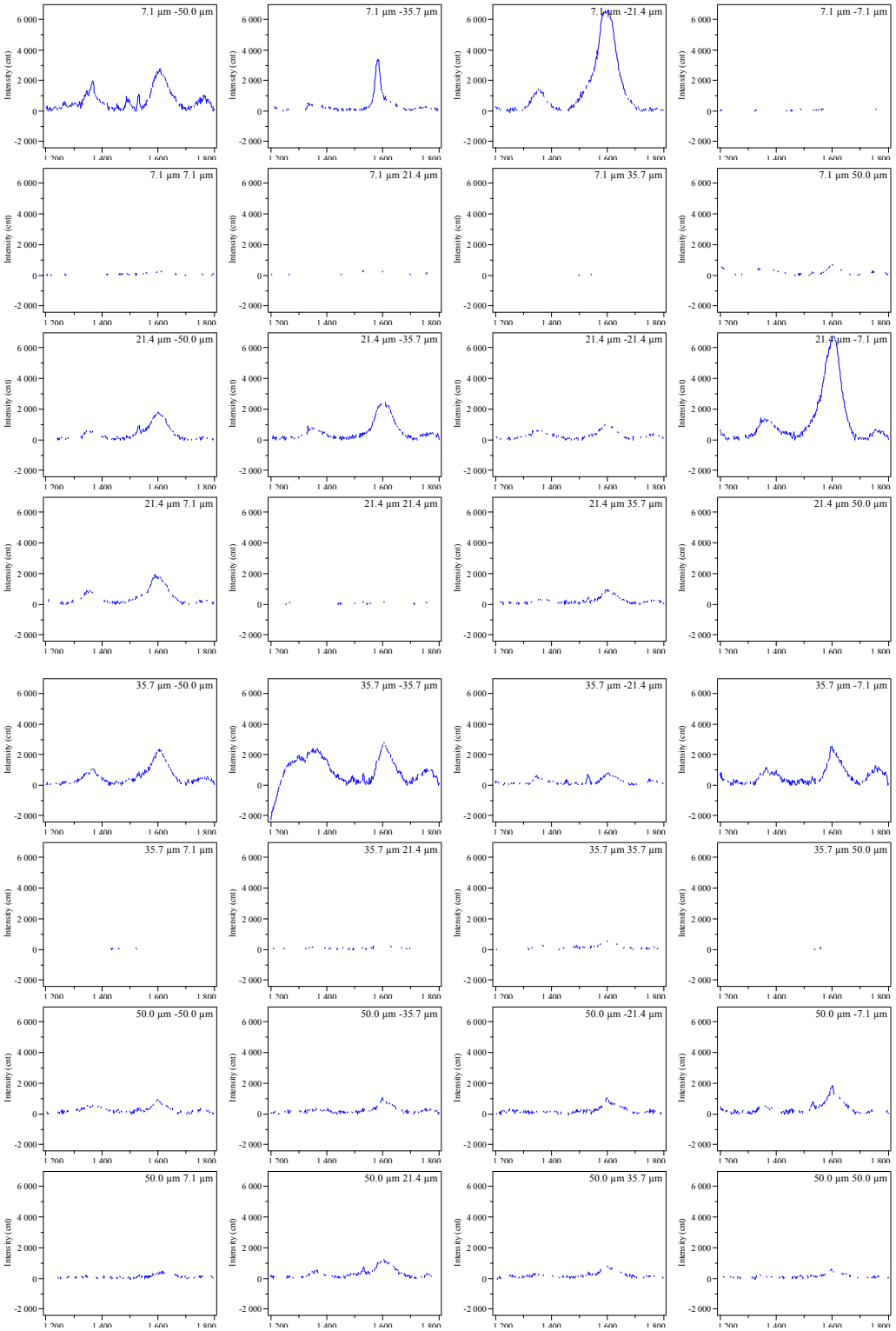
7.1 µm -50.0 µm
7.1 µm -35.7 µm
7.1 µm -21.4 µm
7.1 µm -7.1 µm
7.1 µm 7.1 µm
7.1 µm 21.4 µm
7.1 µm 35.7 µm
7.1 µm 50.0 µm
21.4 µm -50.0 µm
21.4 µm -35.7 µm
21.4 µm -21.4 µm
21.4 µm -7.1 µm
21.4 µm 7.1 µm
21.4 µm 21.4 µm
21.4 µm 35.7 µm
21.4 µm 50.0 µm
35.7 µm -50.0 µm
35.7 µm -35.7 µm
35.7 µm -21.4 µm
35.7 µm -7.1 µm
35.7 µm 7.1 µm
35.7 µm 21.4 µm
35.7 µm 35.7 µm
35.7 µm 50.0 µm
50.0 µm -50.0 µm
50.0 µm -35.7 µm
50.0 µm -21.4 µm
50.0 µm -7.1 µm
50.0 µm 7.1 µm
50.0 µm 21.4 µm
50.0 µm 35.7 µm
50.0 µm 50.0 µm
Intensity (cnt)